Atomistic Insights Into the Transport of Solvents and Salt Ions in Polymer-based Membranes Constructed via an Interfacial Polymerization

by

Gunolla Nagendra Prasad

A thesis submitted

in Partial Fulfillment of the Requirements

for the Degree of

DOCTOR OF PHILOSOPHY

under the supervision of

Prof. Chandan Das & Prof. Anki Reddy Katha

Department of Chemical Engineering

Indian Institute of Technology Guwahati

Guwahati 781039, India

June, 2025

Abstract

Membrane technology stands as a cornerstone in desalination and wastewater treatment, playing a crucial role in the selective separation of solvents and solutes through the active layer of composite membranes. Although significant advancements have been made, there remains substantial potential to enhance membrane performance for desalination applications, which is the primary focus of this thesis. In this study, we conduct a comprehensive computational investigation of polymer-based membranes under diverse conditions, examining the behavior of various solvents and solutes. The research focuses on various membrane types, including polyamide, semi-aromatic, polyester, and polyimine, and evaluates their performance in forward osmosis (FO) and nanofiltration (NF) processes. These evaluations are carried out using both equilibrium and non-equilibrium molecular dynamics simulations, contributing to the ongoing advancements in membrane technology and its applications in desalination.

Despite the increased interest in forward osmosis (FO) in recent years, the technology's advancement in commercial and industrial applications has been hampered by the absence of suitable FO membranes and ideal draw solutes, which demands the exploration of new membranes and novel draw solutes targeted for some specific applications. In this context, we considered a semi−aromatic polyamide (SAPA) for an application where monovalent salt can be permeated but has high selectivity towards divalent salt and with excellent water permeability. In this regard, we constructed an atomistic model for the membrane via a heuristic approach using an equilibrated mixture of hydrolyzed trimesoyl chloride and piperazine monomers and performed non−equilibrium molecular dynamics simulations on the SAPA membrane in the FO process to understand the structural properties and performance of the membrane at the atomistic level. We used pure water as the feed and Na_2SO_4 as the draw solution. It is observed that the SAPA membrane shows excellent water permeability and no reverse draw solute flux. To further test the dynamics of salt ions inside the membranes, we performed two distinct equilibrium simulations on systems consisting of either monovalent salt, such as NaCl, or divalent salt, such as Na_2SO_4. The atomistic details of the interactions between the functional groups of the membrane and salt ions provided in this work can inspire further experiments on SAPA membranes in the context of separation of monovalent and divalent salts, which have applications in the treatment of textile industry wastewater.

We performed equilibrium molecular dynamics simulations to study the transport of wa-

ter and hexane solvents through cyclodextrin(CD)−based membranes (α-/β-/γ-CD/TMC). Although it is known that water and hexane can permeate through the macrocyclic cavity, surprisingly, when it is present in the CD−based membrane (α-/β-/γ-CD/TMC), these solvents are not permeating through the CD cavity. Interactions between membrane functional group atoms with the water and hexane suggest that these solvents primarily permeate through the polar aggregate pores formed via ester-linkage rather than the CD cavity. Our observation reveals that both solvents can permeate through the membrane; however, the hexane flux was one order of magnitude lower than water. Our study suggests that further work is needed to confirm the functional significance of the macrocyclic cavity in solvent permeation and the existence of Janus pathways.

Conventional treatment methods are often ineffective in eliminating organic dyes, which are among the most frequently discharged pollutants in wastewater. The present work explored a polyimine-based membrane in the context of textile wastewater treatment. This study employs classical molecular dynamics simulations to evaluate the efficacy of polyimine membranes. A reliable atomistic model of the membrane was constructed using an equilibrated mixture of melamine and 1,3,5-triformylphloroglucinol monomers. Non-equilibrium molecular dynamics (NEMD) simulations were performed on the constructed membrane system to investigate the performance of the polyimine membrane in a nanofiltration (NF) process using a mixed feed of NaCl salt, dye, and water. We observed that the polyimine membrane demonstrates excellent water permeability, effectively rejects dye, and allows the passage of NaCl salt. The atomistic insights into membrane-salt ion interactions and membrane-dye interactions provided in this work can inspire further experimental investigations into poly-imine membranes for separating salts and dyes, particularly in the treatment of textile industry wastewater.

Polyamide nanofilm composite membranes, featuring an ultrathin polyamide selective layer, are extensively utilized in desalination and water treatment applications. They can also operate as separation membranes in non-aqueous solvents when supported on solvent-stable substrates. The solvent permeance of these membranes is intrinsically linked to the energy consumption in separation processes. Enhancing permeance through solvent activation of the polyamide structure offers a pathway to significant energy savings. Achieving this requires a detailed understanding of the internal structure of polyamide in solvents and the underlying permeation mechanism. In this study, solvent permeation experiments and equilibrium molecular dynamics (EMD) simulations were conducted to unravel the mechanism of solvent transport

in solventactivated polyamide membranes. The activation effect of dimethylformamide (DMF) was examined, demonstrating notable alterations in pore size distribution and a 300% increase in methanol permeance. Interestingly, this enhancement was reversed upon drying, indicating that solvent activation induces a thermodynamic non-equilibrium state, with the membrane structure relaxing to its original state after drying. This study, through precise evaluation of solvent-membrane affinity, provides valuable experimental and molecular insights into the structure-property-performance relationship of polyamide nanofilms, underscoring their potential for broader applications in advanced separation technologies.

Department of Chemical Engineering

Indian Institute of Technology Guwahati

DECLARATION

I, hereby declare that the work contained in this thesis entitled "**Atomistic Insights Into the Transport of Solvents and Salt Ions in Polymer-based Membranes Constructed via an Interfacial Polymerization**" is original and has been done by me at the Department of Chemical Engineering, Indian Institute of Technology Guwahati, Guwahati, India, under the supervision of **Prof. Chandan Das** and **Prof. Anki Reddy Katha**. The work has not been submitted to any other Institute for any degree or diploma. I have followed the guidelines provided by the Institute in preparing the thesis. I have confirmed to the norms and guidelines given in the Ethical Code of Conduct of the Institute.

Gunolla Nagendra Prasad

Registration No: 196107005

Department of Chemical Engineering

IIT Guwahati,

Guwahati-781039, Assam, India.

DATE: .....

Department of Chemical Engineering

Indian Institute of Technology Guwahati

CERTIFICATE

It is certified that the work described in this thesis entitled **"Atomistic Insights Into the Transport of Solvents and Salt Ions in Polymer-based Membranes Constructed via an Interfacial Polymerization"** by **Gunolla Nagendra Prasad** for the award of the degree of Doctor of Philosophy is an authentic record of the results obtained from the research work carried out under our supervision at the Department of Chemical Engineering, Indian Institute of Technology Guwahati, Guwahati, India. This work has not been submitted elsewhere for a degree.

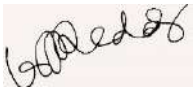

Prof. Chandan Das
Professor
Department of Chemical Engineering
Indian Institute of Technology Guwahati
Guwahati-781039, Assam, India.

Prof. Anki Reddy Katha
Professor
Department of Chemical Engineering
Indian Institute of Technology Tirupati
Tirupati-517619, Andhra Pradesh, India.

Acknowledgements

This doctoral thesis would not be completed without the help and extended hands of several people. I take this opportunity to express my sincere thankfulness to all of them.

Firstly, my sincere gratitude to my supervisors, Prof. Chandan Das and Prof. Anki Reddy Katha for their continuous support, motivation and guidance throughout my Ph.D. thesis work. I would also like to acknowledge my doctoral committee members: Prof. Purkait Mihir Kumar, Prof. Pugazhenthi G., and Prof. Aditya Narayan Panda. Their valuable suggestions and critical comments shaped the presented thesis work. Besides, I would also like to thank all the Chemical Engineering office, Academic office, Student Affair, and Finance staff members. They were always available whenever I required.

I would also like to thank IITG and the Government of India for providing HPC facility (Param-Ishan and Param-Kamrupa) for conducting the simulations, which would have taken a long time otherwise. I want to extend my sincere gratitude to the Ministry of Human Resource Development for providing financial assistance, making the Ph.D. journey much more manageable.

I would like to express my heartfelt gratitude to Dr. Santanu Karan, Principal Scientist in the Membrane Science & Separation Technology (MS&ST) Division at CSIR-CSMCRI, Bhavnagar, Gujarat, India. His insightful discussions and invaluable guidance throughout my Ph.D. have been truly enriching. The knowledge and perspectives he shared have significantly contributed to my research, and I deeply appreciate his support and encouragement.

I want to extend my gratitude to all my fellow friends: Dr. Shivam Tiwari, Dr. Bitang Kwrung Tripura, Dr. Vamsi Krishna Reddy, Mr. Kranthi Kumar, Dr. Pilli Rajasekhar Reddy, Mr. Adupa Vasistha for their contributions towards my Ph.D. work directly or indirectly. Lastly, I would like to thank my family for the unconditional love and support they showered on me.

Contents

1 Introduction **1**

1.1 Why Membrane Technologies? . . . 1

1.1.1 Reverse Osmosis (RO) Process . . . 3

1.1.2 Forward Osmosis (FO) Process . . . 5

1.1.3 Nanofiltration (NF) Process . . . 7

1.2 Literature Review . . . 8

1.2.1 Background of Polyamide Membrane . . . 8

1.2.2 Background of Semi-aromatic Polyamide Membrane . . . 10

1.2.3 Background of Ester-based Membranes . . . 11

1.2.4 Background of Polyimine-based Membranes . . . 12

1.3 Motivation . . . 14

1.4 Objectives . . . 16

1.5 Thesis Organization . . . 16

Bibliography . . . 17

2 Simulation Methodology **31**

2.1 Introduction to Molecular Dynamics . . . 31

2.2 Forcefield . . . 32

2.3 Energy Minimization . . . 35

2.3.1 Steepest Descent . . . 37

2.3.2 Conjugate Gradient . . . 38

2.3.3 Convergence Criteria . . . 38

2.4 Periodic Boundary Condition . . . 39

2.4.1 Minimum Image Convention and Cutoff . . . 39

2.5 Integration of Equations of Motion . . . 41
2.5.1 Verlet Algorithm . . . 41
2.5.2 Velocity Verlet Algorithm . . . 43
2.6 Ewald Summation . . . 44
2.7 Ensemble . . . 45
2.7.1 Microcanonical(NVE) Ensemble . . . 46
2.7.2 Canonical(NVT) Ensemble . . . 47
2.7.3 Isobaric-Isothermal(NPT) Ensemble . . . 49
2.8 Constraints . . . 51
2.9 Water Models . . . 52
2.10 CHARMM Force Field Parametrization . . . 55
2.11 Softwares used and Implementation . . . 57
Bibliography . . . 59

3 Semi−Aromatic Polyamide−Based Membrane in Forward Osmosis: Molecular Insights 63
3.1 Introduction . . . 63
3.2 Methodology . . . 65
3.2.1 Membrane Model . . . 65
3.2.2 FO Simulation System . . . 69
3.3 Results and Discussion . . . 71
3.3.1 Semi−aromatic Membrane Structure . . . 71
3.3.2 Water Structure and Dynamics . . . 75
3.3.3 Water Permeance . . . 78
3.3.4 Reverse Draw Solute Flux . . . 82
3.3.5 Sulphate Salt versus Chloride Salt . . . 82
3.4 Conclusions . . . 87
Bibliography . . . 89

4 Non−Preferential Solvent Transport Through Intrinsic Cyclodextrin Pore in a Polyester Film 98
4.1 Introduction . . . 98
4.2 Methodology . . . 102

4.2.1 Membrane Model . . . 102
4.2.2 Equlibrium Molecular Dynamics Simulations (EMD) . . . 104
4.3 Results and Discussion . . . 105
4.3.1 Membrane Solvation and Structure . . . 105
4.3.2 Water Structure . . . 107
4.3.3 Pathways and Permeation Mechanism . . . 108
4.4 Conclusions . . . 116
Bibliography . . . 117

5 Atomistic Insights into High-Performance Polyimine-based Membranes for Selective Dye Rejection and Salt Permeation in Nanofiltration 127
5.1 Introduction . . . 127
5.2 Methodology . . . 130
5.2.1 Force Field Parameterization . . . 130
5.2.2 Construction of Molecular Membrane Model . . . 134
5.2.3 Details of Nanofiltration (NF) Setup . . . 137
5.3 Results and Discussion . . . 139
5.3.1 Polyimine Membrane Structure . . . 139
5.3.2 Water Structure . . . 141
5.3.3 Permeance and Pathways Mechanism . . . 141
5.3.4 Dynamics of Chloride Salt and BBR Dye . . . 144
5.4 Conclusions . . . 147
Bibliography . . . 147

6 Investigating Solvent Activation of Polyamide Nanofilm Composite Membranes: Insights from Experimental and Molecular Modelling Approaches 156
6.1 Introduction . . . 156
6.2 Simulation Methodology . . . 158
6.2.1 Construction of the Atomic Model of the Membrane . . . 158
6.2.2 Equlibrium Molecular Dynamics Simulations . . . 161
6.3 Results and Discussion . . . 162
6.3.1 Molecular Dynamics Simulation Study of the Membrane and the Effect of Solvent Activation . . . 162

6.3.2 Experimental Validation on DMF Activation of the Polyamide Membrane on the Permeance of Methanol . . . 169
6.4 Conclusions . . . 171
Bibliography . . . 172

7 Conclusions and Future Scope **176**
7.1 Conclusions . . . 176
7.2 Scope for Future Investigations . . . 178

A Research Output **180**

B Supplementary Information for Specific Chapters **182**
B.1 Supplementary Information for Chapter 4 . . . 183
Bibliography . . . 192
B.2 Supplementary Information for Chapter 5 . . . 193
B.3 Supplementary Information for Chapter 6 . . . 201
B.3.1 Fabrication of Freestanding Polyamide Nanofilm and Transfer Onto Porous Alumina Substrates . . . 202
B.3.2 Characterization of the Polyamide Nanofilm Composite Membranes . . . 203
B.3.3 Filtration Setup and Performance Measurements of the Polyamide Membranes . . . 204
B.3.4 Characterization of the Polyamide Nanofilm Before and After DMF Activation . . . 204

Chapter 1

Introduction

In the 21^{st} century, freshwater scarcity remains a critical global challenge. Desalination, leveraging the vast potential of oceanic water, has emerged as a promising solution [1–3]. Over the past two decades, the global desalination market has expanded significantly in arid regions like the Middle East and North Africa, where freshwater is scarce, and in non-arid countries that have adopted desalination to enhance water supply and conservation efforts [4–7]. As urban populations grow, desalination is becoming increasingly competitive with conventional water treatment methods, driving down costs [8]. Desalination technologies are primarily classified into two categories: thermal-based and membrane-based. While thermal desalination is prevalent in the Middle East due to its historical development and suitability for Gulf water, membrane-based desalination dominates the global market. The present chapter of this thesis briefly discusses membrane-based technologies and polymer-based membranes for desalination and wastewater treatment.

1.1 Why Membrane Technologies?

Water scarcity is one of the most pressing challenges of our time, exacerbated by rapid population growth and industrialization. Despite Earth's vast water resources, estimated at 1.4 billion cubic kilometers, only 2.5% is freshwater, with a mere 0.014% readily accessible for human use [9]. This stark reality highlights the urgent need for innovative solutions to ensure a sustainable supply of safe drinking water. Desalination has emerged as a pivotal technology in this endeavor, transforming saline or contaminated water into potable water by removing salts and dissolved solids from seawater and brackish water, providing a crucial source of freshwater for

domestic and industrial applications to meet the growing demand. Various desalination processes, including distillation, geothermal desalination, electro-deionization, ion exchange, solar desalination, and membrane-based methods, have been developed to address this global issue [10]. Among these, membrane-based techniques such as reverse osmosis (RO), forward osmosis, nanofiltration, ultrafiltration, and microfiltration have evolved as leading technologies. These processes are characterized by their ability to selectively reject contaminants based on size, with micro- and ultrafiltration membranes filtering suspended particles and macromolecules (∼10-0.01 μm), and RO and nanofiltration effectively removing ions (∼0.01-0.0001 μm) [11].

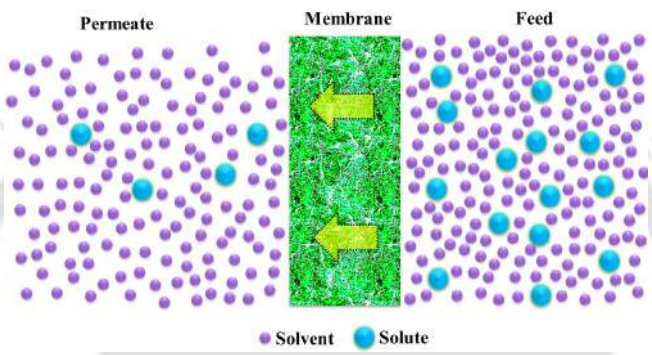

Figure 1.1: A simple membrane separation process.

Membrane separation is recognized as a leading advanced separation technique, marking a significant breakthrough in contemporary separation science and technology. Its vast applications extend across industries such as food and beverage, paper and pulp, metallurgy, textiles, automotive, dairy, pharmaceuticals, water treatment, and various process industries. The versatility of membrane technology has made it indispensable in these fields, offering exceptional flux rates, high efficiency, ease of operation and maintenance, potential for process integration, chemical and thermal stability, resilience under high pressures, and overall cost-effectiveness. A membrane acts as a semi-permeable barrier, selectively allowing specific components to pass through while retaining others, effectively dividing the process stream into retentate and permeate regions. This principle is visually depicted in Figure 1.1, illustrating the membrane material's separation of feed and permeate streams. Membrane separation relies on differences in physical and chemical properties, such as size (membrane filtration), charge (electrodialysis, ion exchange), affinity (reverse osmosis, forward osmosis), and vapor pressure (membrane distillation). The driving forces behind these processes include pressure gradients, concentra-

tion gradients, and electric potential gradients. This thesis explores polymeric membranes for desalination, with a focus on advancing understanding through computational modeling.

1.1.1 Reverse Osmosis (RO) Process

As the name suggests, reverse osmosis is the opposite phenomenon of osmosis. Osmosis describes the spontaneous flow of water from a dilute to a more concentrated solution when separated from each other by a suitable membrane. These membranes allow the free passage of water but not of dissolved substances, and van't Hoff suggested the adjective 'semi-permeable' to describe this property [12]. During osmosis, when water moves away from low concentration regions, it causes these regions to become more concentrated. On the other side, when water moves into areas of high concentration, solute concentration in these areas decreases. The tendency for water to flow through the membrane can be expressed as 'osmotic pressure (symbol, π)' since it is similar to water flow caused by a pressure differential. The osmotic pressure of a solution is related to its dissolved solute concentration and is calculated from van 't Hoff equation:

$$\pi = iCRT, \tag{1.1}$$

where π is the osmotic pressure (kPa) of the solution, R is the universal gas constant, T is the absolute temperature (K), C is the molar concentration of the dissolved salts in the solution, and i is the van't Hoff factor. Instead of water flowing from a pure water chamber to a concentrated salt solution chamber, if water is forced from a region of higher salt concentration (concentrated salt solution chamber) through a semi-permeable membrane to a region of low solute concentration (dilute solution chamber) by applying a pressure in excess of the osmotic pressure differential, the process is reverse of the normal osmosis process and is therefore termed as reverse osmosis. The membranes used for reverse osmosis have a dense barrier layer in the polymer matrix where most separation occurs. In most cases, the membrane is designed to allow only water to pass through this dense layer while preventing the passage of solutes (such as salt ions). This process requires that a high pressure be applied on the high concentration side of the membrane, usually 2–17 bar for fresh and brackish water and 40–70 bar for seawater, which has around 30 bar natural osmotic pressure, which must be overcome. Reverse Osmosis (RO) is a membrane-based process that effectively removes dissolved solids, organics, pyrogens, submicron colloids, color, nitrates, and bacteria from water using semipermeable membranes.

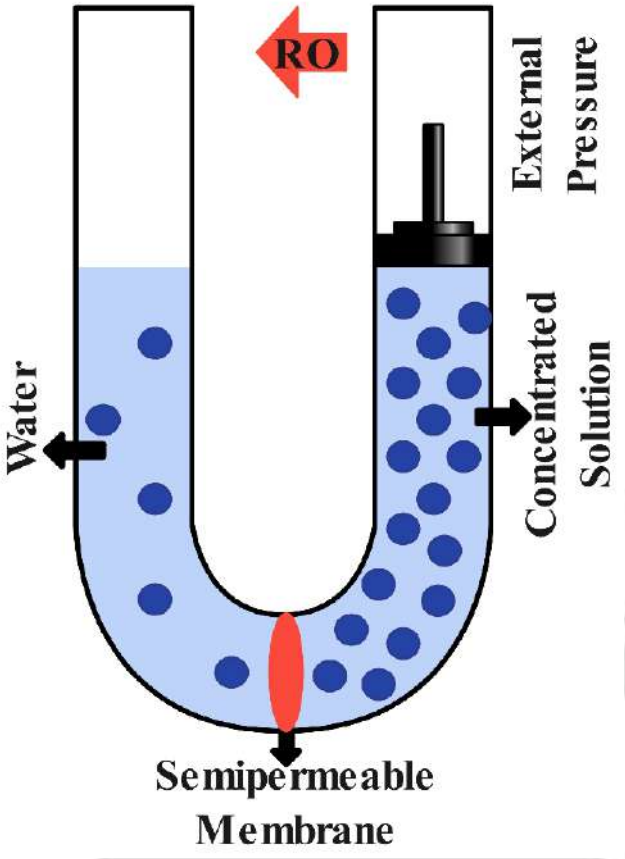

Figure 1.2: A simple RO separation process.

As depicted in Figure 1.2, pressurized feed solution flows through the membrane, allowing only water molecules to permeate while rejecting salt ions and other impurities, resulting in purified permeate water. RO membranes, typically made from materials like cellulose acetate, polyamides, and various polymers, are designed to be cost-effective and durable, ensuring a long and stable lifespan. This process involves managing feed, permeating, and rejecting streams and necessitates the pretreatment of feedwater to remove inorganic solids and suspended particles. High-pressure pumps facilitate the flow of treated water through the membrane, which must exhibit ease of manufacturing, superior salt rejection, high water flux, and resistance to fouling. Additionally, these membranes must be robust enough to withstand high pressures and varying feed water qualities, ensuring their durability and consistent performance under diverse conditions.

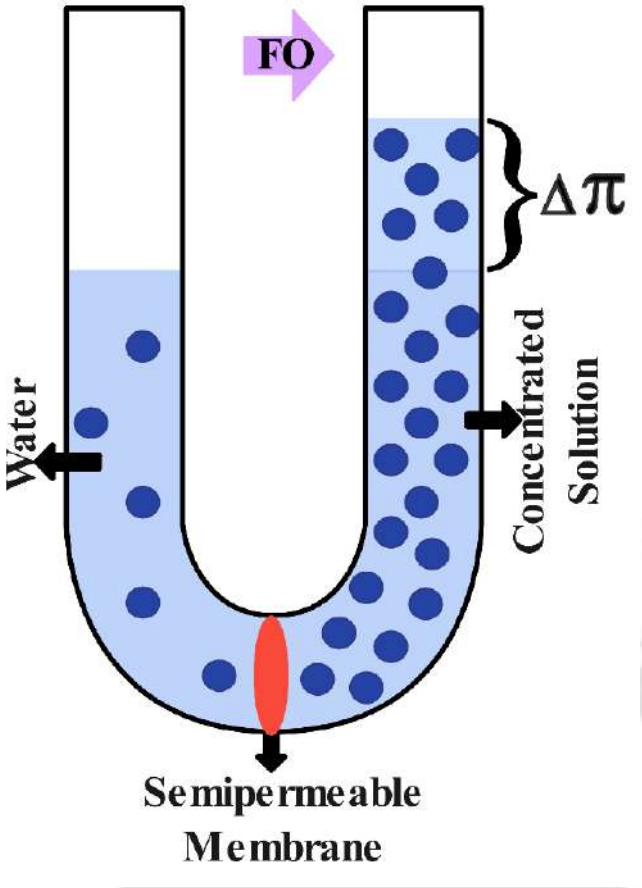

Figure 1.3: A simple FO separation process.

1.1.2 Forward Osmosis (FO) Process

Over the past forty years, membrane technology has primarily focused on pressure-driven processes. However, recent interest has shifted toward osmotically driven processes, particularly forward osmosis (FO). Like reverse osmosis (RO), FO utilizes a selectively permeable membrane to separate two fluids with different osmotic pressures, as illustrated in Figure 1.3. In FO, the osmotic pressure of the draw solution must exceed that of the feed solution. The careful selection of the draw solution is crucial for the process's effectiveness, which generally experiences less fouling than pressure-driven methods.

Forward osmosis consists of three chambers such as feed solution, hydrated membrane, and draw solution. According to the 2nd law of thermodynamics, chemical potential tends to equilibrate in an isolated system. FO processes follow the 2nd law of thermodynamics, where solvent molecules move naturally from a low-concentration solution across a semipermeable membrane to a high-concentration solution to equilibrate their overall chemical potential. The separation

of feed solvent and solutes takes place in the low-concentration solution due to the difference in osmotic pressure ($\Delta\pi$) across the membrane and the unique characteristics of the semipermeable membrane, which only allows solvent molecules to pass through. Therefore, $\Delta\pi$ is the driving force in the transport of solvent molecules across the membrane, while the semipermeable characteristics of the FO membrane control salt rejection or water/solute selectivity. In accordance with the literature [13–17] the terms "draw solution" and "feed solution" represent the high-concentration solution and low-concentration solution, respectively. When an asymmetric membrane is used, there are usually two modes of FO processes according to the membrane orientation, namely, pressure retarded osmosis (PRO) mode and forward osmosis (FO) mode. In the PRO mode, the draw solution flows tangential to the selective layer while the feed solution flows tangential the porous support layer. The reverse holds for the FO mode. Unless otherwise stated, the literature's general term of FO processes includes both PRO and FO modes.

Additionally, the careful selection of the draw solution in Forward Osmosis (FO) is critical because it significantly affects not only the osmotic driving force but also membrane fouling, reverse solute diffusion, and the feasibility of draw solute recovery. An ideal draw solution should generate high osmotic pressure, have low reverse solute flux, be easily separable or reusable, and be non-toxic and compatible with the membrane material, making its careful choice a central design parameter in FO systems [18]. FO processes typically exhibit lower fouling propensity compared to pressure-driven processes such as Reverse Osmosis (RO), primarily due to the absence of hydraulic pressure that reduces the compaction of foulants and promotes a more favorable interaction between the foulant and the membrane surface, resulting in more reversible and less severe fouling [19, 20]. Additionally, there is a possibility of cross-flow in the FO systems as they operate under no or low hydraulic pressure, reducing energy input requirements and mechanical stress on the membrane compared to RO systems, where higher pressure necessitates stronger membrane modules and energy-intensive pumping [21, 22]. This ease of implementing higher cross-flow in FO further reduces fouling and improves performance stability.

FO offers significant potential in emergency drinking solutions, power generation, enhanced oil recovery, fluid concentration, and desalination. Despite its promise, commercial applications remain limited. Fouling continues to be a major challenge; while RO suffers from significant flux decline due to fouling. Consequently, FO is emerging as a viable alternative to RO.

Additionally, the choice of membrane is crucial for wastewater treatment. Research indicates that hydrophilic membranes are less prone to fouling compared to hydrophobic ones, making them a preferred choice for effective wastewater purification [23].

1.1.3 Nanofiltration (NF) Process

Since the pioneering work of Loeb and Sourirajan in developing the first reverse osmosis (RO) membranes, significant advancements in membrane materials have led to a wide range of filtration properties and flux characteristics [24, 25]. While initial research predominantly aimed at desalinating seawater for potable use, there was concurrent interest in creating membranes tailored for specialized applications. These applications often required less than 99% sodium chloride removal and operated at lower pressures [26]. Membranes designed for this range demonstrated moderate to high rejection of divalent ions, relatively high passage of monovalent salts, and efficient rejection of low-molecular-weight organic compounds. Notably, many of these membranes functioned at substantially lower pressures than conventional RO membranes. Initially, they were classified under various categories, such as 'open RO', 'loose RO', 'intermediate RO/UF', 'selective RO', and 'tight UF' [25]. Nanofiltration (NF) was introduced commercially by Filmtec Corporation in the mid-1980s to describe membranes with properties between ultrafiltration (UF) and reverse osmosis (RO) [27]. Despite various patents by Filmtec and Dow Chemical, a clear definition of NF has remained elusive due to the large differences between RO and UF. NF membranes have been characterized by a wide range of properties, including molecular weight cut-offs (MWCO) between 100 and 10,000 Daltons [24, 26, 28, 29], magnesium sulfate rejection of 90-98% [27], sodium chloride rejection below 50% [27], and pore sizes between 0.5 and 2 nm [30].

NF has proven useful in treating textile wastewater rich in salts, dyes, and chemical oxygen demand (COD) [31]. With its high rejection of large dye molecules and efficient salt passage, NF is favored over RO for reducing osmotic pressure and energy consumption [32]. NF can also recycle dye brine and salt-rich permeate, reduce chemical demand [33]. However, the variability in wastewater composition, low molecular weight dyes, and severe fouling from high ionic strength often hinder NF's effectiveness [34, 35]. These challenges lead to flux decline, increased energy demands, and frequent cleanings [36]. NF's salt rejection is complex and influenced by salt concentration, ion valence, membrane properties, and operating conditions, making

performance predictions difficult [36]. Some studies report enhanced salt rejection, which raises osmotic pressure and energy needs [36]. Pretreatment strategies like adsorption [33], coagulation [37, 38], and ozonation [35] have been explored to address fouling and post-treatment using RO or oxidation [35]. Despite being an effective separation technique, NF presents significant challenges in treating and disposing of concentrated textile effluent, necessitating continued research and development.

1.2 Literature Review

1.2.1 Background of Polyamide Membrane

Over 65% of conventional desalination plants rely on Reverse Osmosis (RO) technology due to its continuous operation, energy efficiency, and environmental advantages over thermal distillation and other methods [39, 40]. RO membrane technology, which transitioned from laboratory research to industrial application in the 1960s, has continuously improved, driven by advancements in membrane materials [41]. The initial conceptualization of RO desalination in the 1950s used symmetric cellulose acetate (CA) films, but their limited water flow hindered commercial use [42]. The development of asymmetric CA membranes by Loeb and Sourirajan marked a significant breakthrough, leading to the first practical RO desalination applications in the 1960s and 1970s [42]. However, CA membranes had limitations, such as a narrow pH range (4 to 6.5) and susceptibility to biological degradation [11]. To overcome these issues, thin-film composite (TFC) membranes were introduced in the late 1970s by Cadotte and Peterson [42]. TFC membranes, which consist of a thin selective layer on porous support layers, offered superior desalination performance and stability across a broader pH range [43]. The production of TFC membranes typically involves interfacial polymerization (IP), creating a polyamide (PA) selective layer from *m*-phenylenediamine (MPD) and trimesoyl chloride (TMC) [44]. Ongoing advancements in TFC technology include modified IP processes, surface coatings, adjusted reaction conditions, and nanoscale fillers that enhance membrane performance [45].

Despite these improvements, TFC membranes still face challenges such as high energy consumption, fouling, and the need for enhanced water permeability [46]. Membrane fouling refers to the undesired accumulation of substances—such as suspended solids, organic matter, biological organisms, and inorganic salts—on the membrane surface or within its pores, leading

to a decline in membrane performance. It encompasses several mechanisms, including organic fouling (from natural organic matter or dyes), biofouling (caused by microbial growth and biofilm formation), inorganic scaling (from sparingly soluble salts), and particulate fouling. These fouling processes increase hydraulic resistance, reduce permeability, alter selectivity, and often necessitate chemical cleaning or membrane replacement [47]. Enhancing TFC membranes involves optimizing permeability and selectivity, but achieving high water permeability and salt rejection remains challenging due to inherent trade-offs in synthetic membranes [48]. Nanotechnology offers promising solutions for next-generation TFC membranes, with thin-film nanocomposite (TFNC) membranes incorporating functional nanomaterials like nanotubes and nanosheets to improve structural properties and surface chemistry without compromising salt rejection [49]. For example, incorporating zeolite nanoparticles has significantly increased water permeability while maintaining solute rejection levels [50]. RO has been essential in desalinating seawater and brackish water, making it potable and removing harmful chemicals [51]. In contrast, forward osmosis (FO) is gaining attention for its promising separation performance, minimal fouling, and lower energy requirements [52]. FO's commercial applications include treating industrial wastewater with high salinity or fouling risk [53]. Although FO is not yet widely used to produce potable water in a single step, it is being developed within integrated desalination systems to improve its economic viability [54–56]. Polyamide (PA) thin-film composite (TFC) membranes, which have dominated the RO market for over 30 years, are now also prevalent in FO processes [57]. The PA selective layer's composition critically influences water flux, salt rejection, and membrane longevity [58]. Factors like hydroxyl and carbonyl groups enhance water affinity, while benzene rings inhibit water transport [59]. Understanding water transport at the bulk-membrane interface is essential for optimizing membrane performance.

Early research focused on identifying high-performance polymeric materials and refining interfacial polymerization parameters, such as monomer types and concentrations [60], additives [61], and reaction conditions [62], to enhance the PA selective layer. Solvent activation, involving the post-treatment of PA TFC membranes with organic solvents, has emerged as a promising method for improving membrane performance [63, 64]. Recent research has focused on surface modifications to enhance membrane properties, mainly through advances in chemical surface engineering [65]. However, the PA layer's rugged structure and hydrophobic surface make TFC membranes prone to fouling [47]. To address this, chlorine-resistant TFC membranes are being developed as a cost-effective and sustainable solution for desalination [66].

While synthesizing new monomers to resist chlorine attack presents challenges, particularly in eliminating primary amine and benzene rings, these efforts are crucial for advancing the field [67, 68]. The use of aliphatic diamines like piperazine in fabricating semi-aromatic PA TFC membranes introduces difficulties in achieving the necessary cross-linking and selectivity for RO applications [69, 70].

1.2.2 Background of Semi-aromatic Polyamide Membrane

Polyamide (PA) membranes, derived from aromatic amines like 1,3-phenylenediamine (MPD) and semi-aromatic piperazine (PIP), are crucial for reverse osmosis (RO) and nanofiltration (NF) applications. In these applications, biofouling is a persistent issue, often mitigated by pre-treating the feed water with chlorine. However, conventional aromatic PA membranes are prone to chlorine degradation. In contrast, PIP-based PAs, distinguished by their unique structure, offer high permeance, enhanced hydrophilicity, and improved chlorine resistance, owing to the absence of amidic hydrogen and a chair-shaped configuration that increases free volume in the active layer [69]. Since their development in the late 1970s, polyamide membranes produced through interfacial polymerization (IP) have revolutionized desalination technology [44, 71]. The invention of thin-film composite (TFC) membranes by Cadotte and colleagues marked a significant advancement, achieving over 99% salt rejection in seawater desalination, far surpassing the performance of earlier cellulosic membranes [71, 72]. Unlike integrally-skinned asymmetric cellulosic membranes, TFC membranes consist of a selective layer on a porous support, allowing optimization of each layer for enhanced performance [73]. The robustness, ultra-thin films formed via IP, and scalable manufacturing processes of polyamide TFC membranes have made them dominant in RO applications, outperforming cellulosic membranes and showing potential for organic molecule separations [72, 74, 75] as well as gas separation [76].

The development of semi-aromatic NF membranes, characterized by higher water permeability and lower salt rejection, was driven by the need for specific applications like water softening and the removal of humic substances. These NF membranes, which exhibit around 20% NaCl rejection and high rejection of divalent anions, are ideal for such applications, offering a range of capabilities from brackish water treatment to low-pressure energy-saving operations [72, 73, 77]. Cadotte's pioneering work with fully aromatic polyamide membranes, created through the interfacial condensation of TMC and MPD, laid the foundation for commercially viable seawater

RO technology. Despite the initial modest performance, the membrane's robustness, stability, and ease of preparation led to its global success, with Filmtec's FT-30 membrane setting a benchmark in the industry [71, 73]. Over the years, improvements in synthesis and manufacturing processes have solidified its dominance in seawater desalination. Cadotte's team also developed a semi-aromatic membrane system using PIP and TMC, which, while initially unsuitable for seawater RO due to lower salt rejection, found its niche in NF processes [74]. These NF membranes enable cost-effective purification of low-salinity streams, such as softening and decolorizing water. Both the fully aromatic and semi-aromatic chemistries introduced by Cadotte continue to dominate RO and NF products today, forming the selective top layer or key sublayer in advanced membranes, including those with antifouling coatings [72, 77]. Despite extensive research and widespread industrial use, challenges remain—particularly in understanding the molecular structure and nanoscale morphology of fully aromatic polyamides. Moreover, current polyamide membranes face limitations in rejecting certain micropollutants, such as boron and small, persistent organic molecules. Boron, in particular, is a neutral solute at seawater pH and passes through RO membranes more easily than charged ions, making its removal a persistent challenge in seawater desalination. Advances in modern microscopy, spectroscopy, and theoretical modeling are crucial for overcoming these limitations and guiding the development of alternative membrane materials with enhanced performance in complex water matrices.

1.2.3 Background of Ester-based Membranes

Thin-film composite (TFC) polyamide (PA) membranes are widely used in water treatment due to their high rejection rates for divalent salts and organic contaminants, attributed to a high degree of cross-linking and surface negative charge [78–81]. However, membrane fouling and chlorine intolerance persist, leading to increased energy consumption and reduced membrane lifespan [82–85]. Natural organic matter (NOM) can adsorb onto the PA membrane surface, blocking pores, while chlorine disinfectants degrade the PA layers by attacking amide groups [86]. Nanofiltration (NF) membranes with enhanced chlorine resistance and anti-fouling properties are being developed to address these issues.

Incorporating ester bonds into TFC membranes significantly improves chlorine resistance, as ester bonds lack chlorine erosion sites compared to amide bonds. This can be achieved by using hydroxyl-containing monomers to create polyester-amide (PEA) or polyester (PE) membranes,

which also enhance anti-fouling capabilities [87, 88]. Due to their high water permeance and selective separation performance, PE membranes, particularly those made from polyols, show promise for separating large molecules, such as in dye/salt fractionation and organic solvent nanofiltration.

Hydroxyl-rich polyols like pentaerythritol (PET), small molecule carbohydrates, and cyclodextrins offer abundant hydroxyl groups for membrane preparation. PET-based membranes exhibit high water permeance and salt rejection, alongside superior chlorine resistance compared to commercial membranes [89]. Naturally occurring carbohydrates, such as glucose and sucrose, provide non-toxic and eco-friendly alternatives for membrane fabrication, offering excellent separation performance and fouling resistance [90, 91]. Polyols like erythritol (ERT) and D-sorbitol (DST) have been used to create membranes with high water permeance and effective dye/salt separation [92, 93].

Supramolecular compounds such as cyclodextrins (CDs) and tannic acid (TA) have been explored for membrane preparation due to their functional groups and host-guest complex formation capabilities. CD-based membranes provide tunable pore sizes and enhanced separation performance, while TA-based membranes offer excellent anti-fouling properties [94, 95]. Resveratrol and hyperbranched polymers (HBPs) have also been used to develop high-flux NF membranes with promising separation performance and stability [96, 97].

Compared to traditional PIP/TMC membranes, PET and PEA NF membranes offer solute/solute separation advantages due to their adjustable pore sizes and cross-linking degrees. These membranes can achieve targeted solute rejection or passage, providing unique advantages in ion-selective separation and complex molecule filtration [98, 99]. The use of macrocyclic hydroxyl-containing monomers like cyclodextrins in PET and PEA membranes enhances solute selectivity through internal cavities, offering the potential for specialized separations [100, 101].

1.2.4 Background of Polyimine-based Membranes

Polyimine-based membranes have emerged as promising materials for membrane separations due to their tunable porosity, high surface area, and chemical stability. These membranes are constructed through the Schiff base reaction, which involves the condensation of aldehydes with amines, resulting in imine linkages [102]. The formation of these robust covalent bonds grants polyimines enhanced stability in various chemical environments, including acidic and basic con-

ditions, making them suitable for diverse separation processes [103]. The design flexibility of polyimine membranes allows for the fine-tuning of pore sizes and surface functionalities, which is crucial for selective separations. These materials exhibit high porosity, enabling fast transport of molecules while maintaining selectivity. For instance, the imine linkages can be tailored to incorporate functional groups that interact specifically with specific molecules, enhancing the membranes ability to differentiate between substances based on size, charge, or polarity [104]. This tunability is a significant advantage over traditional polymeric membranes, which often suffer from a trade-off between permeability and selectivity [105]. One of the critical applications of polyimine membranes is gas separation. These membranes inherent porosity and stability allow them to efficiently separate gas mixtures, particularly in the context of carbon dioxide capture [106]. The selective adsorption and diffusion of gases through the polyimine structure are controlled by the size and functionalization of the pores, enabling precise separation. Moreover, incorporating metal ions or other active sites within the structure can further enhance the selectivity and efficiency of gas separation processes [107–109].

In liquid-phase separations, polyimine membranes have shown remarkable performance in water purification and desalination. The hydrophobic nature of the imine linkages can be modified to improve water affinity, enabling effective rejection of salts and other contaminants [110, 111]. Additionally, these membranes can be engineered to possess antifouling properties, which is crucial for maintaining long-term performance in water treatment applications. The ability to functionalize the membrane surface with hydrophilic or hydrophobic groups provides a means to control the interaction with various solutes, thus enhancing the selectivity and permeability of the membrane [112, 113]. Another notable application of polyimine membranes is in organic solvent nanofiltration (OSN) [114–116]. The chemical stability of the imine bonds makes these membranes particularly suitable for use in harsh organic solvents. In OSN, these membranes demonstrate high permeance and selectivity for separating organic molecules of different sizes and polarities. This capability is essential for various industrial processes, including the purification of pharmaceuticals and separating complex organic mixtures. Recent advancements in the synthesis and processing of polyimine membrane have led to the development of more efficient and scalable membrane fabrication methods. Interfacial polymerization and solvent-assisted linker exchange have created defect-free membranes with enhanced performance characteristics. These advancements not only improve the overall performance of the membranes but also open up new possibilities for their application in large-scale industrial processes.

1.3 Motivation

Since the late 1960s, membrane separation technologies have gained significant attention in industrial applications. With energy-saving and environmentally friendly advantages, these technologies are considered promising alternatives to traditional methods such as distillation, evaporation, and extraction [117, 118]. Nanofiltration (NF), developed in the 1980s as an extension of reverse osmosis (RO), stands out for its ability to selectively separate small molecules at lower pressures through mechanisms of size exclusion and electrostatic interactions [119–121]. Typically, NF membranes feature molecular weight cut-offs (MWCO) ranging from 200 to 1000 Da, making them effective in water treatment [122], pharmaceuticals [123], food [124], and textiles [120] industries.

Thin-film composite (TFC) NF membranes, composed of an ultra-thin selective layer on a support structure, have been widely applied due to their low cost and excellent separation efficiency [81, 125–128]. Among various methods for preparing the selective layers of TFC membranes, interfacial polymerization (IP) has been the most popular, providing mild preparation conditions [129]. The resulting polyamide (PA) membranes have been successfully commercialized for water treatment, offering high rejection of divalent salts and organic contaminants [78–81]. However, as discussed earlier in section 1.2.3, issues like membrane fouling and chlorine degradation have posed challenges, reducing efficiency and lifespan [82–85, 130, 131]. Natural organic matter (NOM) tends to accumulate on the PA surfaces, leading to pore blockage, while chlorine-based disinfectants degrade the amide groups, compromising membrane integrity [86]. Developing NF membranes with improved chlorine resistance and anti-fouling properties is critical in response [132]. Research has shown that incorporating ester bonds or hydroxyl-containing monomers in the selective layer significantly enhances chlorine resistance [87, 88, 133]. Polyester and polyester-amide membranes and polymeric NF membranes, like polyimine-based and semi-aromatic, exhibit superior performance in resisting chlorine attack and fouling [105, 134–137].

Future progress in TFC membrane technology requires understanding transport phenomena and material interactions at an atomic level. Molecular dynamics (MD) simulations serve as a powerful tool for investigating these processes, offering detailed insights into adsorption, diffusion, and solute rejection that are challenging to capture experimentally. MD simulations have evolved to handle increasingly complex systems, ranging from all-atom (AA) to coarse-grained (CG) approaches, enabling researchers to study systems with tens to hundreds of thousands of

atoms. These simulations allow for exploring physicochemical interactions in TFC membranes, offering a framework for optimizing membrane performance for water desalination and related applications.

Recent advancements in molecular simulation have enabled the use of molecular dynamics (MD) to study the structural characteristics of polymer membranes at a molecular level, addressing some limitations of experimental methods. Kotelyanskii et al. [138, 139] explored ion and water mobility within polyamide (PA) membranes, discovering that water exhibits jump-diffusion rather than traditional Brownian motion. Harder et al. [140] developed a heuristic model of the PA membrane that simulates the polymerization process, allowing for practical MD simulations. Luo et al. [141] constructed a membrane topology to calculate water flux and ion rejection using equilibrium MD (EMD), achieving results consistent with experimental findings. Ding et al. [142–144] also used EMD to examine the structural and dynamic properties of water and the membrane. Numerous MD studies have further explored water dynamics, ion transport, and the local structure within membranes, confirming that MD simulation holds promise for advancing reverse osmosis (RO) membrane design [145–147]. Gai et al. [59] employed MD simulations to investigate water-polymer interactions, identifying that hydroxyl and carbonyl groups exhibit strong affinities for water, suggesting that increasing these groups could enhance the membrane's water adsorption capacity. Song et al. [148] examined water residence times around functional groups within the PA membrane, finding that water diffuses more rapidly near benzene rings than near carboxyl or amino groups due to the benzene ring's relatively higher hydrophobicity. Despite these insights, prior studies have predominantly focused on intramembrane water transport. Future research should further investigate water transport across bulk/membrane/bulk phases, considering the impact of the bulk/membrane interface. This thesis explores various polymeric membrane types and their performance using molecular dynamics simulations, providing insights into material behavior at the molecular scale. This thesis explores various polymeric membrane types and their performance using molecular dynamics simulations, providing insights into material behavior at the molecular scale.

1.4 Objectives

Based on the literature survey we proposed following objectives:

- Semiaromatic Polyamide-Based Membrane in Forward Osmosis: Molecular Insights.
- Non−Preferential Solvent Transport Through Intrinsic Cyclodextrin Pore in a Polyester Film
- Atomistic Insights into High-Performance Polyimine-based Membranes for Selective Dye Rejection and Salt Permeation in Nanofiltration
- Investigating Solvent Activation of Polyamide Nanofilm Composite Membranes: Insights from Experimental and Molecular Modelling Approaches

1.5 Thesis Organization

Chapter 2 briefly discusses the simulation technique (molecular dynamics) used in this thesis and its basic formalism.
Chapter 3 attempts to address the performance of semi-aromatic membrane in forward osmosis.
Chapter 4 deals with functional significance of cyclodextrin cavities in polyester membranes for transporting polar and non-polar solvents.
Chapter 5 examines the performance of polyimine based membrane in nanofiltration.
Chapter 6 investigate the solvent activation and transport phenomena through polyamide membranes.
Chapter 7 contains the conclusions and some ideas for future works.

Bibliography

[1] Edward Jones, Manzoor Qadir, Michelle TH van Vliet, Vladimir Smakhtin, and Seong-mu Kang. The state of desalination and brine production: A global outlook. *Sci. Total Environ.*, 657:1343–1356, 2019.

[2] Muhammad Wakil Shahzad, Muhammad Burhan, Li Ang, and Kim Choon Ng. Energy-water-environment nexus underpinning future desalination sustainability. *Desalination*, 413:52–64, 2017.

[3] Veera Gnaneswar Gude. Desalination and sustainability–an appraisal and current perspective. *Water Res.*, 89:87–106, 2016.

[4] Erica DeNicola, Omar S Aburizaiza, Azhar Siddique, Haider Khwaja, and David O Carpenter. Climate change and water scarcity: The case of saudi arabia. *Ann. Glob. Heal.*, 81(3):342–353, 2015.

[5] Antonio Gomez-Gotor, B Del Rio-Gamero, I Prieto Prado, and Antonio Casanas. The history of desalination in the canary islands. *Desalination*, 428:86–107, 2018.

[6] S Manju and Netramani Sagar. Renewable energy integrated desalination: A sustainable solution to overcome future fresh-water scarcity in india. *Renew. Sust. Energ. Rev.*, 73: 594–609, 2017.

[7] A Boudghene Stambouli, Z Khiat, S Flazi, H Tanemoto, M Nakajima, H Isoda, F Yokoyama, S Hannachi, K Kurokawa, M Shimizu, et al. Trends and challenges of sustainable energy and water research in north africa: Sahara solar breeder concerns at the intersection of energy/water. *Renew. Sust. Energ. Rev.*, 30:912–922, 2014.

[8] F Silva Pinto and R Cunha Marques. Desalination projects economic feasibility: A standardization of cost determinants. *Renew. Sust. Energ. Rev.*, 78:904–915, 2017.

[9] S Al-Kharabsheh and D Yogi Goswami. Theoretical analysis of a water desalination system using low grade solar heat. *J. Sol. Energy Eng.*, 126(2):774–780, 2004.

[10] Menachem Elimelech and William A Phillip. The future of seawater desalination: energy, technology, and the environment. *science*, 333(6043):712–717, 2011.

[11] Yuchen Liu, Zimeng Zhang, and Shiren Wang. Carbon nanopore-tailored reverse osmotic water desalination. *ACS ES&T Water*, 1(1):34–47, 2020.

[12] Sudhakar M Rao. Reverse osmosis. *Resonance*, 16:1333–1336, 2011.

[13] Tai-Shung Chung, Xue Li, Rui Chin Ong, Qingchun Ge, Honglei Wang, and Gang Han.

Emerging forward osmosis (fo) technologies and challenges ahead for clean water and clean energy applications. *Curr. Opinion Chem. Eng.*, 1(3):246–257, 2012.

[14] Shuaifei Zhao, Linda Zou, Chuyang Y Tang, and Dennis Mulcahy. Recent developments in forward osmosis: Opportunities and challenges. *J. Membr. Sci.*, 396:1–21, 2012.

[15] Tai-Shung Chung, Sui Zhang, Kai Yu Wang, Jincai Su, and Ming Ming Ling. Forward osmosis processes: Yesterday, today and tomorrow. *Desalination*, 287:78–81, 2012.

[16] Tzahi Y Cath, Amy E Childress, and Menachem Elimelech. Forward osmosis: Principles, applications, and recent developments. *J. Membr. Sci.*, 281(1-2):70–87, 2006.

[17] Jeffrey R McCutcheon, Robert L McGinnis, and Menachem Elimelech. A novel ammonia—carbon dioxide forward (direct) osmosis desalination process. *Desalination*, 174(1): 1–11, 2005.

[18] Baoxia Mi and Menachem Elimelech. Organic fouling of forward osmosis membranes: Fouling reversibility and cleaning without chemical reagents. *J. Membr. Sci.*, 348(1-2): 337–345, 2010.

[19] Andrea Achilli, Tzahi Y Cath, and Amy E Childress. Power generation with pressure retarded osmosis: An experimental and theoretical investigation. *J. Membr. Sci.*, 343 (1-2):42–52, 2009.

[20] Thor Thorsen and Torleif Holt. The potential for power production from salinity gradients by pressure retarded osmosis. *J. Membr. Sci.*, 335(1-2):103–110, 2009.

[21] Jincai Su, Sui Zhang, Ming Ming Ling, and Tai-Shung Chung. Forward osmosis: an emerging technology for sustainable supply of clean water. *Clean Technologies and Environmental Policy*, 14:507–511, 2012.

[22] Stein Erik Skilhagen, Jon E Dugstad, and Rolf Jarle Aaberg. Osmotic power—power production based on the osmotic pressure difference between waters with varying salt gradients. *Desalination*, 220(1-3):476–482, 2008.

[23] Thor Thorsen. Concentration polarisation by natural organic matter (nom) in nf and uf. *J. Membr. Sci.*, 233(1-2):79–91, 2004.

[24] BM Watson and CD Hornburg. Low-energy membrane nanofiltration for removal of color, organics and hardness from drinking water supplies. *Desalination*, 72(1-2):11–22, 1989.

[25] Charles Linder and Ora Kedem. History of nanofiltration membranes from 1960 to 1990. *Nanofiltration: Principles, Applications, and New Materials*, 1:1–34, 2021.

[26] J Cadotte, R Forester, M Kim, R Petersen, and T Stocker. Nanofiltration membranes broaden the use of membrane separation technology. *Desalination*, 70(1-3):77–88, 1988.

[27] Peter Eriksson. Nanofiltration extends the range of membrane filtration. *Environ. Prog.*, 7(1):58–62, 1988.

[28] William J Conlon and Stuart A McClellan. Membrane softening: a treatment process comes of age. *J. Am. Water Work Assoc.*, 81(11):47–51, 1989.

[29] Xiao-Lin Wang, Toshinori Tsuru, Shin-ichi Nakao, and Shoji Kimura. Electrolyte transport through nanofiltration membranes by the space-charge model and the comparison with teorell-meyer-sievers model. *J. Membr. Sci.*, 103(1-2):117–133, 1995.

[30] Johannes Martinus Koen Timmer. Properties of nanofiltration membranes: model development and industrial application. 2001.

[31] C Tang and V Chen. Nanofiltration of textile wastewater for water reuse. *Desalination*, 143(1):11–20, 2002.

[32] Li Shu, TD Waite, PJ Bliss, Anthony Fane, and Veeriah Jegatheesan. Nanofiltration for the possible reuse of water and recovery of sodium chloride salt from textile effluent. *Desalination*, 172(3):235–243, 2005.

[33] S Chakraborty, S De, JK Basu, and S DasGupta. Treatment of a textile effluent: application of a combination method involving adsorption and nanofiltration. *Desalination*, 174(1):73–85, 2005.

[34] Emna Ellouze, Nouha Tahri, and Raja Ben Amar. Enhancement of textile wastewater treatment process using nanofiltration. *Desalination*, 286:16–23, 2012.

[35] Chuyang Y Tang, TH Chong, and Anthony G Fane. Colloidal interactions and fouling of nf and ro membranes: a review. *Adv. Colloid Interface Sci.*, 164(1-2):126–143, 2011.

[36] B Van der Bruggen, B Daems, D Wilms, and C Vandecasteele. Mechanisms of retention and flux decline for the nanofiltration of dye baths from the textile industry. *Separ. Purif. Technol.*, 22:519–528, 2001.

[37] M Riera-Torres, C Gutierrez-Bouzan, and M Crespi. Combination of coagulation–flocculation and nanofiltration techniques for dye removal and water reuse in textile effluents. *Desalination*, 252(1-3):53–59, 2010.

[38] A Bes-Pia, MI Iborra-Clar, A Iborra-Clar, JA Mendoza-Roca, B Cuartas-Uribe, and MI Alcaina-Miranda. Nanofiltration of textile industry wastewater using a physicochemical process as a pre-treatment. *Desalination*, 178(1-3):343–349, 2005.

[39] Raquel Garcia-Pacheco, Junkal Landaburu-Aguirre, Patricia Terrero-Rodriguez, E Campos, Francisco Molina-Serrano, Javier Rabadan, Domingo Zarzo, and Eloy Garcia-Calvo. Validation of recycled membranes for treating brackish water at pilot scale. *Desalination*, 433:199–208, 2018.

[40] Qian Liu and Guo-Rong Xu. Graphene oxide (go) as functional material in tailoring polyamide thin film composite (pa-tfc) reverse osmosis (ro) membranes. *Desalination*, 394:162–175, 2016.

[41] AG Fane, Rong Wang, and Yue Jia. Membrane technology: past, present and future. *Membrane and desalination technologies*, pages 1–45, 2011.

[42] Julius Glater. The early history of reverse osmosis membrane development. *Desalination*, 117(1-3):297–309, 1998.

[43] Byeong-Heon Jeong, Eric MV Hoek, Yushan Yan, Arun Subramani, Xiaofei Huang, Gil Hurwitz, Asim K Ghosh, and Anna Jawor. Interfacial polymerization of thin film nanocomposites: a new concept for reverse osmosis membranes. *J. Membr. Sci.*, 294 (1-2):1–7, 2007.

[44] John E Cadotte, RJ Petersen, RE Larson, and EE Erickson. A new thin-film composite seawater reverse osmosis membrane. *Desalination*, 32:25–31, 1980.

[45] Xinglin Lu and Menachem Elimelech. Fabrication of desalination membranes by interfacial polymerization: history, current efforts, and future directions. *Chem. Soc. Rev.*, 50 (11):6290–6307, 2021.

[46] Jay R Werber, Chinedum O Osuji, and Menachem Elimelech. Materials for next-generation desalination and water purification membranes. *Nat. Rev. Mater.*, 1(5):1–15, 2016.

[47] Runnan Zhang, Yanan Liu, Mingrui He, Yanlei Su, Xueting Zhao, Menachem Elimelech, and Zhongyi Jiang. Antifouling membranes for sustainable water purification: strategies and mechanisms. *Chem. Soc. Rev.*, 45(21):5888–5924, 2016.

[48] Ho Bum Park, Jovan Kamcev, Lloyd M Robeson, Menachem Elimelech, and Benny D Freeman. Maximizing the right stuff: The trade-off between membrane permeability and selectivity. *Science*, 356(6343):eaab0530, 2017.

[49] ZC Ng, WJ Lau, T Matsuura, and AF Ismail. Thin film nanocomposite ro membranes: Review on fabrication techniques and impacts of nanofiller characteristics on membrane properties. *Chem. Eng. Res. Des.*, 165:81–105, 2021.

[50] MaryTheresa M Pendergast and Eric MV Hoek. A review of water treatment membrane nanotechnologies. *Energy Environ. Sci.*, 4(6):1946–1971, 2011.

[51] M Talaeipour, J Nouri, AH Hassani, and AH Mahvi. An investigation of desalination by nanofiltration, reverse osmosis and integrated (hybrid nf/ro) membranes employed in brackish water treatment. *J. Environ. Heal. Sci. Eng.*, 15:1–9, 2017.

[52] Wei Lun Ang, Abdul Wahab Mohammad, Daniel Johnson, and Nidal Hilal. Forward osmosis research trends in desalination and wastewater treatment: A review of research trends over the past decade. *J. Water Process Eng.*, 31:100886, 2019.

[53] Devin L Shaffer, Jay R Werber, Humberto Jaramillo, Shihong Lin, and Menachem Elimelech. Forward osmosis: where are we now? *Desalination*, 356:271–284, 2015.

[54] Byeong Gyu Choi, Min Zhan, Kyungyong Shin, Sanghak Lee, and Seungkwan Hong. Pilot-scale evaluation of fo-ro osmotic dilution process for treating wastewater from coal-fired power plant integrated with seawater desalination. *J. Membr. Sci.*, 540:78–87, 2017.

[55] Kiho Park, Yoon Hyuk Jang, Min-gyu Kim, Dae Ryook Yang, Seungkwan Hong, et al. Comprehensive analysis of a hybrid fo/crystallization/ro process for improving its economic feasibility to seawater desalination. *Water Res.*, 171:115426, 2020.

[56] Laura Chekli, Sherub Phuntsho, Jung Eun Kim, Jihye Kim, Joon Young Choi, June-Seok Choi, Suhan Kim, Joon Ha Kim, Seungkwan Hong, Jinsik Sohn, et al. A comprehensive review of hybrid forward osmosis systems: Performance, applications and future prospects. *J. Membr. Sci.*, 497:430–449, 2016.

[57] Guo-Rong Xu, Jian-Mei Xu, Hou-Jun Feng, He-Li Zhao, and Shui-Bo Wu. Tailoring structures and performance of polyamide thin film composite (pa-tfc) desalination membranes via sublayers adjustment-a review. *Desalination*, 417:19–35, 2017.

[58] Woei-Jye Lau, Gwo-Sung Lai, Jianxin Li, Stephen Gray, Yunxia Hu, Nurasyikin Misdan, Pei-Sean Goh, Takeshi Matsuura, Ihsan Wan Azelee, and Ahmad Fauzi Ismail. Development of microporous substrates of polyamide thin film composite membranes for pressure-driven and osmotically-driven membrane processes: A review. *J. Ind. Eng. Chem.*, 77:25–59, 2019.

[59] Jing-Gang Gai, Xiao-Lei Gong, Wu-Li Kang, Xin Zhang, and Wei-Wei Wang. Key factors influencing water diffusion in aromatic pa membrane: Hydrates, nanochannels and functional groups. *Desalination*, 333(1):52–58, 2014.

[60] Lianrui Zhao, Songmiao Liang, Yan Jin, Zhuyuan Wang, Lijie Hu, Yan Kang, Jian Tao,

and Wei Peng. Effect of trifunctional planar monomer on the structure and properties of polyamide membranes. *Appl. Surf. Sci.*, 505:144415, 2020.

[61] In-Chul Kim, Bo-Reum Jeong, Seong-Joong Kim, and Kew-Ho Lee. Preparation of high flux thin film composite polyamide membrane: The effect of alkyl phosphate additives during interfacial polymerization. *Desalination*, 308:111–114, 2013.

[62] Jaber Azizi and Alireza Sharif. Optimization of water flux and salt rejection properties of polyamide thin film composite membranes. *J. Appl. Polym. Sci.*, 137(28):48858, 2020.

[63] Min Gyu Shin, Soon Jin Kwon, Hosik Park, You-In Park, and Jung-Hyun Lee. High-performance and acid-resistant nanofiltration membranes prepared by solvent activation on polyamide reverse osmosis membranes. *J. Memb. Sci.*, 595:117590, 2020.

[64] P Gorgojo, MF Jimenez-Solomon, and AG Livingston. Polyamide thin film composite membranes on cross-linked polyimide supports: Improvement of ro performance via activating solvent. *Desalination*, 344:181–188, 2014.

[65] Die Ling Zhao, Susilo Japip, Yu Zhang, Martin Weber, Christian Maletzko, and Tai-Shung Chung. Emerging thin-film nanocomposite (tfn) membranes for reverse osmosis: A review. *Water Res.*, 173:115557, 2020.

[66] Rhea Verbeke, Veronica Gomez, and Ivo FJ Vankelecom. Chlorine-resistance of reverse osmosis (ro) polyamide membranes. *Prog. Polym. Sci.*, 72:1–15, 2017.

[67] Runlin Han. Formation and characterization of (melamine–tmc) based thin film composite nf membranes for improved thermal and chlorine resistances. *J. Memb. Sci.*, 425:176–181, 2013.

[68] Sihua Liu, Chunrui Wu, Xiaotong Hou, Jingguo She, Su Liu, Xiaolong Lu, Hongwei Zhang, and Stephen Gray. Understanding the chlorination mechanism and the chlorine-induced separation performance evolution of polypiperazine-amide nanofiltration membrane. *J. Memb. Sci.*, 573:36–45, 2019.

[69] Jaydevsinh M Gohil and Paramita Ray. A review on semi-aromatic polyamide tfc membranes prepared by interfacial polymerization: Potential for water treatment and desalination. *Sep. Purif. Technol.*, 181:159–182, 2017.

[70] Xiao-Hua Ma, Zhi-Kan Yao, Zhe Yang, Hao Guo, Zhen-Liang Xu, Chuyang Y Tang, and Menachem Elimelech. Nanofoaming of polyamide desalination membranes to tune permeability and selectivity. *Environ. Sci. Technol. Lett.*, 5(2):123–130, 2018.

[71] John E Cadotte. Evolution of composite reverse osmosis membranes. *Materials science of synthetic membranes*, pages 273–294, 1985.

[72] Robert J Petersen. Composite reverse osmosis and nanofiltration membranes. *J. Membr. Sci.*, 83(1):81–150, 1993.

[73] Marcel Mulder. *Basic principles of membrane technology*. Springer science and business media, 2012.

[74] Kah Peng Lee, Tom C Arnot, and Davide Mattia. A review of reverse osmosis membrane materials for desalination—development to date and future potential. *J. Membr. Sci.*, 370(1-2):1–22, 2011.

[75] Masaru Kurihara and Takao Sasaki. The pursuits of ultimate membrane technology including low pressure seawater reverse osmosis membrane developed by "mega-ton water system" project. *J. Membr. Sci. Res.*, 3(3):157–173, 2017.

[76] Magda Poloncarzova, Jiri Vejrazka, Vaclav Vesely, and Pavel Izak. Effective purification of biogas by a condensing-liquid membrane. *Angew. Chem. Int. Ed.*, 123(3):695–697, 2011.

[77] Andrea Schafer, Anthony G Fane, and T David Waite. *Nanofiltration: principles and applications*. Elsevier, 2005.

[78] Xu Li, Zhi Wang, Xianglei Han, Yingying Liu, Chong Wang, Fangzheng Yan, and Jixiao Wang. Regulating the interfacial polymerization process toward high-performance polyamide thin-film composite reverse osmosis and nanofiltration membranes: A review. *J. Membr. Sci.*, 640:119765, 2021.

[79] Orlando Coronell, Benito J Marinas, and David G Cahill. Depth heterogeneity of fully aromatic polyamide active layers in reverse osmosis and nanofiltration membranes. *Environ. Sci. Technol.*, 45(10):4513–4520, 2011.

[80] Ana M Saenz de Jubera, James H Herbison, Yukako Komaki, Michael J Plewa, Jeffrey S Moore, David G Cahill, and Benito J Marinas. Development and performance characterization of a polyamide nanofiltration membrane modified with covalently bonded aramide dendrimers. *Environ. Sci. Technol.*, 47(15):8642–8649, 2013.

[81] Bingbing Yuan, Shengchao Zhao, Ping Hu, Jiabao Cui, and Q Jason Niu. Asymmetric polyamide nanofilms with highly ordered nanovoids for water purification. *Nat. Commun.*, 11(1):6102, 2020.

[82] Van Thanh Do, Chuyang Y Tang, Martin Reinhard, and James O Leckie. Effects of chlo-

rine exposure conditions on physiochemical properties and performance of a polyamide membrane mechanisms and implications. *Environ. Sci. Technol.*, 46(24):13184–13192, 2012.

[83] Joung-Eun Gu, Byung-Moon Jun, and Young-Nam Kwon. Effect of chlorination condition and permeability of chlorine species on the chlorination of a polyamide membrane. *Water Res.*, 46(16):5389–5400, 2012.

[84] Jongkwan Park, Sungyun Lee, Jeongyeop You, Sanghun Park, Yujin Ahn, Woonggyu Jung, and Kyung Hwa Cho. Evaluation of fouling in nanofiltration for desalination using a resistance-in-series model and optical coherence tomography. *Sci. Total Environ.*, 642: 349–355, 2018.

[85] Joshua Powell, Jeanne Luh, and Orlando Coronell. Amide link scission in the polyamide active layers of thin-film composite membranes upon exposure to free chlorine: kinetics and mechanisms. *Environ. Sci. Technol.*, 49(20):12136–12144, 2015.

[86] Xiafu Shi, Galit Tal, Nicholas P Hankins, and Vitaly Gitis. Fouling and cleaning of ultrafiltration membranes: A review. *J. Water Process Eng.*, 1:121–138, 2014.

[87] Jafar Rezania, Vahid Vatanpour, Abbas Shockravi, and Morteza Ehsani. Preparation of novel carboxylated thin-film composite polyamide-polyester nanofiltration membranes with enhanced antifouling property and water flux. *React. Funct. Polym.*, 131:123–133, 2018.

[88] Ruijun Zhang, Shuili Yu, Wenxin Shi, Wei Wang, Xiaoying Wang, Zhiqiang Zhang, Li Li, Bing Zhang, and Xian Bao. A novel polyesteramide thin film composite nanofiltration membrane prepared by interfacial polymerization of serinol and trimesoyl chloride (tmc) catalyzed by 4-dimethylaminopyridine (dmap). *J. Membr. Sci.*, 542:68–80, 2017.

[89] Jun Cheng, Wenxin Shi, Lanhe Zhang, and Ruijun Zhang. A novel polyester composite nanofiltration membrane formed by interfacial polymerization of pentaerythritol (pe) and trimesoyl chloride (tmc). *Appl. Surf. Sci.*, 416:152–159, 2017.

[90] Junfeng Zheng, Yanling Liu, Junyong Zhu, Pengrui Jin, Tim Croes, Alexander Volodine, Shushan Yuan, and Bart Van der Bruggen. Sugar-based membranes for nanofiltration. *J. Membr. Sci.*, 619:118786, 2021.

[91] Pengrui Jin, Sara Chergaoui, Junfeng Zheng, Alexander Volodine, Xin Zhang, Ziyuan Liu, Patricia Luis, and Bart Van der Bruggen. Low-pressure highly permeable polyester

loose nanofiltration membranes tailored by natural carbohydrates for effective dye/salt fractionation. *J. Hazard. Mater.*, 421:126716, 2022.

[92] Pengrui Jin, Junyong Zhu, Shushan Yuan, Gang Zhang, Alexander Volodine, Miaomiao Tian, Jianxiu Wang, Patricia Luis, and Bart Van der Bruggen. Erythritol-based polyester loose nanofiltration membrane with fast water transport for efficient dye/salt separation. *Chem. Eng. J.*, 406:126796, 2021.

[93] Micah Belle Marie Yap Ang, Guan-Wei Huang, Min-Yi Chu, Jeremiah C Millare, Shu-Hsien Huang, and Kueir-Rarn Lee. Use of aqueous polyol monomer for superior dye separation performance and high chlorine resistance of thin-film composite polyester nanofiltration membranes. *J. Water Process Eng.*, 48:102843, 2022.

[94] Jiangtao Liu, Dan Hua, Yu Zhang, Susilo Japip, and Tai-Shung Chung. Precise molecular sieving architectures with janus pathways for both polar and nonpolar molecules. *Adv. Mater.*, 30(11):1705933, 2018.

[95] Yan Zhang, Yanlei Su, Jinming Peng, Xueting Zhao, Jiazhan Liu, Jiaojiao Zhao, and Zhongyi Jiang. Composite nanofiltration membranes prepared by interfacial polymerization with natural material tannic acid and trimesoyl chloride. *J. Membr. Sci.*, 429: 235–242, 2013.

[96] Junfeng Zheng, Rui Zhao, Adam A Uliana, Yanyan Liu, Damien de Donnea, Xin Zhang, Daliang Xu, Qieyuan Gao, Pengrui Jin, Yanlin Liu, et al. Separation of textile wastewater using a highly permeable resveratrol-based loose nanofiltration membrane with excellent anti-fouling performance. *Chem. Eng. J.*, 434:134705, 2022.

[97] Xiu-Zhen Wei, Li-Ping Zhu, Hui-Yu Deng, You-Yi Xu, Bao-Ku Zhu, and Zhi-Ming Huang. New type of nanofiltration membrane based on crosslinked hyperbranched polymers. *J. Membr. Sci.*, 323(2):278–287, 2008.

[98] Kaiming Fan, Yanling Liu, Xiaoping Wang, Peng Cheng, and Shengji Xia. Comparison of polyamide, polyesteramide and polyester nanofiltration membranes: properties and separation performance. *Sep. Purif. Technol.*, 297:121579, 2022.

[99] Ying Zhao, Nan Li, Jie Shi, Yuanhua Xia, Bo Zhu, Ruiqi Shao, Chunying Min, Zhiwei Xu, and Hui Deng. Extra-thin composite nanofiltration membranes tuned by γ-cyclodextrins containing amphipathic cavities for efficient separation of magnesium/lithium ions. *Sep. Purif. Technol.*, 286:120419, 2022.

[100] KH Mah, HW Yussof, MN Abu Seman, and AW Mohammad. Optimisation of interfacial

polymerization factors in thin-film composite (tfc) polyester nanofiltration (nf) membrane for separation of xylose from glucose. *Sep. Purif. Technol.*, 209:211–222, 2019.

[101] Beibei Tang, Zhibin Huo, and Peiyi Wu. Study on a novel polyester composite nanofiltration membrane by interfacial polymerization of triethanolamine (teoa) and trimesoyl chloride (tmc): I. preparation, characterization and nanofiltration properties test of membrane. *J. Membr. Sci.*, 320(1-2):198–205, 2008.

[102] Sharath Kandambeth, Arijit Mallick, Binit Lukose, Manoj V Mane, Thomas Heine, and Rahul Banerjee. Construction of crystalline 2d covalent organic frameworks with remarkable chemical (acid/base) stability via a combined reversible and irreversible route. *J. Am. Chem. Soc.*, 134(48):19524–19527, 2012.

[103] Shushan Yuan, Xin Li, Junyong Zhu, Gang Zhang, Peter Van Puyvelde, and Bart Van der Bruggen. Covalent organic frameworks for membrane separation. *Chem. Soc. Rev.*, 48 (10):2665–2681, 2019.

[104] Sharath Kandambeth, Digambar Balaji Shinde, Manas K Panda, Binit Lukose, Thomas Heine, and Rahul Banerjee. Enhancement of chemical stability and crystallinity in porphyrin-containing covalent organic frameworks by intramolecular hydrogen bonds. *Angew. Chem.*, (49):13290–13294, 2013.

[105] Karishma Tiwari, Solagna Modak, Pulak Sarkar, Santanu Ray, Vasista Adupa, K Anki Reddy, Sumit Kumar Pramanik, Amitava Das, and Santanu Karan. Interfacial synthesis of large-area ultrathin polyimine nanofilms as molecular separation membrane. *Iscience*, 25(4), 2022.

[106] Minman Tong, Qingyuan Yang, Qintian Ma, Dahuan Liu, and Chongli Zhong. Few-layered ultrathin covalent organic framework membranes for gas separation: a computational study. *J. Mater. Chem. A*, 4(1):124–131, 2016.

[107] Hongwei Fan, Alexander Mundstock, Jiahui Gu, Hong Meng, and Jürgen Caro. An azine-linked covalent organic framework acof-1 membrane for highly selective co 2/ch 4 separation. *J. Mater. Chem. A*, 6(35):16849–16853, 2018.

[108] Meixia Shan, Beatriz Seoane, Elena Rozhko, Alla Dikhtiarenko, Guillaume Clet, Freek Kapteijn, and Jorge Gascon. Azine-linked covalent organic framework (cof)-based mixed-matrix membranes for co2/ch4 separation. *Chem. – Eur. J.*, 22(41):14467–14470, 2016.

[109] Xingyu Wu, Zhizhang Tian, Shaofei Wang, Dongdong Peng, Leixin Yang, Yingzhen Wu, Qingping Xin, Hong Wu, and Zhongyi Jiang. Mixed matrix membranes comprising poly-

mers of intrinsic microporosity and covalent organic framework for gas separation. *J. Membr. Sci.*, 528:273–283, 2017.

[110] Lina Xu, Jia Xu, Baotian Shan, Xiulin Wang, and Congjie Gao. Tppa-2-incorporated mixed matrix membranes for efficient water purification. *J. Membr. Sci.*, 526:355–366, 2017.

[111] Phuoc HH Duong, Valerie A Kuehl, Bruce Mastorovich, John O Hoberg, Bruce A Parkinson, and Katie D Li-Oakey. Carboxyl-functionalized covalent organic framework as a two-dimensional nanofiller for mixed-matrix ultrafiltration membranes. *J. Membr. Sci.*, 574:338–348, 2019.

[112] Muhammad Bilal Asif, Seokjin Kim, Thien S Nguyen, Javeed Mahmood, and Cafer T Yavuz. Covalent organic framework membranes and water treatment. *J. Am. Chem. Soc.*, 146(6):3567–3584, 2024.

[113] Ning Huang, Rajamani Krishna, and Donglin Jiang. Tailor-made pore surface engineering in covalent organic frameworks: systematic functionalization for performance screening. *J. Am. Chem. Soc.*, 137(22):7079–7082, 2015.

[114] Sharath Kandambeth, Bishnu P Biswal, Harshal D Chaudhari, Kanhu Charan Rout, H Shebeeb Kunjattu, Shouvik Mitra, Suvendu Karak, Anuja Das, Rabibrata Mukherjee, Ulhas K Kharul, et al. Selective molecular sieving in self-standing porous covalent-organic-framework membranes. *Adv. Mater.*, 29(2), 2016.

[115] Arjun Halder, Suvendu Karak, Matthew Addicoat, Saibal Bera, Amit Chakraborty, Shebeeb H Kunjattu, Pradip Pachfule, Thomas Heine, and Rahul Banerjee. Ultrastable imine-based covalent organic frameworks for sulfuric acid recovery: an effect of interlayer hydrogen bonding. *Angew. Chem.*, 57(20):5797–5802, 2018.

[116] Wan Wei, Jie Liu, and Jianwen Jiang. Computational design of 2d covalent-organic framework membranes for organic solvent nanofiltration. *ACS Sustainable Chem. Eng.*, 7(1):1734–1744, 2018.

[117] Jun Hui Huang, Xi Quan Cheng, Ya Dong Wu, Yan Qiu Zhang, Song Wei Li, Cher Hon Lau, and Lu Shao. Critical operation factors and proposed testing protocol of nanofiltration membranes for developing advanced membrane materials. *Adv. Compos. Hybrid Mater.*, 4(4):1092–1101, 2021.

[118] Patrizia Marchetti, Maria F Jimenez Solomon, Gyorgy Szekely, and Andrew G Livingston.

Molecular separation with organic solvent nanofiltration: a critical review. *Chem. Rev.*, 114(21):10735–10806, 2014.

[119] Dan Lu, Zhikan Yao, Lei Jiao, Misbah Waheed, Zhilin Sun, and Lin Zhang. Separation mechanism, selectivity enhancement strategies and advanced materials for mono-/multivalent ion-selective nanofiltration membrane. *Adv. Membr.*, 2:100032, 2022.

[120] Abdul Wahab Mohammad, YH Teow, WL Ang, YT Chung, DL Oatley-Radcliffe, and Nidal Hilal. Nanofiltration membranes review: Recent advances and future prospects. *Desalination*, 356:226–254, 2015.

[121] Darren L Oatley-Radcliffe, Matthew Walters, Thomas J Ainscough, Paul M Williams, Abdul Wahab Mohammad, and Nidal Hilal. Nanofiltration membranes and processes: A review of research trends over the past decade. *Journal of water process engineering*, 19: 164–171, 2017.

[122] Bao Lee Phoon, Chong Cheen Ong, Mohamed Shuaib Mohamed Saheed, Pau-Loke Show, Jo-Shu Chang, Tau Chuan Ling, Su Shiung Lam, and Joon Ching Juan. Conventional and emerging technologies for removal of antibiotics from wastewater. *J. Hazard. Mater.*, 400:122961, 2020.

[123] Maryam Homayoonfal and Mohammad Reza Mehrnia. Amoxicillin separation from pharmaceutical solution by ph sensitive nanofiltration membranes. *Sep. Purif. Technol.*, 130: 74–83, 2014.

[124] Katrien Hendrix, Simon Vandoorne, Guy Koeckelberghs, and Ivo FJ Vankelecom. Srnf membranes for edible oil purification: introducing free amines in crosslinked peek to increase membrane hydrophilicity. *Polymer*, 55(6):1307–1316, 2014.

[125] Kunpeng Wang, Xiaomao Wang, Brielle Januszewski, Yanling Liu, Danyang Li, Ruoyu Fu, Menachem Elimelech, and Xia Huang. Tailored design of nanofiltration membranes for water treatment based on synthesis–property–performance relationships. *Chem. Soc. Rev.*, 51(2):672–719, 2022.

[126] Zhuyuan Wang, Songmiao Liang, Yuan Kang, Wang Zhao, Yun Xia, Jindi Yang, Huanting Wang, and Xiwang Zhang. Manipulating interfacial polymerization for polymeric nanofilms of composite separation membranes. *Prog. Polym. Sci.*, 122:101450, 2021.

[127] Xuechen Zhou, Zhangxin Wang, Razi Epsztein, Cheng Zhan, Wenlu Li, John D Fortner, Tuan Anh Pham, Jae-Hong Kim, and Menachem Elimelech. Intrapore energy barriers

govern ion transport and selectivity of desalination membranes. *Sci. Adv.*, 6(48):eabd9045, 2020.

[128] Yifeng Huang, Jingjing Sun, Dihua Wu, and Xianshe Feng. Layer-by-layer self-assembled chitosan/paa nanofiltration membranes. *Sep. Purif. Technol.*, 207:142–150, 2018.

[129] BS Ooi, JY Sum, JJ Beh, Woei Jye Lau, and SO Lai. Materials and engineering design of interfacial polymerized thin film composite nanofiltration membrane for industrial applications. In *Membrane Separation Principles and Applications*, pages 47–83. Elsevier, 2019.

[130] JULIUS GLATER and MICHAEL R ZACHARIAH. A mechanistic study of halogen interaction with polyamide reverse-osmosis membranes. ACS Publications, 1985.

[131] Mikhail Stolov and Viatcheslav Freger. Degradation of polyamide membranes exposed to chlorine: an impedance spectroscopy study. *Environ. Sci. Technol.*, 53(5):2618–2625, 2019.

[132] Qian Wang, Yue Wang, Bo-Zhi Chen, Tian-Dan Lu, Han-Lin Wu, Yi-Qun Fan, Weihong Xing, and Shi-Peng Sun. Designing high-performance nanofiltration membranes for high-salinity separation of sulfate and chloride in the chlor-alkali process. *Ind. Eng. Chem. Res.*, 58(27):12280–12290, 2019.

[133] MM Jayarani, PR Rajmohanan, SS Kulkarni, and UK Kharul. Synthesis of model diamide, diester and esteramide adducts and studies on their chlorine tolerance. *Desalination*, 130(1):1–16, 2000.

[134] Gunolla Nagendraprasad, K Anki Reddy, Santanu Karan, and Chandan Das. Nonpreferential solvent transport through an intrinsic cyclodextrin pore in a polyester film. *J. Phys. Chem. B*, 2024.

[135] Gunolla Nagendraprasad, Vasista Adupa, K Anki Reddy, Chandan Das, and Santanu Karan. Semiaromatic polyamide-based membrane in forward osmosis: Molecular insights. *J. Phys. Chem. B*, 127(30):6751–6766, 2023.

[136] Manas Ranjan Puhan, Pulak Sarkar, Gunolla Nagendraprasad, K Anki Reddy, Bhaumik Sutariya, and Santanu Karan. Unraveling anomalies in preferential liquid transport through the intrinsic pores of cyclodextrin in polyester nanofilms. *Adv. Mater.*, page 2404164, 2024.

[137] Pulak Sarkar, Solagna Modak, Santanu Ray, Vasista Adupa, K Anki Reddy, and Santanu Karan. Fast water transport through sub-5 nm polyamide nanofilms: the new upper-

bound of the permeance–selectivity trade-off in nanofiltration. *J. Mater. Chem. A*, 9(36): 20714–20724, 2021.

[138] MJ Kotelyanskii, NJ Wagner, and ME Paulaitis. Atomistic simulation of water and salt transport in the reverse osmosis membrane ft-30. *J. Membr. Sci.*, 139(1):1–16, 1998.

[139] MJ Kotelyanskii, NJ Wagner, and ME Paulaitis. Molecular dynamics simulation study of the mechanisms of water diffusion in a hydrated, amorphous polyamide. *Comput. Theor. Polym. Sci.*, 9(3-4):301–306, 1999.

[140] Edward Harder, D Eric Walters, Yaroslav D Bodnar, Ron S Faibish, and Benoit Roux. Molecular dynamics study of a polymeric reverse osmosis membrane. *J. Phys. Chem. B*, 113(30):10177–10182, 2009.

[141] Yun Luo, Edward Harder, Ron S Faibish, and Benoit Roux. Computer simulations of water flux and salt permeability of the reverse osmosis ft-30 aromatic polyamide membrane. *J. Membr. Sci.*, 384(1-2):1–9, 2011.

[142] Minxia Ding, Aziz Ghoufi, and Anthony Szymczyk. Molecular simulations of polyamide reverse osmosis membranes. *Desalination*, 343:48–53, 2014.

[143] Minxia Ding, Anthony Szymczyk, and Aziz Ghoufi. Hydration of a polyamide reverse-osmosis membrane. *J. Membr. Sci.*, 501:248–253, 2016.

[144] Minxia Ding, Anthony Szymczyk, Florent Goujon, Armand Soldera, and Aziz Ghoufi. Structure and dynamics of water confined in a polyamide reverse-osmosis membrane: A molecular-simulation study. *J. Membr. Sci.*, 458:236–244, 2014.

[145] Zak E Hughes and Julian D Gale. A computational investigation of the properties of a reverse osmosis membrane. *J. Mater. Chem.*, 20(36):7788–7799, 2010.

[146] Weimin Gao, Fenghua She, Juan Zhang, Ludovic F Dumee, Li He, Peter D Hodgson, and Lingxue Kong. Understanding water and ion transport behaviour and permeability through poly (amide) thin film composite membrane. *J. Membr. Sci.*, 487:32–39, 2015.

[147] Vesselin Kolev and Viatcheslav Freger. Hydration, porosity and water dynamics in the polyamide layer of reverse osmosis membranes: A molecular dynamics study. *Polymer*, 55(6):1420–1426, 2014.

[148] Yang Song, Fang Xu, Mingjie Wei, and Yong Wang. Water flow inside polamide reverse osmosis membranes: A non-equilibrium molecular dynamics study. *J. Phys. Chem. B*, 121(7):1715–1722, 2017.

Chapter 2

Simulation Methodology

This thesis endeavors to uncover the microscopic mechanisms underlying various physical phenomena outlined in the objectives. The intricate atomistic characterization of a system surpasses the capabilities of current experimental techniques. Nevertheless, molecular simulations offer a pathway to unravel these microscopic mechanistic details for numerous chemical, physical, and biological systems. Among the array of molecular simulation techniques, molecular dynamics (MD) stands out as particularly impactful, demonstrating remarkable success in providing atomistic insights into a diverse range of phenomena. In this thesis, MD simulation is employed as the primary tool to investigate all the systems outlined in the objectives. This chapter will discuss the essential theoretical and practical aspects of MD simulation.

2.1 Introduction to Molecular Dynamics

In classical molecular dynamics, the positions and velocities of atoms are updated as a function of time by integrating the equations of motion. This process involves solving equation 2.1, where the sum of forces (F_i) acting on a particle—an atom, in this case—determines its acceleration, which can be integrated twice to obtain its position ($\vec{R}$). The effectiveness of an MD simulation is closely tied to the accuracy of the force model, expressed in equation 2.2 as the negative gradient of the potential energy, U($\vec{R}$).

$$a_i = \frac{d^2 x_i}{dt^2} = \frac{F_i}{m_i} \tag{2.1}$$

$$\vec{F}(\vec{R}) = -\nabla U(\vec{R}) \tag{2.2}$$

Nevertheless, solving equation 2.1 analytically becomes impractical, especially for a many−body system with nonlinear terms in the potential expression. Consequently, MD simulation turns to numerical methods to effectively address equation 2.1 within the context of a many−body system. The subsequent sections of this chapter provide a detailed exploration of these numerical techniques.

Among the pioneering applications of MD simulations to study physical systems, a notable contribution was made by Alder and Wainwright [1, 2]. Their work demonstrated the observation of a solid-liquid phase transition through a hard sphere model. Subsequently, Rahman [3] and Verlet [4] independently conducted MD simulations employing a Lennard−Jones (LJ) potential for a system comprising argon atoms. Their calculations of pair-correlations and other equilibrium properties for the system exhibited favorable agreement with experimental values. Another significant breakthrough occurred through a series of studies conducted by Berne and colleagues [5–8], where they explored the molecular relaxation behavior in diatomic liquids using MD simulations. A pivotal milestone unfolded with the first MD simulations of liquid water by Stillinger and Rahman [9–11]. Following these groundbreaking studies, Karplus and collaborators conducted the inaugural MD simulation of proteins [12, 13]. These early implementations paved the way for the extensive use of MD simulations in exploring diverse physical and chemical phenomena, showcasing the versatility and impact of this computational approach across various scientific disciplines.

In the upcoming sections, we will go into the crucial components of MD calculations and the methodologies employed to execute them. Given the myriad of techniques available, our focus will be specifically on those implemented in the MD code NAMD [14]. It's important to note that all simulations presented in this thesis were conducted using NAMD, making it the central point of reference for our discussions on MD techniques.

2.2 Forcefield

The functional form of a force field is a simple mathematical function, with each function characterizing a specific interaction between two or more atoms. The heart of all atomistic molecular dynamics (MD) simulation is the essential capability to compute the potential energy,

U(R), given a set of coordinates, $\vec{R}$. Although quantum mechanical (QM) calculations could be applied for this purpose, their feasibility diminishes significantly for extensive systems such as condensed−phase biomolecules like proteins due to their computational cost−prohibitive nature. Instead, a common approach is to employ a parametric equation derived from classical mechanics. The forces acting on each atom can then be determined by computing the derivative of this function with respect to the coordinates. Thus, a force field is composed of two integral components: the parameters (numerical constants) utilized in the functional form employed for U(R) computation, and the functional form itself. Equation 2.3 illustrates a typical functional form of a force field.

$$\begin{aligned} U(\vec{R}) = & \sum_{bonds} K_b(b-b_0)^2 + \sum_{angles} K_\theta(\theta-\theta_0)^2 \\ & + \sum_{torsion} K_\phi[1+\cos(n\phi+\delta)] + \sum_{impropers} K_\psi(\psi-\psi_0)^2 \\ & + \sum_{i,j\in nb} \left\{ \left[4\epsilon_{ij} \left(\frac{\sigma_{ij}}{r_{ij}} \right)^{12} - \left(\frac{\sigma_{ij}}{r_{ij}} \right)^{6} \right] + \frac{q_i q_j}{r_{ij}} \right\} \end{aligned} \tag{2.3}$$

where K_b, K_θ, K_ϕ, and K_ψ are the respective force constants; b_0, θ_0, and ψ_0 are the equilibrium bond length, bond angle, and improper dihedral angle, respectively; n is the torsional multiplicity, and δ is the phase angle. σ represents the distance at which the Lennard-Jones potential reaches its minimum, ϵ denotes the depth of the potential well, and q refers to the atomic charge.

The eqn. 2.3 represents a fundamental force field expression frequently employed in biomolecular systems. Each term within this equation incorporates specific parameters tailored to the model representing that particular interaction. Primarily, it encompasses both *"bonded"* and *"non−bonded"* energy terms, encapsulating the essential components that govern the interactions within the molecular system.

Bonded: The interactions between covalently bound atoms, such as bond stretching, valence angle bending, and dihedral rotation, are collectively referred to as "bonded energy terms." The first two terms on the right-hand side of eqn. 2.3, specifically bond stretching and angle bending are commonly represented as harmonic functions. These energy terms require specific parameters such as force constant and an equilibrium bond or angle value. The force constants (K_b and K_θ for bonds and angles, respectively) define the stiffness of the harmonic oscillations associated with these interactions. On the other hand, the bond and angle equilibrium values, denoted

as b_0 and θ_0, respectively, signify the geometric configurations where the associated energy is zero. These values represent the sole energy minimum in the potential energy equation for these interactions and are often derived from optimized quantum mechanical (QM) geometries or crystallographic data. The force constants can be determined by fitting the potential energy profile as a function of perturbing the target bond or angle away from its equilibrium value, and these can be obtained from QM vibrational analysis and/or spectroscopic data. Similarly, the equilibrium bond length or valence angle can be established using crystal structures or from an optimized QM geometry.

The third term is the energy due to the torsional motion between four consecutively bonded atoms. The torsional contribution is expressed in the form of a cosine series due to the oscillatory nature of the torsions, containing multiple minima separated by energy barriers of various sizes, representing different possible dihedral conformations. The K_ϕ in the torsional term is called as barrier height and is a measure of barrier to the bond rotation. The n is the multiplicity and its value represents the number of minimas as the bond is rotated through 360° and the δ is the phase factor which represents the torsional angle at which the value of torsion potential is minimum.

Another energy term commonly employed in force fields is the "improper" dihedral, which delineates interactions among four atoms and the angle between two planes. However, improper energy is specifically associated with the out-of-plane deformation around a planar center. In contrast to proper dihedrals, improper dihedrals are usually treated as harmonic interactions, and their functional form is given in eqn. 2.3. However, in certain instances, proper dihedral angles may be sufficiently balanced to maintain planarity at equilibrium, effectively modeling out-of-plane fluctuations with accuracy.

Non-bonded: The last term in the curly bracket is the potential energy contribution due to non-bonded(NB) interactions. The NB term is made up of two contributions, the first is van der Waals(vdW) interaction between two atoms and is modeled using Lennard-Jones(LJ) potential(the term insided the square bracket of the eqn. 2.3). The σ_i and σ_j are the radius of the two atoms and $\sigma_{ij} = (\sigma_i + \sigma_j)/2$ and the atoms are separated by a distance r_{ij} with a potential well depth of ϵ_{ij}. The second part of the NB term is the electrostatic interaction between two atoms having charges q_i and q_j and are separated by a distance r_{ij}. The electrostatic contribution is evaluated by Coulomb's law.

Some popular forcefields frequently used in MD simulations are AMBER[15], GROMOS[16]

and CHARMM[17, 18]. Each of these forcefields target to reproduce a specific set of experimental properties, and hence are developed and optimized accordingly. Also, these forcefields differ in the parametrization methodologies and treatment of a particular term. However, the basic skeleton of each of these forcefields is same as eqn. 2.3. In this thesis, the CHARMM force field has been used for all the objectives outlined.

2.3 Energy Minimization

In general, the energy minimization is performed to get a physically realistic molecular structure, which would be the most stable one. Energy minimization is crucial for determining the optimal molecular arrangement in space, as the initially drawn chemical structures may not be energetically favorable. The potential energy of a molecule encompasses various energy components such as stretching, bending, and torsion. Therefore, having a reasonable initial structure for the system under consideration is essential before conducting a MD run. Typically, structures obtained from experiments or constructed using software tools like Avogadro [19] are employed to build the initial structures of individual monomeric units intended for polymerization. Subsequently, these individual monomers are packed into a simulation box, subjecting the system to local stresses arising from nonbonded overlaps and distorted bond lengths and angles. As a standard practice, the initial positions of atoms in the system are refined through an energy minimization run using an appropriate technique. This refinement helps alleviate nonbonded overlaps and correct distorted bond lengths and angles, ensuring a more stable and energetically favorable starting point for subsequent simulations.

A schematic representation of the potential energy surface for a specific system is depicted in Figure 2.1. The red ball symbolizes the system's initial potential energy state, corresponding to its position on the surface. Various trenches on the energy surface represent minima. The closest trench to the initial state is referred to as a local minima, while the deepest well is identified as the global minima. The primary objective of energy minimization is to guide the system downhill toward the local minima on the potential energy surface. Fundamentally, energy minimization constitutes an optimization problem where a function (expressed as a forcefield expression) is provided. This function is contingent on numerous independent variables, specifically the Cartesian coordinates of each atom. The challenge lies in determining the set of coordinates that result in the minimum value of the potential energy function. The ultimate

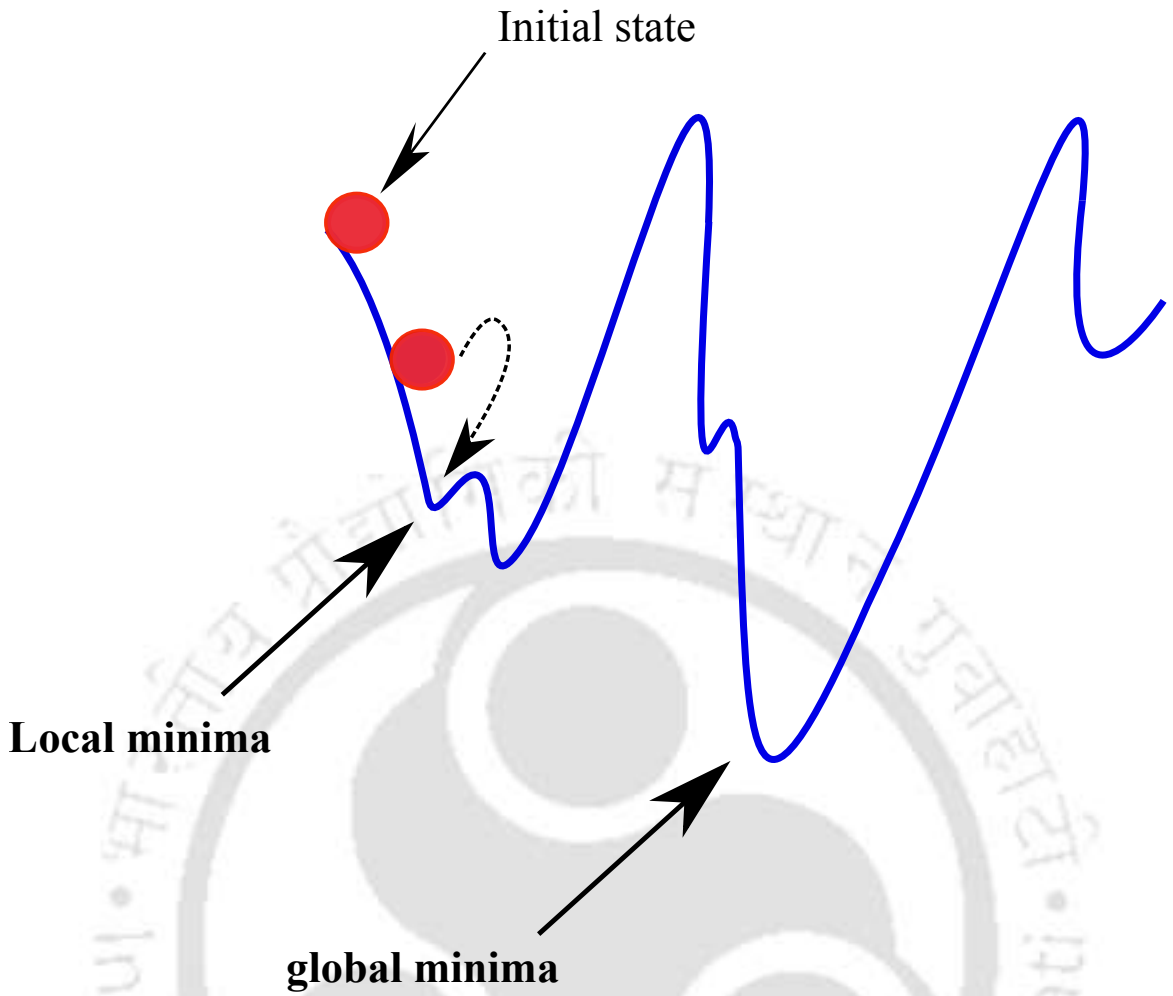

Figure 2.1: A schematic representation of a one dimensional potential energy surface.

goal is to achieve a stable and energetically favorable configuration for the molecular system.

Minimization algorithms are broadly categorized into derivative and non-derivative methods. To illustrate, consider a Taylor series expansion of the potential energy function $U(x)$ around a minimum point x_0.

$$U(x) = U(x_0) + (x - x_0)U'(x_0) + \frac{1}{2}(x - x_0)^2 U''(x_0) \tag{2.4}$$

Where U' and U'' are the first and second derivatives of the function. Here, x represents a vector with 3N components, where 3N denotes the total number of Cartesian coordinates with N atoms. Non−derivative algorithms, also known as zero−order algorithms, solely utilize the function's value during minimization. Conversely, first and second−order algorithms incorporate the values of U' and U'', respectively. The accuracy and computational cost of these algorithms increase in the same order, with second−order algorithms being the most

accurate yet computationally expensive. Therefore, the choice of algorithm depends on the required sophistication level, system size, and available computational resources. In quantum mechanical calculations demanding high accuracy with fewer atoms, second−order algorithms like the Newton−Raphson method are commonly employed. However, in the realm of most molecular dynamics simulation codes, the preference leans towards first-order algorithms such as the steepest descent and conjugate gradient methods due to their computational efficiency. Zero−order methods like the simplex method are considered basic and are often used as a preliminary step before deploying more advanced techniques.

The first-order algorithms are the most frequently used in MD simulations since they strike a fair balance between accuracy and efficiency. All the "order 1" methods use the slope of the energy curve(obtained from the first derivative) to drive the ball(red ball in Figure 2.2) downhill towards the local minima iteratively. In general, all the first-order algorithms inch towards minima with the following equation:

$$\vec{r}_k = \vec{r}_{k-1} + \lambda_k \vec{S}_k \tag{2.5}$$

where $\vec{r}_k$ is the new position at step k, $\vec{r}_{k-1}$ represents the position at previous step $k-1$, λ_k and $\vec{S}_k$ are step size and direction of the step respectively. Here we discuss two of the most commonly used algorithms in MD codes: the steepest descent and the conjugate gradient method.

2.3.1 Steepest Descent

The steepest descent(SD) uses simple logic to perform the energy minimization, that is, to move the system in the direction of the net force since that is the direction downhill towards the local minima. As shown in the eqn 2.2, the force is the negative gradient of the potential; hence we can write the direction term $\vec{S}_k$ in the eqn 2.5 as:

$$\vec{S}_k = -g_k = -\nabla U(\vec{R}) \tag{2.6}$$

after obtaining the direction $\vec{S}_k$, another important choice is the step length λ_k. In most of SD's implementations, the first value of λ_k is an arbitrary value, which is then adjusted during minimization at every iteration based on the energy obtained at that step. If the energy obtained at any step is less than the previous step, then the value of λ_k is increased by a preset factor. The increment is repeated for every step as long as there is a reduction in the energy.

However, an increase in the energy at the next step indicates that the algorithm has crossed over minima. The energy is then reduced by using a smaller λ_k to bring back the system closer to the minima. In this way, the algorithm eventually reaches the minima by oscillating around it and correcting itself at every step.

2.3.2 Conjugate Gradient

Although the SD method works well if the system is far from the minima, it becomes inefficient due to its oscillatory behavior and quadratic shape of the energy surface near the minima. Thus SD is good at bringing the system near to minima; however, it rarely converges to the exact point of minimum. The conjugate gradient(CG) method uses a unique approach, where the first step of the CG method is the same as the SD method; that is, the direction at the first step of CG is given by:

$$\vec{S}_1 = -g_1 \tag{2.7}$$

However, for the subsequent steps, the direction is given by the expression:

$$\vec{S}_k = -g_k + b_k \vec{S}_{k-1} \tag{2.8}$$

where $\vec{S}_{k-1}$ is the direction at the previous step and b_k is the weight factor given by the expression:

$$b_k = |g_k|^2 / |g_{k-1}|^2 \tag{2.9}$$

Where g_k and g_{k-1} are the current and previous steps' gradients, respectively; hence, the direction in the CG method is calculated as a weighted average of the current step's gradient and the previous step's direction. The CG method performs better than the SD method, even for non-quadratic surfaces, due to its ability to use gradient information from previous steps to evaluate the direction for future steps.

2.3.3 Convergence Criteria

While numerical schemes for energy minimization are effective in alleviating stress in structures and providing a reasonable starting point for molecular dynamics simulations, they lack the precision of analytical methods. Consequently, a numerical minimization algorithm will continue adjusting the system towards the minima indefinitely unless stopped using appropriate convergence criteria. One simple criterion involves monitoring the energy difference between

two successive steps; if it drops below a certain threshold and remains there for several steps, the minimization can be considered converged. Another approach is to observe changes in atomic coordinates, stopping when no significant alterations are observed over many steps. A more sophisticated criterion involves calculating the root-mean-square gradient (GRMS). The GRMS is determined by taking the square root of the ratio between the sum of squared gradients and the number of coordinates. This criterion provides a more nuanced evaluation of convergence during the energy minimization process:

$$GRMS = \sqrt{\frac{\sum g^2}{3N}} \tag{2.10}$$

2.4 Periodic Boundary Condition

Periodic Boundary Conditions (PBC) are a common technique used in molecular dynamics simulations to emulate an infinite system and mitigate surface effects. The challenge of explicitly simulating a bulk or macroscopic system, which comprises a staggering number of particles (at least Avogadro's number, 10^{23}), becomes impractical for even the most advanced supercomputers. Additionally, while macroscopic systems tend to downplay the impact of boundaries on bulk properties, these wall effects become significant in smaller systems. To bridge the microscopic states generated in MD simulations with corresponding macroscopic systems and faithfully reproduce bulk properties, smart treatment of MD system boundaries is essential. PBC addresses this by infinitely replicating the simulation box in all three dimensions, forming a periodic lattice. Particles' movement within these imaginary boxes imitates their behavior in the original box. A two-dimensional PBC schematic is shown in Figure 2.2.

Notably, any particle exiting one side of the simulation box seamlessly re-enters from the opposite side, rendering the system virtually infinite and minimizing boundary effects. Consequently, PBC enables accurate reproduction of macroscopic system properties, freeing the simulation from the constraints of a limited volume and allowing it to represent an infinitely extended system.

2.4.1 Minimum Image Convention and Cutoff

The implementation of Periodic Boundary Conditions (PBC) successfully addressed the challenges posed by wall effects, allowing for the simulation of a bulk system without the need to

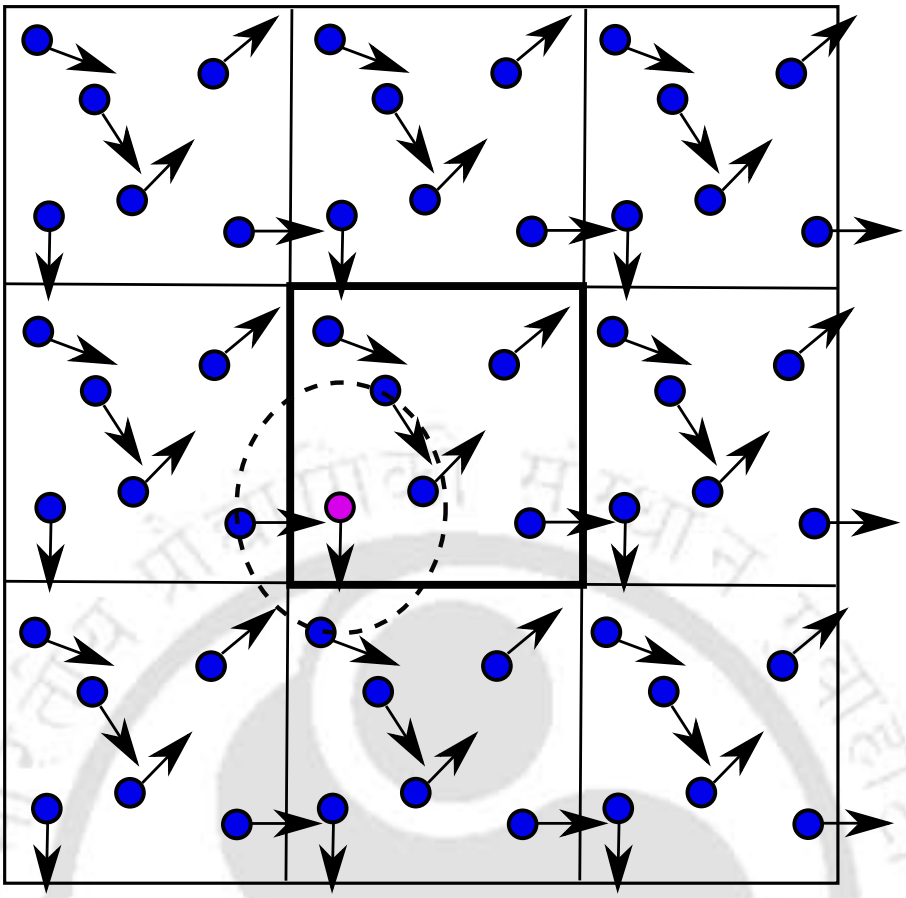

Figure 2.2: A schematic representation of two dimensional periodic boundary condition. The highlighted box in the center is the original simulation box and all other boxes are images of it.

physically enlarge the system. Nevertheless, the introduction of an infinite system through PBC introduced a new challenge when evaluating non-bonded interactions that span periodic boundaries. To tackle this issue, the *minimum image convention* (MIC) is employed. MIC guides the calculation of non-bonded interactions across periodic boundaries by suggesting that, instead of the original particle, the closest periodic image of the other particle should be considered. This approach is justified by the rapid decay of interactions between particles with increasing distance, making the contribution of particles beyond a certain cutoff distance negligible. By focusing on the closest periodic image, the simulation accurately captures the interaction between the two particles without necessitating an excessively large simulation box. This method ensures efficiency in computational resources while maintaining precision in modeling particle interactions.

The evaluation of non-bonded interactions stands out as the most time-consuming aspect

of an MD simulation. While the Minimum Image Convention (MIC) cleverly handles interactions across boundaries, calculating all pairwise interactions, even within the simulation cell, is computationally intensive and often unnecessary. In reality, particle interactions diminish rapidly with distance, becoming inconsequential beyond a certain point. Therefore, introducing a *cutoff* distance allows the simulation to focus solely on interactions between closely situated particles, neglecting those between more distant particles that have minimal impact. Figure 2.2 illustrates this concept, with the solid pink colored particle representing the one under consideration and the dashed circle denoting the cutoff distance. Choosing the right cutoff distance involves striking a balance between accuracy and efficiency. A smaller cutoff distance enhances precision but demands more computational resources, while a larger cutoff distance sacrifices precision for computational savings. The optimal choice depends on the specific characteristics of the simulated system and the desired level of accuracy for the results.

2.5 Integration of Equations of Motion

As mentioned earlier, finding an analytical solution for the equations of motion (EOM) is unfeasible due to the intricate nature of the potential function and the challenge of solving a many-body problem. Consequently, smart algorithms are essential for effective integration. Numerous algorithms exist for this purpose, with two of the most commonly used in MD codes being the Verlet and velocity Verlet algorithms. These algorithms play a pivotal role in simulating molecular dynamics by numerically integrating the equations of motion, allowing for the accurate prediction of particle trajectories over time.

2.5.1 Verlet Algorithm

The idea behind the Verlet algorithm(VA)[4] is quite simple; it uses Taylor series expansion to generate new positions of the atoms. The Taylor expansion for a position $r_i(t + \Delta t)$ can be written as:

$$r_i(t + \Delta t) \approx r_i(t) + \Delta t \dot{r}_i + \frac{1}{2}\Delta t^2 \ddot{r}_i(t) \tag{2.11}$$

The terms higher than second order in the above Taylor expansion are neglected. Also, as is known, the first derivative of the position is the velocity($\dot{r}_i(t) = v_i(t)$), and the second is acceleration($\ddot{r}_i(t) = a_i(t)$), also using Newton's second law we have $a_i(t) = F_i(t)/m_i$. Hence,

we can rewrite the eqn 2.11 as:

$$r_i(t + \Delta t) \approx r_i(t) + \Delta t v_i(t) + \frac{\Delta t^2}{2m_i} F_i(t) \tag{2.12}$$

A similar expression could be written for $r_i(t - \Delta t)$ as:

$$r_i(t - \Delta t) \approx r_i(t) - \Delta t v_i(t) + \frac{\Delta t^2}{2m_i} F_i(t) \tag{2.13}$$

Adding eqns 2.12 and 2.13 and rearranging we get

$$r_i(t + \Delta t) \approx 2r_i(t) - r_i(t - \Delta t) + \frac{\Delta t^2}{2m_i} F_i(t) \tag{2.14}$$

Eqn 2.14 and 2.13 are the most crucial parts of VA. The VA's execution can be elaborated in the following steps:

1. A set of energy-minimized coordinates and initial velocities is provided to the integrator at $t = 0$.

2. The eqn 2.12 is used to kick-start the integrator and obtain the first set of new coordinates $r_1(\Delta t), ..., r_N(\Delta t)$.

3. The eqn 2.14 can now be used to obtain future positions and generate an arbitrary length of the trajectory.

4. The velocities can be computed using the centered difference formula on positions as follows:

$$v_i(t) = \frac{r_i(t + \Delta t) - r_i(t - \Delta t)}{2\Delta t} \tag{2.15}$$

Similar to any algorithm or numerical technique, the Velocity Verlet algorithm (VA) has both advantages and drawbacks. Notably, one of its key features is its simplicity, accuracy, and ease of implementation. Moreover, the memory requirements for VA are modest. The algorithm optimally utilizes force evaluation, performing it just once at each integration step, contributing to its efficiency. Given that force calculation is often the most computationally demanding step in MD simulations, this characteristic is particularly advantageous. Another crucial aspect of VA is its time-reversible property, aligning with the requirements of the equations of motion (EOM) for a good integrator. However, the VA has its limitations. The evaluation of velocities in VA is not straightforward; it is both inaccurate and inefficient, involving an additional set of iterations with equation 2.15. Additionally, VA requires an auxiliary equation (equation 2.13)

to obtain the first step before proceeding with equation 2.14, making it a non-self-starting algorithm. Despite these drawbacks, the overall simplicity, accuracy, and efficiency of VA make it a widely employed and valuable integrator in molecular dynamics simulations.

2.5.2 Velocity Verlet Algorithm

While the VA is an elegant method for integrating equations of motion (EOM), it has a significant drawback−it doesn't evolve velocities simultaneously with positions, which are essential for calculating kinetic energy. To address this limitation, Swope et al. introduced the velocity Verlet algorithm (VVA) [20]. The key insight behind VVA is the recognition that the EOM can evolve backward in time. This advancement overcomes the shortcomings of VA, providing a more comprehensive and accurate approach for simulating molecular dynamics by concurrently updating both positions and velocities. Considering second-order Taylor expansion for position $r_i(t + \Delta t)$ we have:

$$r_i(t + \Delta t) \approx r_i(t) + \Delta t v_i(t) + \frac{\Delta t^2}{2m_i} F_i(t) \tag{2.16}$$

Now if we want to evolve the system backward in time that is from $t + \Delta t)$ to t the Taylor expansion could be written as:

$$r_i(t) \approx r_i(t + \Delta t) - \Delta t v_i(t + \Delta t) + \frac{\Delta t^2}{2m_i} F_i(t + \Delta t) \tag{2.17}$$

substituting the value of $r_i(t + \Delta t)$ from eqn 2.16 in eqn 2.17 and rearranging yields

$$v_i(t + \Delta t) = v_i(t) + \frac{\Delta t}{2m_i}[F_i(t) + F_i(t + \Delta t)] \tag{2.18}$$

Eqn 2.18 is the equation used to perform velocity evolution in VVA and eqn 2.16 for position evolution. Hence, VVA can perform both velocity and position evolution simultaneously. The VVA can be executed in the following steps:

1. A set of energy-minimized coordinates and initial velocities is provided to the integrator at $t = 0$.

2. New set of coordinates are calculated at $t + \Delta t$ using eqn 2.16.

3. Forces are computed at $t + \Delta t$ using the coordinates obtained in the second step.

4. Finally the velocities are calculated at $t + \Delta t$ using the eqn 2.18

Similar to the VA, the VVA also comes with its set of advantages and limitations. A crucial strength of VVA lies in its ability to accurately and efficiently evaluate velocities and positions simultaneously. Implementing VVA is straightforward, requiring a simple transcription of equations 2.16 and 2.18 into the syntax of a specific programming language. The time-reversible nature of VVA contributes to its numerical stability. However, one significant drawback of VVA is that it is slightly more computationally expensive than VA. Despite this additional computational cost, the accuracy and the ease of velocity evaluation provided by VVA often outweigh this drawback, making it a valuable choice for simulating molecular dynamics.

2.6 Ewald Summation

In molecular dynamics (MD) simulations, the concept of a force field revolves around a simple functional form for the potential energy. The potential energy comprises two types of contributions: bonded and non-bonded (NB). Among these, the non-bonded contributions are computationally the most expensive to evaluate in an MD simulation. Van der Waals (vdW) interactions, a part of the non-bonded forces, exhibit a relatively short range and can be managed with an appropriate cutoff, as discussed in section 2.4.1. However, the evaluation of electrostatic interactions poses a challenge due to their long-range nature in Coulombic interactions. The relationship between vdW and Coulombic interactions concerning the length scale is evident from equation 2.19.

$$U_{NB}(\vec{R}) = \sum_{i,j \in nb} \left\{ \left[4\epsilon_{ij} \left(\frac{\sigma_{ij}}{r_{ij}} \right)^{12} - \left(\frac{\sigma_{ij}}{r_{ij}} \right)^{6} \right] + \frac{q_i q_j}{r_{ij}} \right\} \tag{2.19}$$

To address the long-range nature of Coulombic interactions, Ewald introduced a technique now known as Ewald summation [21]. The fundamental concept behind Ewald's summation is that a function that exhibits long-range behavior in real space becomes short-range in reciprocal or Fourier space. Therefore, by transforming the Coulombic term into a Fourier representation, it can be efficiently evaluated. To achieve this, we express the reciprocal term in the Coulombic contribution of equation 2.19 as follows:

$$\frac{1}{r} = \frac{erf(\alpha r)}{r} + \frac{erfc(\alpha r)}{r} \tag{2.20}$$

where the $erf(\alpha r)$ is the error function and $erfc(\alpha r)$ is its complement, both are defined

as:

$$erf(x) = \frac{2}{\sqrt{\pi}} \int_0^x dt\, e^{-t^2} \tag{2.21}$$

$$erfc(x) = 1 - erf(x) = \frac{2}{\sqrt{\pi}} \int_x^\infty dt\, e^{-t^2} \tag{2.22}$$

It can be noted that, based on the definitions given above, the first term of the eqn. 2.20 is long-range while the second is short-range. Hence, the short-range term can be evaluated along with the vdW term in the real space, while the long-range term can be computed in the Fourier space. Thus using eqn. 2.20 the Coulombic term can be written as a sum of two terms as follows:

$$U_{Coloumbic} = \underbrace{\frac{q_i q_j erf(\alpha r_{ij})}{r_{ij}}}_{\text{long}} + \underbrace{\frac{q_i q_j erfc(\alpha r_{ij})}{r_{ij}}}_{\text{short}} \tag{2.23}$$

As explained, the short-range term can be evaluated along with the vdW term. The α in the above equations is used to tune in an appropriate cutoff distance for the short-range Coulombic interactions. The long-range part is computed using the Poisson summation rule leading to a Fourier series expansion of the error function. The final equation obtained is as follows:

$$U_{long} = \frac{1}{V} \sum \frac{4\pi}{|g|^2} exp\left(\frac{|g|^2}{4\alpha^2}\right) \left|\sum q_i exp(ig.r_i)\right|^2 - \frac{\alpha}{\sqrt{\pi}} \sum_i q_i^2 \tag{2.24}$$

The eqn. 2.24 is known as the Ewald sum, where V represents the volume of the simulation cell, and g stands for the reciprocal space vectors. While equation 2.24 ingeniously addresses the calculation of long-range Coulombic interactions, its direct implementation remains computationally expensive, especially for large systems. Essman et al. introduced the smooth particle mesh Ewald (SPME) method [22] as an efficient approach for evaluating the Ewald sum. In SPME, the space is divided into grids, and charges are uniformly distributed across its nodes using an interpolation scheme with a B-spline function.

2.7 Ensemble

The term "ensemble" in molecular dynamics draws a parallel with its literal meaning, rooted in the realm of music where it signifies a group of musicians working together. Analogously, in

the context of molecular dynamics, an ensemble represents a collection of systems characterized by variations in microscopic details (such as positions and momenta) while sharing common macroscopic constraints, such as the number of particles, pressure, total energy, or temperature. This concept, initially introduced by J.W. Gibbs in "Elementary Principles in Statistical Mechanics[23]," underscores the idea that macroscopic observables emerge from the average of microscopic properties across the ensemble. Mathematically, the ensemble concept can be succinctly expressed as follows:

$$M = \frac{1}{\mathcal{Z}} \sum_{i=1}^{\mathcal{Z}} m(X_i) \tag{2.25}$$

Where M is a macroscopic observable, $\mathcal{Z}$ is the number of members in the ensemble, $m(X)$ represents a microscopic phase space function, and X denotes a coordinate on the phase space. In summary, the concept of an ensemble serves as a bridge between the macroscopic and microscopic realms. For an in-depth exploration of this topic, readers are encouraged to refer to comprehensive texts by [24], Bagchi[25] and others. Moving forward, various types of ensembles exist, each defined by specific macroscopic constraints. Among these, the microcanonical, canonical, and isothermal-isobaric ensembles stand out as the three most common and practically useful ones.

2.7.1 Microcanonical(NVE) Ensemble

The microcanonical (NVE) ensemble stands as the most fundamental and straightforward among various ensembles. It is defined by a constant number of particles (N), constant volume (V), and constant total energy (E). An essential principle of the NVE ensemble is its adherence to the fundamental statistical mechanical postulate of "equal a prior probability." This postulate asserts that all microstates within a given ensemble hold equal probability, implying that each microstate shares the same total energy. The distinctive characteristic of the NVE ensemble lies in its ability to generate detailed dynamics for the system at hand, as it can explore all possible microstates given sufficient time. Entropy (S) serves as the unique thermodynamic state function for the NVE ensemble. All other thermodynamic quantities within the NVE ensemble can be derived from entropy through the following relations:

$$\frac{1}{T} = \left(\frac{\partial S}{\partial E}\right)_{N,V}, \qquad \frac{P}{T} = \left(\frac{\partial S}{\partial V}\right)_{N,E}, \qquad \frac{\mu}{T} = -\left(\frac{\partial S}{\partial N}\right)_{V,E} \tag{2.26}$$

Where T is the temperature, P is pressure, and μ is the chemical potential for the given system. The relation between macroscopic observables and a microscopic property for an NVE ensemble is given by the famous "Boltzmann relation":

$$S = k_B ln\Omega \tag{2.27}$$

Where S is the entropy of the system, k_B is known as Boltzmann's constant and is equal to $1.3806 \times 10^{-23} J.K^{-1}$ and Ω is known as the partition function for NVE ensemble and it defines the number of microstates available to the system. Using the eqn 2.27 and eqns 2.26, all thermodynamic properties can be written in terms of Ω. However, the main limitation of the NVE ensemble is that it does not reflect the systems commonly encountered in most of the experiments and other realistic environments. Since, in most of the experiments, the system is allowed to interact with its surroundings, which makes NVE impractical for most cases.

2.7.2 Canonical(NVT) Ensemble

The thermodynamic constraints used for the canonical(NVT) ensemble are the constant number of particles(N), constant volume(V), and constant temperature(T). A clear advantage NVT has over NVE is that NVT mimics the commonly encountered experimental setups more closely. The conditions for an NVT ensemble are achieved theoretically by assuming that the system under consideration is in thermal contact with an external infinite heat bath and the system's energy fluctuates in such a way that its temperature remains constant. The principle thermodynamic state function for the NVT ensemble is the Helmholtz energy(A). The thermodynamic quantities for the NVT ensemble are defined in terms of A as follows:

$$S = -\left(\frac{\partial A}{\partial T}\right)_{N,V}, \qquad \mu = \left(\frac{\partial A}{\partial N}\right)_{V,T}, \qquad P = -\left(\frac{\partial A}{\partial V}\right)_{N,T} \tag{2.28}$$

The connection between macroscopic thermodynamic quantities and microscopic property is given by the relation:

$$A = -k_B T ln Q \tag{2.29}$$

Where Q is known as the canonical partition function and k_B is the Boltzmann's constant.

Although the NVT ensemble exhibits an advantage over NVE of being closer to the realistic systems. However, a straightforward integration of EOM will produce an NVE ensemble. Hence, we require methods to control the temperature in an MD simulation in order to generate

an NVT ensemble. These methods are known as thermostats, and we will discuss a few of these methods in the upcoming section.

Temperature Control or Thermostats

Velocity Rescaling: The easiest way to control the temperature is to rescale the velocities at every time step. The relation between velocities and temperature is given by the well-known result,

$$\langle \sum_i \frac{1}{2} m_i {v_i}^2 \rangle = \frac{1}{2} k_B T \tag{2.30}$$

Then velocities can be rescaled by using an appropriate factor given by:

$$\lambda = \sqrt{\frac{T_{desired}}{T(t)}} \tag{2.31}$$

Although convenient in its approach, the method causes significant perturbation of the trajectory. Moreover, the rescaled velocities may not lie within the Boltzmann distribtion; hence, the method does not guarantee a canonical distribution.

Andersen Thermostat: The method suggested by Andersen[26] to control the temperature in an MD simulation is based on simple velocity assignment from a Maxwell-Boltzmann distribution of velocities. According to this method, the coupling between the system and the heat bath is represented by stochastic dynamics of the collisions between the system's particles and the heat bath. These collisions occur periodically on randomly selected particles. The particle which undergoes collision is assigned a new velocity from a Maxwell-Boltzmann distribution of velocities corresponding to the target temperature. If the frequency of these stochastic collisions is given by ν and t is the time between two successive collisions, then the probability for a collision is by the Poisson process,

$$P(\nu, t) = \nu e^{-\nu t} \tag{2.32}$$

Although the Andersen method successfully generates the canonical ensemble and is also easy to implement, the dynamics generated by it is unphysical. Hence, it must be avoided whenever the goal of the study is to calculate the dynamical properties of the system, e.g., diffusivity, viscosity, thermal conductivity, etc. However, static properties such as pressure, density, etc., remain unaffected.

Nosé–Hoover Thermostat: Andersen showed that a stochastic approach could generate a canonical ensemble. However, Nosé–Hoover[27, 28] devised a clever method to generate canonical phase space distribution with a deterministic approach. In this method, the EOM is tweaked by adding additional terms to attain temperature control; such methods are called extended system methods. The main idea behind the Nosé–Hoover thermostat is that an additional term is introduced in the EOM such that it can monitor any deviation in the instantaneous kinetic energy corresponding to the desired temperature and scale the velocities accordingly. The modified Lagrangian of EOM for Nosé–Hoover method is given by:

$$\mathcal{L}_{N-H} = \sum_{i=1}^{N} \frac{1}{2} m_i (s\dot{r}_i)^2 - U(r^N) + \frac{Q\dot{s}^2}{2} - gk_B T ln s \tag{2.33}$$

Where s is the position of the imaginary heat bath,$\dot{s}$ is the conjugate velocity of the heat bath, and Q is the effective mass of the heat bath. The Nosé–Hoover thermostat generates accurate canonical distribution. Additionally, the dynamics generated within it are more realistic than the Andersen thermostat. However, the convergence of Nosé–Hoover thermostat is a bit slower due to the presence of second-order terms. Hence, it must be avoided for the systems that are far away from the equilibrium.

2.7.3 Isobaric-Isothermal(NPT) Ensemble

Most of the condensed-phase experiments are conducted under constant temperature and pressure. Moreover, most of the standard thermodynamic data are reported under constant temperature and pressure conditions. This makes the isothermal-isobaric(NPT) the most useful of all the ensembles, since it is closest to the physical conditions at which experiments are performed. The thermodynamic control variables of NPT ensemble are constant number of particles(N), constant pressure(P) and constant temperature(T). The basic thermodynamic quantities of NPT ensemble are defined using a new state function, the Gibbs free energy(G). The relations are written as:

$$\mu = \left(\frac{\partial G}{\partial N}\right)_{P,T}, \qquad \langle V \rangle = \left(\frac{\partial G}{\partial P}\right)_{N,T}, \qquad S = -\left(\frac{\partial G}{\partial T}\right)_{N,P} \tag{2.34}$$

The link between macroscopic and microscopic worlds for an NPT ensemble is given by the relation:

$$G = -k_B T ln \Delta \tag{2.35}$$

Where all the variables have the same meaning defined previously, and Δ is the partition function for an NPT ensemble. The concept of free energy obtained in the formulation of NVT and NPT is quite useful since the physical interpretation of it is the work required to change the system's state from state 1 to state 2. Hence free energy is an indicator of the thermodynamic feasibility of a process.

Pressure Control or Barostats

In the previous section, we discussed methods for controlling the temperature to generate an NVT ensemble. However, in order to perform an MD simulation with an NPT ensemble, it is crucial to control pressure along with the temperature. Here we discuss a couple of methods to maintain pressure in an MD simulation.

Berendsen Barostat: In the Berendsen method[29], the system's pressure is controlled by scaling the dimension of the simulation box and coordinates of the particles. The rate of change of pressure is given by the relation:

$$\frac{dP}{dt} = \frac{(P_0 - P)}{\tau_p} \tag{2.36}$$

Where τ_p is the coupling constant, P_0 is the desired pressure, and P is the instantaneous pressure. The scaling factor is given by :

$$\mu = 1 - \frac{\beta \Delta t}{3\tau_p}(P_0 - P) \tag{2.37}$$

Here μ is the scaling tensor used to scale the box size and coordinates of the particles to maintain the system's pressure at the desired value(P_0), β is the isothermal compressibility of the system and Δt is the time step. Berendsen's method is an example of a weak coupling barostat. Hence, it is more appropriate to use it in situations where pressure deviation is significant, mainly in the initial stages of the simulation (e.g., equilibration).

Anderson Barostat: The Anderson pressure coupling method[26] uses an imaginary piston to control the pressure. The piston and the original system form an extended system, and the EOM for such a system is given by:

$$\dot{r} = \frac{p_i}{m_i} + \frac{1}{3}\left(\frac{\dot{V}}{V}\right) r_i \tag{2.38}$$

$$\dot{p} = F_i + \frac{1}{3}\left(\frac{\dot{V}}{V}\right) p_i \tag{2.39}$$

$$\ddot{V} = \frac{P - P_0}{M} \tag{2.40}$$

Here P is the instantaneous pressure, P_0 is the desired pressure, V is the volume, M is the mass of the imaginary piston, and r_i, p_i, m_i and F_i the position, momentum, mass, and force for the ith particle respectively. The EOM of Anderson barostat(2.38-2.40) samples an isobaric-isoenthalpic ensemble. However, combining an appropriate thermostat with Andersen's barostat will generate the NPT ensemble. The choice of mass for the imaginary piston is crucial here since it will decide the decay of volume fluctuations in the ensemble.

2.8 Constraints

Atomistic simulations have a varying degree of freedom(DF) of motions such as bond vibration, angle bending, and torsional motion. The time step for the integration of EOM is usually governed by DF with the fastest motion or the highest frequency present within the system. However, accounting for these higher-frequency motions can slow down the simulation considerably. Moreover, these high-frequency motions are not crucial in general in the overall configurational phase space exploration, particularly for bigger systems such as biomolecular systems. Hence, it is customary in MD simulations to fix or constrain these DF, which allows the use of a bigger time step and eventually speeds up the simulations.

Implementation of constraints requires modifying the EOM to incorporate the effect of constraints. This modification is done by using the method of Lagrange's undetermined multipliers. The resulting EOM can be expressed as:

$$m_i\ddot{r} = F_i + \sum_{k=1}^{N_c} \lambda_k \nabla_i \sigma_k \tag{2.41}$$

The last term in the eqn. 2.41 represents the force experienced by the atom due to constraints. The λ_k is a set of Lagrange's multiplier to enforce the constraints, and σ_k are holonomic(depends only on coordinates of atoms involved) constraints. Although it is possible to obtain an exact solution for Lagrange's multiplier for a few atoms, it becomes increasingly impractical as the system size increases. Additionally, as EOM in an MD simulation is solved using one of the numerical schemes discussed in a previous section, incorporating an exact analytical expression for λ_k will accumulate errors in the calculations. Hence, to avoid these problems, numerical algorithms such as SHAKE[30] and RATTLE[31] to calculate the multipliers during the simulation

run. These algorithms evaluate the multipliers iteratively for each constraint until it converges to a very small tolerance. Although constraints are usually employed to fix the bond vibrations involving hydrogen atoms, they can also be used to fix angle bending in certain molecules by constraining the distance between the two end atoms involved in the angle formation.

2.9 Water Models

Water holds a pivotal role in numerous chemical and biological processes, influencing and mediating various phenomena. In molecular dynamics (MD) simulations, it becomes imperative to incorporate water due to its significance. Various water models have been developed, each designed to address specific properties of water. Consequently, no single water model can accurately replicate all the diverse properties of water. The selection of a particular model hinges on the objectives of the investigation at hand. Moreover, these water models differ in complexity and sophistication. Therefore, the choice of a model should be made considering the desired level of accuracy and the computational resources available for the simulation. The selection process involves a careful balance between the intricacies of the model and the specific properties of water that need to be captured for a given study.

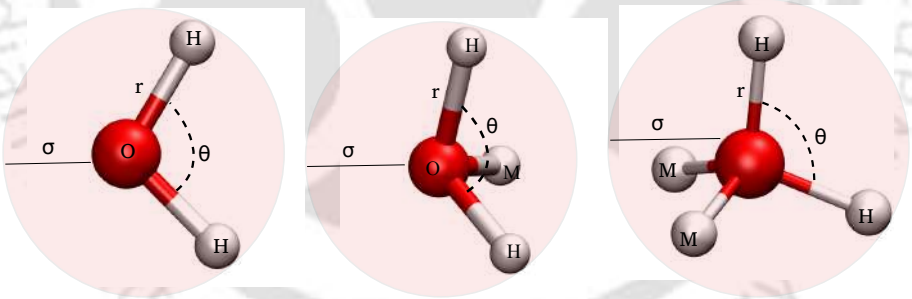

(a) (b) (c)

Figure 2.3: (a) TIP3P (b) TIP4P (c) TIP5P (The geometric structures are adopted from the literature [32, 33], and M represents the massless point M assosiated with the oxygen atom charge)

Among the various water models available 3-site, 4-cite and 5-cite models (refer Figure 2.3) are most commonly used . We will discuss briefly some of the popular water models in each of these categories.

Three Point Models

Three point water models are one of the earliest and simplest models. In this model the water molecule is represented by three point charge for hydrogen and oxygen atoms. Despite their simplicity, three-point water models can provide reasonable approximations of certain properties and behaviors of real water, making them computationally efficient for a wide range of applications. We will discuss two widely used three point models namely TIP3P and SPC/E.

TIP3P

Transferable Intermolecular Potential with Three Points (TIP3P) is one of the earliest and most widely used three point model. It was proposed by Jorgensen et al.[34]. In the TIP3P model, each water molecule is represented by three point charges: a negative charge at the oxygen atom (-1.0 e) and two positive charges at the hydrogen atoms (+0.52 e). The atomic charges and Lennard-Jones parameters are fitted to reproduce experimental properties of water, such as the density and heat of vaporization. The O–H bond length and H–O–H bond angle used in TIP3P model are 0.9572 Åand 104.52° respectively. TIP3P stands out for its simplicity, streamlining the number of interaction terms and contributing to faster computational simulations compared to more intricate models. This model demonstrates reasonable accuracy in replicating fundamental water properties, including density, radial distribution functions, and self-diffusion coefficients. However, TIP3P does exhibit certain limitations, notably in the representation of water structure. One drawback is its tendency to overestimate hydrogen bond length and underestimate the O–H–O bond angle, resulting in deviations from the true water structure. Consequently, TIP3P may not be the optimal choice for studies requiring precise characterization of hydrogen bonding, such as investigations into specific biomolecular systems or phase transitions. Despite its limitations, TIP3P remains a computationally efficient option for simulations that do not heavily rely on accurate hydrogen bonding details.

SPC/E

SPC/E model[35] is very similar to TIP3P, each water molecule is represented as three point charges: one negative charge located at the oxygen atom (-0.8476 e) and two positive charges located at the hydrogen atoms (+0.4238 e). The O–H bond length and H–O–H bond angle used in SPC/E model are 1 Åand 109.47° respectively. The target properties of SPC/E are the density and the vaporization enthalpy at room temperature. However, the key difference between TIP3P and SPC/E is the use of a polarization energy correction in case of SPC/E to correctly reproduce the vapourization enthalpy of real water. The SPC/E model represents a significant advancement over its predecessor, excelling in the reproduction of water's structural

properties such as the O–H–O bond angle and radial distribution functions. This improvement is attributed to the optimization of model parameters to closely align with experimental data. SPC/E introduces a fractional charge distribution and realistic charge interactions, enhancing its capability to facilitate hydrogen bond formation. This feature makes SPC/E particularly well-suited for studies focused on processes dependent on hydrogen bonding. While SPC/E introduces additional complexity compared to simpler three-point models like TIP3P, it maintains a reasonable level of computational efficiency due to its simplified charge distribution and the absence of polarizability. Despite these improvements, SPC/E, like any model, involves simplifications that may result in deviations from real water behavior. Notably, the model does not account for polarization effects, which can be crucial in certain systems.

Four point water models

Four point water models improve upon the limitations of three-point models by incorporating a Lennard-Jones site for the lone pair electrons on the oxygen atom. This inclusion allows for better representation of water's structure and dynamics, but it also increases the model's complexity.

TIP4P

Being a four point model TIP4P is represented by three point charges and one Lennard-Jones site. However, the key feature of this model is that the site carrying the negative charge is not located at the oxygen atom but on the H–O–H bisector at a distance of 0.15 Å, effectively accounting for the oxygen atom's lone pair electrons. The TIP4P model was proposed by Jorgensen et al.[34]. The TIP4P model incorporates a Lennard-Jones site for the lone pair electrons of the oxygen atom, enhancing its ability to accurately represent hydrogen bonding interactions compared to TIP3P. This modification aims to improve the model's transferability, enabling it to reproduce diverse water properties across various systems. TIP4P retains the transferability feature of TIP3P while introducing a slight increase in complexity due to the addition of the Lennard-Jones site. This added complexity may result in slightly longer computation times. While TIP4P enhances accuracy over TIP3P, its implementation requires a more intricate parameterization process to ensure that the new interaction site effectively represents the oxygen atom's lone pair electrons. The model strikes a balance between an improved representation of hydrogen bonding and the computational demands associated with its increased complexity.

Five point water models

The term "5-site water model" typically refers to a more detailed and sophisticated representa-

tion of water molecules in molecular dynamics simulations. The traditional water models like TIP3P, SPC/E, or TIP4P have three interaction sites representing the oxygen and hydrogen atoms. In contrast, a 5-site water model introduces additional sites to capture more accurately the electronic distribution and polarization effects in water molecules.

TIP5P

The five-point TIP5P rigid water model extends the three-point TIP3P model by adding two additional sites, usually massless, where the charge associated with the oxygen atom is placed. These sites are located at a fixed distance away from the oxygen atom, forming a tetrahedral angle that is rotated by 90 degrees from the H–O–H plane (see Figure 2.3). Those sites thus somewhat approximate lone pairs of the oxygen and consequently improve the water structure to become even more "tetrahedral" in comparison to the four-point TIP4P model. It aims to more accurately represent the angle and bond lengths in water molecules. TIP5P accounts for the polarization effects that are crucial in capturing the behavior of water, especially in scenarios involving hydrogen bonding and other intricate interactions. The model is designed to reproduce the dipole moment and other properties of water more closely. TIP5P is often used in simulations that require a higher level of accuracy in describing water-water interactions, such as studies involving phase transitions, solvation, or complex hydrogen-bonding environments.

It's important to note that the choice of a water model depends on the specific requirements of the simulation, including the level of detail needed, the accuracy desired, and the computational resources available. While more detailed models like TIP5P provide a more accurate representation of water, they may also come with an increased computational cost compared to simpler models. Researchers choose a water model based on the balance between accuracy and computational efficiency required for their specific study.

2.10 CHARMM Force Field Parametrization

CHARMM, AMBER, GROMOS, and OPLS force−fields are used in general for classical molecular dynamics simulation studies. Each force−field has its own methodology of developing the parameters and most of them use three site water models (especially to find the partial charges on each atom via quantum chemical calculations). In general, the development of the CHARMM36 force field parameters for organic molecules is based on the TIP3P water model, which imposes a limitation on using other water models in our research. We used the

CHARMM36 force field to understand the dynamics of water molecules through the membranes.

The CHARMM (Chemistry at HARvard Macromolecular Mechanics) force field is a widely utilized all-atom force field designed specifically for simulating biomolecules such as proteins. Its parameterization involves a meticulous process that begins with quantum mechanical (QM) calculations to determine key parameters ensuring accuracy in representing molecular properties. During this stage, various quantities such as molecular dipole moments, optimized geometries, rotational energy profiles, and interactions with water are matched using QM computations. The chosen level of theory is typically MP2/6-31G* for optimizations, with 6-31+G* incorporating diffuse functions for molecular ions. Significantly, explicit water interaction energies are computed using the HF/6-31G* model chemistry, with a low dielectric constant applied for the continuum model instead of the dielectric constant of water ($\epsilon = 78.4$). The subsequent step involves adjusting the obtained parameters to reproduce a range of physical properties, including crystal geometries, heats of vaporization, sublimation, enthalpy of vaporization, and density for neat liquids. Biomolecules undergo conformational sampling, and the force field is refined to align with experimental data related to conformational changes. Charge assignment is a critical aspect, with the Hartree-Fock electronic structure technique used, and a low dielectric constant is employed to implicitly account for polarization effects. Partial charges are assigned, and a scaling factor is applied to target QM-optimized distances between water and interacting groups to maintain a balance among solute-solute and solute-solvent interactions [18, 36]. For neutral compounds, a scaling factor of 1.16 is used. In consideration of molecular ions, no scaling is applied to their target data. Scaling of the distance is necessary to account for missing dispersion interactions using the Hartree-Fock model and to yield an appropriate density in the TIP3P water model [34, 37], which is the model for which the CHARMM force field is parametrized for use. This detailed parameterization process aims to achieve an accurate representation of molecular interactions and dynamics within the CHARMM force field. The combination of QM calculations and empirical adjustments ensures the force field's reliability for a broad range of biomolecular simulations, particularly in the study of biological macromolecules.

2.11 Softwares used and Implementation

Majority of MD simulations in this thesis were performed using NAMD[14] package. VMD[38] and PACKMOL[39] were used to generate the initial configurations of the atomistic models. VMD was used to visualize the simulation trajectories and render the snapshots. Gaussian 16 used to perform QM calculations for CHARMM force field parameterization. The postprocessing of snapshots was done using Inkscape graphics software. All the analysis were performed using in-house developed codes written in Tcl, python, Matlab, and bash. The plots of all the analysis were prepared using Gnuplot. The simulations were performed with high performance computing (HPC) facility, and the runs were submitted to HPC using SLURM scripts.

Finally we present a general scheme for an MD simulation in Figure2.4, first the coordinates of the structure to be simulated is obtained then that structure is minimized using a suitable minimization algorithm, solvent molecules are added if required and the initial velocities are assigned using Boltzmann distribution and then the equilibration and production run are conducted with the desired ensemble.

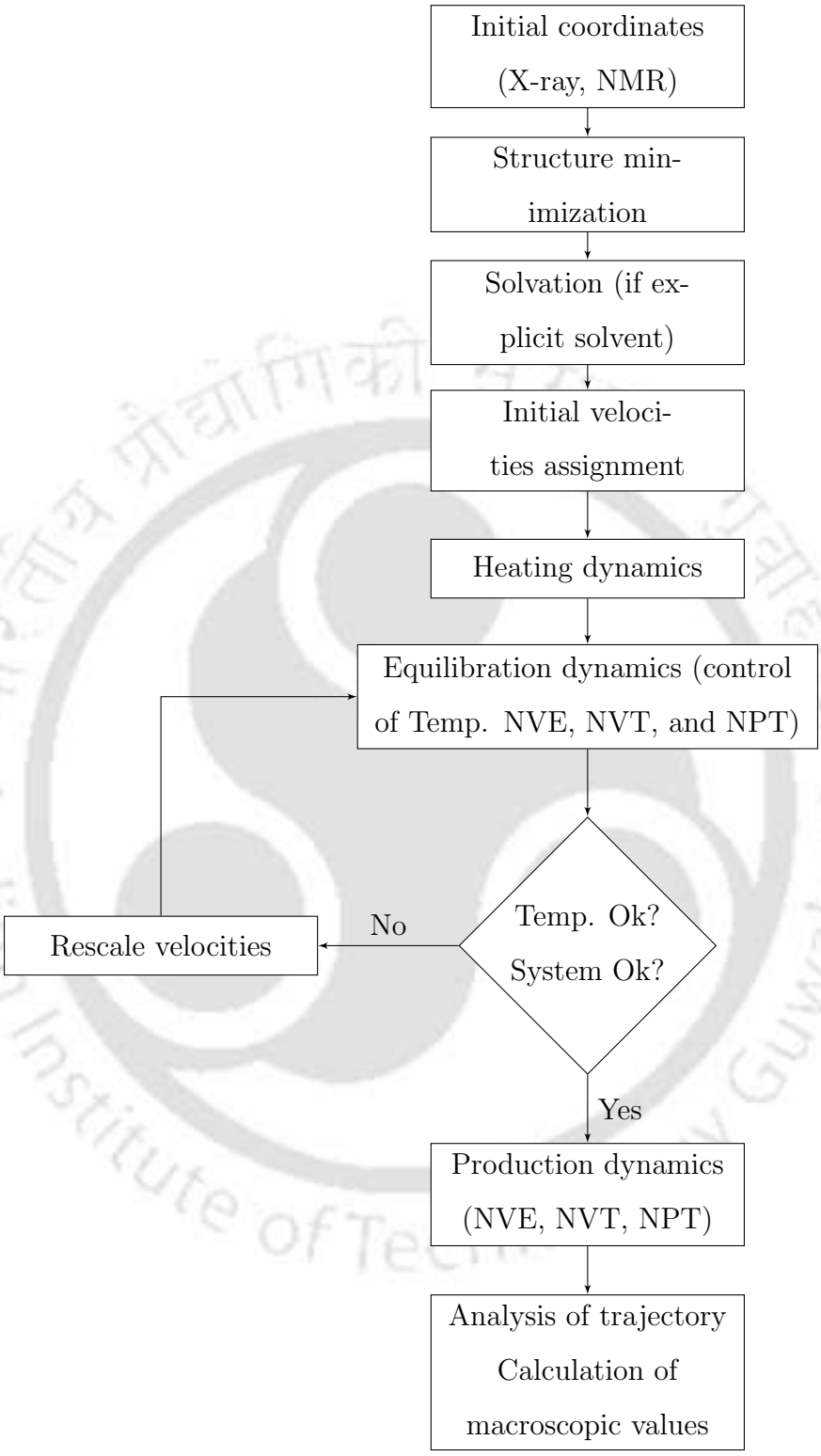

Figure 2.4: A general work flow of operations in general in an MD simulation.

Bibliography

[1] Berni Julian Alder and Thomas Everett Wainwright. Phase transition for a hard sphere system. *The Journal of chemical physics*, 27(5):1208–1209, 1957.

[2] Berni J Alder and Thomas Everett Wainwright. Studies in molecular dynamics. i. general method. *The Journal of Chemical Physics*, 31(2):459–466, 1959.

[3] Aneesur Rahman. Correlations in the motion of atoms in liquid argon. *Physical review*, 136(2A):A405, 1964.

[4] Loup Verlet. Computer" experiments" on classical fluids. i. thermodynamical properties of lennard-jones molecules. *Physical review*, 159(1):98, 1967.

[5] GD Harp and Bruce J Berne. Linear-and angular-momentum autocorrelation functions in diatomic liquids. *The Journal of chemical physics*, 49(3):1249–1254, 1968.

[6] BJ Berne, P Pechukas, and GD Harp. Molecular reorientation in liquids and gases. *The Journal of Chemical Physics*, 49(7):3125–3129, 1968.

[7] GD Harp and BJ Berne. Time-correlation functions, memory functions, and molecular dynamics. *Physical Review A*, 2(3):975, 1970.

[8] BRUCE J BERNE. Time-dependent properties of condensed media. *Physical chemistry, an advanced treatise*, 8:539–716, 1971.

[9] Aneesur Rahman and Frank H Stillinger. Molecular dynamics study of liquid water. *The Journal of Chemical Physics*, 55(7):3336–3359, 1971.

[10] Frank H Stillinger and Aneesur Rahman. Molecular dynamics study of temperature effects on water structure and kinetics. *The Journal of chemical physics*, 57(3):1281–1292, 1972.

[11] Frank H Stillinger and Aneesur Rahman. Improved simulation of liquid water by molecular dynamics. *The Journal of Chemical Physics*, 60(4):1545–1557, 1974.

[12] J Andrew McCammon, Bruce R Gelin, Martin Karplus, and PETER G WOLYNES. The hinge-bending mode in lysozyme. *Nature*, 262(5566):325–326, 1976.

[13] J Andrew McCammon, Bruce R Gelin, and Martin Karplus. Dynamics of folded proteins. *nature*, 267(5612):585–590, 1977.

[14] James C Phillips, Rosemary Braun, Wei Wang, James Gumbart, Emad Tajkhorshid, Elizabeth Villa, Christophe Chipot, Robert D Skeel, Laxmikant Kale, and Klaus Schulten. Scalable molecular dynamics with namd. *Journal of computational chemistry*, 26(16): 1781–1802, 2005.

[15] David A Pearlman, David A Case, James W Caldwell, Wilson S Ross, Thomas E Cheatham III, Steve DeBolt, David Ferguson, George Seibel, and Peter Kollman. Amber, a package of computer programs for applying molecular mechanics, normal mode analysis, molecular dynamics and free energy calculations to simulate the structural and energetic properties of molecules. *Computer Physics Communications*, 91(1-3):1–41, 1995.

[16] Wilfred F van Gunsteren, SR Billeter, AA Eising, PH Hünenberger, PKHC Krüger, AE Mark, WRP Scott, and IG Tironi. Biomolecular simulation: the gromos96 manual and user guide. *Vdf Hochschulverlag AG an der ETH Zürich, Zürich*, 86:1–1044, 1996.

[17] Bernard R Brooks, Robert E Bruccoleri, Barry D Olafson, David J States, S a Swaminathan, and Martin Karplus. Charmm: a program for macromolecular energy, minimization, and dynamics calculations. *Journal of computational chemistry*, 4(2):187–217, 1983.

[18] Alex D MacKerell Jr, Donald Bashford, MLDR Bellott, Roland Leslie Dunbrack Jr, Jeffrey D Evanseck, Martin J Field, Stefan Fischer, Jiali Gao, H Guo, Sookhee Ha, et al. All-atom empirical potential for molecular modeling and dynamics studies of proteins. *The journal of physical chemistry B*, 102(18):3586–3616, 1998.

[19] Marcus D Hanwell, Donald E Curtis, David C Lonie, Tim Vandermeersch, Eva Zurek, and Geoffrey R Hutchison. Avogadro: an advanced semantic chemical editor, visualization, and analysis platform. *Journal of cheminformatics*, 4(1):1–17, 2012.

[20] William C Swope, Hans C Andersen, Peter H Berens, and Kent R Wilson. A computer simulation method for the calculation of equilibrium constants for the formation of physical clusters of molecules: Application to small water clusters. *The Journal of chemical physics*, 76(1):637–649, 1982.

[21] Paul P Ewald. Die berechnung optischer und elektrostatischer gitterpotentiale. *Annalen der physik*, 369(3):253–287, 1921.

[22] Ulrich Essmann, Lalith Perera, Max L Berkowitz, Tom Darden, Hsing Lee, and Lee G Pedersen. A smooth particle mesh ewald method. *The Journal of chemical physics*, 103 (19):8577–8593, 1995.

[23] Josiah Willard Gibbs. *Elementary principles in statistical mechanics: developed with especial reference to the rational foundations of thermodynamics*. C. Scribner's sons, 1902.

[24] Mark Tuckerman. *Statistical mechanics: theory and molecular simulation*. Oxford university press, 2010.

[25] Biman Bagchi. *Statistical mechanics for chemistry and materials science*. CRC Press, 2018.

[26] Hans C Andersen. Molecular dynamics simulations at constant pressure and/or temperature. *The Journal of chemical physics*, 72(4):2384–2393, 1980.

[27] Shūichi Nosé. A molecular dynamics method for simulations in the canonical ensemble. *Molecular physics*, 52(2):255–268, 1984.

[28] William G Hoover. Canonical dynamics: Equilibrium phase-space distributions. *Physical review A*, 31(3):1695, 1985.

[29] Herman JC Berendsen, JPM van Postma, Wilfred F Van Gunsteren, ARHJ DiNola, and Jan R Haak. Molecular dynamics with coupling to an external bath. *The Journal of chemical physics*, 81(8):3684–3690, 1984.

[30] Jean-Paul Ryckaert, Giovanni Ciccotti, and Herman JC Berendsen. Numerical integration of the cartesian equations of motion of a system with constraints: molecular dynamics of n-alkanes. *Journal of computational physics*, 23(3):327–341, 1977.

[31] Hans C Andersen. Rattle: A "velocity" version of the shake algorithm for molecular dynamics calculations. *Journal of computational Physics*, 52(1):24–34, 1983.

[32] Sachini P Kadaoluwa Pathirannahalage, Nastaran Meftahi, Aaron Elbourne, Alessia CG Weiss, Chris F McConville, Agilio Padua, David A Winkler, Margarida Costa Gomes, Tamar L Greaves, Tu C Le, et al. Systematic comparison of the structural and dynamic properties of commonly used water models for molecular dynamics simulations. *J. Chem. Inf. Model.*, 61(9):4521–4536, 2021.

[33] Saeed Izadi, Ramu Anandakrishnan, and Alexey V Onufriev. Building water models: a different approach. *J. Phys. Chem. Lett.*, 5(21):3863–3871, 2014.

[34] William L Jorgensen, Jayaraman Chandrasekhar, Jeffry D Madura, Roger W Impey, and Michael L Klein. Comparison of simple potential functions for simulating liquid water. *The Journal of chemical physics*, 79(2):926–935, 1983.

[35] Herman JC Berendsen, J Raul Grigera, and Tjerk P Straatsma. The missing term in effective pair potentials. *Journal of Physical Chemistry*, 91(24):6269–6271, 1987.

[36] Alexander D MacKerell Jr and Martin Karplus. Importance of attractive van der waals contribution in empirical energy function models for the heat of vaporization of polar liquids. *The Journal of Physical Chemistry*, 95(26):10559–10560, 1991.

[37] William L Jorgensen. Optimized intermolecular potential functions for liquid alcohols. *The Journal of Physical Chemistry*, 90(7):1276–1284, 1986.

[38] William Humphrey, Andrew Dalke, and Klaus Schulten. Vmd: visual molecular dynamics. *Journal of molecular graphics*, 14(1):33–38, 1996.

[39] Leandro Martínez, Ricardo Andrade, Ernesto G Birgin, and José Mario Martínez. Packmol: A package for building initial configurations for molecular dynamics simulations. *Journal of computational chemistry*, 30(13):2157–2164, 2009.

Chapter 3

Semi−Aromatic Polyamide−Based Membrane in Forward Osmosis: Molecular Insights[1]

3.1 Introduction

Desalination is a potential process for transforming seawater or groundwater into drinkable water and addressing water scarcity issues. Because of increased demand from population growth, desalination has become a conventional water treatment technique [1]. Reverse osmosis (RO) is a commonly utilized desalination technique that accounts for more than half of the global desalination capacity to produce drinking water from seawater and brackish water [2]. Forward osmosis (FO) is an osmotic pressure−driven technique that transports fresh water through the semipermeable membrane from the feed solution (low osmotic pressure) to the concentrated draw solution (high osmotic pressure), where the chemical potential difference is used in the form of osmotic pressure [3]. FO can be economical in treating challenging feed solutions (ex., high osmotic pressures), and the diluted draw solution has a direct application in another process, is less prone to fouling [4], and thus is being used in various fields such as power generation [5, 6], wastewater treatment [2], and food processing [7].

Thin−film composite (TFC) fully−aromatic polyamide (PA) membranes (produced from

[1]G. Nagendraprasad, V. Adupa, K. Anki Reddy, C. Das, S. Karan, Semiaromatic polyamide based membrane in forward osmosis: Molecular insights, J. Phys. Chem. B 127 (30) (2023) 6751–6766.

m−phenylenediamine and trimesoyl chloride via interfacial polymerization), where the PA selective layer is fabricated on top of a polysulfone or polyethersulfone ultrafiltration membrane supported on fabric, are known for their high water−salt selectivity [8]. Owing to their high selectivity for monovalent ions, they have been predominantly employed in brackish water and seawater desalination [9, 10]. They are also used in FO processes [11]; however, the low water permeance restricts their potential applications in many separation processes [8]. The chemical property of the PA selective layer is crucial to membrane performance, durability, salt rejection, and water flux [12] and is influenced by functional groups in the PA layer. In general, the water affinity of the PA layer can be increased by the presence of polar hydroxyl and carbonyl functional groups; however, the presence of hydrophobic benzene rings tends to slow down water permeability [13]. Over the last decade, surface modification of the PA layer with hydrophilic materials, for example, PEG derivatives [14], zwitterionic polymers [15, 16], and amine−derivatives [17, 18] and incorporating novel functional monomers [19, 20], nanoparticles [21, 22], etc. have resulted in excellent salt rejection and improved water permeability [23], chlorine resistance, and fouling propensity [24–28]. However, higher water flux is needed for enhanced process efficiency without sacrificing solute/ion selectivity [29]. This is where the water permeance and the water−salt selectivity make the trade−off behavior in most polymer membranes [30]. While the PA membranes used in FO are suitable for desalination where monovalent ions are present, their use in other applications where the processes do not involve the separation of monovalent ions is underestimated. With increased water permeance and compromised rejection of monovalent ions, semi−aromatic polyamide (SAPA) membranes produced from piperazine and trimesoyl chloride via interfacial polymerization can be a better alternative for FO processes with multivalent salts as a draw solution. SAPA membranes are widely known for their use in nanofiltration (NF) applications with almost complete rejection of divalent anions [31]. SAPA membranes exhibited superior hydrophilicity, pure water permeability, and low surface roughness [32, 33]. In addition, compared to the PA, SAPA membranes are more resistant to chlorine−based membrane cleaning agents [34]. We were keen to understand the effectiveness of SAPA membranes in FO with Na_2SO_4 as a draw solution, where the processes do not involve the separation of monovalent ions and the SAPA membrane is completely impermeable to Na_2SO_4 avoiding the reverse salt flux. This needs highly selective SAPA membranes with Na_2SO_4 rejection >99.9%, and recent development of such membranes has opened the avenue to explore them to check their practicability in FO processes [31]. Indeed,

SAPA FO membranes won't be applicable for the separation of NaCl involved in processing drinking water; many industrial separation processes would be benefited where the separation of multivalent ions from the complex feed is needed.

Additionally, regeneration of the draw solution can be done at relatively low pressure with SAPA NF membranes with almost complete rejection of Na_2SO_4 and high selectivity between monovalent and divalent ions [31] to run the FO continuously. Many other recent developments of SAPA membranes have attracted colossal attention to producing high-specification NF membranes with high water permeance and Na_2SO_4 rejection, including interlayers between the active layer and the porous substrate [35–37], modifying the kinetics of polymerization with polymer [38] and surfactant [31], and incorporating porous structures in the selective layer [39, 40]. Thus, there would be an enormous opportunity to design new SAPA membranes for FO processes. Notably, in textile wastewater processing, where large quantities of monovalent and divalent salts are present with small organic dyes, NF membranes are widely used [41]. However, SAPA FO membranes could be a viable solution to avoid fouling in the presence of color molecules. We hypothesized that a highly crosslinked ultrathin SAPA membrane with an extremely high selectivity towards Na_2SO_4 could be used as an FO membrane in combination with the Na_2SO_4 draw solution.

The present study is organized as follows. Simulation method section presents the development of an atomistic model for a cross−linked semi−aromatic polyamide membrane via a heuristic approach, non−equilibrium classical molecular dynamics simulation procedure for a forward osmosis process (which includes the preparation of draw solution and feed solution). Results section presents the data on water dynamics (via orientation and pathways inside the membrane), pore size distribution of the membrane, water permeance and permeability, reverse draw solute flux, transport of monovalent or divalent ions and the applicability of SAPA membrane in treating the textile feeds.

3.2 Methodology

3.2.1 Membrane Model

All−atom, explicit water molecular dynamics simulations were carried out to characterize the membrane and its performance in the FO process. We used

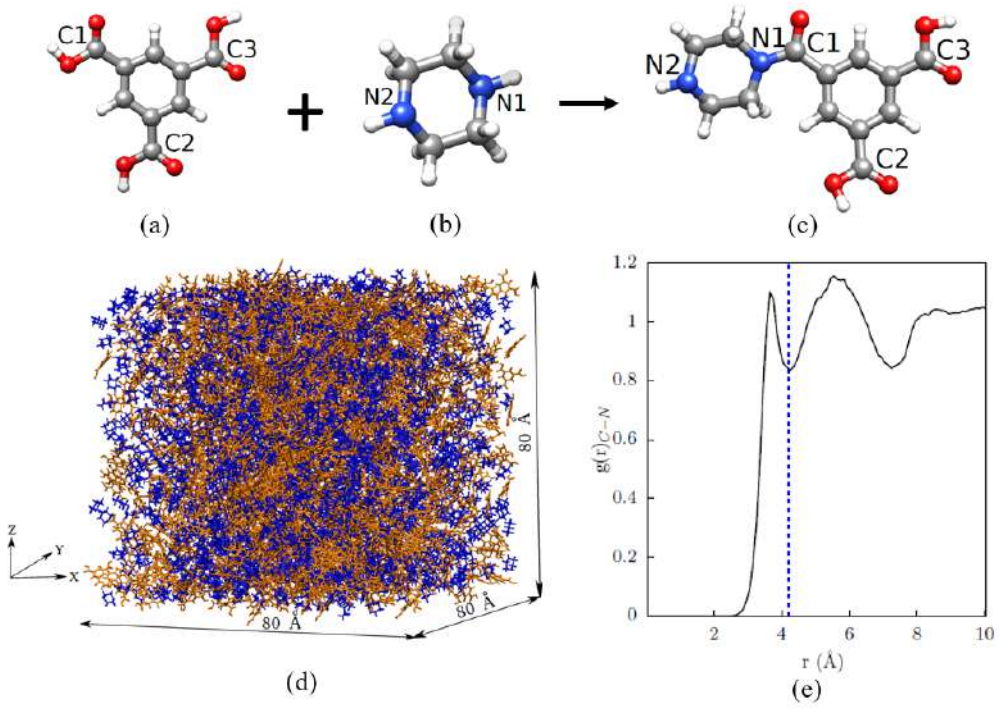

Figure 3.1: (a) Hydrolysed TMC (TMO) (b) Piperazine (PIP) (c) Amide linkage between TMO and PIP (d) Initial configuration prior to polymerization (color code: blue for PIP, orange for TMO) (e) RDF between the carbon atom of a carboxylic acid group (−COOH) of TMO and the amide group (−NH) nitrogen atom of piperazine after annealing in an NVT ensemble.

CHARMM36m [42] force field parameters to compute interactions between atoms using NAMD [43]. In the current study, the membrane to be simulated is prepared via a heuristic approach, where crosslinking of the monomers happens based on distance criteria. Initially, 1200 hydrolyzed trimesoyl chloride (TMO) and 1200 piperazine (PIP) monomers (3D chemical structures are shown in Figure 3.1(a, b) were placed randomly in a computational box of 80 $\mathring{A}$ × 80 $\mathring{A}$ × 80 $\mathring{A}$ using Packmol[44] (see Figure 3.1d), which is then equilibrated in NPT ensemble at 300K and 1 atm pressure for 10 ns. After that, the system is subjected to annealing in an NVT ensemble, where the temperature is gradually increased from 300 K to 1100 K before being cooled back to 300 K with intervals of 50 K. The maximum distance considered for the crosslinking between two reacting monomers is chosen by the first minima of the radial distribution function (RDF) between the carbon atom of a carboxylic acid group (−COOH) of TMO and the amide group (−NH) nitrogen atom of piperazine, which is found to be 4.2 $\mathring{A}$ (see Figure 3.1e). An amide bond will form between the monomer's reaction sites (N and C,

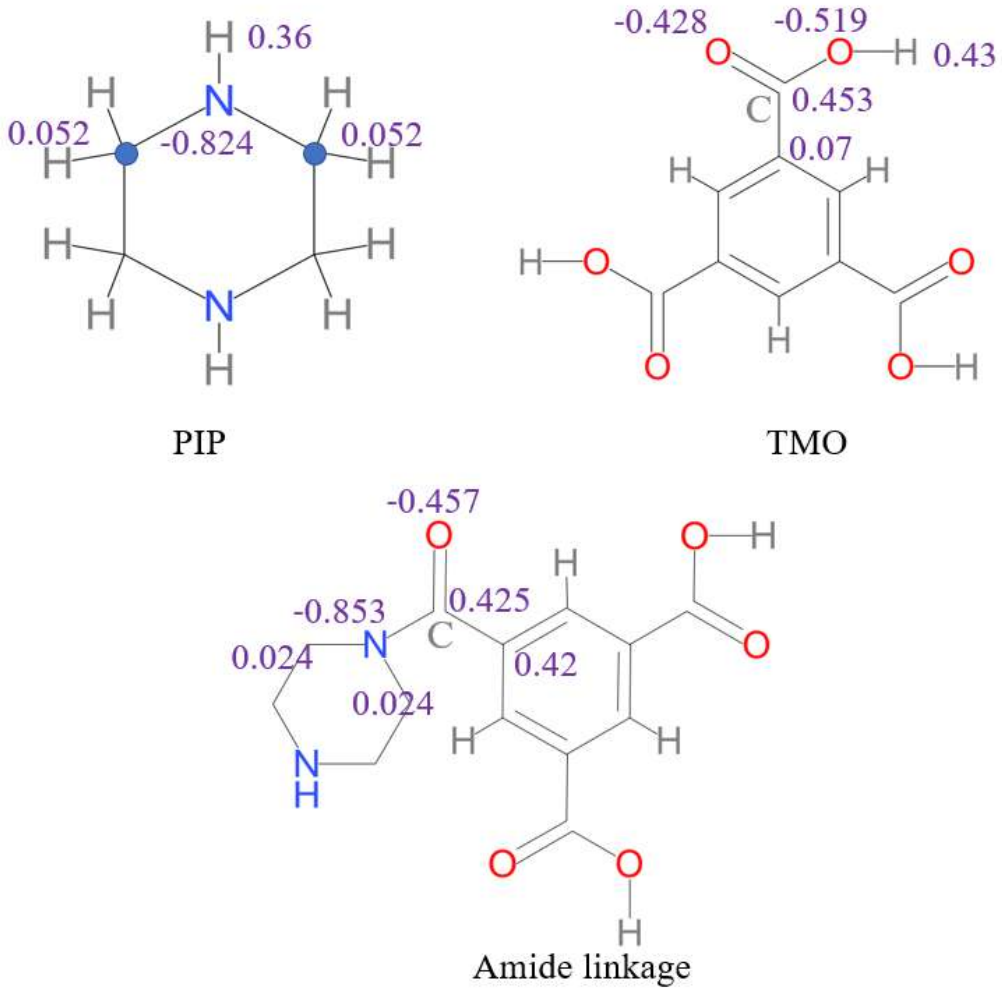

Figure 3.2: CHARMM36m general force field was used for PIP, TMO and amide linkage. Cgenff server is used to obtain the CHARMM compatable force field parameters for monomers and amide linkage. The partial charges of individual monomer atoms that will change after cross−linking (see top panel) and amide−linkage with neighboring atoms (see bottom panel) are shown here.

shown in Figure 3.1c) if the distance between them is less than the distance criteria. During the formation of the amide bond, the hydrogen atom of −NH and a hydroxyl group (OH) of −COOH (which were involved in amide−linkage) are removed, and the simulation is continued in the search of new amide bonds that can be formed for every 10 ps of simulation time. The partial charges will be revised for amide−linkage and its neighboring atoms. The schematic structures of monomers and the amide linkage are shown in Figure 3.2 (partial charges were displayed near to the atoms). Please note that Figure 3.2 shows the partial charges only for

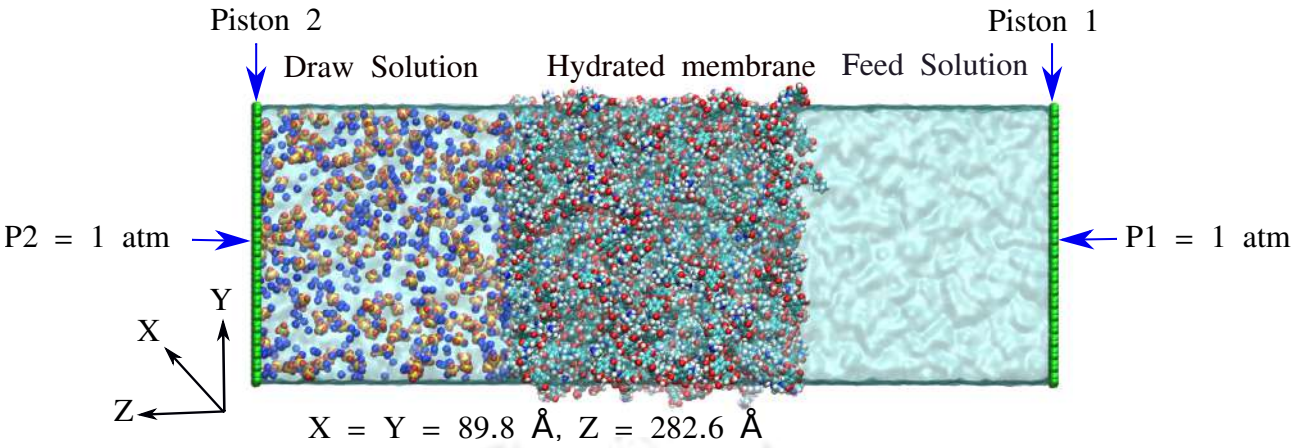

Figure 3.3: The simulation setup consists of Na_2SO_4 draw solution, hydrated SAPA membrane, and pure water as feed solution. There is 30 $\mathring{A}$ of empty space present at both ends of graphene pistons.

a few atoms. Every atom has its unique partial charge in the present simulation. In addition to the partial charges, the bonds, angles, dihedrals, and impropers will be updated after the amide linkage is formed. After each crosslinking step, energy minimization and equilibration are performed. As the simulation progresses, the crosslinked clusters grow, limiting monomer diffusion and slowing the cross−linking process. Initially, bond formation is only permitted if the distance between C1/C2/C3 of TMO and N1/N2 of piperazine (see Figure 3.1(a, b)) is less than 3 $\mathring{A}$. As the simulation progressed, the crosslinking distance was eased to 4.2 $\mathring{A}$ with a step of 0.2 $\mathring{A}$ to accelerate the crosslinking process.

Finally, the membrane's unreacted monomers were removed, and the resultant structure of the membrane was minimized for 10000 steps and equilibrated for 10 ns in the NPT ensemble (300 K, 1 atm). In the end, the equilibrated membrane has a thickness of 78.27 $\mathring{A}$ in X, Y, and Z directions with a density of 0.96 g cm^{-3}, which is less than the reported value in literature for simulated fully aromatic PA membrane [45]. It should be noted that the number of unreacted TMO and PIP units in the membrane out of 1200 are 162 and 61, respectively. Our simulated membrane has higher PIP units with 539 unreacted functional groups (−NH) out of 2278 and TMO units with 1375 unreacted −COOH groups out of 3114 total functional groups. It is reported that, when the PIP concentration is low, compared to TMO, the nanofilm has a smooth appearance, while when it's high, it has a crumpled, striped Turing structure [46]. The degree of crosslinking (DC) is calculated by modifying the equation given in the literature

[31, 47] and shown in egn. 3.1.

$$DC = \frac{100N_N}{N_N + N_{COOH} + N_{NH}} \tag{3.1}$$

where N_N is number of nitrogen atoms in amide−linkage, N_{COOH} is number of unreacted −COOH groups and N_{NH} is number of unreacted −NH groups in the membrane. From an experimental point of view, based on the elemental composition analysis, if the ratio of oxygen to nitrogen (O/N) equals one, it can be inferred that the membrane is fully cross−linked [48], provided every −COOH group in TMO is bonded to the −NH group of PIP. However, determining the unreacted amine content through experiments can be challenging. That means the degree of cross−linking can be overestimated/underestimated when using the O/N ratio to know the DC. The elemental composition (O/N ratio of amide−linkage) and degree of crosslinking (DC) was measured for the simulated membrane and found to be 1 and 47.6%, respectively. The equilibrated dry membrane serves as the initial configuration for the subsequent steps involved in the FO process.

3.2.2 FO Simulation System

The prepared semi−aromatic membrane is submerged in an equilibrated water box (with cell dimensions of 89.8 $\mathring{A}$ × 89.8 $\mathring{A}$ × 90 $\mathring{A}$ in X, Y, and Z directions) using Visual Molecular Dynamics (VMD) [49]. The system is equilibrated for 10 ns in an NPT ensemble (300 K and 1atm). The equilibrated hydrated membrane's size after equilibration has reached 89.8 $\mathring{A}$ × 89.8 $\mathring{A}$ × 100.5 $\mathring{A}$ in X, Y, and Z directions, respectively. The calculated density of the equilibrated hydrated membrane is 1.12 g cm^{-3}, which is consistent with the reported value for a semi−aromatic membrane in literature [46] and less than the hydrated fully aromatic membrane[45, 50]. The equilibrated hydrated membrane is used in the FO process. The simulated FO system consists of three chambers, a feed solution chamber above and a draw solution chamber below the hydrated membrane chamber. Pure water is used as a feed solution, and a water box is created using VMD [49] with cell dimensions of 89.8 $\mathring{A}$ × 89.8 $\mathring{A}$ × 90 $\mathring{A}$ in X, Y, and Z directions. The TIP3P water model [51] is adopted to model water molecules in our simulations. However, there are other water models, such as the 4-site and 5-site models, available in the literature (refer Table 3.1 for force field parameters). The Na_2SO_4 solution with 1.5 M concentration was prepared by introducing 506 Na^+ ions and 253 $SO_4{}^{-2}$ ions into a water box of 89.8 $\mathring{A}$ × 89.8 $\mathring{A}$ × 90 $\mathring{A}$, used as a draw solution (refer Table 3.2 for force field

parameters). The feed and draw solutions are minimized for 10000 steps and equilibrated for 10 ns in the NPT ensemble (300 K, 1 atm) separately.

Table 3.1: Water model parameters

Water Model	$\mathbf{r}_{OH}$ **(Å)**	**∠HOH (°)**	σ_{OO} **(Å)**	ϵ_{OO} **(kcal mol^{-1})**	$\mathbf{q}_O$ **(e)**	$\mathbf{q}_h$ **(e)**	$\mathbf{q}_m$ **(e)**	$\mathbf{r}_{OM}$ **(Å)**
TIP3P [52]	0.9572	104.52	3.1506	0.152	-0.834	0.417	-	-
TIP4P [51]	0.9572	104.52	3.1540	0.155	-	0.52	-1.04	0.15
TIP5P [53]	0.9572	104.52	3.12	0.16	-	0.241	-0.241	0.70

r_{OH} indicates the bond length of OH, ∠HOH represents the H-O-H angle, σ_{OO} represents the LJ σ of OO (i.e., σ is the distance at which the LJ potential between two atoms is zero), ϵ_{OO} represents the LJ ϵ of OO (i.e., ϵ is the well depth at the distance of minimum energy), q_O represents the charge on oxygen atom, q_h represents the charge on hydrogen atom, q_m represents the massless point M assosiated with the oxygen atom charge, r_{OM} represents the bond length of OM.

Table 3.2: Ion force field parameters

Atoms	σ **(Å)**	ϵ **(kcal mol^{-1})**	$\mathbf{q}_O$ **(e)**	θ **(°)**
Na^+ [42, 54]	2.8215	0.0469	1	-
S [42, 54]	4.2	0.47	0.268	-
O [42, 54]	3.4	0.12	-0.567	-
∠OSO [42, 54]	-	-	-	109.47

Equilibrated feed solution, hydrated membrane, and draw solutions are merged to create the FO system using TopoTools [49] package. Graphene sheets are generated with VMD [49] and used as pistons in FO simulation setup as shown in Figure 3.3. The simulation system is minimized for 10000 steps and then equilibrated for 1 ns at 300 K temperature and 1 atm pressure. The pressure of 1 atm is applied on both ends of graphene sheets for an equilibrated FO system and simulated for 30 ns in the NVT ensemble at a temperature of 300 K. It should be noted that all equilibrium simulations were performed in the NPT ensemble, and production simulations were performed in NVT ensemble. Lennard−Jones potential is used to compute the

van der Waals interactions between the atoms with a cutoff distance of 12 $\mathring{A}$ and a switching distance of 10 $\mathring{A}$. Electrostatic interactions are computed by Particle Mesh Ewald (PME) method [55] with a grid spacing of 1 $\mathring{A}$. Pressure and temperature of the system are controlled by modified Nose−Hoover [56] coupled with Langevin dynamics [57]. The Langevin damping coefficient of 1 ps^{-1} is used, and the equations of motion are integrated with the velocity Verlet algorithm [43]. The total time for the FO simulation was 30 ns, with a time step of 1 fs, and the trajectories were saved for every 20 ps. During the production simulations, 3% of the membrane atoms were fixed in a simulation system, compared to techniques used in previous studies, where many atoms of the membrane [58] or the entire membrane is fixed [59], limiting the membrane's ability to respond to flow conditions. Because of the compression of the membrane that occurs when it is subjected to operating pressures, fixing a relatively low number of membrane atoms may have a slight effect on the macroscale water flux [60]. Despite this, it does not affect the transport processes that operate on the Angstrom−scale within the structure of the molecular membrane. Furthermore, the process of fixing certain atoms in a polymer can be thought of as being analogous to the TFC NF membrane. In the TFC NF membrane, a porous polysulfone (PSF) typically supports the NF film. Periodic boundary conditions (PBC) are applied along the X, Y, and Z dimensions for the simulations of FO processes. The vacuum of 30 $\mathring{A}$ is applied along the Z dimension at both ends of the graphene pistons. Three independent simulations were performed, and the results presented in this manuscript are averaged over these three runs. It is important to note that the PSF support layer was not explicitly considered in our simulation study.

3.3 Results and Discussion

3.3.1 Semi−aromatic Membrane Structure

Structural properties of semi−aromatic polyamide membrane are investigated via the density profiles of atoms along the membrane's normal direction, pore size distribution (PSD), and the benzene ring's order parameter. The density profile of atoms (water, ions, and membrane atoms) is shown in Figure 3.4a. It is observed that the interface of the feed solution/membrane (-15 $\mathring{A}$ < Z < 0 $\mathring{A}$) and draw solution/membrane (80 $\mathring{A}$ < Z < 95 $\mathring{A}$) has a thickness of 15 $\mathring{A}$. The densities of membrane and water molecules inside the bulk membrane (0 $\mathring{A}$ < Z <

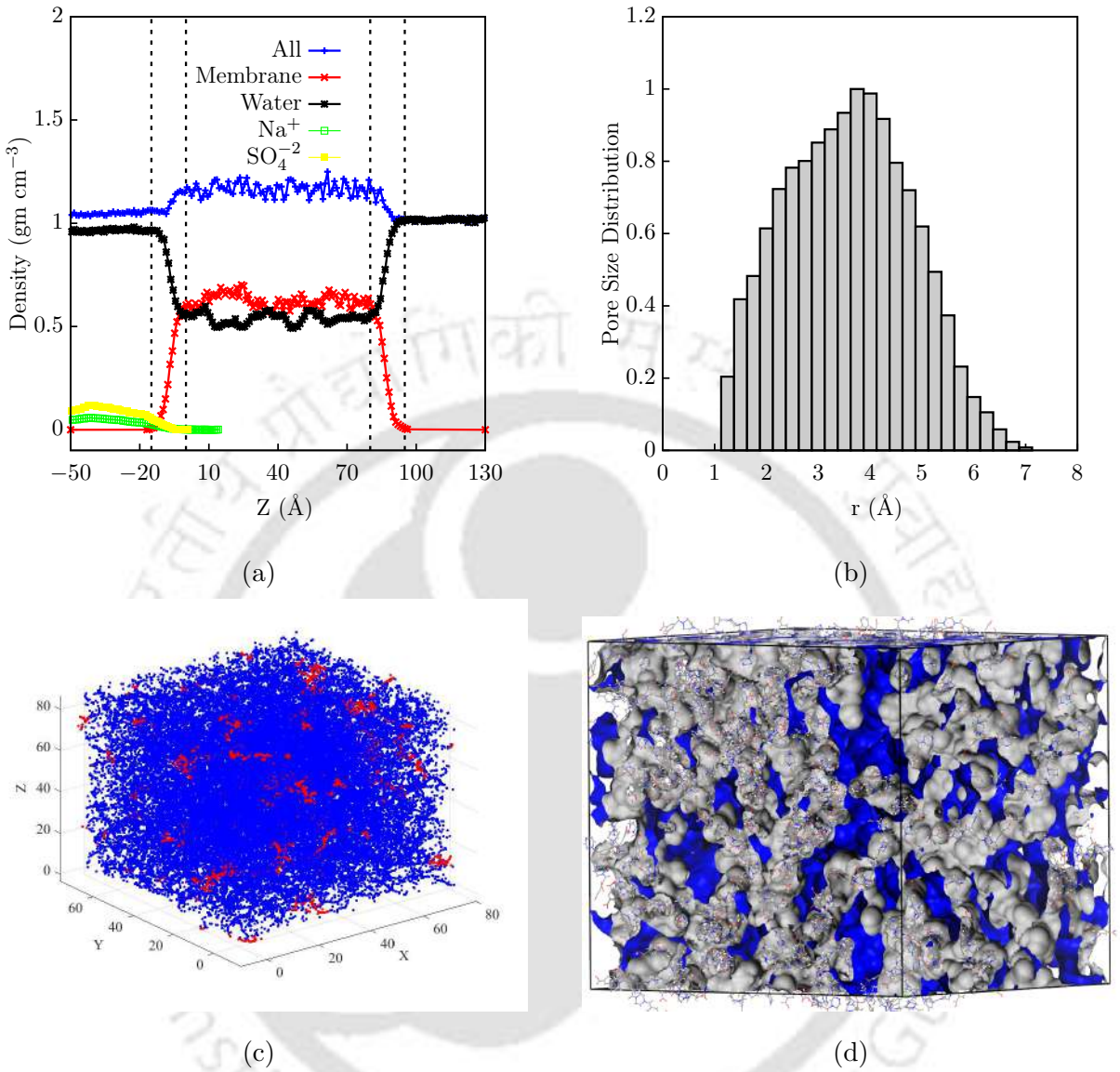

Figure 3.4: (a) Density profiles of water, membrane atoms, Na_2SO_4, and the whole system (dashed line represents the interfacial regions between draw solution/membrane, feed solution/membrane). (b) PSD of the membrane after FO process (c) Free volume of the membrane after the FO process (color code: blue indicates free volume < 4 $\AA$ and red indicates free volume > 4 $\AA$) (d) Membrane's free volume morphology after the FO process, where the blue color indicates free volume accessible to water, and the grey color represents the occupied volume of the membrane.

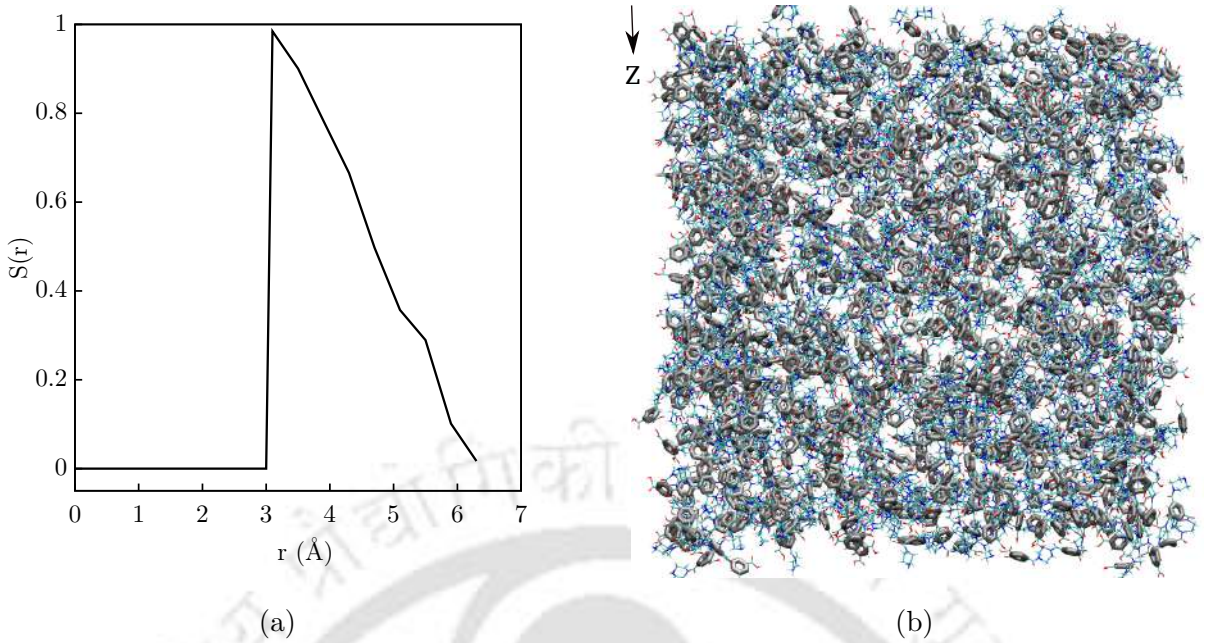

(a) (b)

Figure 3.5: (a) Benzene rings order parameter S(r) (b) Arrangement of benzene rings in the membrane

80 Å) are 0.635 ± 0.001 g cm^{-3} and 0.547 ± 0.008 g cm^{-3}, respectively. The reported fully aromatic membrane's interior density for water and membrane atoms are 0.251 ± 0.029 g cm^{-3} and 1.076 ± 0.049 g cm^{-3} [45]. The water density in the SAPA membrane's interior is higher, and the density of membrane atoms is lower than the reported value in the literature for PA membrane [45]. The water uptake of the bulk membrane is found to be 49.3% by weight, which is higher than the experimental and simulated value reported for fully aromatic PA [45, 61, 62]. It is reported that piperazine−based membranes have maximum water uptake of ≈350% [31]. Strong hydrogen bonds between water and amide groups increase the water uptake of the SAPA membrane [31]. The density profiles of Na_2SO_4 salt ions suggest that very few Na^+ ions can reach the interface region and try to enter the membrane's interior. In contrast, the membrane is impermeable to $SO_4{}^{-2}$ ions.

To investigate the effect of the SAPA membrane's structure on water transport, we calculated the membrane pore structure, which can be analyzed at the molecular level in terms of water−accessible space or free volume. Free volume size inside a membrane can play a role in the selectivity and hence decide the suitability of a particular separation application. The nature of the monomers and the extent of cross−linking of the monomers will determine the

pore structure inside a membrane. The Monte Carlo method [63] was used to analyze free volume sizes in the membrane (In this method, we used a spherical probe of 1 $\mathring{A}$ in radius). The PSD of the membrane after the FO process is shown in Figure 3.4b. Before calculating the PSD of the FO membrane, water and salt ions present in the membrane are removed. The PSD is computed in the membrane's interior (0 $\mathring{A}$ < Z < 80 $\mathring{A}$). The results show that pores within the membrane have radii ranging from 1.25 $\mathring{A}$ to 7 $\mathring{A}$ and the majority of the pores have radii between 3 $\mathring{A}$ to 6 $\mathring{A}$ (see Figure 3.4b). Figure 3.4c displays the water molecule accessible regions of the membrane's free volume. Here for the membrane, the blue color represents the free volume sizes smaller than 4 $\mathring{A}$, and the red color indicates the free volume sizes greater than 4 $\mathring{A}$ in radius. Figure 3.4c was created in MATLAB [64] using the Monte Carlo PSD data. In this study, we have also computed the free volume morphology of the membrane using the Materials Studio [65], and a water molecule is used as a probe. Figure 3.4d shows the free volume morphology in the membrane, where the blue color indicates free volume accessible to water, and the grey color represents the occupied volume of the membrane [66]. It is also observed that pores can have radii ranging from 0.5 to 5.2 $\mathring{A}$ in fully aromatic PA [45]. The higher PIP units (i.e., PIP concentration) in the SAPA membrane cause the formation of large aggregate pores [31]. However, the large scattered cavities which are not interconnected may not facilitate water transport but can take up water resulting in localized water clusters [67]. Therefore water permeation is restricted to smaller pores, possibly favoring a single−file water flow [68]. The diameter of ions attempting to permeate the membrane pore determines the selectivity of pores inside the membrane. The effective radius of ions can be determined using the water molecule's hydration shell radius and the associated energy. The hydrogen bonding energy of water molecules is -23.3 kJ/mol [69], where the water clusters are flexible. In this instance, water may flow through the 2 $\mathring{A}$ radius pore; however, monovalent and divalent ions cannot (only through a 2 $\mathring{A}$ radius pore) because their hydration radius is greater than the pore radius [70].

Additionally, the membrane's local structure is characterized using benzene ring's order parameter S(r) [45], which provide insights into the interactions between benzene rings of TMO (hydrolyzed TMC) units (refer eqn. 3.2):

$$S(r) = \langle \frac{3Cos^2(\theta(r)) - 1}{2} \rangle \tag{3.2}$$

$\theta(r)$ in Eq.2 represents the angle between normal vectors of benzene rings at a radial distance

of r. Figure 3.5a shows the order parameter of the semi−aromatic membrane. In the S(r) profile, S = 0 corresponds to the random structure, and S = 1 signifies the arrangement of benzene rings in the membrane (see figure 3.5b). A sharp peak appeared at r = 3.1 $\mathring{A}$ on the S(r) profile, which confirms π - π stacking in the membrane. The interactions become less prominent and decay to zero at r = 6.4 $\mathring{A}$. In contrast to fully aromatic PA, no "T-shaped" [45] stacking observed in the SAPA membrane. To the best of our knowledge, there is currently no experimental data available for the SAPA membrane benzene ring's order parameter.

3.3.2 Water Structure and Dynamics

The likelihood of locating an atom in a spherical shell around a given atom can be computed with the pair distribution function or radial distribution function (RDF). For example, the RDF of oxygen atoms of water molecules and atom i can be expressed as (refer eqn. 3.3)[71]:

$$g_{iO}(r) = \frac{\rho_O(r)}{\rho_O} \tag{3.3}$$

where $\rho_O(r)$ is the local density of oxygen atoms at a distance r, to the density of water oxygen atoms in simulation system, ρ_O. Water structure is characterized by computing the RDF of water atoms in the membrane's interior (0 $\mathring{A}$ < Z < 80 $\mathring{A}$). The hydration peak is observed at 2.75 $\mathring{A}$ (see Figure 3.6a). The coordination number (N_c) is calculated by integrating RDF at the cutoff distance of 3.25 $\mathring{A}$. The coordination number of water in the membrane's interior is 3.5 (see Figure 3.6b), while it is 2.4 for a fully aromatic system [45]. However, the coordination number for pure water in the feed solution is 4.4. A decrease in N_c in the membrane's interior suggests a decrease in hydrogen bonds per water molecule (see Figure 3.6c). We consider that a hydrogen bond will be formed between the donor (D) and acceptor (A) atoms with D−A cutoff distance of 3 $\mathring{A}$, and a D−H−A cutoff angle of 20° [72–74]. The average number of hydrogen bonds between water molecules along the "Z" direction was computed and shown in Figure 3.6c. It has been observed that there is a decrease in hydrogen bonds in the membrane's interior (see Figure 3.6c). To quantify the decrease in the number of hydrogen bonds per water molecule, we plotted RDF (see figure 3.6d) between hydrogen and oxygen atoms of water molecules in the feed solution and the membrane's interior. The RDFs reveal the first minimum at r = 2.45 $\mathring{A}$, indicating the possible formation of hydrogen bonds (HB) with neighboring water molecules [75]. However, the peak intensity in the membrane's interior is higher than the feed solution due to the excluded volume effect [75, 76]. Based on the coordination number, we found that

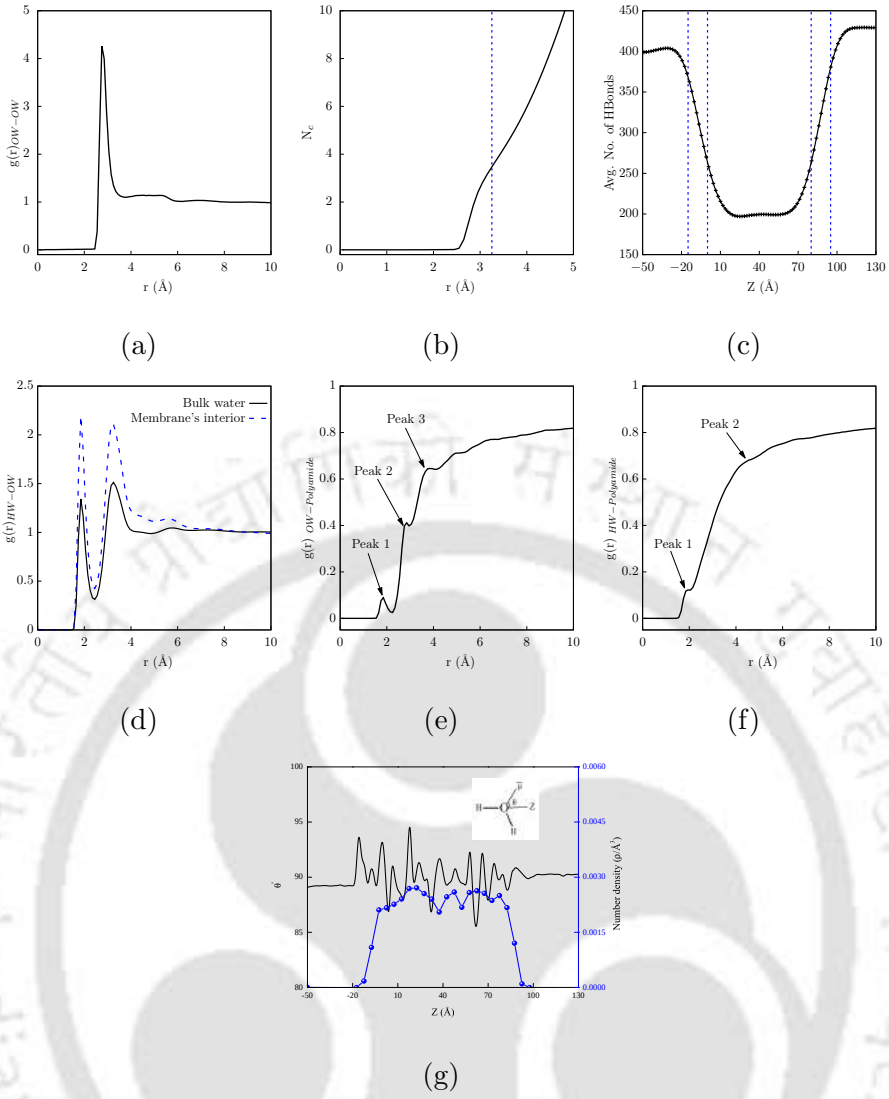

Figure 3.6: (a) RDF between water oxygen atoms in the membrane (b) Water coordination number at cutoff distance of 3.25 $\mathring{A}$ in the membrane (c) Average number of hydrogen bonds along Z−direction (dotted lines represent the interface between the feed solution/membrane and draw solution/membrane) (d) RDF between hydrogen and oxygen atoms of water molecules in pure water (i.e., bulk water) and inside the SAPA membrane (i.e., membrane's interior) (e) RDF between water oxygen atoms and membrane atoms: r = 2 $\mathring{A}$ corresponds to hydrogen atoms in −COOH and −NH groups; r = 2.9 $\mathring{A}$ corresponds to nonpolar hydrogen atoms of PIP and TMO; r = 3.8 $\mathring{A}$ corresponds to carbon atoms of PIP and TMO (f) RDF between water hydrogen atoms and membrane atoms: r = 1.9 $\mathring{A}$ corresponds to the oxygen atoms in amide−linkage and nitrogen atoms in PIP (−NH); r = 5 $\mathring{A}$ for the amide−linkage nitrogen atoms (g) Number density of the unreacted functional groups of the membrane and water orientation in Z−direction

the number of oxygen atoms (OW) around the hydrogen atoms (HW) of water molecules in the feed solution (bulk water) was 0.9, while the number of HW around OW of water molecules was 1.9, resulting in 3.8 HB per water molecule in the feed solution. Our results agree with the reported value in the literature for pure water (i.e., 3.8) [75]. Similarly, we determined the number of OW around HW in the membrane interior (i.e., 0.8) and the number of HW around OW of water molecules (i.e., 1.7). As a result, each water molecule inside the membrane forms 3.4 HB. Additionally, water can form hydrogen bonds with the membrane oxygen atoms and hydrogen atoms of free carboxylic groups (i.e., −COOH). We found that each water molecule forms 0.5 HB with a membrane. So the water molecule forms a total of 3.9 HB inside the membrane. The number of hydrogen bonds per water molecule inside the membrane is higher when compared with the value reported for a fully aromatic membrane (i.e., 2.8 HB) [75]. RDFs have been examined to understand the interaction between water and membrane atoms. Figure 3.6(e, f) shows that water molecules are more likely to cluster around polar groups than the nonpolar benzene groups. Peak representations in RDFs depict the interaction of membrane atoms with water. In Figure 3.6e, peak 1 at r = 2 $\mathring{A}$ corresponds to the hydrogen atom of polar groups (−COOH, −NH), at r = 2.9 $\mathring{A}$ peak 2 corresponds to PIP and TMO (benzene ring's) hydrogen atoms and at r = 3.8 $\mathring{A}$ is for carbon atoms of TMO (benzene ring's) and PIP units. Similarly, peak 1 in RDF of hydrogen atoms of water and SAPA atoms (see Figure 3.6f) corresponds to oxygen atoms of amide−linkage, and peak 2 corresponds to the amide−linkage nitrogen atoms in the membrane.

Additionally, assessing the dipole moments of the water molecules within the membrane will provide insights into the water transport mechanism. It is observed that the unreacted functional groups in the membrane significantly affect water transport behavior [77]. This behavior is quantified via the dipole moment. For convenience, we have quantified the water molecule's orientation in terms of angle distribution in the Z direction (i.e., membrane thickness) using a dipole vector. The interaction between the unreacted functional groups of the membrane (−COOH and −NH) and water molecules in a semi−aromatic membrane helps to understand the water transport mechanism. Figure 3.6g depicts the distribution of the membrane's unreacted functional groups and the orientation of water molecules in a simulated system. For simplicity, θ represents the angle between the water dipole vector and the negative Z−direction of the simulation system. In the feed solution (i.e., pure water, Z < 95 $\mathring{A}$), it has been observed that the angle fluctuates around 90°. This would imply that the water molecules in the feed

solution do not have a preferred orientation in any direction. On the other hand, the angle displays a substantial fluctuation near (80 $\mathring{A}$ < Z < 95 $\mathring{A}$) and within the membrane (0 $\mathring{A}$ < Z < 80 $\mathring{A}$) around 90°. The profile of unreacted functional groups exhibits an apparent fluctuation across the membrane, with a trend comparable to the water orientation profile. It suggests that the unreacted functional groups of a membrane significantly affect water mobility.

3.3.3 Water Permeance

Table 3.3: Permeability comparison with experimentally reported results for PIP/TMC TFC membrane

Sl. No	Author	Permeace $Lm^{-2}hr^{-1}bar^{-1}$	Thickness nm	Permeability ($\times 10^7$) $Lm^{-1}hr^{-1}bar^{-1}$
1	Present work	356	11	39.16
2	Sarkaret al. [31]	57.1	7	3.99
3	Liang et al. [78]	17.1	20	3.42
4	Peng et al. [79]	31	20.3	6.29
5	Mei et al. [80]	21.8	21.7	4.73
6	Xiong et al. [81]	18.9	22	4.16
7	Subrahmanya et al. [82]	15	56	8.40
8	Qiu et al. [83]	22.3	78.1	17.42
9	Wang et al. [84]	53.5	145	77.56

The membrane's permeability is calculated based on the number of water molecules that permeated the membrane in a simulated time due to osmotic pressure gradient. The difference in the osmotic pressures of pure water and Na_2SO_4 solution drives the water permeation through the membrane. The water permeability achieved in our simulations is 39.16 ± 1.98 × 10^{-7} $Lm^{-1}hr^{-1}bar^{-1}$, which is several times higher than the experimentally reported value for a piperazine−based membrane in NF mode [31]. Figure 3.7a depicts the total number of water molecules (N_A) present in both the feed and draw solutions. As a result of the osmotic

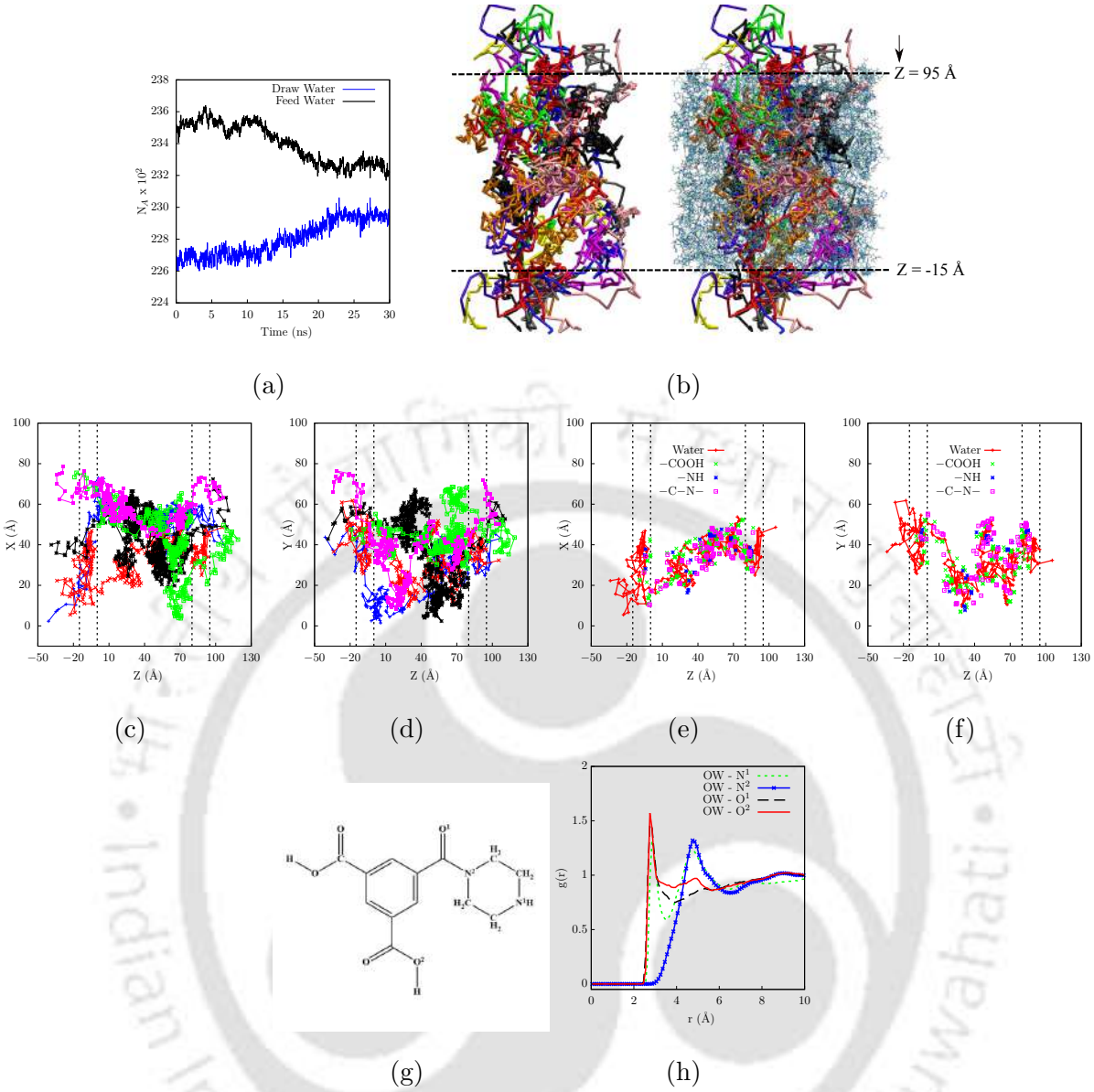

Figure 3.7: (a) The average number of water molecules present in feed and draw solutions in a simulation time (t = 30 ns) (b) The pathways of water molecules in the Z−direction, where the left side represents pathways without a membrane, while the right side depicts pathways with a membrane (c) The trajectories of five water molecules are represented in a 2D XZ plane (d) The trajectories of five water molecules are represented in a 2D YZ plane (e) The trajectory of single water molecule and membrane functional groups present within a 5 $\mathring{A}$ radius along the trajectory is represented in a 2D XZ plane (f) The trajectory of single water molecule and membrane functional groups present within a 5 $\mathring{A}$ radius along the trajectory is represented in a 2D YZ plane; note: all dotted lines in c, d, e, f indicate the interfacial regions between feed solution/membrane and draw solution/membrane (g) Schematic representation of the functional group atoms in the membrane (h) RDF between water oxygen atoms and membrane functional group atoms

pressure difference, 396 water molecules permeated the SAPA membrane from the feed solution to the draw solution. Random thermal movements of the molecules in the system and collisions between the molecules and membrane atoms could cause fluctuations in the water molecule's profile. As the simulation progress, the water molecule's permeation through the membrane reduces due to the dilution of the draw solution concentration. The comparison between the present simulation work with experimental reports is shown in Table 3.3, revealing that the simulated membrane exhibits higher permeability. It is worth mentioning that the membranes reported in the literature (refer to Table 3.3) are PIP/TMC polymerized membranes specifically employed in nanofiltration processes to separate multivalent salt ions, such as Na_2SO_4. In addition, the simulated SAPA FO membrane exhibits high permeability compared to a fully aromatic polyamide membrane. Tomohisa Yoshioka et al. [47] prepared a 30 $\mathring{A}$ thick, fully aromatic PA membrane and used it in the FO process with NaCl (i.e., osmotic pressure difference $\approx$ 83 atm) as the draw solution. The reported water permeability is 0.45 - 0.75 $\times$ 10^{-7} $Lm^{-1}hr^{-1}bar^{-1}$ [47]. Based on the comparisons made in the Table 3.3, SAPA membrane shows promise as a favorable candidate for FO process in the context of textile wastewater treatment.

To understand the membrane's water transport mechanism, individual molecules' pathways (trajectories) are presented. The benefit of non−equilibrium molecular dynamics (NEMD) simulations is that we can understand the transport at the molecular level by following individual water molecules as they move across the membrane. Even though many water molecules permeated the membrane, for the sake of clarity, we only depicted 20 water molecules in Figure 3.7b, where the left side illustrates the pathways of water molecules without a membrane, and the right side shows the same with a membrane. For a better understanding, five water molecules' trajectories are picked from Figure 3.7b and represented in a 2D plot on XZ and YZ planes (see Figure 3.7(c, d)). Each water molecule begins from the feed solution (Z > 95 $\mathring{A}$) and enters into the membrane's interfacial region (80 $\mathring{A}$ < Z < 95 $\mathring{A}$), then moves across its dense region (0 $\mathring{A}$ < Z < 80 $\mathring{A}$) and traverses towards draw solution. Figure 3.7(c, d) shows that water molecules in pure water initially follow a random path, Brownian motion, as it collides with neighboring water molecules. The molecules approach the interfacial region of the membrane several times before reaching the bulk portion of the membrane. Once a molecule enters the bulk membrane, it travels rapidly in some parts and appears trapped in the other areas of the membrane. For example, if you consider a water molecule (magenta color line segment between 70 $\mathring{A}$ - 80 $\mathring{A}$) in Figure 3.7(c, d) becomes trapped in a pore, following a random path and occupying the pore

as it bumps into other water molecules and polymeric chains of the membrane. The membrane molecules surrounding the pore keep it from getting out. It appears that the diameter of this pore is around 10 $\mathring{A}$. The water molecule then quickly jumps to another pore that has a length of 40 $\mathring{A}$ (30 $\mathring{A}$ - 70 $\mathring{A}$), and later it hops into another pore with a length of 30 $\mathring{A}$ (0 $\mathring{A}$ - 30 $\mathring{A}$). It is observed that the water molecule is again trapped for quite some time and eventually passes through the interfacial region (-15 $\mathring{A}$ < Z < 0 $\mathring{A}$), exits the membrane through this pore, and then goes to the draw solution on the left side of the membrane. Similarly, Figure 3.7(c, d) shows the path followed by other water molecules. The fast water pathways are mostly found around a low degree of cross−linking of the membrane (i.e., ≈ 42%), which is lower than the overall value of 47.60%. For the sake of comparison, the degree of cross−linking of fully aromatic RO membrane is around 70% [45]. The degree of network crosslinking is known to be linked with the mechanical strength of the SAPA film [31, 48]. It is also a basic property of the separation layer of a membrane where a higher degree of crosslinking provides higher ion selectivity but negatively impacts its water permeance. Thus to achieve high ion selectivity in SAPA based FO membrane, it needs a higher degree of crosslinking. However, we showed in this manuscript that ≈ 47% of crosslinking is good to achieve an excellent ion separation compared to a ≈ 70% crosslinking for PA membrane used for desalination via reverse osmosis where high hydraulic stability is needed. Further, the ion rejection details will be discussed in the reverse draw solute flux section. The pores along the trajectories are interconnected, resulting in a smaller membrane tortuosity and allowing water to move through it quickly. We have also computed the role of the functional groups of the membrane in water transport along the water molecule trajectory by calculating the positions of reacted and unreacted functional groups within 5 $\mathring{A}$ of a water molecule. Figure 3.7(e, f) shows that the unreacted −COOH group facilitates the transport of water molecules along the Z−direction more than the other reacted and unreacted functional groups. RDFs were also studied to quantify interactions between water and membrane functional groups. The schematic representation of the functional groups in the membrane is presented in Figure 3.7g, and Figure 3.7h displays their RDFs. A peak in RDF of g_{OW-N2} (r) is located at 4.8 $\mathring{A}$, suggesting significant water aggregation surrounding the amino groups. It shows that the amino groups and water have a strong interaction. The RDFs of g_{OW-N1} (r), g_{OW-O1} (r), and g_{OW-O2} (r) have initial peaks located at 2.75, 2.79, and 2.8 $\mathring{A}$, respectively, implying attraction between membrane functional group atoms and water molecules. Click here to see pathways movie. Even though 3% of the membrane atoms are fixed

during the production simulations to prevent them from translating, significant movement in the membrane atoms is observed as water molecules interact with membrane polymer chains. It is known that the membrane structure significantly affects the water trajectories [85].

3.3.4 Reverse Draw Solute Flux

In FO process, there is a possibility that draw solute can diffuse through the membrane towards a feed solution. Reverse draw solute flux is one of the performance metrics of FO membranes. Typically, the salt rejection can be calculated based on the number of ions permeating through the membrane:

$$Rejection(\%) = (1 - \frac{C_p}{C_i}) \times 100 \tag{3.4}$$

where C_p is the number of ions permeated the membrane at time t = t, and C_i is the number of ions in the draw solution at time t = 0. In our simulation study, we observed the excellent Na_2SO_4 salt rejection by the SAPA membrane (which could be due to the high concentration of $-COOH$ at the interface between the draw solution and membrane (see Figure 3.8a). Our observations are in agreement with a recent experimental study of the NF process using sub-5 nm SAPA nanofilm prepared via interfacial polymerization of PIP with TMC [31]. Figure 3.8b, 3.8c depicts the RDFs of Na_2SO_4 ions with water. The sharp peak in Figure 3.8b indicates the presence of higher water molecules in the first hydration shell of the ions. The first maximum of the RDF between Na^+ and hydrogen atoms of a water molecule has appeared at r = 3.45 $\mathring{A}$ (see Figure 3.8c), which is close to the reported solvation shell radius (i.e., 3.58 $\mathring{A}$). Electrostatic interaction energies between the functional group atoms of the SAPA membrane and the salt ions are shown in Figure 3.8d. The higher amount of PIP units makes the membrane partially positive at the interface region [31] and repels the Na^+ ions, and the high amount of $-COOH$ units repel the SO_4^{-2} ions.

3.3.5 Sulphate Salt versus Chloride Salt

Equilibrium molecular dynamic simulations were performed to investigate the diffusive behavior of water molecules and mono/divalent ions within the SAPA membrane. Figure 3.9a displays the equilibrated hydrated membrane. Two different systems were created by inserting 20 NaCl and 10 Na_2SO_4 salt ions inside the equilibrated hydrated membrane separately, as shown in Figure 3.9(b, c). Initially, these two systems were energy minimized and then equilibrated in

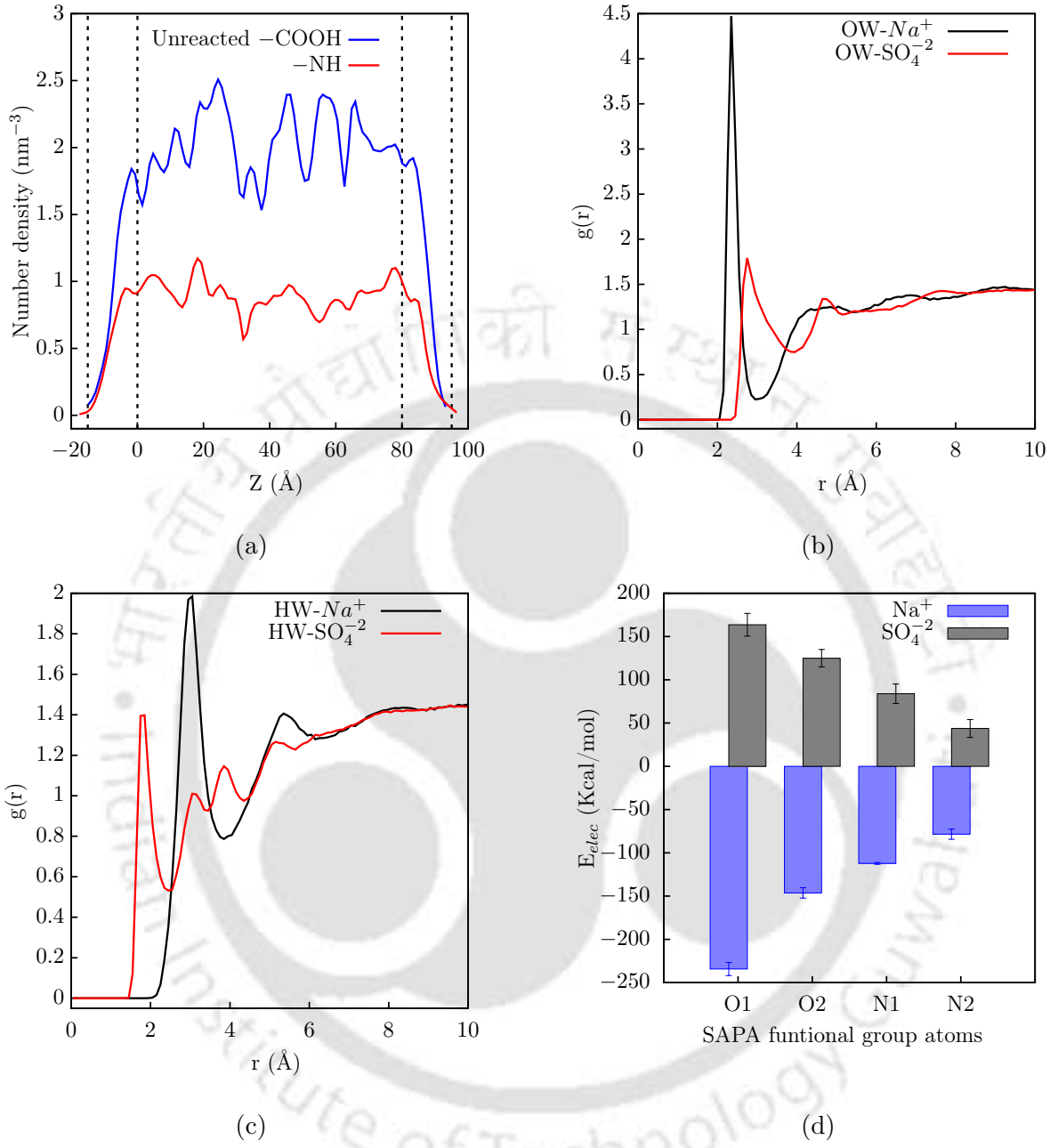

Figure 3.8: (a) The number density of unreacted functional groups in the membrane (dashed lines represent the interfacial regions between feed solution/membrane and draw solution/membrane) (b) RDF between water oxygen atoms and Na_2SO_4 ions (c) RDF between water hydrogen atoms and Na_2SO_4 ions (d) The electrostatic interaction energies of Na_2SO_4 ions with membrane functional group atoms.

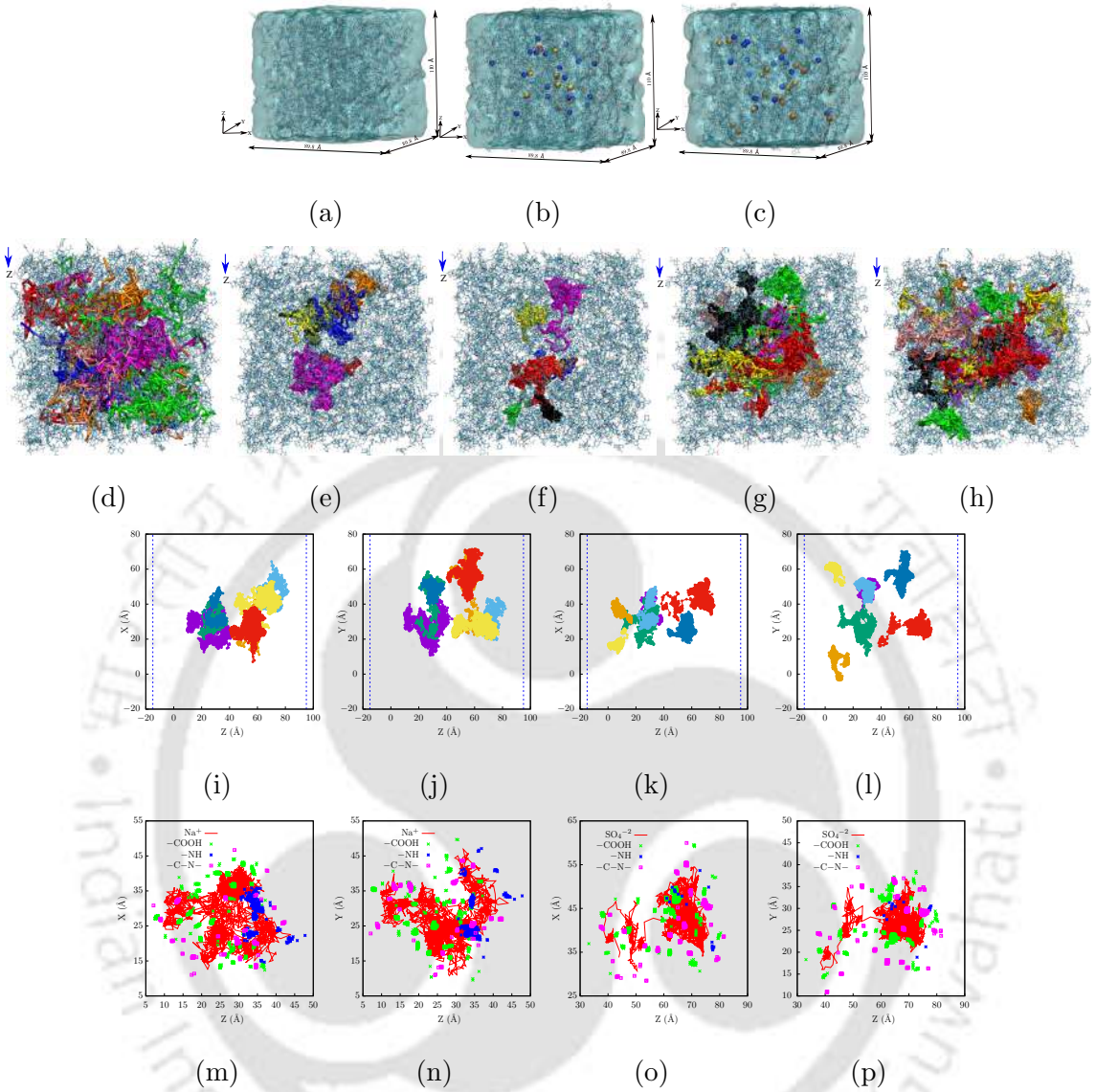

Figure 3.9: (a) Equilibrated hydrated membrane (b) Equilibrated hydrated membrane with Na^+ and SO_4^{-2} ions (c) Equilibrated hydrated membrane with Na^+ and Cl^- ions (d) The pathways of water molecules in the Z−direction (e) The pathways of Na^+ ions from Na_2SO_4 in the Z−direction (f) The pathways of SO_4^{-2} ions from Na_2SO_4 in the Z−direction (g) The pathways of Na^+ ions from NaCl in the Z−direction (h) The pathways of Cl^- ions from NaCl in the Z−direction (i) The trajectories of Na^+ ions from Na_2SO_4 represented in a 2D XZ plane (j) The trajectories of Na^+ ions from Na_2SO_4 represented in a 2D YZ plane (k) The trajectories of SO_4^{-2} ions from Na_2SO_4 represented in a 2D XZ plane (l) The trajectories of SO_4^{-2} ions from Na_2SO_4 represented in a 2D YZ plane; note: all dashed lines in i, j, k, l represent the membrane region (-15 $\AA$ < Z < 95 $\AA$) (m) The trajectory of a single Na^+ ion from Na_2SO_4 and the membrane functional groups present within a 5 $\AA$ radius along the trajectory is represented in a 2D XZ plane (n) The trajectory of a single Na^+ ion from Na_2SO_4 and the membrane functional groups present within a 5 $\AA$ radius along the trajectory is represented in a 2D YZ plane (o) The trajectory of a single SO_4^{-2} ion from Na_2SO_4 and the membrane functional groups present within a 5 $\AA$ radius along the trajectory is represented in a 2D XZ plane (p) The trajectory of a single SO_4^{-2} ion from Na_2SO_4 and the membrane functional groups present within a 5 $\AA$ radius along the trajectory is represented in a 2D YZ plane

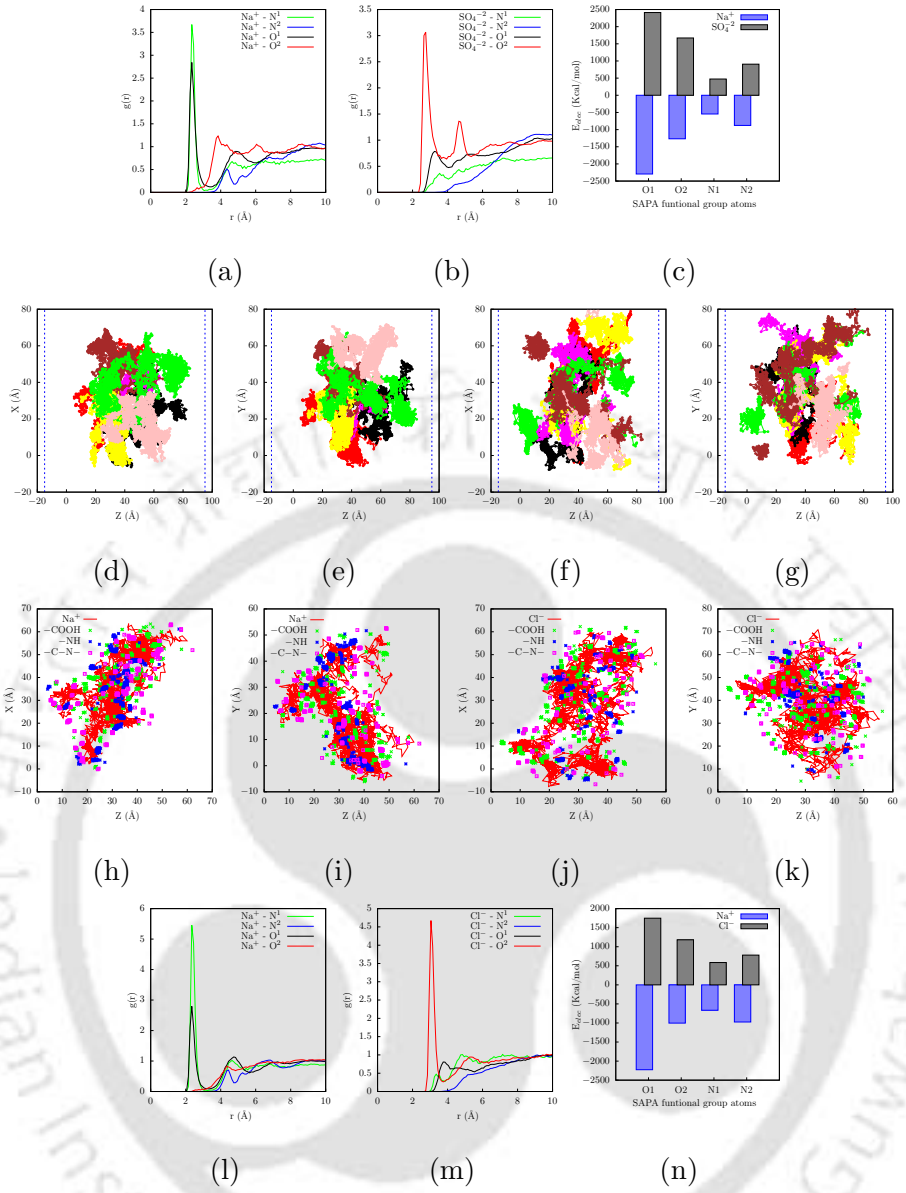

Figure 3.10: (a) RDF between Na^+ ions from Na_2SO_4 and membrane functional group atoms (b) RDF between SO_4^{-2} ions from Na_2SO_4 and membrane functional group atoms (c) The electrostatic interaction energy of sulphate salt with membrane functional group atoms (d) The trajectories of Na^+ ions from NaCl represented in a 2D XZ plane (e) The trajectories of Na^+ ions from NaCl represented in a 2D YZ plane (f) The trajectories of Cl^- ions from NaCl represented in a 2D XZ plane (g) The trajectories of Cl^- ions from NaCl represented in a 2D YZ plane; note: all dashed lines in d, e, f, g represent the membrane region (-15 $\AA$ < Z < 95 $\AA$) (h) The trajectory of a single Na^+ ion from NaCl and membrane functional groups present within a 5 $\AA$ radius along the trajectory is represented in a 2D XZ plane (i) The trajectory of a single Na^+ ion from NaCl and membrane functional groups present within a 5 $\AA$ radius along the trajectory is represented in a 2D YZ plane (j) The trajectory of a single Cl^- ion from NaCl and membrane functional groups groups present within a 5 $\AA$ radius along the trajectory is represented in a 2D XZ plane (k) The trajectory of a single Cl^- ion from NaCl and membrane functional groups groups present within a 5 $\AA$ radius along the trajectory is represented in a 2D YZ plane (l) RDF between Na^+ ions from NaCl and membrane functional group atoms (m) RDF between Cl^- ions from NaCl and membrane functional group atoms (n) The electrostatic interaction energy of chloride salt ions with membrane functional group atoms

an NPT ensemble for 5 ns at room temperature and pressure (300K, 1 atm). The production simulations were performed in the NVT ensemble for 60 ns at 300K temperature with a time step of 1 fs. Figure 3.9(d, e, f, g, h) shows the pathways of seven water molecules, sulphate salt ions, and chloride salt ions. The pathways of NaCl ions imply that chloride salt ions diffuse more rapidly and in the same fashion (see Figure 3.9(g, h)) as water molecules (see Figure 3.9d). The pathways of Na_2SO_4 (see Figure 3.9(e, f)) ions demonstrate that sulphate salt ions appear confined in some regions of the membrane. However, for better understanding, trajectories of sulphate salt ions are shown in a 2D plot (see Figure 3.9(i, j, k,l)). Figure 3.9(i, j) depicts the 2D trajectories of Na^+ ions of Na_2SO_4. It is observed that Na^+ ions are diffusing to some extent and are not permeating the entire membrane, whereas SO_4^{-2} ions appear to be trapped (see Figure 3.9(k, l)). The effect of membrane functional groups on the trajectories of sulphate salt ions was investigated by following the trajectory of a single ion and membrane functional groups within 5 $\mathring{A}$ of the trajectory (see Figure 3.9(m, n, o, p)). From figure 3.9(m,n), it is evident that Na^+ ions interact more with unreacted $-COOH$ and $-NH$ groups; in contrast, SO_4^{-2} ions are confined by $-COOH$ groups (see Figure 3.9(o, p)). The RDF profile of Na_2SO_4 further demonstrates its affinity towards the membrane functional group atoms. Sharp peaks at r = 2.5 $\mathring{A}$ indicate that Na^+ ions exhibit an affinity towards amide$-$linkage oxygen atoms and unreacted nitrogen atoms of $-NH$ groups (see Figure 3.10a). Figure 3.10b depicts the interaction between SO_4^{-2} ions and the oxygen atoms in $-COOH$ groups. Electrostatic interaction energies were computed for sulphate salt ions with membrane functional group atoms. Figure 3.10c shows that Na^+ ions exhibit a higher affinity toward the membrane functional group atoms than the SO_4^{-2} ions. In addition, we have computed the trajectories of chloride salt and reported in figure 3.10(d, e, f, g). Figure 3.10(h, i, j, k) represents the single chloride salt trajectory and membrane functional groups within 5 $\mathring{A}$ along the trajectory. It is observed that chloride salt trajectories follow the same fashion as water molecule's trajectories by interacting with the functional groups of the membrane. RDF profile (see Figure 3.10(l, m)) and interaction energies (see Figure 3.10n) follow the same trend as the sulphate salt.

Membrane techniques can be used to treat dye effluents of wastewater from textile industries. Dye effluents have high COD, salt content (e.g., Na_2SO_4 and NaCl), and rich color. The combination of monovalent (e.g., NaCl) and divalent (e.g., Na_2SO_4) salts in the dyeing process form "dye/dual$-$salts" in an aqueous solution, leading to problems in post$-$treatment operation [41]. Even though diffusion time scales are much less compared to real$-$time experiments,

however, from the trajectories and the distance traveled by both salt ions inside the membrane, it is found that chloride salt ions were able to travel faster and have longer pathways (or trajectories) than sulphate salt ions leading to high sulphate salt rejection. Additionally, the mobility of ions is restricted by surrounding water molecules in the hydrated shell. The average number of water molecules in the first hydration shell of Na^+ and SO_4^{-2} ions within the SAPA membrane are 5 and 11.5, respectively. Moreover, the desolvation energy of hydrated Na^+ ion is 365 kJ mol^{-1} [86], which is highly impossible to stripping waters off to permeate through membrane pores due to water clusters around the ions are tight and restrict the mobility of ions. Similarly, SO_4^{-2} ions also get solvated and are unable to permeate through the membrane since the hydration energy of sulphate ion is higher than Na^+ (i.e., 1080 kJ mol^{-1} [86]). This suggests that sulphate salt can be separated from the mixed feed of the textile industry wastewater. Furthermore, the EMD simulation results presented in this study offer valuable insights to experimentalists seeking to design membranes with a high selectivity towards sulphate salt. Intuitively, one might anticipate that monovalent salts diffuse more rapidly than divalent salts within the membrane. However, it remains crucial to comprehend the influence of the membrane's functional groups in facilitating salt ion diffusion and to identify membrane structures that exhibit exceptional selectivity towards Na_2SO_4. The atomistic−level details presented in this work will help in the better design of FO membranes for the targeted application. As we observed in our simulations, the SAPA membrane can permeate NaCl while rejecting Na_2SO_4, implying that this membrane can play a role in the textile waste treatment process.

3.4 Conclusions

In this work, we investigated the applicability of the SAPA membrane in forward osmosis via non−equilibrium as well as equilibrium molecular dynamics simulations. The feed in the present study is pure water, and the draw is Na_2SO_4 solution. Water structure and dynamics inside the membrane are characterized via radial distribution function, coordination number, hydrogen bonds, and dipole moment. As the water molecules transit through the SAPA membrane, it is observed that water permeates through the membrane with a reduced coordination number; hence the number of hydrogen bonds per water molecule decreases inside the membrane. The unreacted functional groups in the membrane at the feed solution/membrane interface facilitate the water molecules to enter the membrane interior. Water permeability computed based on

the number of permeated water molecules is 39.16 $\times$ 10^{-7} $Lm^{-1}hr^{-1}bar^{-1}$. The present study suggests that a high density of $-COOH$ functional groups at the water$-$interfacial region and the appropriate cross$-$linking density in the SAPA membrane play a main role in the efficient water transport across the membrane. The analysis of the trajectories of NaCl and Na_2SO_4 ions inside the SAPA membrane (via EMD simulations) and the interaction of the salt ions with the functional groups of the membrane suggest that the membrane can trap divalent anions. However, monovalent anions seem to have longer trajectories leading to efficient separation of divalent salt using SAPA membrane. A membrane which can reject Na_2SO_4 but allow NaCl can play a significant role in the textile industry waste treatment process. As our simulation work provided atomistic level details about the rejection of Na_2SO_4 and water permeation, we hope that these findings can inspire further experiments towards a better SAPA membrane in FO applications.

Bibliography

[1] F Silva Pinto and R Cunha Marques. Desalination projects economic feasibility: A standardization of cost determinants. *Renewable Sustainable Energy Rev.*, 78:904–915, 2017.

[2] Nour AlSawaftah, Waad Abuwatfa, Naif Darwish, and Ghaleb Husseini. A comprehensive review on membrane fouling: Mathematical modelling, prediction, diagnosis, and mitigation. *Water*, 13(9):1327, 2021.

[3] Tzahi Y Cath, Amy E Childress, and Menachem Elimelech. Forward osmosis: Principles, applications, and recent developments. *J. Membr. Sci.*, 281(1-2):70–87, 2006.

[4] Wei Lun Ang, Abdul Wahab Mohammad, Daniel Johnson, and Nidal Hilal. Forward osmosis research trends in desalination and wastewater treatment: A review of research trends over the past decade. *J. Water Process. Eng.*, 31:100886, 2019.

[5] Ngai Yin Yip, Alberto Tiraferri, William A Phillip, Jessica D Schiffman, Laura A Hoover, Yu Chang Kim, and Menachem Elimelech. Thin-film composite pressure retarded osmosis membranes for sustainable power generation from salinity gradients. *Environ. Sci. Technol.*, 45(10):4360–4369, 2011.

[6] Xue Li, Sui Zhang, Fengjiang Fu, and Tai-Shung Chung. Deformation and reinforcement of thin-film composite (tfc) polyamide-imide (pai) membranes for osmotic power generation. *J. Membr. Sci.*, 434:204–217, 2013.

[7] Bukke Vani, Sugali Chandra Sekhar, Nivedita Sahu, and Sundergopal Sridhar. Development of a uv coupled indigenous hydrophilized polyamide membrane system for enhanced shelf life of mature coconut water. *J. Food Process Eng.*, 44(3):e13636, 2021.

[8] Lu Elfa Peng, Zhe Yang, Li Long, Shenghua Zhou, Hao Guo, and Chuyang Y Tang. A critical review on porous substrates of tfc polyamide membranes: Mechanisms, membrane performances, and future perspectives. *J. Membr. Sci.*, 641:119871, 2022.

[9] Mark A Shannon, Paul W Bohn, Menachem Elimelech, John G Georgiadis, Benito J Marinas, and Anne M Mayes. Science and technology for water purification in the coming decades. *Nature*, pages 337–346, 2010.

[10] Israr Ali, Muhammad Asim Raza, Rashid Mehmood, Atif Islam, Aneela Sabir, Nafisa Gull, Bilal Haider, Sang Hyun Park, and Rafi Ullah Khan. Novel maleic acid, crosslinked, nanofibrous chitosan/poly (vinylpyrrolidone) membranes for reverse osmosis desalination. *Int. J. Mol. Sci.*, 21(19):7338, 2020.

[11] Guo-Rong Xu, Jian-Mei Xu, Hou-Jun Feng, He-Li Zhao, and Shui-Bo Wu. Tailoring structures and performance of polyamide thin film composite (pa-tfc) desalination membranes via sublayers adjustment-a review. *Desalination*, 417:19–35, 2017.

[12] Woei-Jye Lau, Gwo-Sung Lai, Jianxin Li, Stephen Gray, Yunxia Hu, Nurasyikin Misdan, Pei-Sean Goh, Takeshi Matsuura, Ihsan Wan Azelee, and Ahmad Fauzi Ismail. Development of microporous substrates of polyamide thin film composite membranes for pressure-driven and osmotically-driven membrane processes: A review. *Ind. Eng. Chem.*, 77:25–59, 2019.

[13] Jing-Gang Gai, Xiao-Lei Gong, Wu-Li Kang, Xin Zhang, and Wei-Wei Wang. Key factors influencing water diffusion in aromatic pa membrane: Hydrates, nanochannels and functional groups. *Desalination*, 333(1):52–58, 2014.

[14] Santiago Romero-Vargas Castrillon, Xinglin Lu, Devin L Shaffer, and Menachem Elimelech. Amine enrichment and poly (ethylene glycol)(peg) surface modification of thin-film composite forward osmosis membranes for organic fouling control. *J. Membr. Sci.*, 450: 331–339, 2014.

[15] Si Zhang, Quang Viet Ly, Long D Nghiem, Jing Wang, Jianxin Li, and Yunxia Hu. Optimization and organic fouling behavior of zwitterion-modified thin-film composite polyamide membrane for water reclamation: a comprehensive study. *J. Membr. Sci.*, 596:117748, 2020.

[16] Hossein Mahdavi and Akram Rahimi. Zwitterion functionalized graphene oxide/polyamide thin film nanocomposite membrane: Towards improved anti-fouling performance for reverse osmosis. *Desalination*, 433:94–107, 2018.

[17] Xinglin Lu, Santiago Romero-Vargas Castrillon, Devin L Shaffer, Jun Ma, and Menachem Elimelech. In situ surface chemical modification of thin-film composite forward osmosis membranes for enhanced organic fouling resistance. *Environ. Sci. Technol.*, 47(21):12219–12228, 2013.

[18] Devin L Shaffer, Humberto Jaramillo, Santiago Romero Vargas Castrillon, Xinglin Lu, and Menachem Elimelech. Post-fabrication modification of forward osmosis membranes with a poly (ethylene glycol) block copolymer for improved organic fouling resistance. *J. Membr. Sci.*, 490:209–219, 2015.

[19] Haifeng Wang, Lei Li, Xiaosa Zhang, and Suobo Zhang. Polyamide thin-film composite

membranes prepared from a novel triamine 3, 5-diamino-n-(4-aminophenyl)-benzamide monomer and m-phenylenediamine. *J. Membr. Sci.*, 353(1-2):78–84, 2010.

[20] Meihong Liu, Dihua Wu, Sanchuan Yu, and Congjie Gao. Influence of the polyacyl chloride structure on the reverse osmosis performance, surface properties and chlorine stability of the thin-film composite polyamide membranes. *J. Membr. Sci.*, 326(1):205–214, 2009.

[21] Sara Sorribas, Patricia Gorgojo, Carlos Tellez, Joaquin Coronas, and Andrew G Livingston. High flux thin film nanocomposite membranes based on metal–organic frameworks for organic solvent nanofiltration. *J. Am. Chem. Soc.*, 135(40):15201–15208, 2013.

[22] Ning Ma, Jing Wei, Rihong Liao, and Chuyang Y Tang. Zeolite-polyamide thin film nanocomposite membranes: Towards enhanced performance for forward osmosis. *J. Membr. Sci.*, 405:149–157, 2012.

[23] Menachem Elimelech and William A Phillip. The future of seawater desalination: energy, technology, and the environment. *science*, 333(6043):712–717, 2011.

[24] Jonggeon Jegal, Sung Gyu Min, and Kew-Ho Lee. Factors affecting the interfacial polymerization of polyamide active layers for the formation of polyamide composite membranes. *J. Appl. Polym. Sci.*, 86(11):2781–2787, 2002.

[25] Yue Cui, Xiang-Yang Liu, and Tai-Shung Chung. Enhanced osmotic energy generation from salinity gradients by modifying thin film composite membranes. *Chem. Eng. J.*, 242: 195–203, 2014.

[26] Asim K Ghosh, Byeong-Heon Jeong, Xiaofei Huang, and Eric MV Hoek. Impacts of reaction and curing conditions on polyamide composite reverse osmosis membrane properties. *J. Membr. Sci.*, 311(1-2):34–45, 2008.

[27] Y Mansourpanah, K Alizadeh, SS Madaeni, A Rahimpour, and H Soltani Afarani. Using different surfactants for changing the properties of poly (piperazineamide) tfc nanofiltration membranes. *Desalination*, 271(1-3):169–177, 2011.

[28] Y Mansourpanah, SS Madaeni, and A Rahimpour. Fabrication and development of interfacial polymerized thin-film composite nanofiltration membrane using different surfactants in organic phase; study of morphology and performance. *J. Membr. Sci.*, 343(1-2):219–228, 2009.

[29] Hai Huang, Xinying Qu, Xiaosheng Ji, Xin Gao, Lin Zhang, Huanlin Chen, and Lian Hou. Acid and multivalent ion resistance of thin film nanocomposite ro membranes loaded with silicalite-1 nanozeolites. *J. Mater. Chem. A*, 1(37):11343–11349, 2013.

[30] Jiaxu Qin, Saisai Lin, Shuqin Song, Lin Zhang, and Huanlin Chen. 4-dimethylaminopyridine promoted interfacial polymerization between hyperbranched polyesteramide and trimesoyl chloride for preparing ultralow-pressure reverse osmosis composite membrane. *ACS Appl. Mater. Interfaces*, 5(14):6649–6656, 2013.

[31] Pulak Sarkar, Solagna Modak, and Santanu Karan. Ultraselective and highly permeable polyamide nanofilms for ionic and molecular nanofiltration. *Adv. Funct. Mater.*, 31(3): 2007054, 2021.

[32] Chuyang Y Tang, Young-Nam Kwon, and James O Leckie. Effect of membrane chemistry and coating layer on physiochemical properties of thin film composite polyamide ro and nf membranes: Ii. membrane physiochemical properties and their dependence on polyamide and coating layers. *Desalination*, 242(1-3):168–182, 2009.

[33] Noeon Park, Boksoon Kwon, In S Kim, and Jaeweon Cho. Biofouling potential of various nf membranes with respect to bacteria and their soluble microbial products (smp): characterizations, flux decline, and transport parameters. *J. Membr. Sci.*, 258(1-2):43–54, 2005.

[34] Jaydevsinh M Gohil and Paramita Ray. A review on semi-aromatic polyamide tfc membranes prepared by interfacial polymerization: Potential for water treatment and desalination. *Sep. Purif. Technol.*, 181:159–182, 2017.

[35] Xi Yang, Yong Du, Xi Zhang, Ai He, and Zhi-Kang Xu. Nanofiltration membrane with a mussel-inspired interlayer for improved permeation performance. *Langmuir*, 33(9):2318–2324, 2017.

[36] Xi Yang. Controllable interfacial polymerization for nanofiltration membrane performance improvement by the polyphenol interlayer. *ACS omega*, 4(9):13824–13833, 2019.

[37] Xiaoli Wu, Yifan Li, Xulin Cui, Jingtao Wang, Xingzhong Cao, Peng Zhang, and Lingyun Zheng. Adsorption-assisted interfacial polymerization toward ultrathin active layers for ultrafast organic permeation. *ACS Appl. Mater. Interfaces*, 10(12):10445–10453, 2018.

[38] Zhe Tan, Shengfu Chen, Xinsheng Peng, Lin Zhang, and Congjie Gao. Polyamide membranes with nanoscale turing structures for water purification. *Science*, 360(6388):518–521, 2018.

[39] Mohammad Reza Mahdavi, Mohammad Delnavaz, and Vahid Vatanpour. Fabrication and water desalination performance of piperazine–polyamide nanocomposite nanofiltration

membranes embedded with raw and oxidized mwcnts. *J. Taiwan Inst. Chem. Eng.*, 75: 189–198, 2017.

[40] Pulak Sarkar, Solagna Modak, and Santanu Karan. Effect of porous and nonporous nanostructures on the permeance of positively charged nanofilm composite membranes. *Adv. Mater. Interfaces*, 7(19):2000251, 2020.

[41] Xiao Ma, Pengli Chen, Ming Zhou, Zhaoxiang Zhong, Feng Zhang, and Weihong Xing. Tight ultrafiltration ceramic membrane for separation of dyes and mixed salts (both nacl/na2so4) in textile wastewater treatment. *Ind. Eng. Chem. Res.*, 56(24):7070–7079, 2017.

[42] Jing Huang and Alexander D MacKerell Jr. Charmm36 all-atom additive protein force field: Validation based on comparison to nmr data. *J. Comput. Chem.*, 34(25):2135–2145, 2013.

[43] James C Phillips, David J Hardy, Julio DC Maia, John E Stone, Joao V Ribeiro, Rafael C Bernardi, Ronak Buch, Giacomo Fiorin, Jerome Henin, Wei Jiang, et al. Scalable molecular dynamics on cpu and gpu architectures with namd. *J. Chem. Phys.*, 153(4):044130, 2020.

[44] Leandro Martinez, Ricardo Andrade, Ernesto G Birgin, and Jose Mario Martinez. Packmol: a package for building initial configurations for molecular dynamics simulations. *J. Comput. Chem.*, 30(13):2157–2164, 2009.

[45] Tao Wei, Lin Zhang, Haiyang Zhao, Heng Ma, Md Symon Jahan Sajib, Hua Jiang, and Sohail Murad. Aromatic polyamide reverse-osmosis membrane: an atomistic molecular dynamics simulation. *J. Phys. Chem. B*, 120(39):10311–10318, 2016.

[46] Pulak Sarkar, Solagna Modak, Santanu Ray, Vasista Adupa, K Anki Reddy, and Santanu Karan. Fast water transport through sub-5 nm polyamide nanofilms: the new upper-bound of the permeance–selectivity trade-off in nanofiltration. *J. Mater. Chem. A*, 9(36): 20714–20724, 2021.

[47] Tomohisa Yoshioka, Keisuke Kotaka, Keizo Nakagawa, Takuji Shintani, Hao-Chen Wu, Hideto Matsuyama, Yu Fujimura, and Takahiro Kawakatsu. Molecular dynamics simulation study of polyamide membrane structures and ro/fo water permeation properties. *Membranes*, 8(4):127, 2018.

[48] Santanu Karan, Zhiwei Jiang, and Andrew G Livingston. Sub–10 nm polyamide nanofilms with ultrafast solvent transport for molecular separation. *Science*, 348(6241):1347–1351, 2015.

[49] William Humphrey, Andrew Dalke, and Klaus Schulten. VMD – Visual Molecular Dynamics. *J. Mol. Graphics*, 14:33–38, 1996.

[50] Minxia Ding, Anthony Szymczyk, Florent Goujon, Armand Soldera, and Aziz Ghoufi. Structure and dynamics of water confined in a polyamide reverse-osmosis membrane: A molecular-simulation study. *J. Membr. Sci.*, 458:236–244, 2014.

[51] William L Jorgensen, Jayaraman Chandrasekhar, Jeffry D Madura, Roger W Impey, and Michael L Klein. Comparison of simple potential functions for simulating liquid water. *J. Chem. Phys.*, 79(2):926–935, 1983.

[52] Alexander D MacKerell Jr, Bernard Brooks, Charles L Brooks III, Lennart Nilsson, Benoit Roux, Youngdo Won, and Martin Karplus. CHARMM: the energy function and its parameterization. *Encyclopedia of computational chemistry*, 1, 2002.

[53] Michael W Mahoney and William L Jorgensen. A five-site model for liquid water and the reproduction of the density anomaly by rigid, nonpolarizable potential functions. *J. Chem. Phys.*, 112(20):8910–8922, 2000.

[54] Jumin Lee, Xi Cheng, Jason M Swails, Min Sun Yeom, Peter K Eastman, Justin A Lemkul, Shuai Wei, Joshua Buckner, Jong Cheol Jeong, Yifei Qi, et al. CHARMM-GUI input generator for namd, gromacs, amber, openmm, and CHARMM/OpenMM simulations using the CHARMM36 additive force field. *J. Chem. Theory Comput.*, 12(1):405–413, 2016.

[55] Tom Darden, Darrin York, and Lee Pedersen. Particle mesh ewald: An n log (n) method for ewald sums in large systems. *J. Chem. Phys.*, 98(12):10089–10092, 1993.

[56] Chaoyuan Zhu and Hiroki Nakamura. Two-state linear curve crossing problems revisited. iv. the best analytical formulas for scattering matrices. *J. Chem. Phys.*, 108(17):7501–7501, 1998.

[57] Scott E Feller, Yuhong Zhang, Richard W Pastor, and Bernard R Brooks. Constant pressure molecular dynamics simulation: the langevin piston method. *J. Chem. Phys.*, 103(11):4613–4621, 1995.

[58] Weimin Gao, Fenghua She, Juan Zhang, Ludovic F Dumee, Li He, Peter D Hodgson, and Lingxue Kong. Understanding water and ion transport behaviour and permeability through poly (amide) thin film composite membrane. *J. Membr. Sci.*, 487:32–39, 2015.

[59] Minxia Ding, Anthony Szymczyk, and Aziz Ghoufi. On the structure and rejection of ions by a polyamide membrane in pressure-driven molecular dynamics simulations. *Desalination*, 368:76–80, 2015.

[60] MJ Kotelyanskii, NJ Wagner, and ME Paulaitis. Molecular dynamics simulation study of the mechanisms of water diffusion in a hydrated, amorphous polyamide. *Comput. Theor. Polym. Sci.*, 9(3-4):301–306, 1999.

[61] Xijing Zhang, David G Cahill, Orlando Coronell, and Benito J Marinas. Absorption of water in the active layer of reverse osmosis membranes. *J. Membr. Sci.*, 331(1-2):143–151, 2009.

[62] MJ Kotelyanskii, NJ Wagner, and ME Paulaitis. Atomistic simulation of water and salt transport in the reverse osmosis membrane ft-30. *J. Membr. Sci.*, 139(1):1–16, 1998.

[63] Supriyo Bhattacharya and Keith E Gubbins. Fast method for computing pore size distributions of model materials. *Langmuir*, 22(18):7726–7731, 2006.

[64] MATLAB. *version 7.10.0 (R2010a)*. The MathWorks Inc., Natick, Massachusetts, 2010.

[65] Accelrys. *Materials Studio 4.4*. Accelrys Software Inc., San Diego, CA., 2008.

[66] SS M Lock, KK Lau, AM Shariff, YF Yeong, and MA Bustam. Computational insights on the role of film thickness on the physical properties of ultrathin polysulfone membranes. *RSC advances*, 7(70):44376–44393, 2017.

[67] Alexey Yushkin, Vladimir Vasilevsky, Valery Khotimskiy, Anthony Szymczyk, and Alexey Volkov. Evaluation of liquid transport properties of hydrophobic polymers of intrinsic microporosity by electrical resistance measurement. *J. Membr. Sci.*, 554:346–356, 2018.

[68] J Muscatello, EA Muller, AA Mostofi, and AP Sutton. Multiscale molecular simulations of the formation and structure of polyamide membranes created by interfacial polymerization. *J. Membr. Sci.*, 527:180–190, 2017.

[69] SJ Suresh and VM Naik. Hydrogen bond thermodynamic properties of water from dielectric constant data. *J. Chem. Phys.*, 113(21):9727–9732, 2000.

[70] Kevin R Hinkle, Cynthia J Jameson, and Sohail Murad. Using molecular simulations to develop reliable design tools and correlations for engineering applications of aqueous electrolyte solutions. *J. Chem. Eng. Data*, 61(4):1578–1584, 2016.

[71] Jester N Itliong, C Villagracia Al Rey, Joaquin Lorenzo V Moreno, Kurt Irvin M Rojas, Gian Paolo O Bernardo, Melanie Y David, Robby B Manrique, Aristotle T Ubando, Alvin B Culaba, Allan Abraham B Padama, et al. Investigation of reverse ionic diffusion in forward-osmosis-aided dewatering of microalgae: A molecular dynamics study. *Bioresour. Technol.*, 279:181–188, 2019.

[72] Angel E Garcia and Gerhard Hummer. Water penetration and escape in proteins. *Proteins: Struct., Funct., Bioinf.*, 38(3):261–272, 2000.

[73] Sergei Grudinin, Georg Buldt, Valentin Gordeliy, and Artur Baumgaertner. Water molecules and hydrogen-bonded networks in bacteriorhodopsin—molecular dynamics simulations of the ground state and the m-intermediate. *Biophys. J.*, 88(5):3252–3261, 2005.

[74] George A Jeffrey and George A Jeffrey. *An introduction to hydrogen bonding*, volume 12. Oxford university press New York, 1997.

[75] Minxia Ding, Aziz Ghoufi, and Anthony Szymczyk. Molecular simulations of polyamide reverse osmosis membranes. *Desalination*, 343:48–53, 2014.

[76] Denis Morineau and Christiane Alba-Simionesco. Liquids in confined geometry: How to connect changes in the structure factor to modifications of local order. *J. Chem. Phys.*, 118(20):9389–9400, 2003.

[77] Ning Zhang, Shaomin Chen, Boyun Yang, Jun Huo, Xiaopeng Zhang, Junjiang Bao, Xuehua Ruan, and Gaohong He. Effect of hydrogen-bonding interaction on the arrangement and dynamics of water confined in a polyamide membrane: A molecular dynamics simulation. *J. Phys. Chem. B*, 122(17):4719–4728, 2018.

[78] Yuanzhe Liang, Yuzhang Zhu, Cheng Liu, Kueir-Rarn Lee, Wei-Song Hung, Zhenyi Wang, Youyong Li, Menachem Elimelech, Jian Jin, and Shihong Lin. Polyamide nanofiltration membrane with highly uniform sub-nanometre pores for sub-1 å precision separation. *Nat. Commun.*, 11(1):2015, 2020.

[79] Huawen Peng, Wen-Hai Zhang, Wei-Song Hung, Naixin Wang, Jian Sun, Kueir-Rarn Lee, Quan-Fu An, Cheng-Mei Liu, and Qiang Zhao. Phosphonium modification leads to ultrapermeable antibacterial polyamide composite membranes with unreduced thickness. *Adv. Mater.*, 32(23):2001383, 2020.

[80] Ying Mei, Zhe Yang, Peng-Fei Sun, Shenghua Zhou, Hao Guo, Lu Elfa Peng, Zhikan Yao, Wulin Yang, and Chuyang Y Tang. Polyelectrolyte-assisted interfacial polymerization for polyamide nanofiltration membrane with enhanced separation and anti-biofouling properties in groundwater treatment. *Desalination*, 555:116546, 2023.

[81] Yuhua Xiong, Xingtao Zuo, Jiajie He, Juan Xiong, Cong Ma, Zhongbing Chen, Yun Zhou, and Shuili Yu. l-tartaric acid tailored polyamide thin-film composite membrane with enhanced performance for salt and molecular removal. *Desalination*, 549:116327, 2023.

[82] TM Subrahmanya, Jing-Yang Lin, Januar Widakdo, Hannah Faye M Austria, Yu-Hsuan

Chiao, Tsung-Han Huang, Wei-Song Hung, Hideto Matsuyama, Kueir-Rarn Lee, Juin-Yih Lai, et al. Effect of functionalized nanodiamonds and surfactants mediation on the nanofiltration performance of polyamide thin-film nanocomposite membranes. *Desalination*, 555: 116540, 2023.

[83] Zhiwei Qiu, Hongyi Han, Tianlin Wang, Ruobin Dai, and Zhiwei Wang. Nanofoaming by surfactant tunes morphology and performance of polyamide nanofiltration membrane. *Desalination*, 552:116457, 2023.

[84] Jing-Jing Wang, Hao-Cheng Yang, Ming-Bang Wu, Xi Zhang, and Zhi-Kang Xu. Nanofiltration membranes with cellulose nanocrystals as an interlayer for unprecedented performance. *J. Mater. Chem. A*, 5(31):16289–16295, 2017.

[85] Meng Shen, Sinan Keten, and Richard M Lueptow. Dynamics of water and solute transport in polymeric reverse osmosis membranes via molecular dynamics simulations. *J. Membr. Sci.*, 506:95–108, 2016.

[86] Yizhak Marcus. Thermodynamics of solvation of ions. part 5.—gibbs free energy of hydration at 298.15 k. *J. Chem. Soc., Faraday Trans.*, 87(18):2995–2999, 1991.

Chapter 4

Non−Preferential Solvent Transport Through Intrinsic Cyclodextrin Pore in a Polyester Film[1]

4.1 Introduction

Nanofiltration membranes are crucial in molecular separation [1–3], ion separation [4–6], and water purification [7–9]. Thin-film composite membranes of polyester or polyamide are generally prepared via interfacial polymerization between hydroxyl or amine monomers with trimesoyl chloride (TMC). Polyamide membranes are known for their excellent salt rejection and are widely used commercially. However, they are susceptible to chlorine degradation [10–12]. In contrast, polyester membranes, which have stable ester bonds that resist oxidants like sodium hypochlorite [10, 13], have gained significant interest over the past decade for their high chlorine resistance. Many hydroxyl monomers such as zwitterions [14–16], carbohydrates [17, 18], cyclodextrins [19–21] and polyphenols [22–24] have been employed for membrane preparation, resulting in better chlorine resistance and performance in both aqueous and organic solvent nanofiltration. For example, carbohydrate monomers enable sustainable membrane production, while cyclodextrin monomers with defined cavities allow precise separation [1, 19, 21]. Yao et al. [25] developed a resilient polyester membrane that is entirely chlorine-resistant

[1]G. Nagendraprasad, K. Anki Reddy, C. Das, S. Karan, Non−Preferential Solvent Transport Through Intrinsic Cyclodextrin Pore in a Polyester Film, J. Phys. Chem. B 127 (30) (2023) 6751–6766.

and resistant to hydrolytic degradation up to pH 9, reducing fouling and mineral scaling compared to polyamide membranes, thus minimizing desalination pretreatment steps. TET-based polyester nanofiltration membrane showed outstanding salt rejection (95.5%), significantly surpassing state-of-the-art polyester membranes (<50%) [26]. Recent work shows that replacing MPD with amino-BIPOL improved polar solvent permeation and dye rejection [23]. Additionally, polyester membranes are robust and flexible and exhibit dual superhydrophobicity under liquid for efficient oil-water separation [27], which is helpful in zero-discharge textile wastewater treatment [28]. Polymers with intrinsic microporosity showed very low permeance of non-polar solvents, and the role of intrinsic microporosity in the transport of non-polar-solvent molecules is yet to be understood [22].

The molecular separation process, recognized for its substantial energy consumption and environmental impact, is a pivotal yet expensive industrial undertaking [29]. In pursuing more energy−efficient alternatives to conventional phase change methods [30], high-performance membranes have emerged as a promising solution. Achieving superior membrane performance necessitates meticulous material selection and precise control over the thickness and porosity of the selective layer [31]. Amorphous polymers have gained attention as membrane materials due to their cost−effectiveness and ease of production. However, the effectiveness of these membranes in separating small molecules is intricately tied to the size and distribution of pores within their disordered cavities [31]. Numerous strategies have been employed to enhance the performance of amorphous polymer membranes, including the incorporation of nanofillers such as graphene oxide [32], carbon nanotubes [33], zeolites [31], porous aromatic frameworks [34], metal-organic frameworks (MOFs) [35], covalent organic frameworks (COFs) [36], and polyhedral oligomeric silsesquioxane (POSS) [37]. These techniques leverage the self−assembly of block copolymers to synthesize polymers with intrinsic microporosity and thermally induced segmental rearrangements [21]. While the introduction of nanofillers has shown promise in enhancing solvent permeability, it may also result in aggregation within the polymer matrix, thereby reducing rejection and forming interfacial microvoids [38]. Moreover, conventional polyamide selective layers, formed through interfacial polymerization, exhibit robustness in certain solvents but often prove ineffective in transporting non−polar organic solvents [39]. Consequently, current research is centered on exploring the potential of the polymer of intrinsic microporosity (PIM-1) in organic solvent nanofiltration (OSN) processes [40]. PIM-1 membranes, notably when delicate and featuring a nanoscale thickness, demonstrate rapid

permeabilities to non-polar organic solvents [41]. Nonetheless, the vulnerability of PIM-1 to aging and swelling becomes apparent when exposed to polar organic solvents, marking a key consideration in further studies [42].

The investigation of solvent transport through nanomaterials has become a focal point in recent years, given its significant implications across various domains, ranging from drug delivery to environmental remediation [43]. Among the diverse nanomaterials under scrutiny, nanofilms based on polyester cyclodextrin have emerged as promising contenders for facilitating the transport of polar and non-polar solvents [21]. Comprising cyclodextrin host molecules and polyester backbones, these films provide a unique platform with the potential to control and enhance solvent transport properties intricately at the molecular level. A comprehensive understanding of the complex interplay between solvents and cyclodextrin-based nanofilms is imperative for optimizing their performance across diverse applications. Cyclodextrin (CD), a macrocyclic molecule extensively investigated in scientific research, stands out for its distinctive conical hourglass cavities formed by the inward protrusion of glycosidic oxygens derived from adjacent α-glucose units. Within these cavities, water confinement presents a scenario of energetic frustration while simultaneously facilitating enthalpically driven hydrophobic interactions with non-polar molecules [44]. The membrane crosslinking of CDs manifests intrinsic microporosity, endowing them with the ability for rapid solvent transport and shape-selective permeability. In membrane form, CDs showcase a remarkable capacity for selectively transporting non-polar solvents through intrinsic pores, alongside facilitating the passage of polar solvents through aggregate pores formed via ester linkage between CD and hydrolyzed trimesoyl chloride (TMC) molecules [21]. Despite this versatile functionality, challenges arise in achieving precise alignment of CD cavities normal to the solvent flow direction, attributed to the disordered packing of CD units that may impede pore interconnectivity. Additionally, the hydrophobic inner cavity of crosslinked CD films may be surrounded by polar groups, potentially hindering the transport of non-polar solvents through the CD cavity. Notably, larger aggregate pores can enhance non-polar solvent permeance while concurrently reducing salt rejection [20], opening avenues for novel membrane design and application advancements. Therefore, it is essential to gain a detailed understanding at the molecular level regarding the transport characteristics of these solvents through CD-based nanofilms.

The investigation of membrane transport properties can be effectively studied through either Equilibrium Molecular Dynamics (EMD) or Non-Equilibrium Molecular Dynamics (NEMD)

simulations. EMD does not introduce biasing force and derives transport properties from mean square displacements or correlation function integrals based on linear response theory [45]. It has been used to examine the transport behavior of water molecules and ions through carbon nanotubes [46–48]. In contrast, NEMD applies non-equilibrium conditions, such as pressure [49, 50] or concentration differences [51, 52], to directly observe transport phenomena at the Angstrom scale. NEMD has revealed the promise of zeolitic metal-organic frameworks (MOFs) [53] for water desalination and has also been used to investigate gas permeation through the membranes [54, 55]. EMD has been used to study the pore structures[56], revealing hydration of ions as key in rejection [57], while simulations of complex atomic structures of membranes allow the analysis of additional factors like membrane structure and interactions. The MD studies have advanced the understanding of structurally simple inorganic membranes, such as carbon nanotube membranes [46, 47, 51, 57–60]; investigating polymeric membranes remains challenging due to their complex structures. Additionally, EMD was employed to assess the diffusion of monovalent and divalent salts [52]. Notably, MD simulations have yet to be used to explore the transport of organic molecules in the CD-based membranes.

Solvent transport through membranes is typically explained by the non-equilibrium thermodynamics [61, 62], pore-flow (PF)[63, 64], or solution-diffusion models [65–68]. Meng Shen et al.[69] studied the transport of water through reverse osmosis membranes via molecular dynamics. Their results indicate that water permeance increases with the increase in connected free volume. The average pore size significantly contributes to overall water permeance [70–76]. Recent studies suggest that water molecules form chains as they traverse through the interconnected pores within the polyamide membrane, with continuous water percolation [56, 77, 78]. Li Wang et al. [49] recently proposed a mechanism for water transport through RO membranes at high pressures, asserting that water transport is entirely governed by the pore-flow model rather than the solution-diffusion mechanism. Hanqing Fan et al. [79] reported that solvent molecules migrate as clusters through interconnected pathways within the membrane pores, and permeance depends on the solvent affinity with the membrane, influencing the pore structure. Jinlong He et al. [80] reported organic solvent transport in dense polymer membranes, finding that solvent transport under a pressure gradient depends on the membrane free volume or pore size and the solvent size, supporting the PF mechanism. Pedro et al. [81] proposed a transport mechanism for solvents such as methanol, toluene, ethyl acetate, and their mixtures through nanofiltration membranes in cross-flow. Their findings indicate that the solution-diffusion and

pore-flow models can predict solvent permeation, but the solution-diffusion model provides more accurate results. The membrane–solvent interaction plays a crucial role in solvent transport, although the study could not explain the flux difference between toluene and ethyl acetate. However, the permeation mechanism has not been explored in detail in cyclodextrin-based polyester membranes, which is the main objective of the present work.

In this work, we analyzed the transport of polar and non-polar solvents through CD−based nanofilms via molecular dynamics (MD) simulations. Our analysis primarily centers on elucidating the structural properties of these membranes and the role of functional groups in solvent transport.

4.2 Methodology

4.2.1 Membrane Model

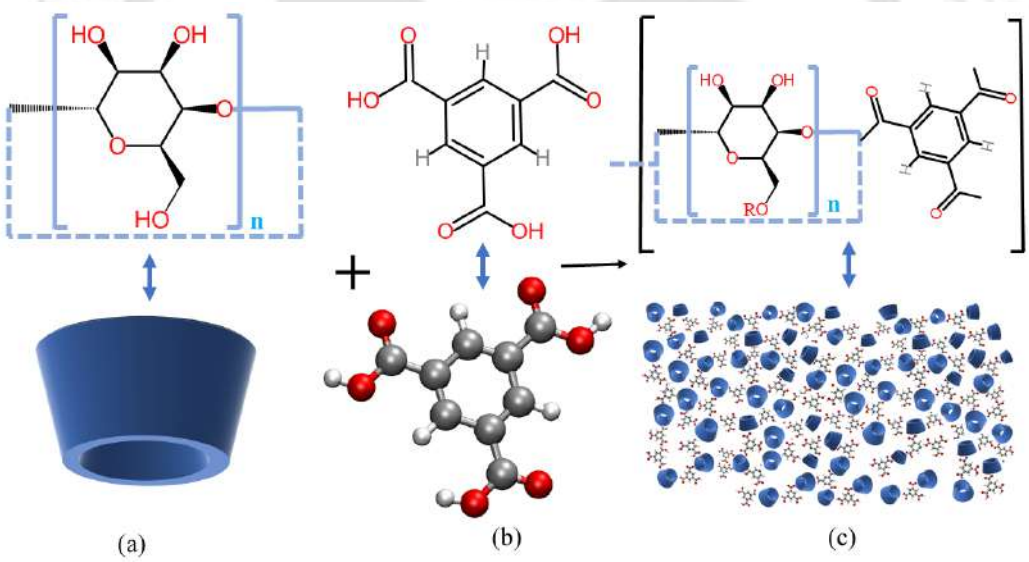

Figure 4.1: Chemical structure of the monomers and ester linkage (a) Cyclodextrin (n = 6 for α-CD, n = 7 for β-CD, and n = 8 for γ-CD) (b) Hydrolyzed trimesoyl chloride (TMC) (c) Ester linkage. Top panel depicts the schematic representation of 2D structures and bottom panel represents the 3D structures. The CHARMM36-compatible force field parameters were obtained from the CGenFF server.

By mimicking the interfacial polymerization via a heuristic approach, we build an atomistic

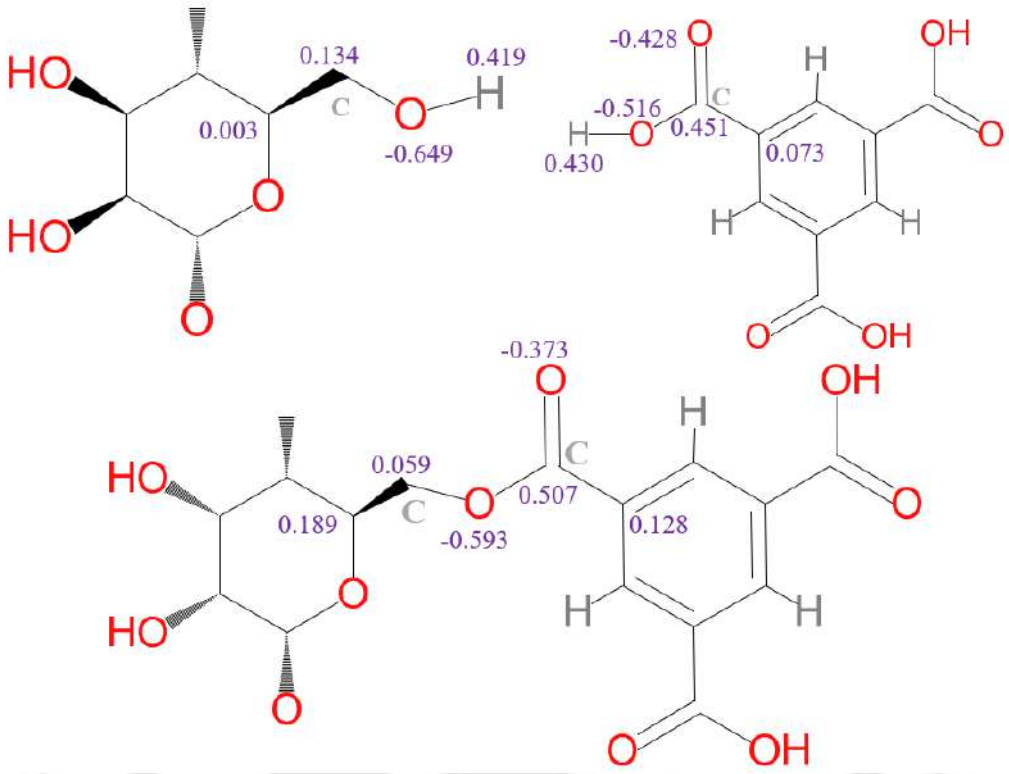

Figure 4.2: The partial charges of atoms involved in ester linkage and neighboring atoms are shown here, where, for simplicity, one glucose unit in cyclodextrin (top panel left side schematic structure) and hydrolyzed trimesoyl chloride (top panel right side schematic structure) are represented. The bottom panel depicts the partial charges of ester linkage atoms and their neighboring atoms.

model for the crosslinked polyester membrane. In this study, the crosslink process involves the formation of ester bonds between cyclodextrin (CD) and hydrolyzed trimesoyl chloride (TMC) in a vacuum based on distance criteria. The monomers used in this study to create a polyester are shown in Figure 4.1. All MD simulations were performed using NAMD [82]. CGenFF version 2.5 [83] is used to obtain the CHARMM36 [84] compatible force field parameters for monomers and ester linkage. Initially, CD ($\alpha/\beta/\gamma$) and TMC molecules were randomly packed in a simulation box of dimensions 100 $\times$ 100 $\times$ 50 $\mathring{A}^3$ using PACKMOL [85], maintaining a 1:2 ratio. The monomeric mixture is then energy minimized and equilibrated in an NPT ensemble (constant temperature and pressure) at 300 K and 1 atm. The equilibrated mixture was annealed in an NVT ensemble, gradually increasing the temperature of the system to 1100 K and cooling it back to 300 K with a step of 50 K. This annealed monomeric mixture was then

used in polymerization runs to create a polyester membrane. The crosslinking process consisted of 2000 steps, each lasting 10 ps with a time step of 1 fs. During polymerization, ester linkages were formed between the monomers based on a cutoff distance. When the distance between the carbon atoms of the −COOH group in the TMC monomer and the oxygen atoms of the hydroxyl (−OH) groups on the narrow rim of the cyclodextrin molecule was less than 3.5 $\mathring{A}$, an ester linkage was formed. This involved removing a hydrogen atom from the hydroxyl group of the CD monomer and the −OH group from the carboxylic group of the TMC monomer. The simulation continued to search for new ester linkages for every 10 ps of simulation time. The partial charges of the atoms involved in the ester linkage and its neighboring atoms were adjusted accordingly. Figure 4.2 illustrates the schematic structures of the monomers and the ester linkage, with the partial charges depicted near the atoms. It should be noted that Figure 4.2 only represents the partial charges of a few atoms, while every atom in the simulation possesses its unique partial charge. Energy minimization and equilibration were performed after each crosslinking step. As the simulation progressed, the crosslinked clusters grew, which hindered monomer diffusion and slowed down the crosslinking process. The cutoff distance was increased to 4.5 $\mathring{A}$ to accelerate the crosslinking process. After the polymerization process, unreacted monomers (which did not form ester linkages) were removed, and the resulting membrane was further utilized in this study.

4.2.2 Equlibrium Molecular Dynamics Simulations (EMD)

The EMD procedure involved immersing previously polymerized dry membranes separately into reservoirs of equilibrated water and hexane solvent, as depicted in Figure 4.3(a, b). The water molecules used in our simulations were modeled using the TIP3P water model [86], and the CHARMM36-compatible force field parameters for hexane molecules were obtained from the CGenFF server. These simulation systems were then subjected to an NPT ensemble at a constant temperature of 300 K and a pressure of 1 atm for 50 ns. The van der Waals forces were computed using the Lennard−Jones potential to model the interactions between atoms with a cutoff distance of 12 $\mathring{A}$ and a switching distance of 10 $\mathring{A}$. The Particle Mesh Ewald (PME) method is used to compute electrostatic interactions with a grid spacing of 1 $\mathring{A}$[87]. The pressure and temperatures were controlled by a modified Nose−Hoover method [88] coupled with Langevin dynamics, with a damping factor of 5 ps^{-1} [89]. The equations of

motion were integrated using the velocity Verlet algorithm [90], with a time step of 1 fs and trajectories saved at intervals of every 20 ps. Periodic boundary conditions (PBC) were applied along the X, Y, and Z dimensions. It is important to note that the results presented in this manuscript are based on the average outcomes obtained from three independent simulations, and trajectory analysis was carried out for the last 30 ns simulations.

4.3 Results and Discussion

4.3.1 Membrane Solvation and Structure

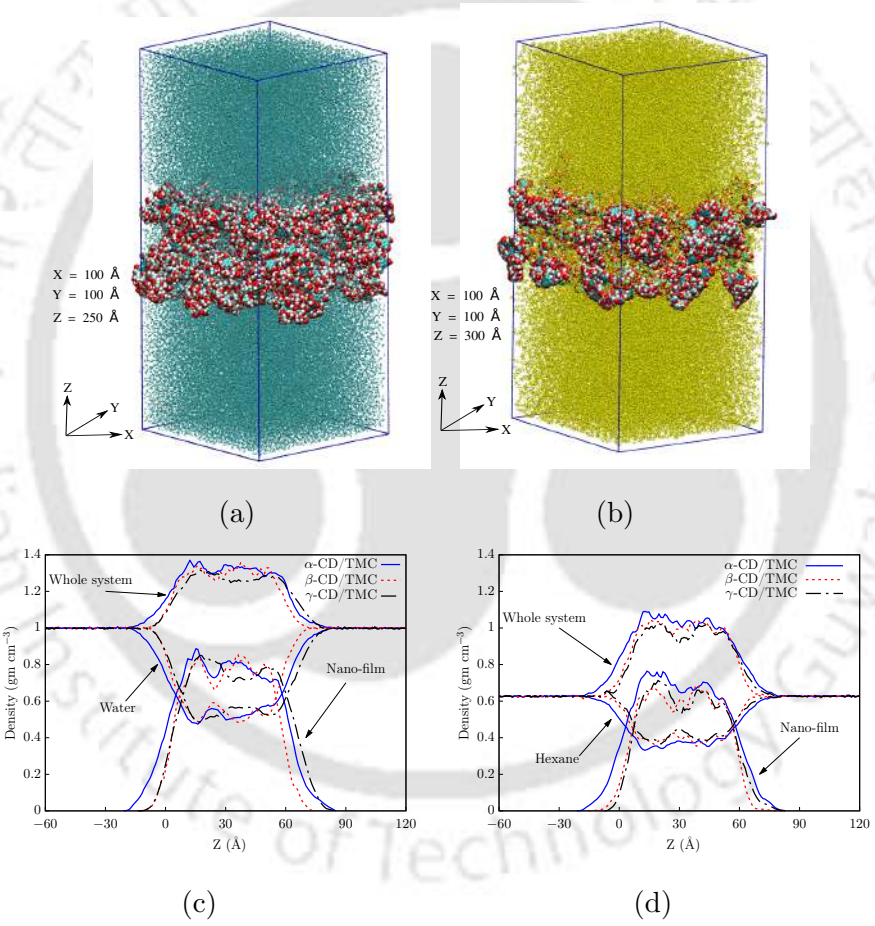

Figure 4.3: (a) Membrane submerged in water reservoir (b) Membrane submerged in hexane reservoir (c) Density profile dipicting the water and membrane atoms distribution along the z-axis in the simulated system (d) Density profile dipicting the hexane and membrane atoms distribution along the z-axis in the simulated system

Figure 4.3(a, b) shows the equilibrated membrane system within water and hexane reser-

voirs, respectively. We computed the water and hexane content along the membrane normal to analyze the membrane structure and interactions with membrane atoms. As shown in Figure B.1(a, b), the water and hexane content of the membrane varies depending on the interfacial region and the interior part of the membrane. An increase in water and hexane content was observed at the interfacial regions along the membrane/reservoir interfaces, which suggests favorable interactions between the membrane and solvents. The water uptake in the α, β, and γ-CD/TMC membranes are found to be 52.8, 52.9, and 53.8 wt%, respectively. Similarly, the hexane uptake for these membranes is measured at 58.5, 62, and 64.4 wt% for α, β, and γ-CD/TMC, respectively (we consider the region of 15 $\mathring{A}$ < z < 50 $\mathring{A}$ for computing solvent uptake in the membrane).

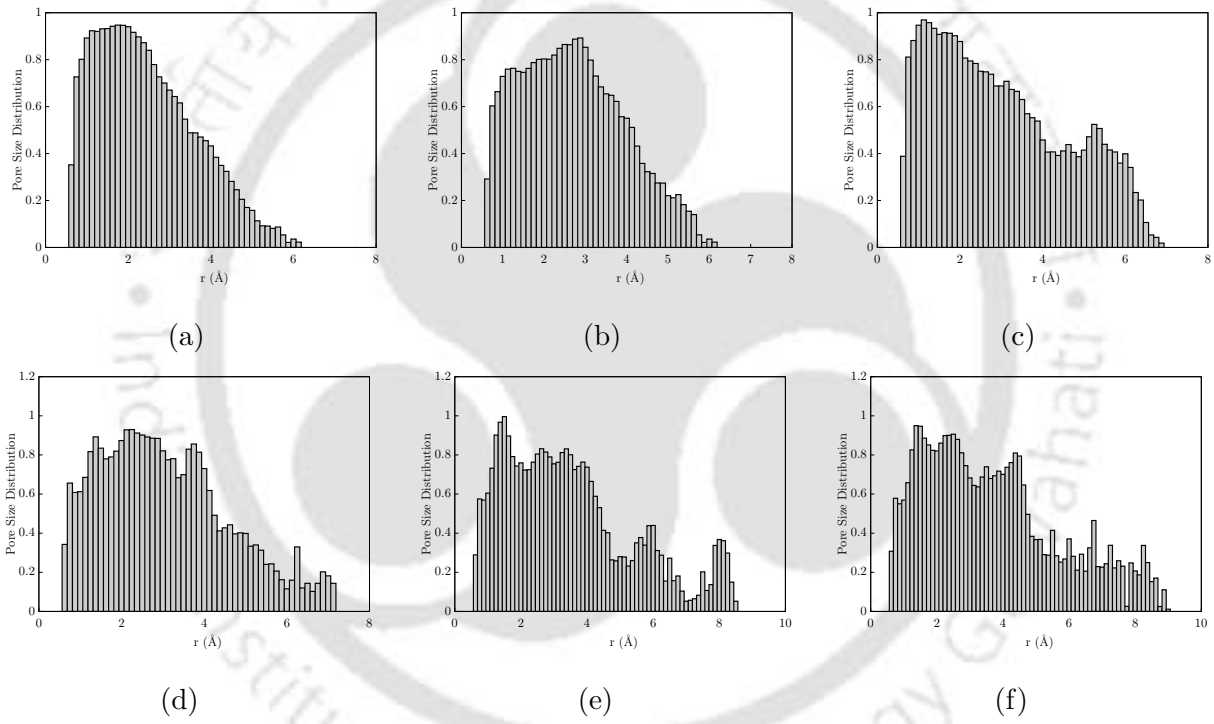

Figure 4.4: The pore size distribution of the fully hydrated membranes in water (a) α-CD/TMC (b) β-CD/TMC (c) γ-CD/TMC; The pore size distribution of the fully equlibrated membranes in hexane solvent (d) α-CD/TMC (e) β-CD/TMC (f) γ-CD/TMC

We proceeded to partition the simulation system along the z−direction, segmenting it into uniformly spaced slabs of 2 $\mathring{A}$ thickness. For each slab, we counted the number of atoms (i.e., membrane/water/hexane) and divided them by the slab volume to get the density for each slab. Figure 4.3c presents the density profile of water within the membrane, the distribution of atoms in the membrane, and the overall simulation system. The density profiles for the

hexane simulation system are shown in Figure 4.3d. Variations in water and hexane transport (or uptake) across (or in) these membranes are likely attributed to differences in their pore structures, which can be elucidated in terms of the accessible space. We used the Monte Carlo technique[91] to compute the pore size distribution (PSD). The last 10 ns of the production run have been used to compute the PSD reported in the present work with the probe of 1 $\mathring{A}$ radius. For water hydrated α-CD/TMC membrane, the pore radii range from 0.5 - 6 $\mathring{A}$ with the prominent pores ranging from 1.5 - 4 $\mathring{A}$ (Figure 4.4a), and for β-CD/TMC membrane, more prominent pores observed at 2 - 5 $\mathring{A}$ radius (Figure 4.4b). On the other hand, for γ-CD/TMC membrane, more prominent pore radii range from 2 - 6 $\mathring{A}$ (Figure 4.4c). The hexane−solvated membranes PSDs are shown in Figure 4.4 (d-f). Notably, the distribution of the pores in the hexane−solvated membranes enhanced compared to water−hydrated membranes. For hexane solvated α-CD/TMC membrane, the prominent pore radii range from 2 - 6 $\mathring{A}$ (Figure 4.4d), and for β/γ-CD/TMC membranes, prominent pore radii range from 2 - 8 $\mathring{A}$ (Figure 4.4(e, f). Figure B.2(a-f) shows the 3D morphology of the solvated membranes computed via Material Studio Connolly surface visualization module [92] using water molecule as a probe. Blue indicates the accessible free volume for water, and gray indicates the volume occupied by the membrane atoms. It is worth noting that non−interconnected pores may have the capacity to hold, but they do not contribute to the solvent transport. Effective transport occurs exclusively through interconnected free volumes within the membrane structure [52, 93].

4.3.2 Water Structure

The pair correlation function, or radial distribution function (RDF), was computed between the oxygen atoms of water molecules present inside cyclodextrin(CD)−based membranes. The RDF between oxygen atoms (OW) of water in the bulk water and the hydrated membranes is presented in Figure B.3a. Notably, the location of the first peak in RDF appears at 2.75 $\mathring{A}$ for bulk and water in the membrane, with a slight difference in the peak intensity. To quantify the coordination number of water molecules (N_c), we integrated the RDF (between the oxygen atoms of water molecules (OW)), as shown in Figure B.3b. Inside the membrane for α-CD/TMC, β-CD/TMC, and γ-CD/TMC, the coordination number of water molecules decreases to 3.3, 3.4, and 3.5, respectively, compared to 4.4 in the bulk water (Figure B.3b). This decrease in coordination numbers suggests a reduction in the number of hydrogen bonds

(HB) for each water molecule (see Figure B.3c). It is assumed that donor (D) and acceptor (A) atoms can form hydrogen bonds, with donor−acceptor (D−A) cutoff distance of 3 $\AA$ and a D−H−A cutoff angle of 20°. [52, 94, 95]. Figure B.3c displays the average number of hydrogen bonds between water molecules along the membrane normal, which indicates a decrease in hydrogen bonds inside the membrane. Furthermore, the RDF (see Figure B.3d) between the hydrogen and oxygen atoms of water molecules in bulk water and inside the membrane was computed. The first minima in the RDF at r = 2.45 $\AA$ signifies the hydrogen bond formation with adjacent water molecules [52, 96]. As a result of the excluded volume effect, the peak intensity within the membrane is slightly higher than the bulk water [52, 96]. We observed 0.9 oxygen atoms (OW) around the hydrogen atoms (HW) of water molecules and 1.9 HW around the OW of water molecules in the bulk water. So, each water molecule forms approximately 3.8 hydrogen bonds (HB) in bulk water. Similarly, 0.8 OW around HW and 1.7 HW around OW were observed, resulting in 3.4 HB for each water molecule within the membrane. Moreover, water molecules can form hydrogen bonds with functional group atoms of the membrane and each water molecule forms 0.5 HB with the membrane. As a result, with $\alpha/\beta/\gamma$-CD/TMC, each water molecule forms approximately 3.9 HB inside the membrane.

4.3.3 Pathways and Permeation Mechanism

The solvent flux is calculated based on the number of solvent molecules that permeate the membrane in a simulated time. As it is an equilibrium molecular dynamics (EMD) simulation, no external pressure is applied, and the permeance is purely based on the thermal motion of solvent molecules through the membrane. Since there is no pressure gradient in EMD simulations, solvent molecules can permeate in both directions (+z or -z) at an equal rate. Based on this number of molecules, the solvent flux is calculated as V/(2.A.t), where V is the volume of the solvent permeated through the membrane area (A) in a simulated time (t). It is observed that permeance depends on the nature of the macrocyclic cavity, and the $\alpha/\beta/\gamma$-CD/TMC membranes exhibit varying flux characteristics. The calculated water fluxes for $\alpha/\beta/\gamma$-CD/TMC membranes based on the number of permeated water molecules are 14.79 $\times 10^4$, 20.97 $\times 10^4$, and 33.06 $\times 10^4$ $Lm^{-2}h^{-1}$, respectively (Figure B.4a). Similarly, the hexane fluxes for these membranes, calculated based on the number of permeated hexane molecules, are 1.42 $\times 10^4$, 2.11 $\times 10^4$, and 2.91 $\times 10^4$ $Lm^{-2}h^{-1}$, respectively (Figure B.4b). Thus, an

order of magnitude higher flux for water was observed.

Various research groups have examined the performance of CD−based membranes, showcasing high permeances for both polar and non−polar solvents [19, 21, 97]. Liu et al. [21] developed polyester (PE) membranes with a distinctive pore size distribution by using three distinct cyclodextrins ($\alpha/\beta/\gamma$-CDs). Their unique composition, featuring hydrophobic inner cavities and hydrophilic channels, sets the CD/TMC nanofiltration (NF) membranes apart from the commercial polyamide membranes. This distinctive structure empowers these membranes with exceptionally high permeability, allowing for the efficient passage of polar and non−polar solvents [19, 97]. Additionally, functionalized CD-based membranes also showed high liquid permeance [1, 98], however hexane permeance is much lower [1]. These studies suggest that there are certain discrepancies in liquid transport through CD−based membranes, necessitating a deeper understanding of the functional significance of the CD-cavity in transporting polar and non-polar solvents.

To understand the transport mechanisms within these CD−based membranes, we meticulously analyze the trajectories of individual water and hexane molecules, tracking their pathways as they traverse the membrane. In Figure 4.5(a-c), we present the trajectories of 20 selected water molecules for each type of CD−based membrane. In each membrane, we track the pathways of water molecules from the top reservoir to the bottom reservoir. Figure 4.5a portrays the pathways of water molecules in α-CD/TMC membrane. As the water molecules traverse the membrane, they interact with nearby molecules and the membrane atoms, resulting in their seemingly random movement. These trajectories are also visualized in the 2D XZ plane (Figure 4.5d) and the 2D YZ plane (Figure B.5) as line segments. We observe that these water molecules traverse from the top and bottom water reservoirs through the membrane; they initially follow a random motion and approach the interfacial region of the membrane multiple times before finally reaching the bulk portion of the membrane. Once within the bulk region, they travel relatively quickly through certain membrane parts while appearing momentarily confined in other regions, likely corresponding to voids or pores within the membrane structure. Consider the blue line segment in Figure 4.5g, where a water molecule follows a random path, interacting with neighboring water molecules and membrane atoms. However, its movement is slightly restricted by the membrane atoms in the interfacial region. Later, it enters the bulk section of the membrane. Subsequently, the molecule hops into another pore by rapidly returning to its starting place in the bulk membrane. This pore appears to be 10 $\mathring{A}$ long (40 $\mathring{A}$ < z < 50 $\mathring{A}$).

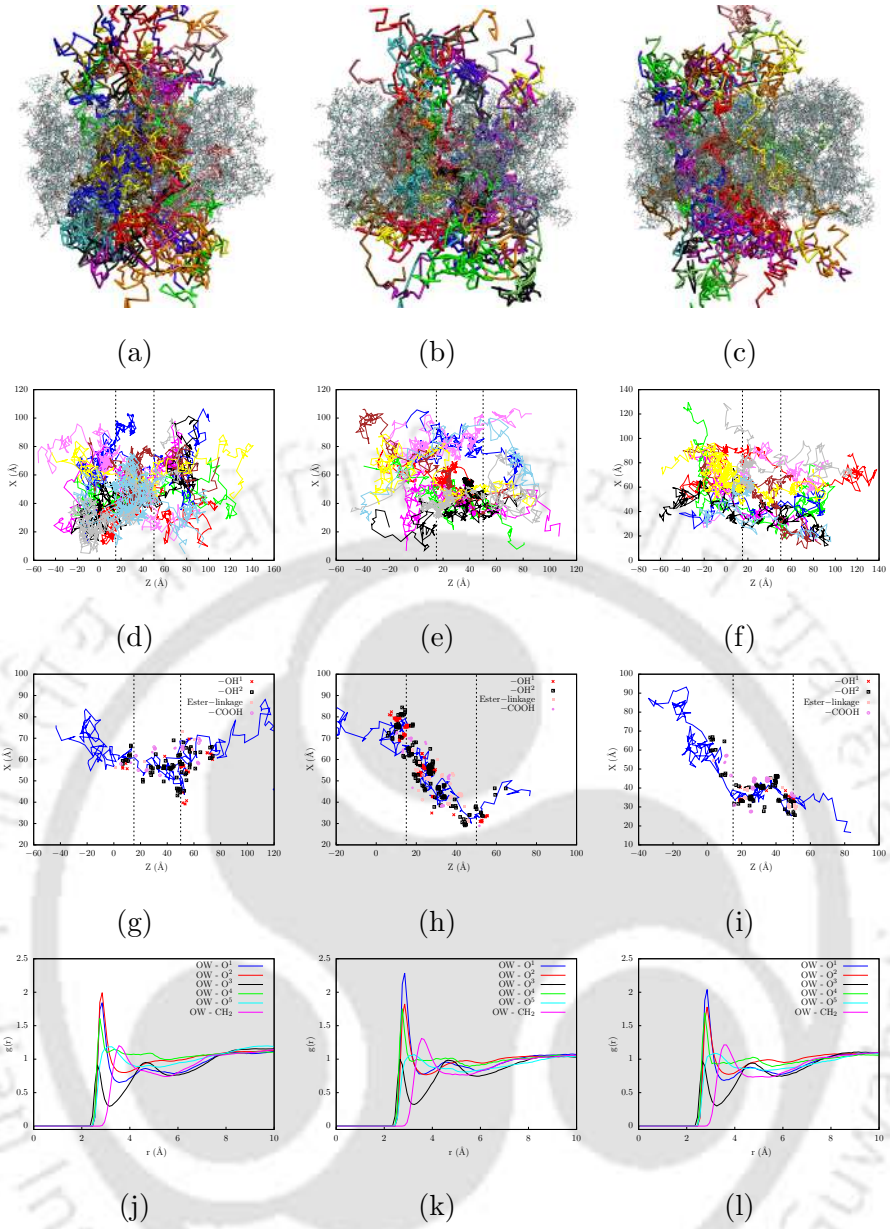

Figure 4.5: Pathways of selected water molecules through the CD-based membrane in (a) α-CD/TMC (b) β-CD/TMC (c) γ-CD/TMC; Trajectories of ten water molecules perameating through CD−based membrane in 2D XZ plane (d) α-CD/TMC (e) β-CD/TMC (f) γ-CD/TMC; Trajectory of single water molecule permeating through the CD−based membrane in 2D XZ plane and the functional groups present within 5 $\AA$ along the trajectory, where -OH^1 represents primary hydroxyl group, and -OH^2 represents the secondary hydroxyl groups (g) α-CD/TMC (h) β-CD/TMC (i) γ-CD/TMC; RDF between water oxygen atoms(OW) and the membrane functional group atoms, where O^1 is primary hydroxyl group oxygen atom, O^2 represents secondary hydroxyl group oxygen atoms, O^3 represents the ester−linkage atom between CD and TMC, O^4 represents the hydroxyl group oxygen atoms of TMC monomers, O^5 represents the −C=O of −COOH in TMC monomer, and $-CH_2$ refers to the carbon atoms adjacent to the primary hydroxyl groups (j) α-CD/TMC (k) β-CD/TMC (l) γ-CD/TMC

The water molecule finally passes through this pore and enters the interfacial region (shown at z = 15 $\AA$ in Figure 4.5g) before exiting the membrane towards the membrane other side. It is observed that most water molecules follow similar pathways from one side to the other

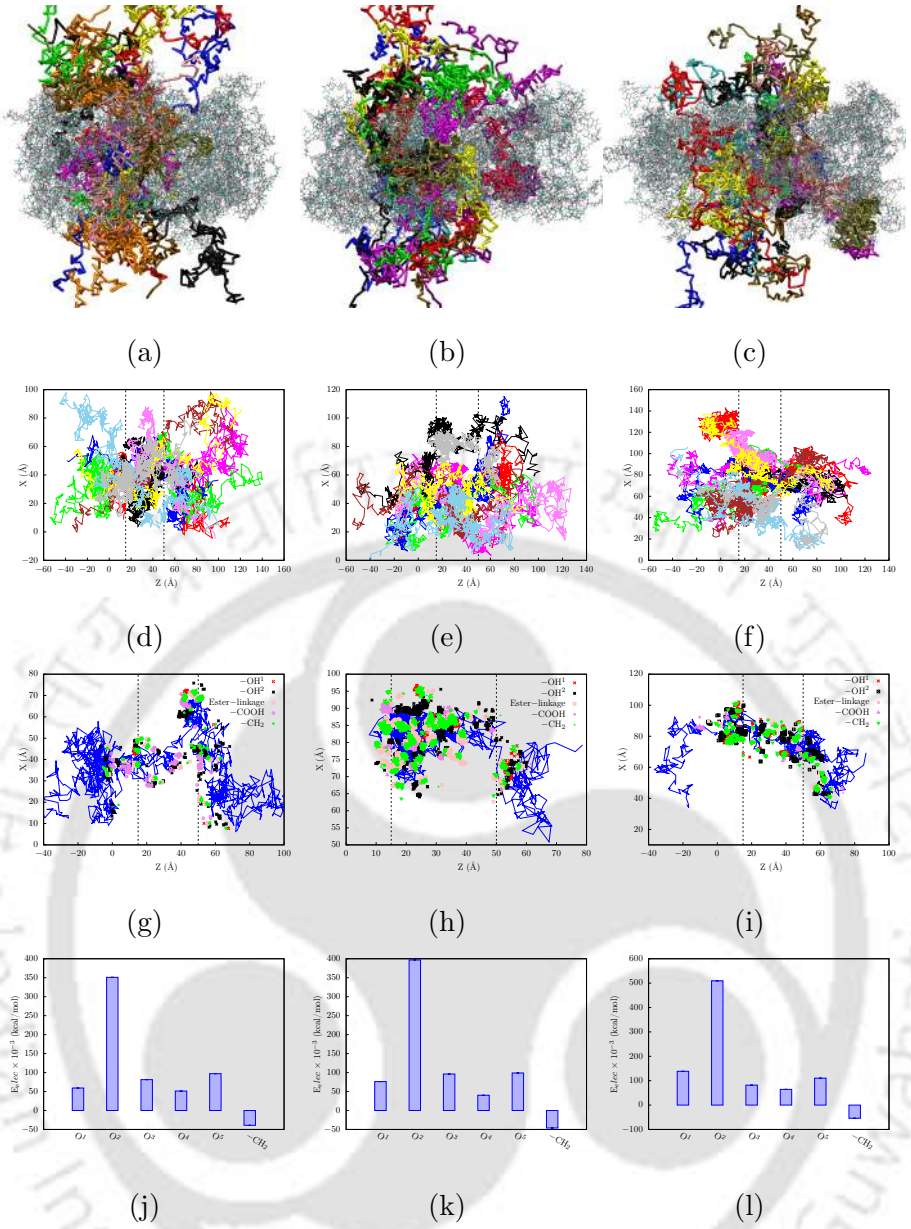

Figure 4.6: Pathways of selected hexane molecules through the CD-based membrane in (a) α-CD/TMC (b) β-CD/TMC (c) γ-CD/TMC; Trajectories of ten hexane molecules perameating through CD−based membrane in 2D XZ plane (d) α-CD/TMC (e) β-CD/TMC (f) γ-CD/TMC; Trajectory of single hexane molecule perameating through CD−based membrane in 2D XZ plane and the functional groups present within 5 $\AA$ along the trajectory, where -OH^1 represents primary hydroxyl group, -OH^2 represents the secondary hydroxyl groups, and $-CH_2$ refers to the carbon atom adjacent to the primary hydroxyl group (g) α-CD/TMC (h) β-CD/TMC (i) γ-CD/TMC; Ineraction energies between carbon atoms in hexane molecules and membrane fucntional group atoms, here functional group atoms identities are same as Figure 4.5 (j) α-CD/TMC (k) β-CD/TMC (l) γ-CD/TMC

(Movie1). As the water molecules permeate the membrane, it is observed that they are permeating through the aggregate pores while interacting with functional groups that assist water transport. Figure 4.5g shows that the majority of the permeated water molecules are favored by the hydroxyl and ester−linkage in the membrane. This observation is evident from the

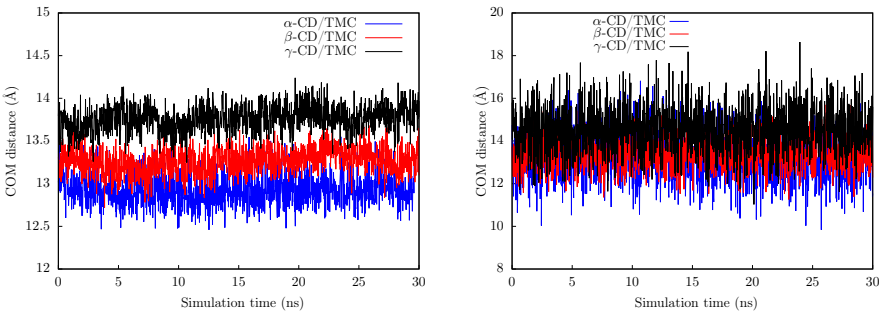

(a) (b)

Figure 4.7: The variation of the distance between the mass centers of (a) Water and CD cavity (b) Hexane and CD cavity

RDF profiles. The RDF shown in Figure 4.5j informs that water is predominantly transported through aggregated pores. Figure 4.5e and B.5b display the 2D trajectories of selected water molecules in the β-CD/TMC membrane. Consider the black color line segment at z = 35 $\AA$ to z = 45 $\AA$ in Figure 4.5e; the water molecule remains trapped in the membrane until random fluctuations drive it to a path where it quickly moves to an enlarged pore deeper into the membrane (Movie2). Figure 4.5f and B.5c display the 2D trajectories of selected water molecules in the γ-CD/TMC membrane. It is observed that γ-CD/TMC exhibit similar transport phenomena for water as α/β-CD/TMC membrane (Movie3). Figure 4.5(h, i) represents the functional groups along the selected water molecule trajectory for β/γ-CD/TMC membranes (see Figure B.5(e, f) for 2D YZ plane trajectory). The RDF in Figure 4.5(k, l) exhibits similar behavior as shown in α-CD/TMC membrane. Additionally, in the β/γ membranes, there were instances of pore spanning across the membrane have been observed (see Figure B.6). Overall, in $\alpha/\beta/\gamma$-CD/TMC membrane, transport of the majority of water molecules is facilitated by hydroxyl and ester−linkage groups.

The trajectories of hexane molecules within each CD−based membrane exhibit distinct behavior compared to water molecules. In Figure 4.6a, we can observe the path hexane molecules take as they traverse the α-CD/TMC membrane. It is observed that hexane molecules navigate through considerably narrower channels compared to water. This is primarily due to hexane molecules being larger than water molecules. Consequently, their random movement within the pores is more constrained owing to their larger size and the resulting steric effects. Furthermore, their movement through the pores is restricted to a greater extent. It is observed that both the random motions of hexane molecules and the membrane dynamic structure play

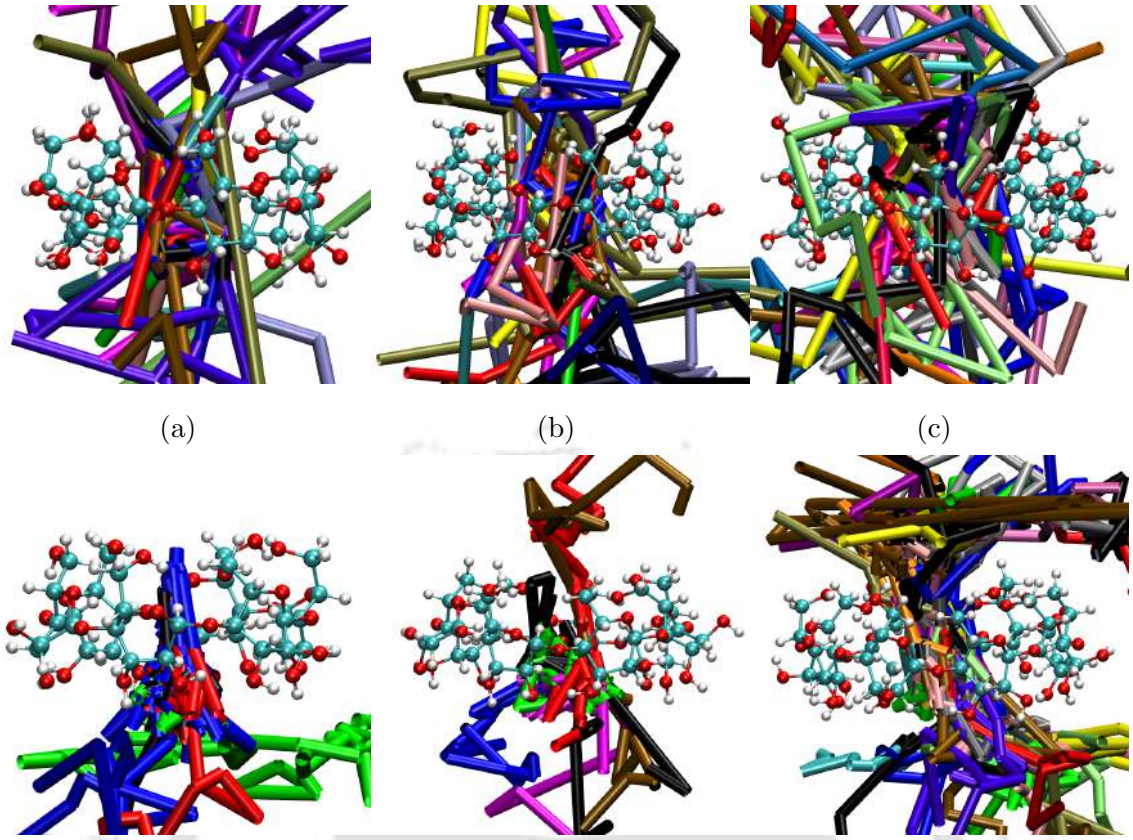

(a) (b) (c)

(d) (e) (f)

Figure 4.8: Pathways of water molecules through the CD cavity (a) α-CD (b) β-CD (c) γ-CD; Pathways of hexane molecules through the CD cavity (d) α-CD (e) β-CD (f) γ-CD

a role in transporting hexane through the membrane. This is prominent in a video depicting the hexane trajectory over a 30 ns duration (refer to Movie4). The 2D trajectories of selected hexane molecules along the XZ plane are shown in Figure 4.6d, and the YZ plane is represented in Figure B.7a. Notably, the hexane molecule (represented by the line segment) initially enters the bulk region of the membrane at z = 50 $\mathring{A}$. Eventually, it reaches the opposite side of the membrane at z = 15 $\mathring{A}$. It is observed that hexane molecules spend more time within the bulk membrane than water molecules. The thicker trajectories depicted in Figure 4.6(a, d) clearly illustrate that hexane molecules exhibit a significantly longer residence time within the bulk membrane than water molecules. The quantification of functional groups facilitating hexane transport is observed through 2D trajectory analysis and interaction energies with the membrane functional groups. Figure 4.6g and B.7d depict the positions of functional groups within a 5 $\mathring{A}$ range along the trajectory. Notably, carbon atoms adjacent to the primary hydroxyl groups on the wider rim of CD exhibit increased interaction with hexane molecules, thereby

aiding their transport through the membrane, as illustrated in Figure 4.6j. The electrostatic interaction profile reveals that hexane experiences repulsions towards hydroxyl and carboxyl groups but displays an electrostatic attraction to carbon atoms adjacent to the primary hydroxyl groups. Furthermore, hexane exclusively traverses ester−linkage aggregate pores and avoids passage through the CD cavity.

Similarly, hexane molecules exhibit analogous behavior in both the β-CD/TMC (Figure 4.6b) and γ-CD/TMC (Figure 4.6c) membranes. The typical motion of hexane molecules in the β-CD/TMC and the γ-CD/TMC membranes can be observed in Movie5 and Movie6, respectively. Additionally, the transport phenomena for water and hexane molecules in CD−based membranes remain consistent in each membrane, owing to the presence of functional groups within the membrane. The primary distinction lies in the spatial distribution of membrane atoms, which creates varying degrees of free volume within the membrane. Figure 4.6 (e, f) and B.7(b, c) represent the 2D trajectories for β/γ-CD/TMC membranes, respectively. Figure 4.6 (h, i) and B.7(e, f) show the membrane functional groups along the trajectory. Figure 4.6(k, l) reports interaction energy profiles. It is observed that the trend for the interaction energy profile is the same for all the membranes. The presence of unreacted functional groups on the narrow rim, along with the neighboring TMC and other CD molecules, hinders hexane entry into the CD cavity. Additionally, these unreacted functional groups on CD molecules are oriented towards the CD cavity, posing an obstacle to hexane molecules. Furthermore, unreacted primary hydroxyl groups on the CD rim and nearby TMC molecules make a more polar environment, impeding hexane permeation through CD-cavity (see Figure B.8).

To discern the transport of water or hexane molecules through the cyclodextrin (CD) cavity, we computed the center of mass (COM) distance between these molecules and the CD cavity. Figure 4.7 shows the average distance between the CD centroid and water/hexane molecules over the simulated time. Values exceeding 6.5 $\mathring{A}$ are categorized as outside the cavity, while those equal to or less than 6.5 $\mathring{A}$ are considered inside the cavity. As illustrated in Figure 4.7a, the COM profile reveals that most water molecules remain above 6.5 $\mathring{A}$, confirming that water transport occurs exclusively through aggregate pores formed by ester−linkage. Notably, the non-uniform distribution of CD molecules in the membrane, with intrinsic cavities not perpendicular to the flow direction, poses challenges for pore permeation. In membrane form, these CD cavities are not easily accessible due to their disordered arrangement. Moreover, Figure 4.7b demonstrates that the COM distance for hexane molecules consistently exceeds 6.5

Å, indicating that most hexane molecules do not traverse through intrinsic cavities but solely through aggregate pores. Additionally, unreacted functional groups (−OH) on the CD rim impede the entry of hexane molecules.

In order to gain insights into the characteristics of the CD cavity, we performed EMD simulations on pure CD molecules, where CD molecules were immersed in water and hexane reservoirs separately. We performed NPT simulations under standard conditions of room temperature and pressure (300 K, 1 atm) for 20 ns. The trajectories of water molecules through the CD cavity are illustrated in Figure 4.8. Figure 4.8a depicts the pathways of water molecules passing through α-CD, while Figure 4.8b and 4.8c showcase the trajectories followed by water molecules within β-CD and γ-CD, respectively. Our observations reveal that water molecules traverse each CD pore by establishing hydrogen bonds (Figure B.9). These water molecules confined within the supramolecular cavity are often referred to as activated or high-energy waters [99–102]. The number of hydrogen bonds these cavity-bound water molecules form is a crucial parameter characterizing their energy frustration level [44]. For instance, a TIP3P water molecule confined within the cavities of α-CD, β-CD, and γ-CD forms only 2.3, 3.4, and 3.9 hydrogen bonds, respectively. The ability to engage in hydrogen bonding within the CD cavity is believed to be a significant driving factor enabling water molecules to exit the cavity more readily [44]. We observed the maximum water occupancy inside the cavity to be 5 in α-CD, 9 in β-CD, and 14 in γ-CD. The precise positions of these water molecules are shown in Figure B.9. In addition, we observed the maximum hexane occupancy inside the cavity to be 1 in α-CD (see Figure B.10(a, b)) and 2 in β/γ-CD (see Figure B.10(c-f)). Figure 4.8d shows that the hexane molecule is confined in the α-CD pore, but it is passing through the β-CD (see Figure 4.8e) and γ-CD pore (see Figure 4.8f). Figure 4.8 highlights a vital observation as both water (in $\alpha/\beta/\gamma$-CD) and hexane molecules (in β/γ-CD) can pass through the hydrophobic cyclodextrin inner cavity. Furthermore, our observations highlight the simultaneous exclusion and inclusion of molecules throughout the simulations. From the transport behavior of water and hexane through cyclodextrin (CD)-based membranes and pure CD molecules, we observed that the preferred pathways for transporting both solvents in the membrane form primarily involve hydrophilic pores formed by ester−linkages rather than the CD pores. Without a linker, the CD cavity allows for the passage of both polar and non-polar solvents. Additionally, for pure CD cavity, the primary hydroxyl groups remain away from the rim, which allows hexane to go through it. This observation suggests that forming Janus membranes, which accommodate

distinct transport pathways for polar and non-polar solvents, presents significant challenges, and CD cavities can facilitate solvent transport through it when they are perfectly aligned to liquid flow without polar functional groups on the periphery of the narrow rim. Nevertheless, the potential for designing ideal membranes remains open, primarily through meticulous and controlled interfacial polymerization of cyclodextrin membranes on porous supports. Experimentalists may explore this avenue to engineer membranes that meet specific design criteria and exhibit enhanced performance characteristics.

4.4 Conclusions

With a realistic atomistic model for a cross−linked cyclodextrin(CD)−based polyester membranes, we investigated the membrane structure and transport of water and hexane in the membranes via classical molecular dynamics simulations. Despite a slight difference in the densities of the membranes, pore connectivity under dynamic conditions and the resulting tortuous pathways for the transport of water and hexane molecules varied amongst membranes. The water and hexane uptake of the membrane directly depends on the free volume within the membrane. It is observed that the membrane water uptake for CD−based membrane is $\approx$ 53 wt%, and hexane uptake is $\approx$ 63 wt%. Water and hexane pathways imply that solvent transport through the membrane is relatively fast in some places and appears to be trapped in others, waiting to hop into the next pore until they find pathways that open as a result of membrane dynamics. Furthermore, the EMD simulations have revealed that the interconnected hydrophilic cavities formed through ester linkages are more favorable channels for transporting polar and non−polar solvents through the membranes. We also performed EMD simulations on pure CD macrocyclic molecules in water and hexane solvents. It is observed that uncross−linked cyclodextrin molecules facilitate the transport of both solvents, and water molecules permeate the CD−pore via hydrogen bonds among the water molecules. In our simulations, we observed that the hexane solvent flux is an order of magnitude lower compared to the water permeance. Our findings conclude that both solvents primarily traverse through the polar aggregate pores in the cross−linked membranes rather than the CD cavity, indicating a lack of functional significance of macrocyclic molecules in solvent transport and the existence of Janus pathways. We hope that the atomic−level insights from the present study will inspire further experimental investigations on CD−based membranes.

Bibliography

[1] Zhiwei Jiang, Ruijiao Dong, Austin M Evans, Niklas Biere, Mahmood A Ebrahim, Siyao Li, Dario Anselmetti, William R Dichtel, and Andrew G Livingston. Aligned macrocycle pores in ultrathin films for accurate molecular sieving. *Nature*, 609(7925):58–64, 2022.

[2] Siyao Li, Ruijiao Dong, Valentina-Elena Musteata, Jihoon Kim, Neel D Rangnekar, JR Johnson, Bennett D Marshall, Stefan Chisca, Jia Xu, Scott Hoy, et al. Hydrophobic polyamide nanofilms provide rapid transport for crude oil separation. *Science*, 377(6614):1555–1561, 2022.

[3] Bratin Sengupta, Qiaobei Dong, Rajan Khadka, Dinesh Kumar Behera, Ruizhe Yang, Jun Liu, Ji Jiang, Pawel Keblinski, Georges Belfort, and Miao Yu. Carbon-doped metal oxide interfacial nanofilms for ultrafast and precise separation of molecules. *Science*, 381(6662):1098–1104, 2023.

[4] Zhe Tan, Shengfu Chen, Xinsheng Peng, Lin Zhang, and Congjie Gao. Polyamide membranes with nanoscale turing structures for water purification. *Science*, 360(6388):518–521, 2018.

[5] Huawen Peng, Wen-Hai Zhang, Wei-Song Hung, Naixin Wang, Jian Sun, Kueir-Rarn Lee, Quan-Fu An, Cheng-Mei Liu, and Qiang Zhao. Phosphonium modification leads to ultrapermeable antibacterial polyamide composite membranes with unreduced thickness. *Adv. Mater.*, 32(23):2001383, 2020.

[6] Yang Lu, Ruoyu Wang, Yuzhang Zhu, Zhenyi Wang, Wangxi Fang, Shihong Lin, and Jian Jin. Two-dimensional fractal nanocrystals templating for substantial performance enhancement of polyamide nanofiltration membrane. *Proc. Natl. Acad. Sci.*, 118(37):e2019891118, 2021.

[7] Ruobin Dai, Huimin Zhou, Tianlin Wang, Zhiwei Qiu, Li Long, Shihong Lin, Chuyang Y Tang, and Zhiwei Wang. Nanovehicle-assisted monomer shuttling enables highly permeable and selective nanofiltration membranes for water purification. *Nat. Water*, 1(3):281–290, 2023.

[8] Li Ding, Libo Li, Yanchang Liu, Yi Wu, Zong Lu, Junjie Deng, Yanying Wei, Jurgen Caro, and Haihui Wang. Effective ion sieving with ti3c2t x mxene membranes for production of drinking water from seawater. *Nat. Sustainability*, 3(4):296–302, 2020.

[9] Bingbing Yuan, Shengchao Zhao, Ping Hu, Jiabao Cui, and Q Jason Niu. Asymmetric

polyamide nanofilms with highly ordered nanovoids for water purification. *Nat. Commun*, 11(1):6102, 2020.

[10] Yujian Yao, Pingxia Zhang, Chao Jiang, Ryan M DuChanois, Xuan Zhang, and Menachem Elimelech. High performance polyester reverse osmosis desalination membrane with chlorine resistance. *Nat. Sustainability*, 4(2):138–146, 2021.

[11] Rhea Verbeke, Veronica Gomez, and Ivo FJ Vankelecom. Chlorine-resistance of reverse osmosis (ro) polyamide membranes. *Prog. Polym. Sci*, 72:1–15, 2017.

[12] Kwun Lun Cho, Anita J Hill, Frank Caruso, and Sandra E Kentish. Chlorine resistant glutaraldehyde crosslinked polyelectrolyte multilayer membranes for desalination. *Adv. Mater*, 27(17):2791–2796, 2015.

[13] Shaochong Cao, Aiwen Zhang, Miaomiao Tian, Yuanli Jiang, Guanying Dong, Yatao Zhang, and Junyong Zhu. Fabrication of amino-alcohol based polyesteramide thin film composite membranes for nanofiltration. *Sep. Purif. Technol*, 305:122547, 2023.

[14] Pooria Karami, Md Mizanul Haque Mizan, Carolin Ammann, Amirhossein Taghipour, Joao BP Soares, and Mohtada Sadrzadeh. Novel lignosulfonated polyester membranes with remarkable permeability and antifouling characteristics. *J. Membr. Sci*, 687:122034, 2023.

[15] Liuqing Yang, Ximeng Zhang, Jalal Rahmatinejad, Bahareh Raisi, and Zhibin Ye. Triethanolamine-based zwitterionic polyester thin-film composite nanofiltration membranes with excellent fouling-resistance for efficient dye and antibiotic separation. *J. Membr. Sci*, 670:121355, 2023.

[16] Rui Li, Shaochong Cao, Xiaoquan Feng, Jiayu Don, Xiaoxi Guo, Huixian Wang, and Yatao Zhang. Guanidinium-based loose nanofiltration membranes for dye purification and chlorine resistance. *Sep. Purif. Technol*, 300:121941, 2022.

[17] Pengrui Jin, Junyong Zhu, Shushan Yuan, Gang Zhang, Alexander Volodine, Miaomiao Tian, Jianxiu Wang, Patricia Luis, and Bart Van der Bruggen. Erythritol-based polyester loose nanofiltration membrane with fast water transport for efficient dye/salt separation. *Chem. Eng. J.*, 406:126796, 2021.

[18] Junfeng Zheng, Yanling Liu, Junyong Zhu, Pengrui Jin, Tim Croes, Alexander Volodine, Shushan Yuan, and Bart Van der Bruggen. Sugar-based membranes for nanofiltration. *J. Membr. Sci*, 619:118786, 2021.

[19] Luis Francisco Villalobos, Tiefan Huang, and Klaus-Viktor Peinemann. Cyclodex-

trin films with fast solvent transport and shape-selective permeability. *Adv. Mater.*, 29(26):1606641, 2017.

[20] Jing Xue, Zhiwei Jiao, Ran Bi, Runnan Zhang, Xinda You, Fei Wang, Linjie Zhou, Yanlei Su, and Zhongyi Jiang. Chlorine-resistant polyester thin film composite nanofiltration membranes prepared with β-cyclodextrin. *J. Membr. Sci.*, 584:282–289, 2019.

[21] Jiangtao Liu, Dan Hua, Yu Zhang, Susilo Japip, and Tai-Shung Chung. Precise molecular sieving architectures with janus pathways for both polar and nonpolar molecules. *Adv. Mater.*, 30(11):1705933, 2018.

[22] Maria F Jimenez-Solomon, Qilei Song, Kim E Jelfs, Marta Munoz-Ibanez, and Andrew G Livingston. Polymer nanofilms with enhanced microporosity by interfacial polymerization. *Nat. Mater*, 15(7):760–767, 2016.

[23] Shao-Lu Li, Guoliang Chang, Yangzheng Huang, Ken Kinooka, Yanting Chen, Wenming Fu, Genghao Gong, Tomohisa Yoshioka, Neil B McKeown, and Yunxia Hu. 2, 2'-biphenol-based ultrathin microporous nanofilms for highly efficient molecular sieving separation. *Angew. Chem., Int*, 61(46), 2022.

[24] Jincheng Ding, Huiqing Wu, and Peiyi Wu. Development of nanofiltration membranes using mussel-inspired sulfonated dopamine for interfacial polymerization. *J. Membr. Sci*, 598:117658, 2020.

[25] Yujian Yao, Pingxia Zhang, Fei Sun, Wen Zhang, Meng Li, Gang Sha, Long Teng, Xianze Wang, Mingxin Huo, Ryan M DuChanois, et al. More resilient polyester membranes for high-performance reverse osmosis desalination. *Science*, 384(6693):333–338, 2024.

[26] Jiapeng Li, Huawen Peng, Kuankuan Liu, and Qiang Zhao. Polyester nanofiltration membranes for efficient cations separation. *Adv. Mater.*, 36(9):2309406, 2024.

[27] Yulei Li, Mengke Jia, Baoying Shi, Songlin Wang, Xiayu Luan, Zhanhua Hao, and Yufeng Wang. Robust and flexible polyester fiber membrane with under-liquid dual superlyophobicity for efficient on-demand oil-water separation. *Int. J. Biol. Macromol.*, page 130138, 2024.

[28] Xiongwei Luo, Lei Jiang, Rui Zhao, Yue Wang, Xin Xiao, Sabrine Ghazouani, Lihua Yu, Zhaohuan Mai, Hideto Matsuyama, and Pengrui Jin. Energy-efficient trehalose-based polyester nanofiltration membranes for zero-discharge textile wastewater treatment. *J. Hazard. Mater.*, 465:133059, 2024.

[29] Patrizia Marchetti, Maria F Jimenez Solomon, Gyorgy Szekely, and Andrew G Livingston.

Molecular separation with organic solvent nanofiltration: a critical review. *Chem. Rev.*, 114(21):10735–10806, 2014.

[30] David F Sanders, Zachary P Smith, Ruilan Guo, Lloyd M Robeson, James E McGrath, Donald R Paul, and Benny D Freeman. Energy-efficient polymeric gas separation membranes for a sustainable future: A review. *Polymer*, 54(18):4729–4761, 2013.

[31] Peter M Budd, Neil B McKeown, and Detlev Fritsch. Free volume and intrinsic microporosity in polymers. *J. Mater. Chem.*, 15(20):1977–1986, 2005.

[32] Ashique Hussain Jatoi, Kyung Hwan Kim, Muhammad Ali Khan, Fida Hussain Memon, Muzaffar Iqbal, Dahar Janwery, Shah Nawaz Phulpoto, Anupama Samantasinghar, Kyung Hyun Choi, and Khalid Hussain Thebo. Functionalized graphene oxide-based lamellar membranes for organic solvent nanofiltration applications. *RSC advances*, 13(19):12695–12702, 2023.

[33] Sagar Roy, Susana Addo Ntim, Somenath Mitra, and Kamalesh K Sirkar. Facile fabrication of superior nanofiltration membranes from interfacially polymerized cnt-polymer composites. *J. Membr. Sci.*, 375(1-2):81–87, 2011.

[34] Xi Quan Cheng, Kristina Konstas, Cara M Doherty, Colin D Wood, Xavier Mulet, Zongli Xie, Derrick Ng, Matthew R Hill, Lu Shao, and Cher Hon Lau. Hyper-cross-linked additives that impede aging and enhance permeability in thin polyacetylene films for organic solvent nanofiltration. *ACS Appl. Mater. Interfaces*, 9(16):14401–14408, 2017.

[35] Sara Sorribas, Patricia Gorgojo, Carlos Tellez, Joaquin Coronas, and Andrew G Livingston. High flux thin film nanocomposite membranes based on metal–organic frameworks for organic solvent nanofiltration. *J. Am. Chem. Soc.*, 135(40):15201–15208, 2013.

[36] Sharath Kandambeth, Bishnu P Biswal, Harshal D Chaudhari, Kanhu Charan Rout, Shebeeb Kunjattu H, Shouvik Mitra, Suvendu Karak, Anuja Das, Rabibrata Mukherjee, Ulhas K Kharul, et al. Selective molecular sieving in self-standing porous covalent-organic-framework membranes. *Adv. Mater.*, 29(2):1603945, 2017.

[37] Yan Chao Xu, Yu Pan Tang, Li Fen Liu, Zhan Hu Guo, and Lu Shao. Nanocomposite organic solvent nanofiltration membranes by a highly-efficient mussel-inspired co-deposition strategy. *J. Membr. Sci.*, 526:32–42, 2017.

[38] Andreas Mautner, K-Y Lee, Panu Lahtinen, Minna Hakalahti, Tekla Tammelin, K Li, and AJCC Bismarck. Nanopapers for organic solvent nanofiltration. *Chem. Commun.*, 50(43):5778–5781, 2014.

[39] In-Chul Kim, Jonggeon Jegal, and Kew-Ho Lee. Effect of aqueous and organic solutions on the performance of polyamide thin-film-composite nanofiltration membranes. *J. Polym. Sci., Part B: Polym. Phys.*, 40(19):2151–2163, 2002.

[40] Peter M Budd, Bader S Ghanem, Saad Makhseed, Neil B McKeown, Kadhum J Msayib, and Carin E Tattershall. Polymers of intrinsic microporosity (pims): robust, solution-processable, organic nanoporous materials. *Chem. Commun.*, (2):230–231, 2004.

[41] Patricia Gorgojo, Santanu Karan, Him Cheng Wong, Maria F Jimenez-Solomon, João T Cabral, and Andrew G Livingston. Ultrathin polymer films with intrinsic microporosity: anomalous solvent permeation and high flux membranes. *Adv. Funct. Mater.*, 24(30):4729–4737, 2014.

[42] Detlev Fritsch, Petra Merten, Kathleen Heinrich, Marina Lazar, and Markus Priske. High performance organic solvent nanofiltration membranes: Development and thorough testing of thin film composite membranes made of polymers of intrinsic microporosity (pims). *J. Membr. Sci.*, 401:222–231, 2012.

[43] Benjamin Gabriel Poulson, Qana A Alsulami, Abeer Sharfalddin, Emam F El Agammy, Fouzi Mouffouk, Abdul-Hamid Emwas, Lukasz Jaremko, and Mariusz Jaremko. Cyclodextrins: Structural, chemical, and physical properties, and applications. *Polysaccharides*, 3(1):1–31, 2021.

[44] Avilasha A Sandilya, Upendra Natarajan, and M Hamsa Priya. Molecular view into the cyclodextrin cavity: Structure and hydration. *ACS omega*, 5(40):25655–25667, 2020.

[45] Michael P Allen. Computational soft matter: From synthetic polymers to proteins. *Lecture Notes*, 23:1–28, 2004.

[46] Gerhard Hummer, Jayendran C Rasaiah, and Jerzy P Noworyta. Water conduction through the hydrophobic channel of a carbon nanotube. *nature*, 414(6860):188–190, 2001.

[47] Alexander Berezhkovskii and Gerhard Hummer. Single-file transport of water molecules through a carbon nanotube. *Phys. Rev. Lett.*, 89(6):064503, 2002.

[48] Christine Peter and Gerhard Hummer. Ion transport through membrane-spanning nanopores studied by molecular dynamics simulations and continuum electrostatics calculations. *Biophys. J.*, 89(4):2222–2234, 2005.

[49] Li Wang, Jinlong He, Mohammad Heiranian, Hanqing Fan, Lianfa Song, Ying Li, and Menachem Elimelech. Water transport in reverse osmosis membranes is governed by pore flow, not a solution-diffusion mechanism. *Science Advances*, 9(15):eadf8488, 2023.

[50] Luying Wang, Randall S Dumont, and James M Dickson. Nonequilibrium molecular dynamics simulation of water transport through carbon nanotube membranes at low pressure. *J. Chem. Phys.*, 137(4), 2012.

[51] Amrit Kalra, Shekhar Garde, and Gerhard Hummer. Osmotic water transport through carbon nanotube membranes. *Proc. Natl. Acad. Sci.*, 100(18):10175–10180, 2003.

[52] Gunolla Nagendraprasad, Vasista Adupa, K Anki Reddy, Chandan Das, and Santanu Karan. Semiaromatic polyamide-based membrane in forward osmosis: Molecular insights. *J. Phys. Chem. B*, 127(30):6751–6766, 2023.

[53] Zhongqiao Hu, Yifei Chen, and Jianwen Jiang. Zeolitic imidazolate framework-8 as a reverse osmosis membrane for water desalination: Insight from molecular simulation. *J. Chem. Phys.*, 134(13), 2011.

[54] Hendrik Frentrup, Kyle E Hart, Coray M Colina, and Erich A Muller. In silico determination of gas permeabilities by non-equilibrium molecular dynamics: Co2 and he through pim-1. *Membranes*, 5(1):99–119, 2015.

[55] Tomohisa Yoshioka, Masashi Asaeda, and Toshinori Tsuru. A molecular dynamics simulation of pressure-driven gas permeation in a micropore potential field on silica membranes. *J. Membr. Sci.*, 293(1-2):81–93, 2007.

[56] Tao Wei, Lin Zhang, Haiyang Zhao, Heng Ma, Md Symon Jahan Sajib, Hua Jiang, and Sohail Murad. Aromatic polyamide reverse-osmosis membrane: an atomistic molecular dynamics simulation. *J. Phys. Chem. B*, 120(39):10311–10318, 2016.

[57] Laura A Richards, Andrea I Schafer, Bryce S Richards, and Ben Corry. The importance of dehydration in determining ion transport in narrow pores. *Small*, 8(11):1701–1709, 2012.

[58] Jie Zheng, Erin M Lennon, Heng-Kwong Tsao, Yu-Jane Sheng, and Shaoyi Jiang. Transport of a liquid water and methanol mixture through carbon nanotubes under a chemical potential gradient. *J. Chem. Phys.*, 122(21), 2005.

[59] Fangqiang Zhu and Klaus Schulten. Water and proton conduction through carbon nanotubes as models for biological channels. *Biophys. J.*, 85(1):236–244, 2003.

[60] ME Suk, AV Raghunathan, and NR Aluru. Fast reverse osmosis using boron nitride and carbon nanotubes. *Appl. Phys. Lett.*, 92(13), 2008.

[61] Kurt S Spiegler and Ora Kedem. Thermodynamics of hyperfiltration (reverse osmosis): criteria for efficient membranes. *Desalination*, 1(4):311–326, 1966.

[62] Ora Kedem and Aharon Katchalsky. Permeability of composite membranes. part 1.—electric current, volume flow and flow of solute through membranes. *Trans. Faraday Soc.*, 59:1918–1930, 1963.

[63] Takeshi Matsuura and S Sourirajan. Reverse osmosis transport through capillary pores under the influence of surface forces. *Ind. Eng. Chem. Proc. Des. Dev.*, 20(2):273–282, 1981.

[64] Tomoyuki Okada and Takeshi Matsuura. A new transport model for pervaporation. *J. Membr. Sci.*, 59(2):133–149, 1991.

[65] Johannes G Wijmans and Richard W Baker. The solution-diffusion model: a review. *J. Membr. Sci.*, 107(1-2):1–21, 1995.

[66] HK Lonsdale, Ulrich Merten, and RL Riley. Transport properties of cellulose acetate osmotic membranes. *J. Appl. Polym. Sci.*, 9(4):1341–1362, 1965.

[67] Mohammad Soltanieh and WILLIAM N GILL'. Review of reverse osmosis membranes and transport models. *Chem. Eng. Commun.*, 12(4-6):279–363, 1981.

[68] Geoffrey M Geise, Donald R Paul, and Benny D Freeman. Fundamental water and salt transport properties of polymeric materials. *Prog. Polym. Sci.*, 39(1):1–42, 2014.

[69] Meng Shen, Sinan Keten, and Richard M Lueptow. Dynamics of water and solute transport in polymeric reverse osmosis membranes via molecular dynamics simulations. *J. Membr. Sci.*, 506:95–108, 2016.

[70] Takahiro Fujioka, Nagayasu Oshima, Ryoichi Suzuki, William E Price, and Long D Nghiem. Probing the internal structure of reverse osmosis membranes by positron annihilation spectroscopy: Gaining more insight into the transport of water and small solutes. *J. Membr. Sci.*, 486:106–118, 2015.

[71] Sung Ho Kim, Seung-Yeop Kwak, and Takenori Suzuki. Positron annihilation spectroscopic evidence to demonstrate the flux-enhancement mechanism in morphology-controlled thin-film-composite (tfc) membrane. *Environ. Sci. Technol.*, 39(6):1764–1770, 2005.

[72] Edward Harder, D Eric Walters, Yaroslav D Bodnar, Ron S Faibish, and Benoît Roux. Molecular dynamics study of a polymeric reverse osmosis membrane. *J. Phys. Chem. B*, 113(30):10177–10182, 2009.

[73] Minxia Ding, Anthony Szymczyk, Florent Goujon, Armand Soldera, and Aziz Ghoufi.

Structure and dynamics of water confined in a polyamide reverse-osmosis membrane: A molecular-simulation study. *J. Membr. Sci.*, 458:236–244, 2014.

[74] Hui Zhang, Mao See Wu, Kun Zhou, and Adrian Wing-Keung Law. Molecular insights into the composition–structure–property relationships of polyamide thin films for reverse osmosis desalination. *Environ. Sci. Technol.*, 53(11):6374–6382, 2019.

[75] Jinlong He, Jason Yang, Jeffrey R McCutcheon, and Ying Li. Molecular insights into the structure-property relationships of 3d printed polyamide reverse-osmosis membrane for desalination. *J. Membr. Sci.*, 658:120731, 2022.

[76] Jinlong He, Jeffrey R McCutcheon, and Ying Li. Effect of different manufacturing methods on polyamide reverse-osmosis membranes for desalination: Insights from molecular dynamics simulations. *Desalination*, 547:116204, 2023.

[77] Zak E Hughes and Julian D Gale. A computational investigation of the properties of a reverse osmosis membrane. *J. Mater. Chem.*, 20(36):7788–7799, 2010.

[78] Ning Zhang, Shaomin Chen, Boyun Yang, Jun Huo, Xiaopeng Zhang, Junjiang Bao, Xuehua Ruan, and Gaohong He. Effect of hydrogen-bonding interaction on the arrangement and dynamics of water confined in a polyamide membrane: A molecular dynamics simulation. *J. Phys. Chem. B*, 122(17):4719–4728, 2018.

[79] Hanqing Fan, Jinlong He, Mohammad Heiranian, Weiyi Pan, Ying Li, and Menachem Elimelech. The physical basis for solvent flow in organic solvent nanofiltration. *Science Advances*, 10(24):eado4332, 2024.

[80] Jinlong He, Hanqing Fan, Menachem Elimelech, and Ying Li. Molecular simulations elucidate the transport mechanisms of organic solvents in dense polymer membranes. *J. Membr. Sci.*, page 123055, 2024.

[81] Pedro Silva, Shejiao Han, and Andrew G Livingston. Solvent transport in organic solvent nanofiltration membranes. *J. Membr. Sci.*, 262(1-2):49–59, 2005.

[82] James C Phillips, David J Hardy, Julio DC Maia, John E Stone, Joao V Ribeiro, Rafael C Bernardi, Ronak Buch, Giacomo Fiorin, Jerome Henin, Wei Jiang, et al. Scalable molecular dynamics on cpu and gpu architectures with namd. *J. Chem. Phys.*, 153(4):044130, 2020.

[83] Jumin Lee, Xi Cheng, Jason M Swails, Min Sun Yeom, Peter K Eastman, Justin A Lemkul, Shuai Wei, Joshua Buckner, Jong Cheol Jeong, Yifei Qi, et al. CHARMM-GUI input generator for namd, gromacs, amber, openmm, and CHARMM/OpenMM simula-

tions using the CHARMM36 additive force field. *J. Chem. Theory Comput.*, 12(1):405–413, 2016.

[84] Jing Huang and Alexander D MacKerell Jr. Charmm36 all-atom additive protein force field: Validation based on comparison to nmr data. *J. Comput. Chem.*, 34(25):2135–2145, 2013.

[85] Leandro Martinez, Ricardo Andrade, Ernesto G Birgin, and Jose Mario Martinez. Packmol: a package for building initial configurations for molecular dynamics simulations. *J. Comput. Chem.*, 30(13):2157–2164, 2009.

[86] William L Jorgensen, Jayaraman Chandrasekhar, Jeffry D Madura, Roger W Impey, and Michael L Klein. Comparison of simple potential functions for simulating liquid water. *J. Chem. Phys.*, 79(2):926–935, 1983.

[87] Tom Darden, Darrin York, and Lee Pedersen. Particle mesh ewald: An n log (n) method for ewald sums in large systems. *J. Chem. Phys.*, 98(12):10089–10092, 1993.

[88] Giovanni Bussi, Tatyana Zykova-Timan, and Michele Parrinello. Isothermal-isobaric molecular dynamics using stochastic velocity rescaling. *J. Chem. Phys.*, 130(7), 2009.

[89] Scott E Feller, Yuhong Zhang, Richard W Pastor, and Bernard R Brooks. Constant pressure molecular dynamics simulation: the langevin piston method. *J. Chem. Phys.*, 103(11):4613–4621, 1995.

[90] William C Swope, Hans C Andersen, Peter H Berens, and Kent R Wilson. A computer simulation method for the calculation of equilibrium constants for the formation of physical clusters of molecules: Application to small water clusters. *J. Chem. Phys.*, 76(1):637–649, 1982.

[91] Supriyo Bhattacharya and Keith E Gubbins. Fast method for computing pore size distributions of model materials. *Langmuir*, 22(18):7726–7731, 2006.

[92] Accelrys. *Materials Studio 4.4*. Accelrys Software Inc., San Diego, CA., 2008.

[93] Alexey Yushkin, Vladimir Vasilevsky, Valery Khotimskiy, Anthony Szymczyk, and Alexey Volkov. Evaluation of liquid transport properties of hydrophobic polymers of intrinsic microporosity by electrical resistance measurement. *J. Membr. Sci.*, 554:346–356, 2018.

[94] Sergei Grudinin, Georg Buldt, Valentin Gordeliy, and Artur Baumgaertner. Water molecules and hydrogen-bonded networks in bacteriorhodopsin—molecular dynamics simulations of the ground state and the m-intermediate. *Biophys. J.*, 88(5):3252–3261, 2005.

[95] George A Jeffrey and George A Jeffrey. *An introduction to hydrogen bonding*, volume 12. Oxford university press New York, 1997.

[96] Minxia Ding, Aziz Ghoufi, and Anthony Szymczyk. Molecular simulations of polyamide reverse osmosis membranes. *Desalination*, 343:48–53, 2014.

[97] Huiqing Wu, Beibei Tang, and Peiyi Wu. Preparation and characterization of anti-fouling β-cyclodextrin/polyester thin film nanofiltration composite membrane. *J. Membr. Sci.*, 428:301–308, 2013.

[98] Tiefan Huang, Tiara Puspasari, Suzana P Nunes, and Klaus-Viktor Peinemann. Ultrathin 2d-layered cyclodextrin membranes for high-performance organic solvent nanofiltration. *Adv. Funct. Mater.*, 30(4):1906797, 2020.

[99] Kenneth A Connors. The stability of cyclodextrin complexes in solution. *Chem. Rev.*, 97(5):1325–1358, 1997.

[100] Frank Biedermann, Werner M Nau, and Hans-Jörg Schneider. The hydrophobic effect revisited—studies with supramolecular complexes imply high-energy water as a noncovalent driving force. *Angew. Chem., Int. Ed.*, 53(42):11158–11171, 2014.

[101] Frank Biedermann, Vanya D Uzunova, Oren A Scherman, Werner M Nau, and Alfonso De Simone. Release of high-energy water as an essential driving force for the high-affinity binding of cucurbit [n] urils. *J. Am. Chem. Soc.*, 134(37):15318–15323, 2012.

[102] Herbert C Georg, Kaline Coutinho, and Sylvio Canuto. A look inside the cavity of hydrated α-cyclodextrin: A computer simulation study. *Chem. Phys. Lett.*, 413(1-3):16–21, 2005.

Chapter 5

Atomistic Insights into High-Performance Polyimine-based Membranes for Selective Dye Rejection and Salt Permeation in Nanofiltration[1]

5.1 Introduction

In the past decade, the increasing presence of toxic dye contaminants has significantly degraded water quality. Reactive dyes are particularly prevalent due to their ease of application and vibrant colors [28]. Dyes are widely used across various industries, including textiles, paper, plastics, and leather, with synthetic dyes being applied in vast quantities daily [4, 5, 9, 11, 42, 44]. Azo dyes [6, 60], the most common type, pose severe threats to aquatic life and human health, particularly affecting the nervous system [3, 7, 62]. These dyes, characterized by their aromatic ring structures, are highly resistant to degradation, making the treatment of textile wastewater particularly challenging [25, 34]. Several techniques, such as adsorption, photocatalysis, ozonation, and anaerobic/aerobic processes, have been explored to remove dyes from wastewater [3, 34, 44, 53]. Another technique that has been widely utilized in dye wastewater treatment is

[1]G. Nagendraprasad, K. Anki Reddy, C. Das, S. Karan, Atomistic Insights into High-Performance Polyimine-based Membranes for Selective Dye Rejection and Salt Permeation in Nanofiltration, revision submitted to Chemical Engineering Science.

membrane-based nanofiltration at low operating pressures.

In recent decades, membrane separation technologies have gained significant attention due to their low energy consumption, minimal carbon footprint, operational simplicity, and scalability [46]. Nanofiltration membranes with high permeance and tailored molecular weight cutoff (MWCO) enable selective separation of molecules by size [58, 77]. However, achieving high solute-solute selectivity remains critical for efficient molecular separation in nanofiltration processes [57, 68]. For years, semi- or fully-aromatic polyamide thin-film and nanocomposite membranes have dominated the industry due to their suitability for commercial-scale production [23, 37, 56, 57]. Despite their advantages, these membranes often exhibit high rejection rates for salt ions due to their densely crosslinked structures [23, 56, 57].

Various strategies exist for membrane modification, with the incorporation of nanomaterials being particularly prominent [64]. To enhance membrane separation performance, micro- and nanomaterials are synthesized and integrated with polymeric matrices, resulting in high-performance mixed matrix membranes [40]. However, the effectiveness of inorganic materials in these membranes is often limited by the low adsorption of inorganic particles in the polymer phase, which reduces separation efficiency [43]. Developing organic porous materials has been proposed to address this issue to solve the challenges associated with nanoparticles [75]. Interfacial polymerization (IP) is the leading method for producing thin-film composite (TFC) membranes [37, 46, 50], forming a dense selective layer that offers moderate to high salt rejection (30-60% for monovalent salts and 95-99% for divalent salts), though efficient separation of low molecular weight compounds can be challenging [2, 12, 74, 81]. For instance, polyethyleneimine (PEI)-based TFC membranes exhibit a higher molecular weight cutoff while maintaining high rejection of mono- and divalent salts with high water flux [12]. Similarly, PEI/piperazine membranes offer excellent salt separation, particularly for $MgCl_2$, with moderate water flux [74]. Recent efforts have focused on developing loose nanofiltration (NF) membranes that maximize salt passage while selectively rejecting dyes from salt-dye mixtures [39, 72]. For example, Wang et al. [72] and Li et al. [39] developed loose NF membranes using crosslinked PEI, achieving high dye rejection rates (≈99%) for dye (Congo red) and low salt rejection for NaCl and Na_2SO_4 [39, 72]. Additionally, integrally skinned asymmetric membranes are known for separating small organic molecules, though they offer marginal selectivity [21, 46, 59, 61]. Conventional polyamide-based NF membranes, while effective in some applications, often suffer from chlorine degradation and fouling issues, limiting their long-term performance [13, 71, 76]. Imine-based porous organic

polymers (POPs) have recently gained attention for their unique porous structures, making them ideal for molecular separation with high MWCO. These imine-based membranes are particularly notable for their hydrolysis resistance, which enhances their suitability for membrane technologies [15, 35]. Polyimine NF membranes are synthesized through Schiff base chemistry, forming imine linkages (C=N) between aldehyde and amine groups [79]. This simple yet highly versatile polymerization method allows for the creation of membranes with high crosslinking density, improving their rejection properties and mechanical strength. The intrinsic stability of polyimines in harsh chemical environments, including their resistance to acidic and alkaline conditions, makes them particularly suitable for industrial wastewater treatment applications where high concentrations of salts and dyes are present. Recent research has shown that these membranes exhibit high water permeance and selective rejection of dyes and salts [67]. Nevertheless, the large-scale production of imine-based thin-film membranes has faced challenges due to the extended reaction times or high temperatures typically required for their synthesis [15, 19, 35, 79]. Progress has been made in synthesizing these membranes at room temperature with shorter reaction times, facilitating the production of thin films [67]. One of the key advantages of polyimine membranes in dye separation is their ability to selectively reject large organic molecules, such as dyes, while allowing the passage of smaller ions like salts. The strong electrostatic interactions between the membrane and dye molecules contribute to high dye rejection rates, typically exceeding 95% for common textile dyes [67, 68, 80]. In addition, the size exclusion mechanism ensures that salts, which are much smaller in molecular size than dyes, can permeate through the membrane, making it an ideal choice for processes requiring simultaneous dye removal and salt recovery [67].

In the present manuscript, the methodology section discusses the forcefield parameterization, the development of the atomistic model for the polyimine nanofilm, and the procedure for non-equilibrium molecular dynamics simulations with the hydrated membrane and the feed solution of NaCl salt and dye. The results and discussion section presents the data on water permeance, transport of monovalent ions, and dye rejection mechanism.

5.2 Methodology

5.2.1 Force Field Parameterization

The molecule Brilliant Blue R (BBR; molecular weight = 825.9 g mol^{-1}), triformylphloroglucinol (TFP), and the polyimine linkage were uploaded to the CGenFF webserver [29, 70, 78] using interface version 1.0.0 and force field version 3.0.1. The CHARMM [29] force field parameters for each molecule were generated by analogy with pre-existing parameters within the CGenFF server. A penalty score was assigned to evaluate how closely each parameter pair matched the existing ones. If the penalty exceeded 10, further optimization was necessary [70]. All force field parameters, including charges, bonds, angles, and dihedral parameters with penalties above 10, were refined using ffTK. The ffTK tool was employed to generate configuration files for quantum mechanics (QM) calculations and to fine-tune the parameters to ensure that molecular mechanics (MM) features aligned with QM results. QM calculations were conducted using Gaussian 16 software [22], while MM calculations were performed using NAMD [54]. The optimized penalty parameters for the molecular geometry were obtained by minimizing the ground state energy through density functional theory (DFT) simulations at the MP2/6-31G* level.

Water Interactions

CHARMM [29] compatible partial atomic charges for a molecule (BBR) is optimized with a TIP3P [33] water model. For polyimine linkage of the membrane, the average partial charges were assigned to symmetrically related atoms in each monomer [26]. Each partial atomic charge was fitted by positioning a water molecule near an atom of interest (on BBR molecule) so that it could donate a hydrogen bond to (or accept one from) the atom. One hydrogen atom in the water molecule was positioned to face the target atom to facilitate the formation of a hydrogen bond. In the case of donor atoms, the oxygen atom of the water molecule was oriented towards the atom. Figure 5.1 depicts the optimized structure (see Figure B.12 for atom identities) and its interactions with TIP3P [33] water molecules. Nitrogen and oxygen atoms are considered to be acceptors, whereas carbon atoms are treated as both acceptors and donors. So, QM calculations performed in both directions and low interaction energies are considered for optimization for carbon atoms. Hartree-Fock (HF (6−31G*)) level theory

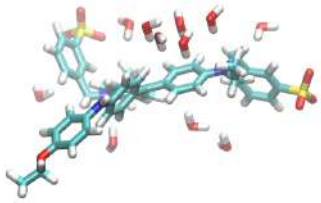

Figure 5.1: Optimised structure of BBR Water interactions

is employed for finding an optimum distance between the targeted atom and water molecule. Furthermore, direct interactions between water and carbon were computed for non$-sp^3$ carbon atoms, whereas sp^3 carbons were chosen to calculate interactions for bonded hydrogen and water molecules. The ffTK generated all QM input configuration files, and the QM calculation outputs were extracted and optimized to obtain the partial charges of the target atoms. Also, ffTK optimizes molecule dipole moment along with MM interaction energy and distance with cutoff ratios of dipole: energy: distance = 1: 1: 3. The optimized partial charges for BBR are shown Table B.1. During a QM computation, certain atoms in the molecule may sterically affect how water molecules interact with other atoms than the targeted atoms, and some water molecules might fly away. In these situations, the "divide-and-conquer" strategy, which divides a giant molecule into smaller components while keeping the same atom types as the original molecule, is advisable. BBR interaction energies with water were calculated from QM and MM optimization, and the partial charges were tabulated in Table B.2. The average absolute deviation of MM energies with QM energies is 0.350 Kcal/mol.

Angle Parameter Optimization

The Hessian optimization method was used to calculate the internal coordinates of molecules at the MP2/6-31G* level of theory [69], optimizing both bond and angle parameters. Frequency calculations are quite computationally expensive, so Hessian calculations were performed on a reduced compound in which the sulfate and benzene rings were removed from BBR. Figure 5.2 depicts the reduced structures, and BBR@1 has just 55 atoms while preserving all the original molecule characteristics we sought to improve. The reduced compound BBR@2 has 33

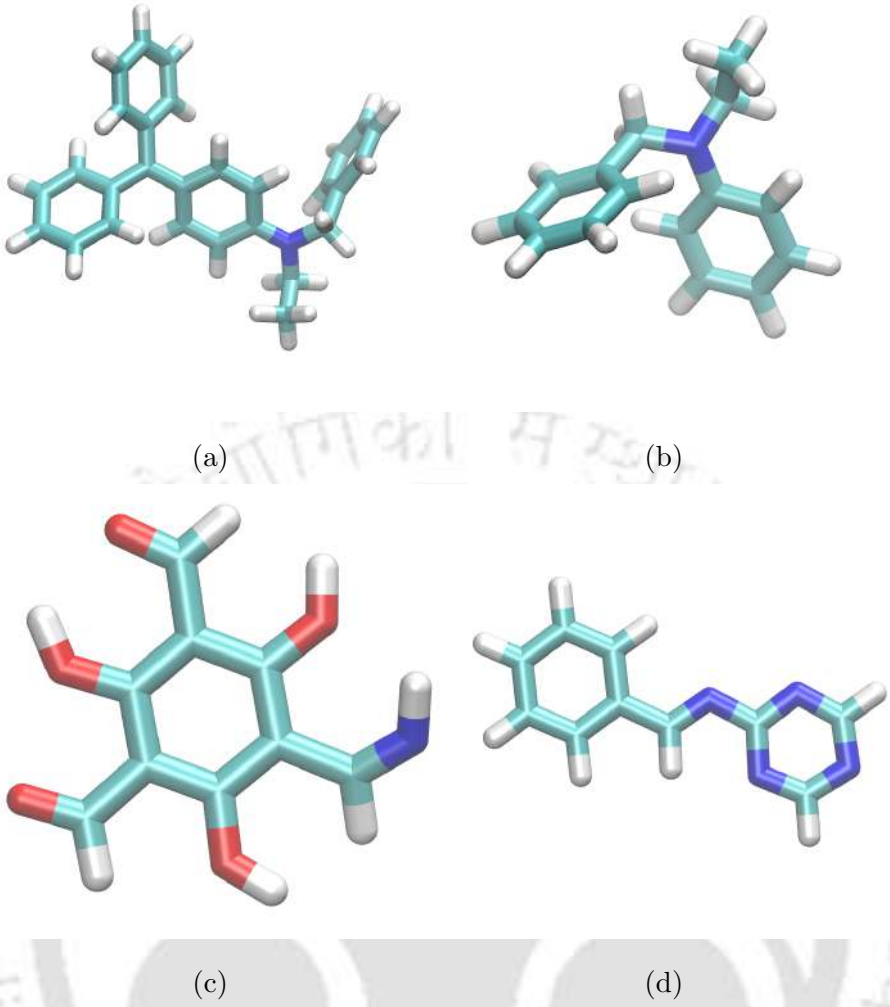

Figure 5.2: Optimised reduced structure of (a) BBR@1 (b) BBR@2 (c) TFP−MEL@1 (d) TFP−MEL@2

atoms and shares only one dihedral (CG2R61-CG321-NG301-CG2R61) of the original molecule. BBR@1 geometry is used to calculate angles, dihedrals, and improper parameters for BBR, and TFP−MEL@2 is used to calculate angle parameters and some dihedral parameters for the polymer, whereas TFP−MEL@1 used to derive the rest of dihedral parameters. For the best fit between the QM and MM, ffTK optimized the bond and angle parameters with energy: geometry weighting of 2:1. We used this weighting such that energy offsets and geometry offsets each contribute an equal amount to the penalty. Table B.3 lists angle parameters of BBR, where K_θ reported in Kcal/mol/rad^2 and θ in degrees. The penalty angle parameters C9-N1-C1m or atomtype CG2DC1-NG2D1-CG2R64 from CGenFF is $K_\theta = 100$ Kcal/mol/rad^2, $\theta = 107°$, where as K_θ and θ derived from ffTK is 97.007 Kcal/mol/rad^2 and 117.34°.

Dihedral Parameter Optimization

The diedral parameters were optimized using MP2(6−31G*) level theory, where MM geometry dihedral scans were used to fit with QM data. The refined dihedrals were rotated by ±90° with increment of 15°. The penalty dihedrals were optimized with a force constant of 17 Kcal/mol using different multiplicity combinations for BBR@1 geometry. Initially, a cutoff energy of 12 Kcal/mol is used to cover the potential energy surface of MM geometry and then reduced to 5 Kcal/mol in downhill optimization. The force constant of 12 Kcal/mol was applied to optimize

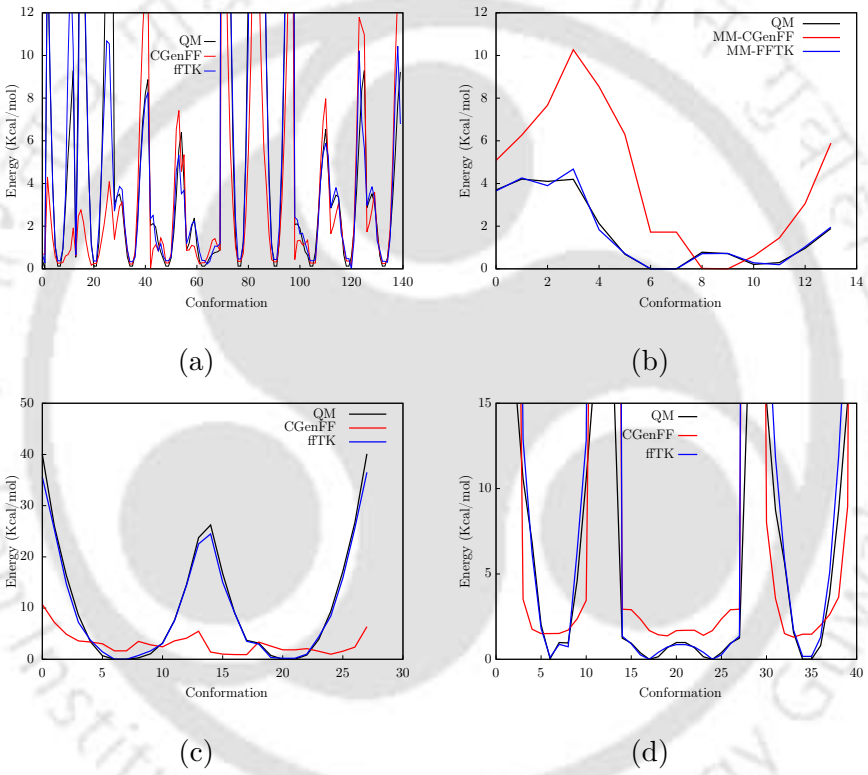

Figure 5.3: Dihedral fitting for (a) BBR@1 (b) BBR@2 (c) TFP−MEL@1 (d) TFP−MEL@2

BBR@2 geometry dihedral (C4-C7-N1-C10) with an energy cutoff of 5 Kcal/mol. The root mean square errors (RMSE) of 0.3630 for BBR@1 and 0.1660 for BBR@2 MM energy surface were maintained while optimizing penalty dihedrals. The fitting of dihedrals is shown in Figure 5.3 for both BBR and TFP-MEL polymer. Tables B.4 and B.5 list the dihedral parameters for BBR and TFP-MEL polymer, respectively. Cutoff energy of 5 Kcal/mol with the force constant of 19.5 Kcal/mol was used to fit dihedrals of TFP-MEL polymer.

Impropers Optimization

Lastly, the improper for CG2DC1-CG2DC2-CG2DC2-NG2P1 atom types of atoms C23-C22-C20-N2 of BBR fitted in Figure 5.4. Here, we performed impropers optimization for BBR only; however, the polyimine linkage improper parameters do not have penalties. Improper optimization is done by performing semi-empirical calculations on MM-generated PES using the PM6 [65] Hamiltonian. An improper force constant of 12 Kcal/mol and a cutoff of 10 Kcal/mol were maintained in simulated annealing process optimization, and later, the cutoff energy was reduced to 5 Kcal/mol in the downhill process. Finally, downhill optimization iterations have reduced the root mean square errors (RMSE) to zero. The optimized force constant k_ω and equilibrium constant ω_o of improper are 0.2055 and zero, respectively.

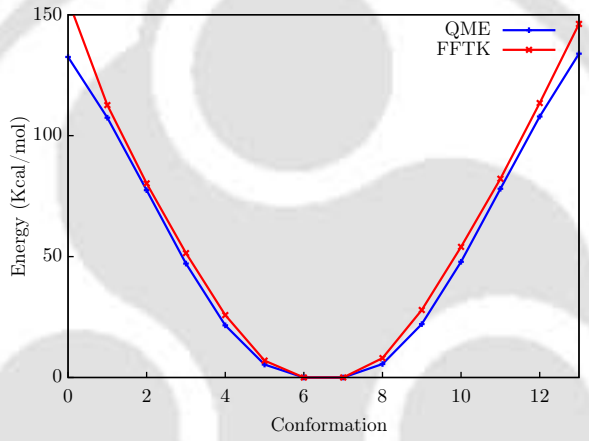

Figure 5.4: Improper (C23-C22-C20-N2) fitting of BBR@1 geometry.

5.2.2 Construction of Molecular Membrane Model

In this study, the polyimine-based membrane is modeled using triformylphloroglucinol (TFP) and melamine (MEL) through a heuristic approach based on distance criteria. Molecular dynamics simulations were performed using NAMD software [54]. The 3D structures of the monomers and imine linkages are depicted in Figure 5.5(a-c). Initially, 1000 TFP and 4000 MEL molecules were randomly distributed in a 110 × 110 × 60 $\AA^3$ computational box using Packmol [48]. The system was energy minimized for 10 ps and equilibrated for 10 ns in an NPT ensemble at 300 K and 1 atm. An annealing process was performed in an NVT ensemble, gradually heating the system to 1100 K and cooling it to room temperature in 50 K steps. At

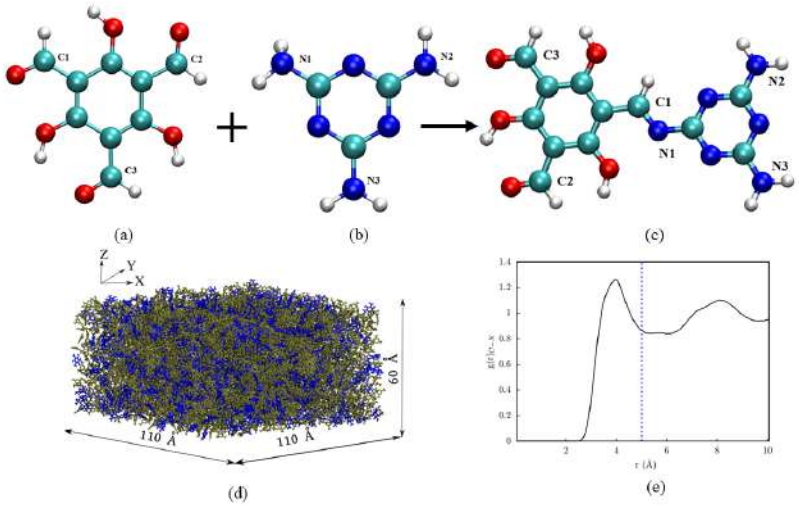

Figure 5.5: 3D structures of (a) triformylphloroglucinol (TFP) (b) Melamine (MEL) (c) Imine-linkage between TFP and MEL (d) Initial configuration prior to polymerization (color code-blue for TFP and tan for MEL) (e) RDF between the Aldehyde carbon of TFP and the amine nitrogen of MEL after annealing in an NVT ensemble.

each temperature step, the system was equilibrated for 100 ps to allow sufficient relaxation. Upon reaching the maximum temperature, the system underwent an additional equilibration period of 1 ns. Subsequently, the system was cooled back to room temperature using the same stepwise approach, ensuring a controlled and uniform temperature transition. Following this, the mixture (Figure 5.5d) underwent a polymerization process in an NVT ensemble. The user-defined crosslinking cutoff distance was determined from the radial distribution function (RDF) between the carbon atom of the aldehyde group ($-$CHO) in TFP and the nitrogen atom of the amine group ($-NH_2$) in melamine. As shown in Figure 5.5(e), the crosslinking criterion was found to be $L^C = 5\ \mathring{A}$. If the C$-$N distance between active monomer sites was less than the cutoff, an imine linkage was formed, and the hydrogen atoms in the $-NH_2$ group of melamine and the oxygen atom in the $-$CHO group of TFP were removed. The simulation continued searching for new imine bonds every 10 ps and partial charges were updated for the imine linkage and neighboring atoms. Average partial charges were assigned to symmetrically related atoms in each monomer of the polyimine linkage [26]. The schematic representations of the monomers and imine linkages are provided in Figure 5.6, which also illustrates the partial charges on selected atoms (note that each atom in the simulation has a unique partial charge). Other forcefield parameters were updated following each imine formation, along with

partial charges. After each crosslinking step, the system was energy minimized and equilibrated. As crosslinking progressed, the clusters expanded, restricting monomer diffusion and gradually slowing the crosslinking process. Initially, bond formation was allowed only when the distance between C1/C2/C3 of TFP and N1/N2/N3 of MEL was less than 3.2 $\mathring{A}$. Over time, this crosslinking distance was increased to 5 $\mathring{A}$ in 0.2 $\mathring{A}$ increments to accelerate the process. Finally, unreacted monomers were removed from the membrane.

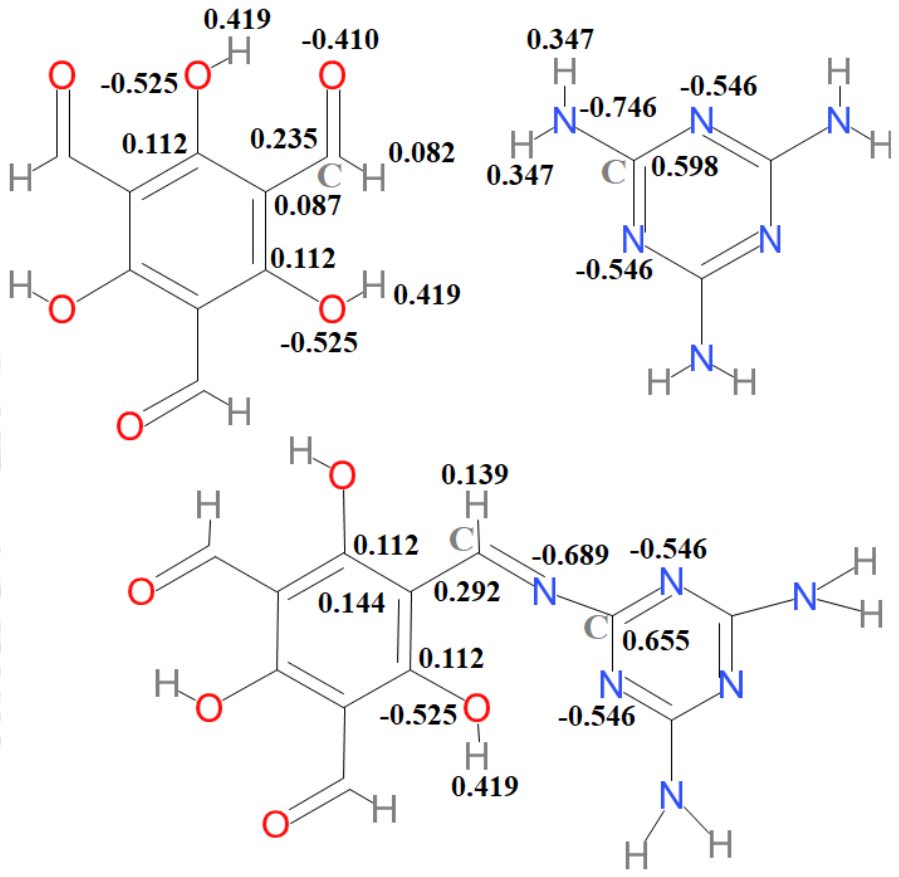

Figure 5.6: The CHARMM36-compatible force field parameters were obtained from the CGenFF server. Top panel depicts the schematic representation of 2D structures of individual monomers and bottom panel represents the polyimine linkage with partial charges. Average partial charges were assaigned to symmetrically related atoms in each monomers of the polyimine linkage.

Our simulated membrane contains more MEL units (1304), with 2012 unreacted functional groups ($-NH_2$) out of 3912. In contrast, there are 634 TFP units with only two unreacted $-CHO$ groups out of 1902 functional groups. The polymerized membrane contains various

polymeric clusters, with the largest comprising 152 and another comprising 146 monomeric units. The remaining clusters vary in size from 10 to 82 monomeric units. The degree of crosslinking (DC) is calculated using the following equation from the literature [51, 52]:

$$DC = \frac{100N_N}{N_N + N_{CHO} + N_{NH_2}} \tag{5.1}$$

where N_N in Eq 5.1 is the number of imine linkages, N_{CHO} is the number of unreacted $-$CHO groups from TFP monomers, and N_{NH_2} is the number of unreacted $-NH_2$ groups from MEL monomers in the membrane. The overall crosslinking degree of the membrane is 48.54%. Experimentally, thin-film composite membranes of this type have been extensively investigated, with crosslinking degrees often determined via X-ray photoelectron spectroscopy (XPS) [37]. However, XPS analysis captures only the membrane's surface, potentially leading to an inaccurate estimation of the overall crosslinking degree. To our knowledge, no experimental reports are available for direct comparison of the crosslinking degree in membranes synthesized using TFP and melamine. Although Tiwari et al. [67] reported a polyimine membrane, they did not specify its crosslinking degree. Generally, nanofiltration membranes exhibit crosslinking degrees in the range of 25 - 70% [20, 27, 41, 51, 52, 55]. The dry membrane density is 0.78 g cm^{-3}.

5.2.3 Details of Nanofiltration (NF) Setup

The polymerized membrane was submerged in a pre-equilibrated water box (via VMD [30]) and equilibrated for 10 ns in an NPT ensemble at 300 K and 1 atm. The calculated density of the hydrated membrane is 1.12 g cm^{-3}. Unfortunately, there is no experimental value reported on polyimine; however, polymers made out of C, N, and O should not have a very different value other than polyamide. Typically, polyamide based nanofiltration membranes densities falls in the range of 1.10 - 1.20 g cm^{-3} [32, 37, 51]. This hydrated membrane was then used in the production simulation runs of the nanofiltration (NF) system. A feed solution comprising a dye (BBR) and NaCl salt was used for the NF simulation. A feed simulation box of 110 $\times$ 110 $\times$ 80 $\AA^3$ was created, containing 30,522 water molecules, 5 BBR molecules, 331 Na^+ ions, and 326 Cl^- ions to replicate seawater concentration with the dye. The TIP3P water model [33] was employed to model the water molecules. The feed solution was energy minimized for 20 ps and equilibrated for 20 ns in an NPT ensemble at 300 K and 1 atm. As shown in Figure 5.7, the system consists of the feed solution, hydrated membrane, and a permeate region, with

graphene sheets acting as pistons at both ends. The NF system was equilibrated for 1 ns in an NPT ensemble at 300 K and 1 atm. A pressure of 20 atm was applied to the feed-side graphene piston, while 1 atm was maintained on the permeate-side graphene piston (Figure 5.7).

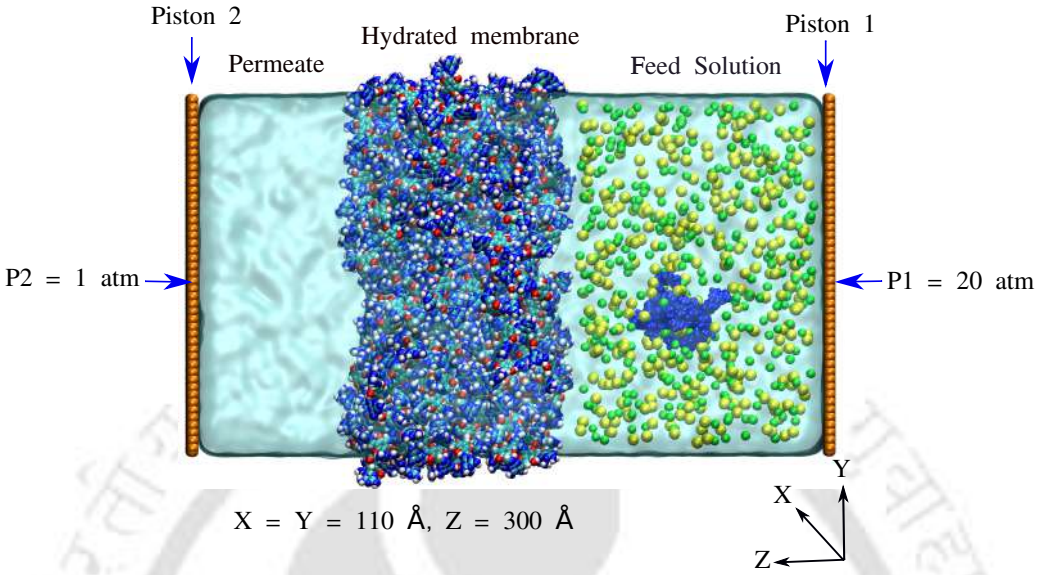

Figure 5.7: The simulation setup consists of NaCl and BBR dye as feed solution, hydrated membrane, and permeate region. A vacuum of 30 $\mathring{A}$ is applied at both ends of the graphene pistons in the Z-direction.

The production simulations were performed in the NVT ensemble at 300 K. The van der Waals interactions were computed between the atoms using Lennard-Jones potential with a switching distance of 10 $\mathring{A}$ and a cutoff distance of 12 $\mathring{A}$. Long-range electrostatic interactions were computed using the Particle Mesh Ewald (PME) method [14], with a grid spacing of 1 $\mathring{A}$. The Nose−Hoover thermostat [10] is used to maintain the temperature of the system. The velocity Verlet algorithm [66] is used to integrate the equations of motion. The total simulation time was 30 ns, with a 1 fs timestep, and trajectories were saved every 20 ps. In contrast to previous studies where many or all membrane atoms were fixed [17, 24], only 2% of the membrane atoms were fixed in our simulations. This approach allows the membrane to respond more dynamically to flow conditions, enhancing accuracy in transport behavior at the molecular level. However, it may influence macroscale water flux due to membrane compression under operating pressures [38]. Fixing certain atoms mimics the structure of thin-film composite (TFC) nanofiltration membranes, where a porous polysulfone (PSF) layer supports the NF film. Periodic boundary conditions (PBC) were applied in all three dimensions, with a 30 $\mathring{A}$ vacuum

introduced along the Z-axis at both ends of the graphene pistons. Results were averaged from three independent simulations, and the PSF support layer was not included in the present simulations.

5.3 Results and Discussion

5.3.1 Polyimine Membrane Structure

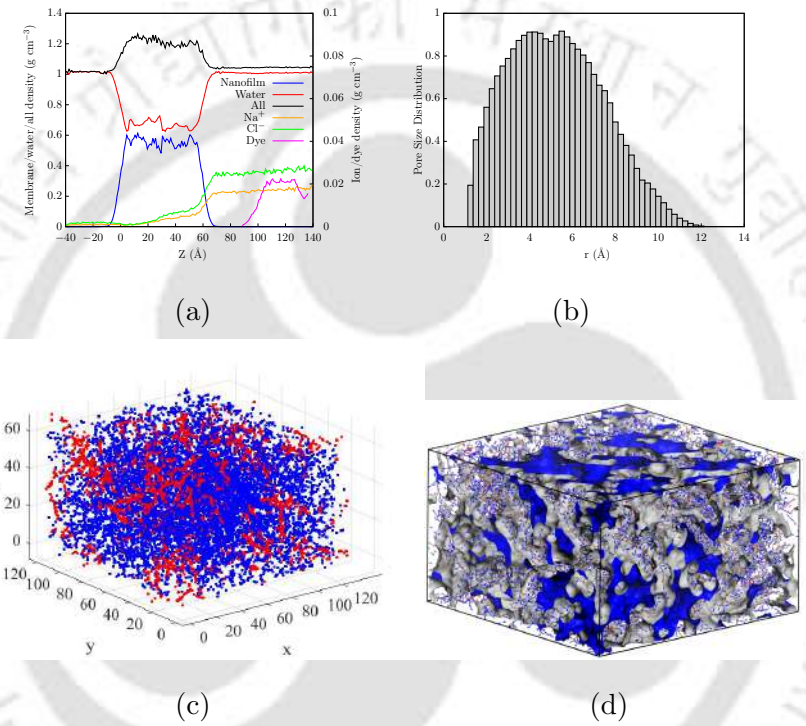

Figure 5.8: (a) Density profiles of water, membrane atoms, NaCl, Dye and the wholesystem (b) PSD of the membrane after NF process (c) Free volume of the membrane after the NF process (colorcode:blue indicates free volume < 5 $\mathring{A}$ and red indicates free volume > 5 $\mathring{A}$) (d) 3D free volume morphology of the membrane after the NF process, where the blue color indicates free volume accessible to water, and the gray color represents the occupied volume of the membrane.

The structural properties of the polyimine-based membrane were characterized by analyzing atomic density profiles along the normal direction of the membrane, pore size distribution (PSD), and the order parameter of benzene rings. Figure 5.8a shows the density profile of membrane atoms, water, ions, and dye. The density profiles of salt ions reveal that ions permeate the membrane while dye molecules are rejected, demonstrating selective permeability of the

membrane. To explore the impact of the polyimine membrane structure on water transport, we analyzed its pore structure at the molecular level, focusing on water-accessible space. The free volume of the membrane significantly impacts its selectivity, influencing its suitability for specific separations. The nature of the monomers and cross-linking degree play key roles in shaping the pore structure of the membrane. The Monte Carlo method [8] was used to calculate the PSD. Before computing PSD, water, NaCl, dye, and graphene sheets were removed from the simulated NF system. PSD was computed at every 1 ns for the last 10 ns of simulation over three independent systems, using a 1 $\mathring{A}$ probe. Figure 5.8b shows the PSD of the membrane, with notable pores ranging from 1.25 to 12 $\mathring{A}$ and prominent radii between 4 and 7 $\mathring{A}$. Typically, nanofiltration membranes have similar pore size distribution in the membrane [20, 27, 41, 51, 52]. Figure 5.8c illustrates the free volume of the membrane accessible to water molecules, with blue representing pores smaller than 5 $\mathring{A}$ and red representing pores larger than 5 $\mathring{A}$, based on Monte Carlo PSD data processed in MATLAB [49]. Additionally, the 3D morphology of the free volume was computed using Materials Studio [1], where blue indicates water-accessible free volume and gray represents the occupied volume of the membrane atoms (Figure 5.8d).

The local structure of the membrane was further analyzed using Herman's order parameter to assess the isotropy and interactions between neighboring benzene rings. The order parameter *S(r)* is defined as:

$$S(r) = \langle \frac{3Cos^2(\theta(r)) - 1}{2} \rangle \tag{5.2}$$

where θ in Eq 5.2 is the angle between the normal vectors of two neighboring benzene rings at a radial distance r. *S(r)* ranges from 0 to 1, with S = 0 indicating a fully isotropic structure and $S = 1$ representing completely ordered packing [63]. As shown in Figure B.13a, a sharp peak at r = 4.3 $\mathring{A}$ in the *S(r)* profile indicates π - π stacking interactions (see Figure B.13b). These interactions decay rapidly and reach zero at r = 6.7 $\mathring{A}$, indicating no multiple benzene ring stacking. This rapid decay suggests short-range anisotropic interactions between benzene rings [73]. Although no experimental data exists on the atomistic local structure of polyimine thin films, similar stacking structures of aromatic rings have been studied in proteins [47]. Additionally, polyimine membranes are known to undergo enol-keto tautomerization [36, 67]. Figure B.14 shows that the simulated membrane exhibits an enol structure, likely due to intramolecular hydrogen bonding between the hydroxyl group hydrogen atom of the TFP

monomer and the nitrogen atom of the imine linkage, with a bond distance of 1.93 $\AA$.

5.3.2 Water Structure

The water structure was characterized using radial distribution functions (RDF), defined as [31]:

$$g_{iO}(r) = \frac{\rho_O(r)}{\rho_O} \tag{5.3}$$

where $\rho_O(r)$ in Eq 5.3 is the local water oxygen atoms density at distance r, and ρ_O is the overall water oxygen density in the system. RDFs for water oxygen (OW) atoms were analyzed in the feed solution and inside the membrane. The first peak appeared at 2.75 $\AA$ in both environments (see Figure B.15a). The variations in RDF intensities indicated differences in hydrogen bonds (HB) per water molecule and coordination number (Figure B.15b). Integrating the RDF up to a 3.25 $\AA$ cutoff revealed coordination numbers (N_c) of 3.9 within the membrane and 4.3 in the feed solution, suggesting a decrease in hydrogen bonds per water molecule inside the membrane (Figure B.15c). A similar approach for computing HBs was used in our previous work [51, 52]. The RDF between hydrogen (HW) and oxygen atoms of water molecules is shown in Figure B.15d. The first minima at 2.45 $\AA$ indicated hydrogen bond formation with neighboring water molecules, with slightly higher peak intensity inside the membrane due to the excluded volume effect [16, 51]. In the feed solution, 0.9 OW around HW and 1.9 HW around OW, resulting in 3.8 HBs per water molecule. Inside the membrane, 0.9 OW around HW and 1.8 HW around OW, resulting in 3.6 HBs per molecule. Including HBs with membrane atoms, each water molecule formed 0.3 HBs with the membrane, resulting in 3.9 HBs inside the membrane.

5.3.3 Permeance and Pathways Mechanism

The water permeance of the polyimine-based membrane is determined by calculating the average number of water molecules permeating the membrane in a simulated time. Based on this number of molecules, the water permeance is calculated as V/(A.t.ΔP), where V is the volume of the water permeated through the membrane area (A) in a simulated time (t). Under transmembrane pressure, water molecules from the feed solution permeate the polyimine nanofilm towards the permeate region. Figure 5.9a shows the net count of water molecules permeating the nanofilm with time. The net water permeance in our study is $8.3 \pm 0.3 \times 10^3$ $Lm^{-2}hr^{-1}bar^{-1}$. Support membranes formed by phase inversion typically have a porosity of

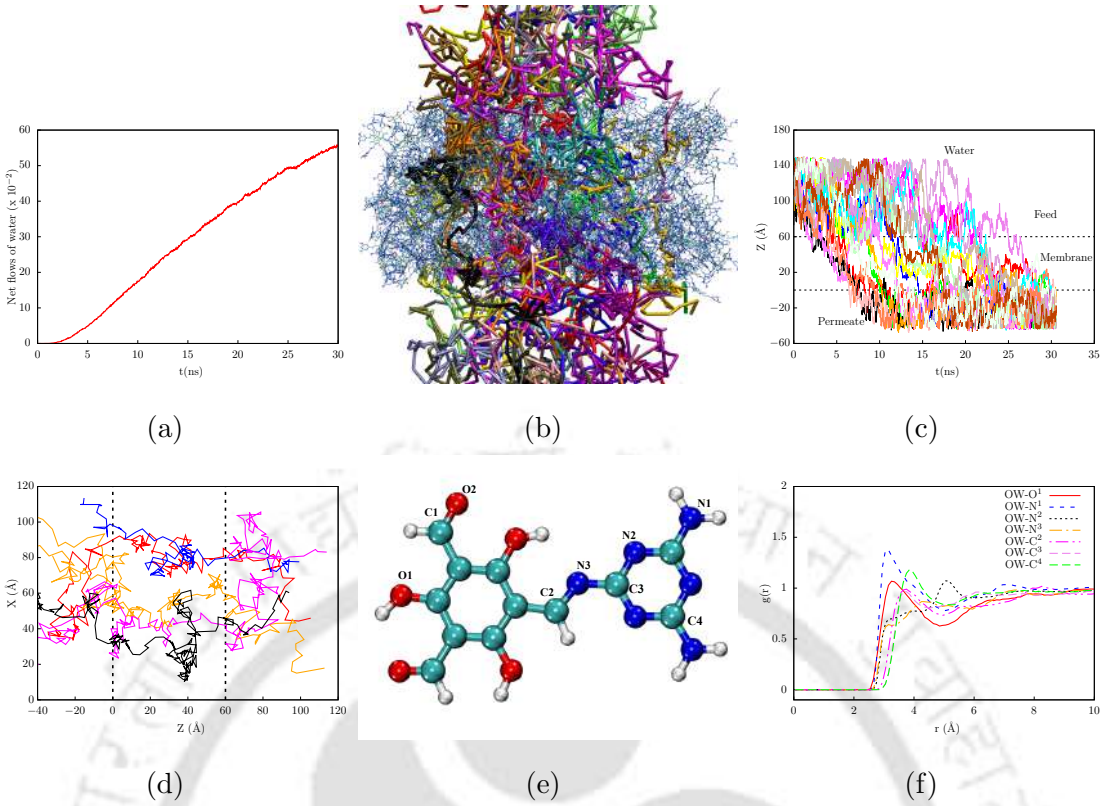

Figure 5.9: (a) Time evolution of water molecules permeating the membrane (b) Pathways of selected water molecules with the membrane (c) Trajectories of selected water molecules as a function of time (d) Trajectories of selected water molecules represented in a 2D XZ plane (e) 3D Schematic representation of the polyimine-linkage with atom identities (f) RDF between water oxygen atoms and membrane atoms; here, C^1, O^2 profiles are not shown due to negligible peaks as our membrane contains only two unreacted $-$CHO groups.

10%. Considering the porosity of the support membrane in a thin film composite membrane, a typical support porosity of $\approx$ 10% is expected. This would yield only 10% of the overall water permeance through the composite membrane compared to the permeance of the nanofilm layer alone. Additionally, the experimental membrane (the polyimine separation layer) is nearly 10 times thicker than our simulated nanofilm. This would reduce the water permeance of the composite membrane proportionally, considering the convective flow in nanofiltration membranes. Considering the thickness of the separation layer and the effect of the porosity of the support membrane, and assuming that permeance decreases linearly with thickness, the normalized water permeance would be nearly 100 times lower than the computed water permeance in the case of a composite membrane. Thus, an approximated normalized water permeance would

be nearly 83 $Lm^{-2}hr^{-1}bar^{-1}$, which is comparable with the experimentally reported value by Tiwari et al. (i.e., 78 $Lm^{-2}hr^{-1}bar^{-1}$) [67] and others [37, 57].

To understand the water transport mechanism through the polyimine membrane, we present the trajectories of a few selected water molecules. Figure 5.9b shows pathways of selected water molecules along the membrane. Figure 5.9c displays these trajectories as a function of time, revealing that after entering the membrane, some water molecules exhibit slow local motion before jumping to the permeate side, while others under to-and-fro motion between the membrane and feed side before permeating. Molecular dynamics simulations provide insights into molecular-level transport by tracking individual water molecules. Although many water molecules permeated the membrane, we depicted only five in Figure 5.9d for clarity, showcasing their 2D XZ pathways (see Figure B.16 for 2D YZ plane). Each line segment traces a water molecule path from the feed solution through the membrane to the permeate side. Initially, these molecules follow random Brownian motion, influenced by interactions with surrounding water and solute molecules. Upon reaching the interfacial region of the membrane, they traverse quickly through some regions but appear momentarily trapped in others, likely within voids or pores present in the membrane. For instance, the water molecule (black line segment) follows a random path within a pore, interacting with water and membrane chains while remaining confined. This pore is approximately 15 $\mathring{A}$ in diameter (30 $\mathring{A}$ < Z < 45 $\mathring{A}$). The molecule then swiftly jumps to an elongated pore (5 $\mathring{A}$ < Z < 25 $\mathring{A}$), as seen in Figure 5.9d. It transitions to another pore at Z = 5 $\mathring{A}$, then hops to another pore and eventually reaches the interfacial region (Z = 0 $\mathring{A}$) before exiting to the permeate side. Other water molecules follow similar mechanisms with distinct permeation pathways (Movie1). While traversing the membrane, water molecules interact with the membrane atoms. These interactions were quantified by computing pair correlation functions. Figure 5.9e depicts the imine-linkage structure, showcasing atom identities. Figure 5.9f depicts the g(r) for water oxygen atoms around selected membrane atoms. Peaks at r = 3.15 $\mathring{A}$ around the nitrogen (N^1) atom of unreacted amine ($-NH_2$) groups and r = 3.25 $\mathring{A}$ for oxygen (O^1) of hydroxyl groups indicate preferential interactions with these functional groups while transporting through the membrane.

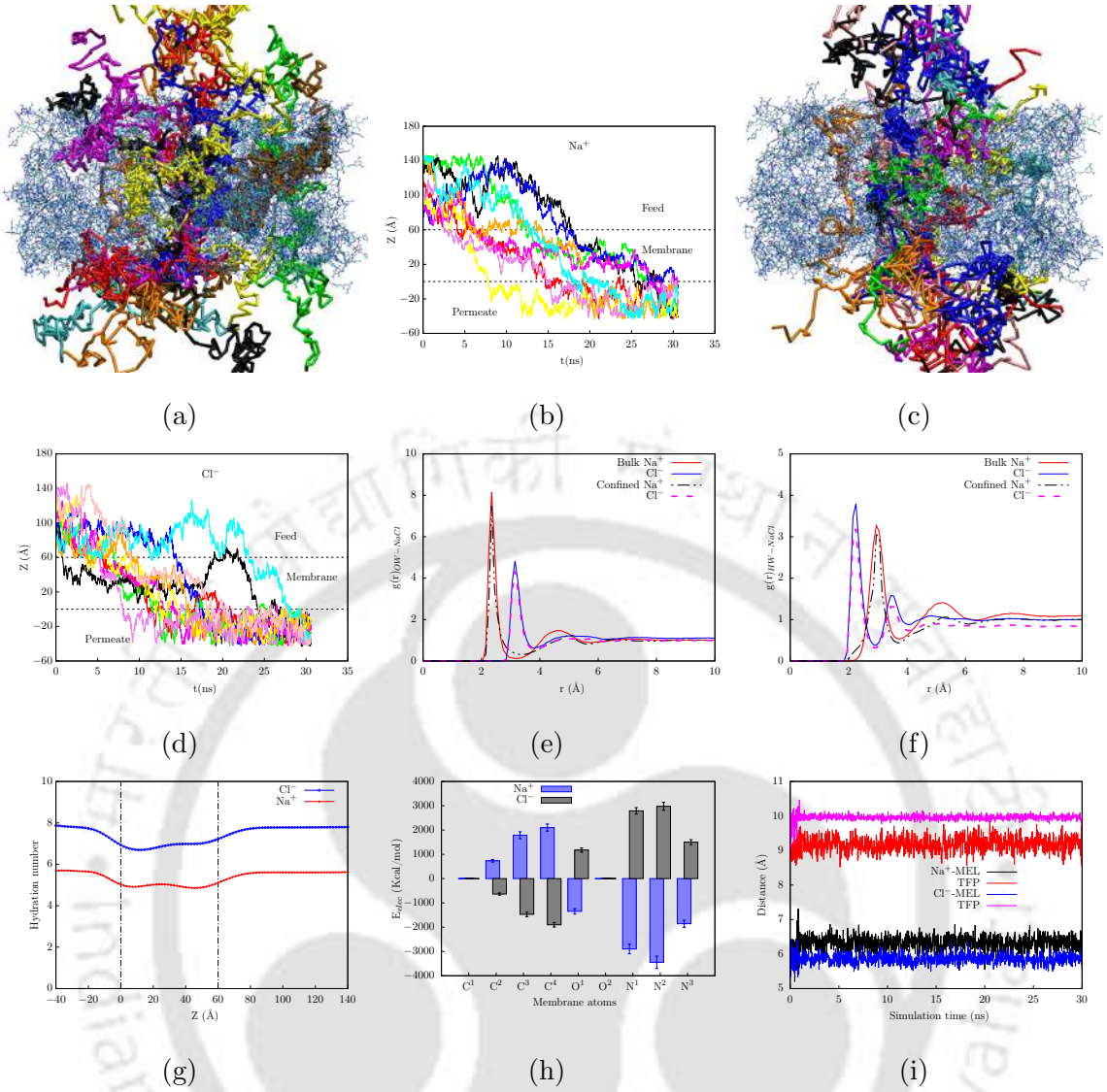

Figure 5.10: (a) Pathways of selected Na^+ ions with the membrane (b) Trajectories of selected Na^+ ions with time (c) Pathways of selected Cl^- ions with the membrane (d) Trajectories of selected Cl^+ ions with time (e) The RDF between water oxygen atoms with NaCl salt ions (f) The RDF between water hydrogen atoms with NaCl salt ions (g) Hydration number profile along the Z-axis (dot-dash line represents the membrane) (h) Electrostatic interaction energies between NaCl ions with membrane atoms; here atom identies same as Figure 5.9c (i) COM distance between chloride salt ions with MEL heterocyclic ring and TFP benzene ring

5.3.4 Dynamics of Chloride Salt and BBR Dye

To understand the ion transport through the membrane, trajectories, ion-water pair correlation functions, and electrostatic interaction energies were computed. Figure 5.10a illustrates the

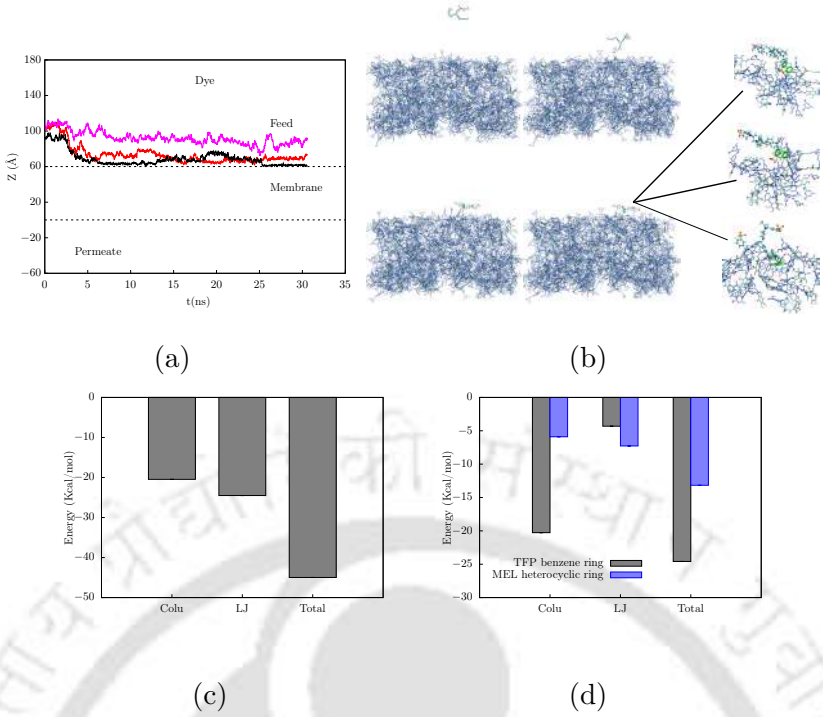

Figure 5.11: (a) Trajectories of BBR dye with time (b) Snapshot of the BBR dye reaching to the membrane surface and getting rejected via strong interactions between benzene rings (heighlighted in green color) of dye and TFP monomer of the polyimine membrane (c) Interaction energies between BBR dye and membrane surface (d) Interaction energies of BBR dye with benzene rings of TFP and heterocyclic ring of MEL on the membrane surface

pathways of selected Na^+ ions through the membrane. As depicted in Figure 5.10b and Figure B.17(a, b), few Na^+ ions exhibit slow local motion within the membrane before eventually moving to the permeate side. In contrast, few others oscillate between the membrane and feed solution before permeation. Similarly, Cl^- ions also permeate the membrane, as shown in Figure 5.10(c, d) (see Figure B.17(c, d) for 2D plane trajectories). The radial distribution function (RDF) between oxygen atoms of water molecules and chloride salt ions is elucidated in Figure 5.10e. Distinct peaks in the RDF are observed, notably a sharp peak at r = 2.35 $\AA$ for Na^+ and r = 3.15 $\AA$ for Cl^- ions in the feed solution, indicative of a higher number of water molecules in their hydration shells. Inside the polyimine membrane, the RDF profiles for chloride salt ions exhibit a less pronounced peak intensity, reflecting a decrease in a number of water molecules in the hydration shell (Figure 5.10e). Examining the RDF between the hydrogen atoms of water molecules with salt ions (Figure 5.10f), the first maxima occurs at 3.15 $\AA$ for Na^+ and 2.25 $\AA$ for Cl^-, agree with previously reported hydrated radii (3.2 $\AA$ for Na^+ and 2.5 $\AA$ for

Cl^-) [45]. The decrease in RDF intensity signifies a small reduction in the number of water molecules within the ion hydration shell, as evident in Figure 5.10f. To quantify this reduction, the number of water molecules within the hydration shell is used to compute the hydration or coordination number of Na^+ and Cl^- ions. The cutoff radius, derived from Figure 5.10f, is set at 3.1 $\mathring{A}$ for Na^+ and 3.89 $\mathring{A}$ for Cl^-. The resulting hydration number profile along the Z−axis, as illustrated in Figure 5.10g, reveals an average hydration number of approximately 5.6 for sodium ions and 7.8 for chloride ions in the bulk feed solution, in agreement with the existing literature [18]. Within the membrane, a reduction is observed, with a hydration number of 4.9 for Na^+ and 6.8 for Cl^-. The reduction in hydration number is insignificant since the pore size is much higher than the ions hydration radius. As the simulation progresses, salt ions diffuse into the membrane and traverse to the permeate region (Movie2). Figure 5.10h presents the electrostatic interaction energy profile for chloride salt ions with membrane atoms, indicating that the salt ions exhibit strong interactions with melamine atoms during transport through the membrane. This observation is further supported by the van der Waals interaction energies (see Figure B.18a). To elucidate the role of functional groups in chloride salt transport, we analyzed the functional groups of the membrane within 5 $\mathring{A}$ along the ion trajectory. Figure B.18(b-e) shows the functional groups present in the membrane along the ion trajectory. Even though −OH groups on the TFP molecules interacting with the salt ions (see Figure 5.10h), Figure 5.10i and Figure B.19 suggest that permeated chloride salt is transported near melamine heterocyclic ring, indicating that it plays a significant role in salt transport compared TFP benzene ring. Based on the ion concentrations in the feed solution (c_f) and the permeate region (c_p), the rejection is computed using (1 - (c_p/c_f)) × 100. The chloride salt rejection was found to be 34%, close to the experimentally reported value of ≈20% [67].

The rejection of BBR dye molecules was analyzed to assess membrane performance. Figure 5.11a shows the trajectories of selected dye molecules along the Z-axis as a function of time, revealing that none of the BBR molecules penetrated the membrane, indicating 100% rejection. As time progressed, the dye molecules approached closer to the membrane surface and began interacting with it (Movie2). Figure 5.11b illustrates that upon reaching the membrane surface, the dye was rejected due to strong interactions between the benzene rings of the dye and the TFP monomers on the membrane surface. The interaction energy was predominantly hydrophilic, with Lennard-Jones (LJ) forces playing a more significant role than Coulombic interactions (Figure 5.11c). Additionally, we computed the interaction energies between the

dye and the TFP benzene rings and the MEL heterocyclic rings on the membrane surface (Figure 5.11d). These results indicate that TFP benzene rings and dye interactions significantly contributed to the total interaction energy compared to the MEL heterocyclic ring, promoting dye rejection. Experimental studies have further shown that negatively charged BBR dye is preferentially rejected by polyimine-based nanofilms, with minimal salt rejection (≈20%) [67].

5.4 Conclusions

Non-equilibrium molecular dynamics simulations were performed on a polyimine-based membrane, where the feed solution consists of NaCl salt and dye in water. We observed that this polyimine membrane exhibits a high water permeance of 8.3×10^3 $Lm^{-2}hr^{-1}bar^{-1}$, complete rejection of BBR dye (100%), and selective passage of chloride salt (i.e., rejection = 34%). Our study suggests that, while chloride salt ions permeate the membrane, they permeate near the melamine heterocyclic ring compared to the benzene ring of the TFP monomer in the membrane, and dye is rejected due to strong interactions between the benzene rings of dye and the TFP monomer on the membrane surface. This study suggests that monomers with non-aromatic rings are the preferred choices for the permeation of monovalent salt. Analysis of NaCl and dye trajectories and salt ion interactions with membrane atoms suggests that the membrane allows chloride salt permeation while completely rejecting dye, enabling efficient dye separation using a polyimine membrane. Such a membrane, capable of rejecting dye while allowing NaCl passage, could significantly enhance wastewater treatment in the textile industry.

Bibliography

[1] Accelrys. *Materials Studio 4.4*. Accelrys Software Inc., San Diego, CA., 2008.

[2] Habis Al-Zoubi, Nidal Hilal, Naif A Darwish, and Abdul W Mohammad. Rejection and modelling of sulphate and potassium salts by nanofiltration membranes: neural network and spiegler–kedem model. *Desalination*, 206(1-3):42–60, 2007.

[3] Ali Ayati, Mahdi Niknam Shahrak, Bahareh Tanhaei, and Mika Sillanpaa. Emerging adsorptive removal of azo dye by metal–organic frameworks. *Chemosphere*, 160:30–44, 2016.

[4] Said Benkhaya, Hassane Lgaz, Awad A Alrashdi, Souad M'rabet, Abderrahim El Bachiri,

Mohammed Assouag, Ill-Min Chung, and Ahmed El Harfi. Upgrading the performances of polysulfone/polyetherimide ultrafiltration composite membranes for dyes removal: Experimental and molecular dynamics studies. *J. Mol. Liq.*, 331:115743, 2021.

[5] Said Benkhaya, Hassane Lgaz, Selma Chraibi, Awad A Alrashdi, Mohamed Rafik, Han-Seung Lee, and Ahmed El Harfi. Polysulfone/polyetherimide ultrafiltration composite membranes constructed on a three-component nylon-fiberglass-nylon support for azo dyes removal: Experimental and molecular dynamics simulations. *Colloids Surf., A*, 625:126941, 2021.

[6] Said Benkhaya, Souad M'rabet, and Ahmed El Harfi. Classifications, properties, recent synthesis and applications of azo dyes. *Heliyon*, 6(1), 2020.

[7] Mohamed Berradi, Rachid Hsissou, Mohammed Khudhair, Mohammed Assouag, Omar Cherkaoui, Abderrahim El Bachiri, and Ahmed El Harfi. Textile finishing dyes and their impact on aquatic environs. *Heliyon*, 5(11):e02711, 2019.

[8] Supriyo Bhattacharya and Keith E Gubbins. Fast method for computing pore size distributions of model materials. *Langmuir*, 22(18):7726–7731, 2006.

[9] SM Burkinshaw and O Kabambe. Attempts to reduce water and chemical usage in the removal of bifunctional reactive dyes from cotton: Part 2 bis (vinyl sulfone), aminochlorotriazine/vinyl sulfone and bis (aminochlorotriazine/vinyl sulfone) dyes. *Dyes Pigm.*, 88(2):220–229, 2011.

[10] Giovanni Bussi, Tatyana Zykova-Timan, and Michele Parrinello. Isothermal-isobaric molecular dynamics using stochastic velocity rescaling. *J. Chem. Phys.*, 130(7):074101–074109, 2009.

[11] JN Chakraborty. *Fundamentals and practices in colouration of textiles*. CRC Press, 2015.

[12] Yen-Che Chiang, Yi-Zhe Hsub, Ruoh-Chyu Ruaan, Ching-Jung Chuang, and Kuo-Lun Tung. Nanofiltration membranes synthesized from hyperbranched polyethyleneimine. *J. Membr. Sci.*, 326(1):19–26, 2009.

[13] Kwun Lun Cho, Anita J Hill, Frank Caruso, and Sandra E Kentish. Chlorine resistant glutaraldehyde crosslinked polyelectrolyte multilayer membranes for desalination. *Adv. Mater*, 27(17):2791–2796, 2015.

[14] Tom Darden, Darrin York, and Lee Pedersen. Particle mesh ewald: An n· log (n) method for ewald sums in large systems. *J. Chem. Phys.*, 98(12):10089–10092, 1993.

[15] Kaushik Dey, Manas Pal, Kanhu Charan Rout, Shebeeb Kunjattu H, Anuja Das, Ra-

bibrata Mukherjee, Ulhas K Kharul, and Rahul Banerjee. Selective molecular separation by interfacially crystallized covalent organic framework thin films. *J. Am. Chem. Soc.*, 139(37):13083–13091, 2017.

[16] Minxia Ding, Aziz Ghoufi, and Anthony Szymczyk. Molecular simulations of polyamide reverse osmosis membranes. *Desalination*, 343:48–53, 2014.

[17] Minxia Ding, Anthony Szymczyk, and Aziz Ghoufi. On the structure and rejection of ions by a polyamide membrane in pressure-driven molecular dynamics simulations. *Desalination*, 368:76–80, 2015.

[18] T Driesner, TM Seward, and IG Tironi. Molecular dynamics simulation study of ionic hydration and ion association in dilute and 1 molal aqueous sodium chloride solutions from ambient to supercritical conditions. *Geochim. Cosmochim. Acta*, 62(18):3095–3107, 1998.

[19] Hani M El-Kaderi, Joseph R Hunt, Jose L Mendoza-Cortes, Adrien P Cote, Robert E Taylor, Michael O'Keeffe, and Omar M Yaghi. Designed synthesis of 3d covalent organic frameworks. *Science*, 316(5822):268–272, 2007.

[20] Hanqing Fan, Jinlong He, Mohammad Heiranian, Weiyi Pan, Ying Li, and Menachem Elimelech. The physical basis for solvent flow in organic solvent nanofiltration. *Science Advances*, 10(24):eado4332, 2024.

[21] Mahdi Fathizadeh, Huynh Ngoc Tien, Konstantin Khivantsev, Jung-Tsai Chen, and Miao Yu. Printing ultrathin graphene oxide nanofiltration membranes for water purification. *J. Mater. Chem. A*, 5(39):20860–20866, 2017.

[22] M. J. Frisch, G. W. Trucks, H. B. Schlegel, G. E. Scuseria, M. A. Robb, J. R. Cheeseman, G. Scalmani, V. Barone, G. A. Petersson, H. Nakatsuji, X. Li, M. Caricato, A. V. Marenich, J. Bloino, B. G. Janesko, R. Gomperts, B. Mennucci, H. P. Hratchian, J. V. Ortiz, A. F. Izmaylov, J. L. Sonnenberg, D. Williams-Young, F. Ding, F. Lipparini, F. Egidi, J. Goings, B. Peng, A. Petrone, T. Henderson, D. Ranasinghe, V. G. Zakrzewski, J. Gao, N. Rega, G. Zheng, W. Liang, M. Hada, M. Ehara, K. Toyota, R. Fukuda, J. Hasegawa, M. Ishida, T. Nakajima, Y. Honda, O. Kitao, H. Nakai, T. Vreven, K. Throssell, J. A. Montgomery, Jr., J. E. Peralta, F. Ogliaro, M. J. Bearpark, J. J. Heyd, E. N. Brothers, K. N. Kudin, V. N. Staroverov, T. A. Keith, R. Kobayashi, J. Normand, K. Raghavachari, A. P. Rendell, J. C. Burant, S. S. Iyengar, J. Tomasi, M. Cossi, J. M. Millam, M. Klene, C. Adamo, R. Cammi,

J. W. Ochterski, R. L. Martin, K. Morokuma, O. Farkas, J. B. Foresman, and D. J. Fox. Gaussian˜16 revision c.01, 2016. Gaussian Inc. Wallingford CT.

[23] Shoujian Gao, Yuzhang Zhu, Yuqiong Gong, Zhenyi Wang, Wangxi Fang, and Jian Jin. Ultrathin polyamide nanofiltration membrane fabricated on brush-painted single-walled carbon nanotube network support for ion sieving. *ACS nano*, 13(5):5278–5290, 2019.

[24] Weimin Gao, Fenghua She, Juan Zhang, Ludovic F Dumee, Li He, Peter D Hodgson, and Lingxue Kong. Understanding water and ion transport behaviour and permeability through poly (amide) thin film composite membrane. *J. Membr. Sci.*, 487:32–39, 2015.

[25] A Giwa, SW Hasan, A Yousuf, S Chakraborty, DJ Johnson, and N Hilal. Biomimetic membranes: A critical review of recent progress. *Desalination*, 420:403–424, 2017.

[26] Edward Harder, D Eric Walters, Yaroslav D Bodnar, Ron S Faibish, and Benoît Roux. Molecular dynamics study of a polymeric reverse osmosis membrane. *J. Phys. Chem. B*, 113(30):10177–10182, 2009.

[27] Jinlong He, Hanqing Fan, Menachem Elimelech, and Ying Li. Molecular simulations of organic solvent transport in dense polymer membranes: Solution-diffusion or pore-flow mechanism? *J. Membr. Sci.*, 708:123055, 2024.

[28] Natalia Candido Homem, Natalia de Camargo Lima Beluci, Sara Amorim, Rui Reis, Angelica Marquetotti Salcedo Vieira, Marcelo Fernandes Vieira, Rosangela Bergamasco, and Maria Teresa Pessoa Amorim. Surface modification of a polyethersulfone microfiltration membrane with graphene oxide for reactive dyes removal. *Appl. Surf. Sci.*, 486:499–507, 2019.

[29] Jing Huang and Alexander D MacKerell Jr. Charmm36 all-atom additive protein force field: Validation based on comparison to nmr data. *J. Comput. Chem.*, 34(25):2135–2145, 2013.

[30] William Humphrey, Andrew Dalke, and Klaus Schulten. VMD – Visual Molecular Dynamics. *J. Mol. Graphics*, 14:33–38, 1996.

[31] Jester N Itliong, C Villagracia Al Rey, Joaquin Lorenzo V Moreno, Kurt Irvin M Rojas, Gian Paolo O Bernardo, Melanie Y David, Robby B Manrique, Aristotle T Ubando, Alvin B Culaba, Allan Abraham B Padama, et al. Investigation of reverse ionic diffusion in forward-osmosis-aided dewatering of microalgae: A molecular dynamics study. *Bioresour. Technol.*, 279:181–188, 2019.

[32] Maria F Jimenez-Solomon, Qilei Song, Kim E Jelfs, Marta Munoz-Ibanez, and Andrew G

Livingston. Polymer nanofilms with enhanced microporosity by interfacial polymerization. *Nat. Mater.*, 15(7):760–767, 2016.

[33] William L Jorgensen, Jayaraman Chandrasekhar, Jeffry D Madura, Roger W Impey, and Michael L Klein. Comparison of simple potential functions for simulating liquid water. *J. Chem. Phys.*, 79(2):926–935, 1983.

[34] Mohammed Kadhom, Noor Albayati, Hayder Alalwan, and Mustafa Al-Furaiji. Removal of dyes by agricultural waste. *Sustainable Chem. Pharm.*, 16:100259, 2020.

[35] Sharath Kandambeth, Bishnu P Biswal, Harshal D Chaudhari, Kanhu Charan Rout, H Shebeeb Kunjattu, Shouvik Mitra, Suvendu Karak, Anuja Das, Rabibrata Mukherjee, Ulhas K Kharul, et al. Selective molecular sieving in self-standing porous covalent-organic-framework membranes. *Adv. Mater.*, 29(2), 2016.

[36] Sharath Kandambeth, Arijit Mallick, Binit Lukose, Manoj V Mane, Thomas Heine, and Rahul Banerjee. Construction of crystalline 2d covalent organic frameworks with remarkable chemical (acid/base) stability via a combined reversible and irreversible route. *J. Am. Chem. Soc.*, 134(48):19524–19527, 2012.

[37] Santanu Karan, Zhiwei Jiang, and Andrew G Livingston. Sub–10 nm polyamide nanofilms with ultrafast solvent transport for molecular separation. *Science*, 348(6241):1347–1351, 2015.

[38] MJ Kotelyanskii, NJ Wagner, and ME Paulaitis. Molecular dynamics simulation study of the mechanisms of water diffusion in a hydrated, amorphous polyamide. *Comput. Theor. Polym. Sci.*, 9(3-4):301–306, 1999.

[39] Qin Li, Zhipeng Liao, Xiaofeng Fang, Dapeng Wang, Jia Xie, Xiuyun Sun, Lianjun Wang, and Jiansheng Li. Tannic acid-polyethyleneimine crosslinked loose nanofiltration membrane for dye/salt mixture separation. *J. Membr. Sci.*, 584:324–332, 2019.

[40] Wanbin Li. Metal–organic framework membranes: Production, modification, and applications. *Prog. Mater. Sci.*, 100:21–63, 2019.

[41] Yuanzhe Liang, Yuzhang Zhu, Cheng Liu, Kueir-Rarn Lee, Wei-Song Hung, Zhenyi Wang, Youyong Li, Menachem Elimelech, Jian Jin, and Shihong Lin. Polyamide nanofiltration membrane with highly uniform sub-nanometre pores for sub-1 å precision separation. *Nat. Commun.*, 11(1):2015, 2020.

[42] Jiuyang Lin, Wenyuan Ye, Jie Huang, Borrego Ricard, Marian-Cornel Baltaru, Benjamin Greydanus, Stefan Balta, Jiangnan Shen, Maria Vlad, Arcadio Sotto, et al. Toward re-

source recovery from textile wastewater: dye extraction, water and base/acid regeneration using a hybrid nf-bmed process. *ACS Sustainable Chem. Eng.*, 3(9):1993–2001, 2015.

[43] J Lyu, X Wen, U Kumar, Y You, V Chen, and RK Joshi. Separation and purification using go and r-go membranes. *RSC Adv.*, 8(41):23130–23151, 2018.

[44] Xiao Ma, Pengli Chen, Ming Zhou, Zhaoxiang Zhong, Feng Zhang, and Weihong Xing. Tight ultrafiltration ceramic membrane for separation of dyes and mixed salts (both nacl/na2so4) in textile wastewater treatment. *Ind. Eng. Chem. Res.*, 56(24):7070–7079, 2017.

[45] R Mancinelli, A Botti, F Bruni, MA Ricci, and AK Soper. Hydration of sodium, potassium, and chloride ions in solution and the concept of structure maker/breaker. *J. Phys. Chem. B*, 111(48):13570–13577, 2007.

[46] Patrizia Marchetti, Maria F Jimenez Solomon, Gyorgy Szekely, and Andrew G Livingston. Molecular separation with organic solvent nanofiltration: a critical review. *Chem. Rev.*, 114(21):10735–10806, 2014.

[47] Chelsea R Martinez and Brent L Iverson. Rethinking the term "pi-stacking". *Chem. Sci.*, 3(7):2191–2201, 2012.

[48] Leandro Martinez, Ricardo Andrade, Ernesto G Birgin, and Jose Mario Martinez. Packmol: a package for building initial configurations for molecular dynamics simulations. *J. Comput. Chem.*, 30(13):2157–2164, 2009.

[49] MATLAB. *version 7.10.0 (R2010a)*. The MathWorks Inc., Natick, Massachusetts, 2010.

[50] Abdul Wahab Mohammad, YH Teow, WL Ang, YT Chung, DL Oatley-Radcliffe, and Nidal Hilal. Nanofiltration membranes review: Recent advances and future prospects. *Desalination*, 356:226–254, 2015.

[51] Gunolla Nagendraprasad, Vasista Adupa, K Anki Reddy, Chandan Das, and Santanu Karan. Semiaromatic polyamide-based membrane in forward osmosis: Molecular insights. *J. Phys. Chem. B*, 127(30):6751–6766, 2023.

[52] Gunolla Nagendraprasad, K Anki Reddy, Santanu Karan, and Chandan Das. Nonpreferential solvent transport through an intrinsic cyclodextrin pore in a polyester film. *J. Phys. Chem. B*, 2024.

[53] K Grace Pavithra, VJJOI Jaikumar, et al. Removal of colorants from wastewater: A review on sources and treatment strategies. *J. Ind. Eng. Chem.*, 75:1–19, 2019.

[54] James C Phillips, David J Hardy, Julio DC Maia, John E Stone, João V Ribeiro, Rafael C

Bernardi, Ronak Buch, Giacomo Fiorin, Jérôme Hénin, Wei Jiang, et al. Scalable molecular dynamics on cpu and gpu architectures with namd. *J. Chem. Phys.*, 153(4):044130, 2020.

[55] Manas Ranjan Puhan, Pulak Sarkar, Gunolla Nagendraprasad, K Anki Reddy, Bhaumik Sutariya, and Santanu Karan. Unraveling anomalies in preferential liquid transport through the intrinsic pores of cyclodextrin in polyester nanofilms. *Advanced Materials*, 36(36):2404164, 2024.

[56] Pulak Sarkar, Solagna Modak, and Santanu Karan. Effect of porous and nonporous nanostructures on the permeance of positively charged nanofilm composite membranes. *Adv. Mater. Inter.*, 7(19):2000251, 2020.

[57] Pulak Sarkar, Solagna Modak, and Santanu Karan. Ultraselective and highly permeable polyamide nanofilms for ionic and molecular nanofiltration. *Adv. Funct. Mater.*, 31(3):2007054, 2021.

[58] Pulak Sarkar, Santanu Ray, Bhaumik Sutariya, Jayesh C Chaudhari, and Santanu Karan. Precise separation of small neutral solutes with mixed-diamine-based nanofiltration membranes and the impact of solvent activation. *Sep. Purif. Technol.*, 279:119692, 2021.

[59] Matthias Georg Schwab, Birgit Fassbender, Hans Wolfgang Spiess, Arne Thomas, Xinliang Feng, and Klaus Mullen. Catalyst-free preparation of melamine-based microporous polymer networks through schiff base chemistry. *J. Am. Chem. Soc.*, 131(21):7216–7217, 2009.

[60] Sudip Kumar Sen, Smita Raut, Partha Bandyopadhyay, and Sangeeta Raut. Fungal decolouration and degradation of azo dyes: a review. *Fungal Biol. Rev.*, 30(3):112–133, 2016.

[61] Issara Sereewatthanawut, Fui Wen Lim, Yogesh S Bhole, Dominic Ormerod, Andras Horvath, Andrew T Boam, and Andrew G Livingston. Demonstration of molecular purification in polar aprotic solvents by organic solvent nanofiltration. *Org. Process Res. Dev.*, 14(3):600–611, 2010.

[62] Maulin P Shah and Susana Rodriguez-Couto. *Microbial wastewater treatment*. Elsevier, 2019.

[63] Meng Shen, Sinan Keten, and Richard M Lueptow. Rejection mechanisms for contaminants in polyamide reverse osmosis membranes. *J. Membr. Sci.*, 509:36–47, 2016.

[64] Na Song, Xueli Gao, Zhun Ma, Xiaojuan Wang, Yi Wei, and Congjie Gao. A review of graphene-based separation membrane: Materials, characteristics, preparation and applications. *Desalination*, 437:59–72, 2018.

[65] James JP Stewart. Optimization of parameters for semiempirical methods i. method. *J. Comput. Chem.*, 10(2):209–220, 1989.

[66] William C Swope, Hans C Andersen, Peter H Berens, and Kent R Wilson. A computer simulation method for the calculation of equilibrium constants for the formation of physical clusters of molecules: Application to small water clusters. *J. Chem. Phys.*, 76(1):637–649, 1982.

[67] Karishma Tiwari, Solagna Modak, Pulak Sarkar, Santanu Ray, Vasista Adupa, K Anki Reddy, Sumit Kumar Pramanik, Amitava Das, and Santanu Karan. Interfacial synthesis of large-area ultrathin polyimine nanofilms as molecular separation membrane. *Iscience*, 25(4), 2022.

[68] Karishma Tiwari, Pulak Sarkar, Solagna Modak, Harwinder Singh, Sumit Kumar Pramanik, Santanu Karan, and Amitava Das. Large area self-assembled ultrathin polyimine nanofilms formed at the liquid–liquid interface used for molecular separation. *Adv. Mater.*, 32(8):1905621, 2020.

[69] Kenno Vanommeslaeghe, Elizabeth Hatcher, Chayan Acharya, Sibsankar Kundu, Shijun Zhong, Jihyun Shim, Eva Darian, Olgun Guvench, P Lopes, Igor Vorobyov, et al. Charmm general force field: A force field for drug-like molecules compatible with the charmm all-atom additive biological force fields. *J. Comput. Chem.*, 31(4):671–690, 2010.

[70] Kenno Vanommeslaeghe and Alexander D MacKerell Jr. Automation of the charmm general force field (cgenff) i: bond perception and atom typing. *J. Chem. Inf. Model.*, 52(12):3144–3154, 2012.

[71] Rhea Verbeke, Veronica Gomez, and Ivo FJ Vankelecom. Chlorine-resistance of reverse osmosis (ro) polyamide membranes. *Prog. Polym. Sci*, 72:1–15, 2017.

[72] Jing Wang, Junyong Zhu, Misgina Tilahun Tsehaye, Jian Li, Guanying Dong, Shushan Yuan, Xin Li, Yatao Zhang, Jindun Liu, and Bart Van der Bruggen. High flux electroneutral loose nanofiltration membranes based on rapid deposition of polydopamine/polyethyleneimine. *J. Mater. Chem. A*, 5(28):14847–14857, 2017.

[73] Tao Wei, Lin Zhang, Haiyang Zhao, Heng Ma, Md Symon Jahan Sajib, Hua Jiang, and Sohail Murad. Aromatic polyamide reverse-osmosis membrane: an atomistic molecular dynamics simulation. *J. Phys. Chem. B*, 120(39):10311–10318, 2016.

[74] Dihua Wu, Sanchuan Yu, Darren Lawless, and Xianshe Feng. Thin film composite nanofiltration membranes fabricated from polymeric amine polyethylenimine imbedded with

monomeric amine piperazine for enhanced salt separations. *React. Funct. Polym.*, 86:168–183, 2015.

[75] Mengyuan Wu, Jinqiu Yuan, Hong Wu, Yanlei Su, Hao Yang, Xinda You, Runnan Zhang, Xueyi He, Niaz Ali Khan, Roni Kasher, et al. Ultrathin nanofiltration membrane with polydopamine-covalent organic framework interlayer for enhanced permeability and structural stability. *J. Membr. Sci.*, 576:131–141, 2019.

[76] Yujian Yao, Pingxia Zhang, Chao Jiang, Ryan M DuChanois, Xuan Zhang, and Menachem Elimelech. High performance polyester reverse osmosis desalination membrane with chlorine resistance. *Nat. Sustainability*, 4(2):138–146, 2021.

[77] Xinda You, Ke Xiao, Hong Wu, Yafei Li, Runlai Li, Jinqiu Yuan, Runnan Zhang, Zhiming Zhang, Xu Liang, Jianliang Shen, et al. Electrostatic-modulated interfacial polymerization toward ultra-permselective nanofiltration membranes. *Iscience*, 24(4), 2021.

[78] Wenbo Yu, Xibing He, Kenno Vanommeslaeghe, and Alexander D MacKerell Jr. Extension of the charmm general force field to sulfonyl-containing compounds and its utility in biomolecular simulations. *J. Comput. Chem.*, 33(31):2451–2468, 2012.

[79] Daqiang Yuan, Weigang Lu, Dan Zhao, and Hong-Cai Zhou. Highly stable porous polymer networks with exceptionally high gas-uptake capacities. *Adv. Mater.*, 23(32):3723–3725, 2011.

[80] Jianhua Yun, Yixing Wang, Zhenying Liu, Yujie Li, Hu Yang, and Zhen-liang Xu. High efficient dye removal with hydrolyzed ethanolamine-polyacrylonitrile uf membrane: Rejection of anionic dye and selective adsorption of cationic dye. *Chemosphere*, 259:127390, 2020.

[81] Noureddine Zouhri, Mohamed Igouzal, Majdouline Larif, Mahmoud Hafsi, Mohamed Taky, and Azzedine Elmidaoui. Prediction of salt rejection by nanofiltration and reverse osmosis membranes using spiegler-kedem model and an optimisation procedure. *Desalin. Water Treat.*, 120:41–50, 2018.

Chapter 6

Investigating Solvent Activation of Polyamide Nanofilm Composite Membranes: Insights from Experimental and Molecular Modelling Approaches[1]

6.1 Introduction

Membrane-based separation processes using nanofilm composite membranes hold significant potential in organic solvent nanofiltration for removing undesired organic molecules from organic solvents, size-selective molecular separation from mixed solutes, and solvent recycling [1]. These membranes are widely used for reverse osmosis applications and are generally fabricated via interfacial polymerization using traditional monomers such as $m-$phenylenediamine (MPD) and trimesoyl chloride (TMC) which produces a network crosslinked fully aromatic polyamide structure with a molecular weight cut-off (MWCO) of ≈300 Da [2]. Additionally, advanced materials and fabrication methods, including intrinsically microporous polymers [3, 4], spiro-cyclic

[1]G. Nagendraprasad, Pulak Sarkar, K. Anki Reddy, C. Das, Manas Ranjan Puhan, S. Karan, Investigating Solvent Activation of Polyamide Nanofilm Composite Membranes: Insights from Experimental and Molecular Modelling Approaches, submitted to Journal of Membrane Science.

polymers [5], covalent organic frameworks (COFs) [6], and conjugated microporous polymers (CMPs) [7], have also been developed using solvent-stable supports to produce membranes with superior solvent permeance. However, their economic viability for industrial-scale applications remains a key concern.

To address this, the effect of post-solvent-activation of traditional fully aromatic polyamide membranes has been studied in recent years [2, 8–15]. Furthermore, the impact of treating polyamide membranes with alcohols [9–12], polar aprotic solvents [2, 8], or their aqueous mixtures [13–15] has been widely studied. These treatments show variable outcomes, with permeance enhancements often being negligible or accompanied by compromised salt rejection [9–15]. For instance, mild solvents like aliphatic alcohols result in minimal improvements in water permeance [9–12], while stronger solvents such as N-methylpyrrolidone (NMP), dimethylformamide (DMF), and dimethyl sulfoxide (DMSO) significantly enhance water permeance but often reduce NaCl rejection [13–15]. Despite these challenges, solvent activation has shown potential for repurposing high salt-rejecting brackish water reverse osmosis (BWRO) membranes into nanofiltration (NF) membranes with reduced NaCl rejection while retaining high rejection of divalent anions [15]. Short-term activation with polar aprotic solvents or their aqueous mixtures induces swelling and performance changes in polyamide membranes [14, 15]. Although water permeance may significantly increase after post-activation, the permeance of aqueous solutions containing polar aprotic solvents remains relatively low [14]. These permeance enhancements are primarily attributed to the activation effects of polar aprotic solvents on aromatic polyamide membranes derived from MPD and TMC monomers. However, semi-aromatic polyamide membranes (e.g., PIP-TMC and PEI-TMC) show minimal improvement with mild polar solvents like methanol or ethanol compared to strong polar aprotic solvents [8, 10, 12]. Activation with DMF has also been shown to improve methanol permeance while maintaining dye rejection [2].

Despite these advances, the full potential of polyamide nanofilm composite membranes for their applications in various organic solvents remains largely unexplored. Further research is required to better understand their separation properties, selective ion transport behaviour in aqueous phases, and the structural dynamics of their interactions with solvents. The structural modifications of nanofilms following post-solvent activation need to be examined in detail to elucidate changes in pore size distribution and their correlation with solvent permeance. Concerns also persist regarding the structural stability of post-solvent-activated nanofilms, particularly

in the absence of solvent or during solvent exchange processes.

In this study, we investigate the behaviour of solvent permeation through post-solvent-activated polyamide membranes, validated by molecular dynamics (MD) simulations. Experimentally, a freestanding polyamide nanofilm was synthesized via interfacial polymerization at the water-hexane interface and transferred onto a porous alumina substrate. A corresponding model polyamide nanofilm was designed for simulation studies, where equilibrium molecular dynamics (EMD) simulations analyzed its structure and properties. The simulation results corroborate experimental findings, offering insights into density profiles, pore size distribution, solvent uptake, and solvent permeance. Additionally, the mechanism of solvent transport through the membrane, including solvent pathways and interactions, was elucidated. These findings provide a comprehensive understanding on the permeation behaviour of polyamide membranes in methanol and DMF, paving the way for optimized applications and identifying their limitations.

6.2 Simulation Methodology

6.2.1 Construction of the Atomic Model of the Membrane

All molecular dynamics (MD) simulations were performed using NAMD [16], with force field parameters compatible with CHARMM36m obtained via CGenFF v2.5 [17, 18]. The average partial charges were assigned to symmetrically related atoms in each monomer [19], and their 2D schematic structures with partial charges on the atoms are presented in Figure 6.1. A computationally constructed crosslinked polyamide membrane was generated via a heuristic approach. Initially, 1500 MPD and 960 TMO monomers, whose 3D chemical structures are depicted in 6.2(a,b), were randomly distributed within a simulation box (100 Å × 100 Å × 50 Å) using PACKMOL [20], as illustrated in Figure 6.2d. The randomly packed monomeric mixture was energy minimized and equilibrated at constant pressure for 5 ns under periodic boundary conditions. Subsequently, the system was annealed at 1100 K for 1 ns under constant volume, followed by a gradual cooling to 300 K in 50 K steps. The simulation was then continued in an NVT ensemble at 300 K but interrupted every 5 ps to form amide bonds by removing a $-OH$ from the TMO carboxylic ($-COOH$) group and a hydrogen atom in $-NH_2$ from the MPD monomer (see 6.2c) when a TMO monomer was within a user-defined

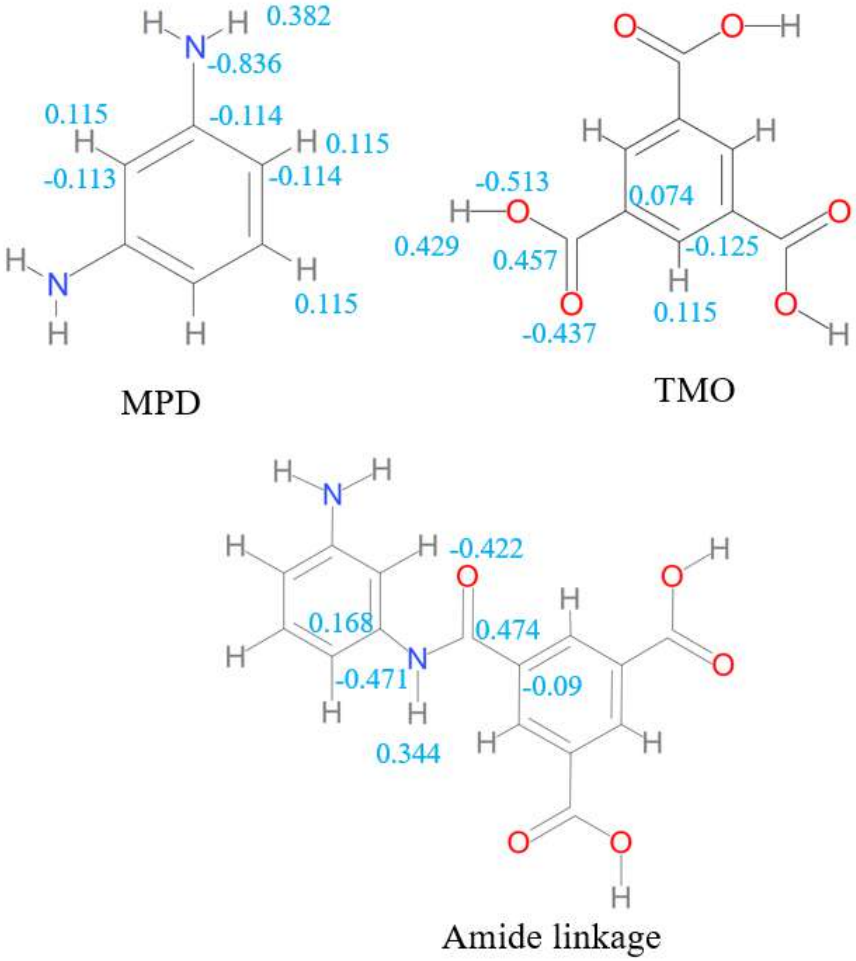

Figure 6.1: CHARMM36m general force field was used for MPD, TMO and amide linkage. Cgenff server is used to obtain the CHARMM compatable force field parameters for monomers and amide linkage. Average partial charges were assaigned to symmetrically related atoms in each monomers

distance (see Figure 6.2e). This user-defined distance varied from 3.5 $\AA$ to 4.5 $\AA$ with a step of 0.2 $\AA$ (incremented for every 200 steps). Following each crosslinking event, the system was energy minimized and equilibrated to identify new amide bonds. Figure 6.3a illustrates the number of bonds formed during each 5 ps cycle, demonstrating the formation of polymeric clusters within 1 ns. After 1 ns, the formation of new amide bonds slowed significantly as the crosslinked monomer clusters grew, hindering further monomer diffusion. After continuing the polymerization process for 5 ns, unreacted monomers were removed from the simulation box resulting in a polymerized membrane. This polymerized membrane comprises several polymeric

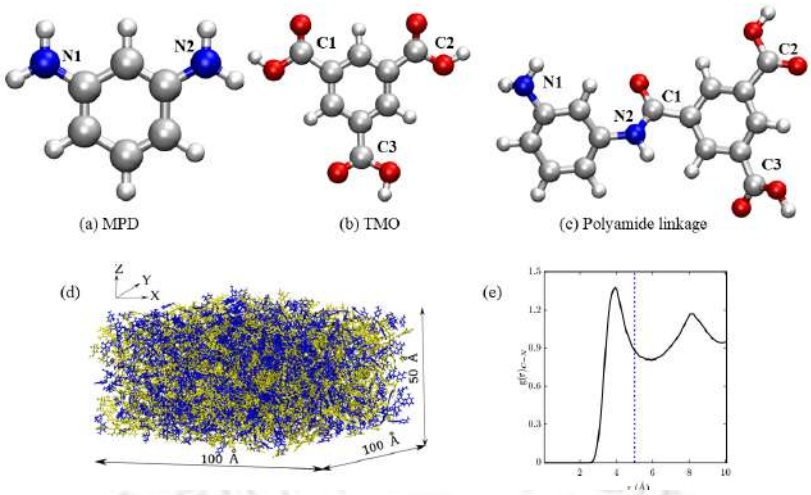

Figure 6.2: (a) $m-$phenylenediamine (MPD) (b) Hydrolysed trimesoyl chloride (TMO) (c) Amide linkage between MPD and TMO (d) Initial configuration prior to polymerization (color code: blue for MPD, yellow for TMO) (e) RDF between the carbon atom of a carboxylic acid group ($-$COOH) of TMO and the amide group ($-NH_2$) nitrogen atom of MPD after annealing in an NVT ensemble.

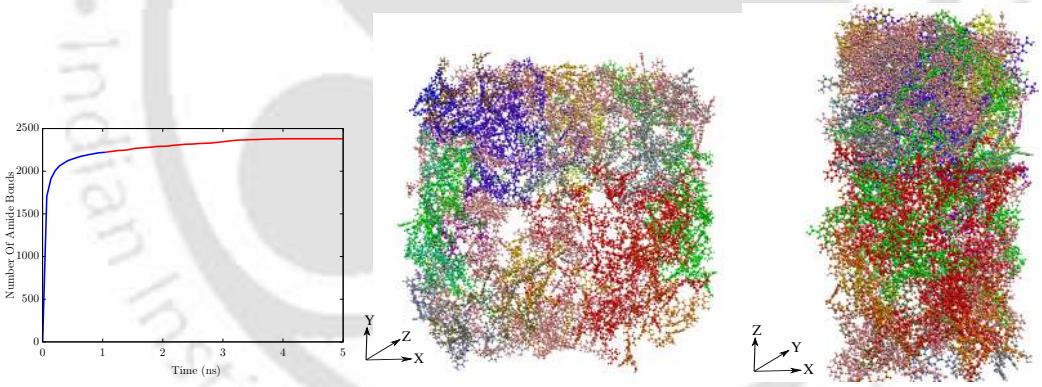

Figure 6.3: (a) Number of amide bonds formed during polymerisation (b) Top view of polymerised clusters in the membrane (c) Side view of polymerised clusters in the membrane

chains with different number of monomers. As shown in Figure 6.3 (b, c) the largest polymer chain contains 204 monomeric units, while another polymer chain consists of 134 units. The remaining polymer chains within the membrane contain between 10 and 72 monomeric units. The degree of crosslinking was determined using the equation provided in the literature [21].

$$DC = \frac{100N_N}{N_N + N_{COOH} + N_{NH_2}} \tag{6.1}$$

where N_N is the number of amide−linkages, N_{COOH} is the number of unreacted −COOH groups of TMO monomer and N_{NH_2} is the number of unreacted $-NH_2$ groups of MPD monomer in the membrane. The crosslinking degree of the membrane was found to be 69.8%, which is consistent with the value from the previously reported atomistic simulations [22]. Additionally, the monomeric ratio between MPD and TMO (1.46), the oxygen-to-nitrogen ratio in the amidelinkage (1.24), and the dry membrane density (0.80 g cm^{-3}) were in agreement with the values reported in previous simulation studies [22–24].

6.2.2 Equlibrium Molecular Dynamics Simulations

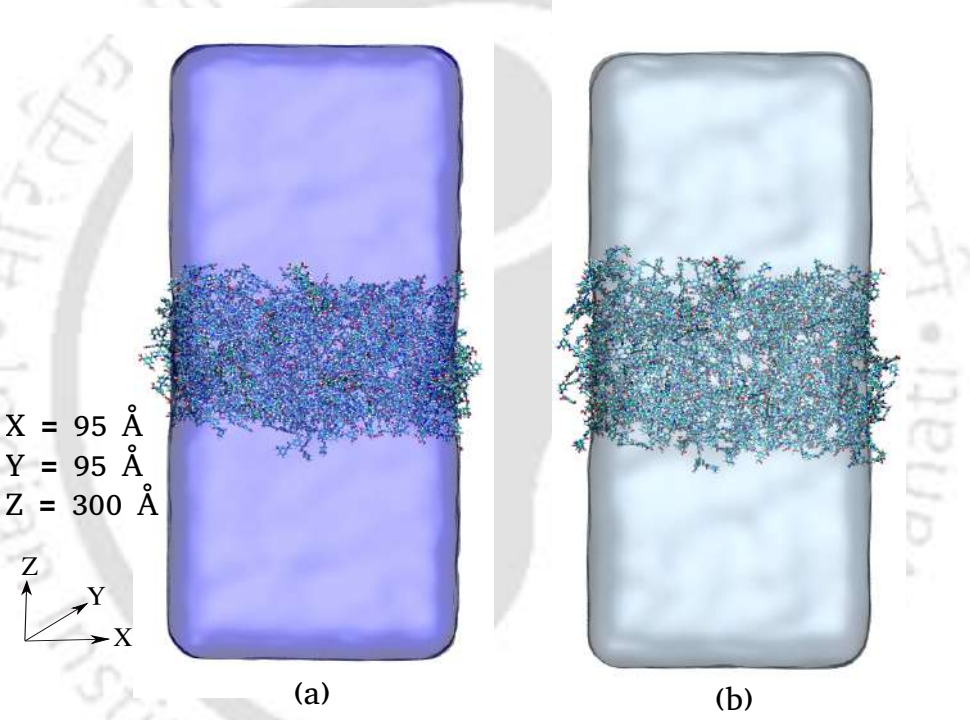

Figure 6.4: (a) Membrane is submerged in methanol (b) Membrane is submerged in DMF

To understand the transport of methanol and DMF in a polyamide membrane, we solvated the dry membrane (M_1) in equilibrated solvents separately. The resulting systems (Figure 6.4) were labeled M_2 (dry membrane equilibrated in methanol) and M_3 (dry membrane equilibrated in DMF). These systems were further equilibrated for 100 ns in an NPT ensemble at a temperature of 300 K and a pressure of 1 atm. The DMF was then removed from M_3, and again, it was equilibrated in methanol, creating the M_4 system. The M_4 system was then equilibrated in an NPT ensemble at 300 K and 1 atm pressure for 100 ns. In this process, some of the membrane

atoms were constrained. Later, methanol was removed from the equilibrated M_4 membrane, and subsequently, the resulting system was further equilibrated in the NPT ensemble for 30 ns to get a dry membrane (M_5). This process is considered a single cycle of DMF activation. The interactions of the membrane with the solvents were considered as a combination of van der Waals (vdW) and electrostatic interactions. The vdW interactions were calculated using the Lennard-Jones potential with a cut-off distance of 12 $\mathring{A}$ and a switching distance of 10 $\mathring{A}$, and the long-range electrostatic interactions were evaluated by the Particle Mesh Ewald (PME) method with a grid spacing of 1 $\mathring{A}$ [25]. The temperature was maintained using a modified Nose-Hoover thermostat [26], and the pressure was controlled using Langevin dynamics with a damping factor of 5 ps^{-1}[27]. The velocity Verlet integrator [28] is used to integrate the equations of motion, and the time step was set to 1 fs with trajectories saved every 20 ps. Periodic boundary conditions (PBC) were applied in all the three directions. The results presented in this manuscript are averaged over three independent simulations, we consider the last 30 ns of the simulation run to compute density, pore-size distribution, solvent flux, and free energy.

6.3 Results and Discussion

6.3.1 Molecular Dynamics Simulation Study of the Membrane and the Effect of Solvent Activation

Table 6.1: Density of the membranes

Serial no.	Membrane name	Conditions	ρ (g.cm^{-3})
1	M_1	Dry membrane	0.80
2	M_2	M_1 in methanol	1.06
3	M_3	M_1 in DMF	1.08
4	M_4	DMF−activated membrane (M_3) in methanol	0.97
5	M_5	M_4 after drying	1.29

To further provide insights on the influence of solvent activation in the permeation of the solvents through the polyamide nanofilm, we performed atomistic molecular dynamics (MD)

simulations. A single cycle of DMF activation followed by drying of the polyamide membrane was considered to investigate the structural properties of the solvent-activated membranes and solvent transport inside the membrane. To analyse the membrane structure, we computed the density profiles of the solvent and membrane atoms in the simulation system along the z-direction. The bulk densities of the membranes are shown in Table 6.1. Figure 6.5a shows the mass density profile of methanol molecules inside the membrane (M_2) and the overall simulation system, it suggests that the density of the membrane in methanol after DMF activation (M_4) is lower than that of the membrane in methanol before DMF activation (M_2) due to swelling. Figure 6.5b represents the mass density profile of DMF molecules inside the membrane (M_3) and the overall system. Additionally, Figure 6.5c shows the mass density profile of the membranes and highlights the significant increase in the dried membrane density due to a decrease in the free volume in the membrane (Table 6.1).

The pore size distribution (PSD) of the membranes was computed using the Monte Carlo method [29] with a 0.5 $\mathring{A}$ radius spherical probe. The PSD of each membrane is displayed in Figure 6.5(d-h). Before calculating the PSD, the methanol and DMF within the membrane were removed from their respective simulation systems. The result shows that the pore radii within the M_1 membrane range from $0.6 - 5.4$ $\mathring{A}$, with prominent pores ranging from $1 - 4$ $\mathring{A}$. The pore radii for M_2, M_3, and M_4 range from 0.6 - 6 $\mathring{A}$, with prominent pores ranging from $2 - 5$ $\mathring{A}$. As shown in Figure 6.5e and f, the pores with slightly larger areas appear in the DMF-activated membrane (M_3) as compared to the membrane in methanol (M_2) solvent due to the swelling effect. In addition, for the dry membrane (M_5) after DMF activation, the pores get narrower due to the structural re-arrangement in the membrane. Based on the PSD data, it is evident that the choice of solvent plays a crucial role for the overall structural modification of the membrane, and predominant structural modification was observed for the DMF-activated membrane. To better understand the structural modifications upon solvent activation, the 3D morphology of the membranes is presented in Figure 6.6. The grey colour indicates the occupied volume of the membrane and the blue colour indicates the accessible volume for the solvent transport.

To further understand the membrane interaction with methanol and DMF, we computed the solvent uptake, defined as $m_{solvent}/m_{polymer} \times 100\%$, where $m_{solvent}$ and $m_{polymer}$ are the masses of solvent and polymer, respectively. The solvent content as a function of time inside the membrane is shown in Figure 6.7a. The amount of DMF uptake was found to be ≈150

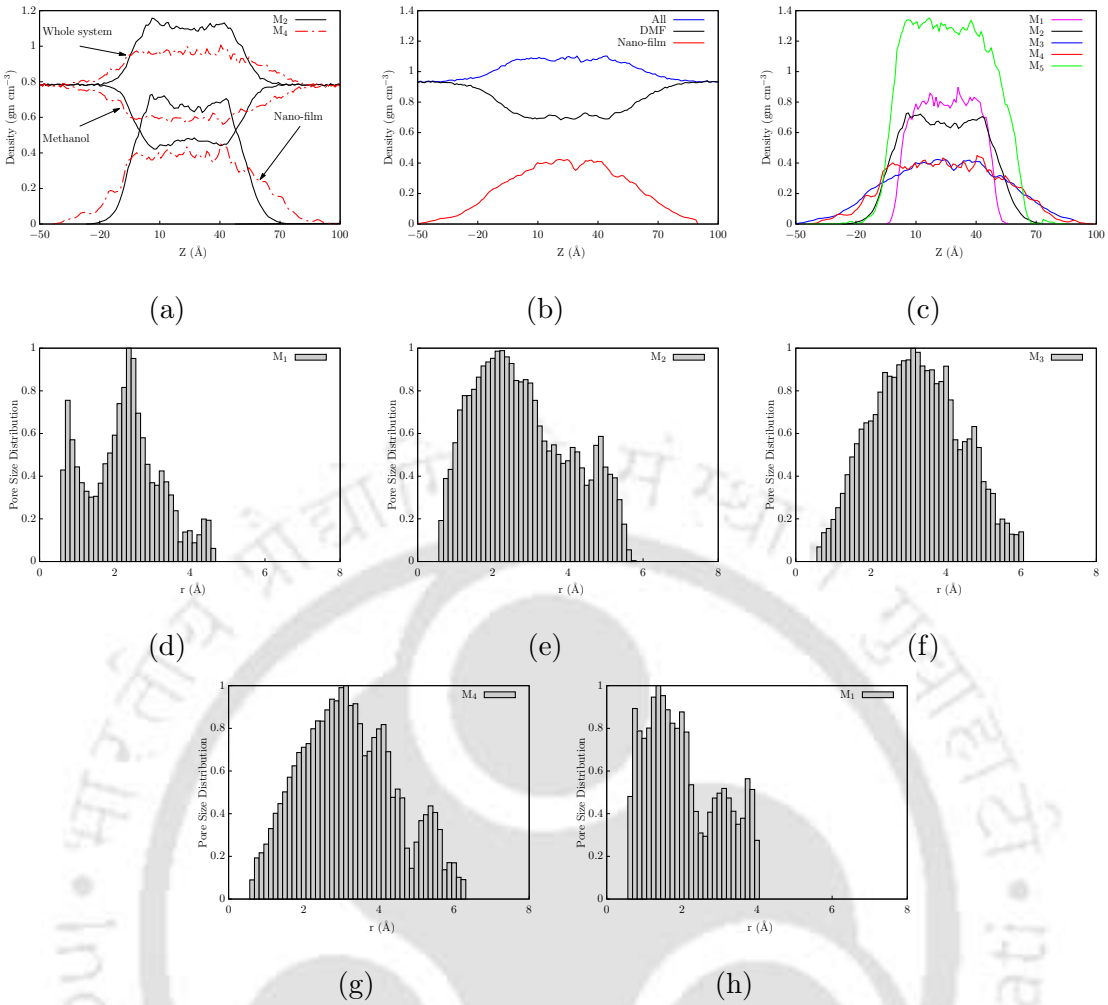

Figure 6.5: Density profiles of the polyamide membranes used in molecular modelling. Where (a) Density profiles of methanol inside the membrane, membrane (M_2 and M_4), and the overall system. (b) Density profiles of DMF inside the membrane, membrane (M_3), and the overall system. (c) Density profiles of the nanofilms (d), (e), (f), (g), (h) shows the pore size distribution of M_1, M_2, M_3, M_4, and M_5, respectively.

wt% in the membrane (M_3). The DMF-activated membrane exhibits a much higher uptake of methanol (≈220 wt%) in the membrane (M_4) than the methanol uptake (≈60 wt%) in the non-DMFactivated membrane (M_2). The smaller kinetic diameter of methanol helps to accommodate the higher amount of methanol molecules inside the membrane compared to DMF. For comparison, polyamide-based TFC membranes may swell up to 109 wt% in methanol and 140 wt% in DMF [30, 31]. Our simulated results are consistent with these experimentally reported values [30, 31].

To understand the impact of solvent activation and transport, the free energy barrier for

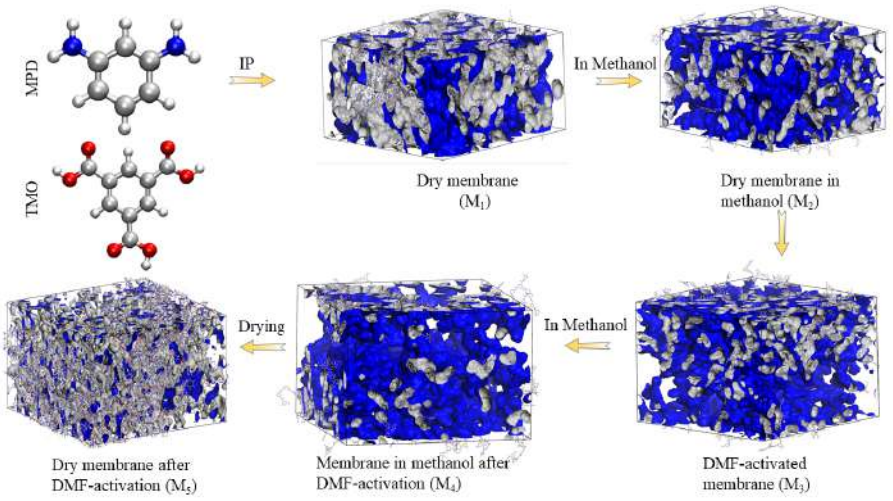

Figure 6.6: Three-dimensional (3D) view of the simulated polyamide membrane's free volume as a result of molecular modelling. Where M_1 represents the 3D morphology of the dry membrane, M_2 represents the 3D morphology of the dry membrane in methanol, M_3 represents the 3D morphology of the DMF−activated membrane, M_4 represents the 3D morphology of the membrane in methanol after DMF activation, and M_5 represents the 3D morphology of the dry membrane after DMF activation. The voids in the membrane models are shown by the gray shading, while the openings to the voids are shown in blue.

the solvents along the membrane thickness (Z-axis) was computed using below equation [32]:

$$F(Z) = -k_B T ln \frac{\rho(Z)}{\rho} \tag{6.2}$$

where F(Z) is the free energy profile, ρ(Z) is the density profile at position Z, k_B is the Boltzman constant, and T is the temperature. Figure 6.7b plots -k_BTln(ρ(Z)/ρ) of methanol and DMF along the Z-direction of the membranes (M_2, M_3, and M_4). It is observed that M_2 membrane exhibits the greatest energy barrier for methanol transport, followed by M_3 membrane; M_4 shows the lowest barrier, concluding DMF−activated membrane provides high methanol transport.

Solvent flux is determined by the solvent-membrane affinity combination with the physicochemical properties of that solvent. The solvent flux, influenced by the solventmembrane affinity, was determined by counting the number of molecules that permeated through the membrane in a simulated time. In equilibrium molecular dynamics (EMD) simulations, no external pressure is applied; solvent flux relies solely on the thermal motion of solvent molecules.

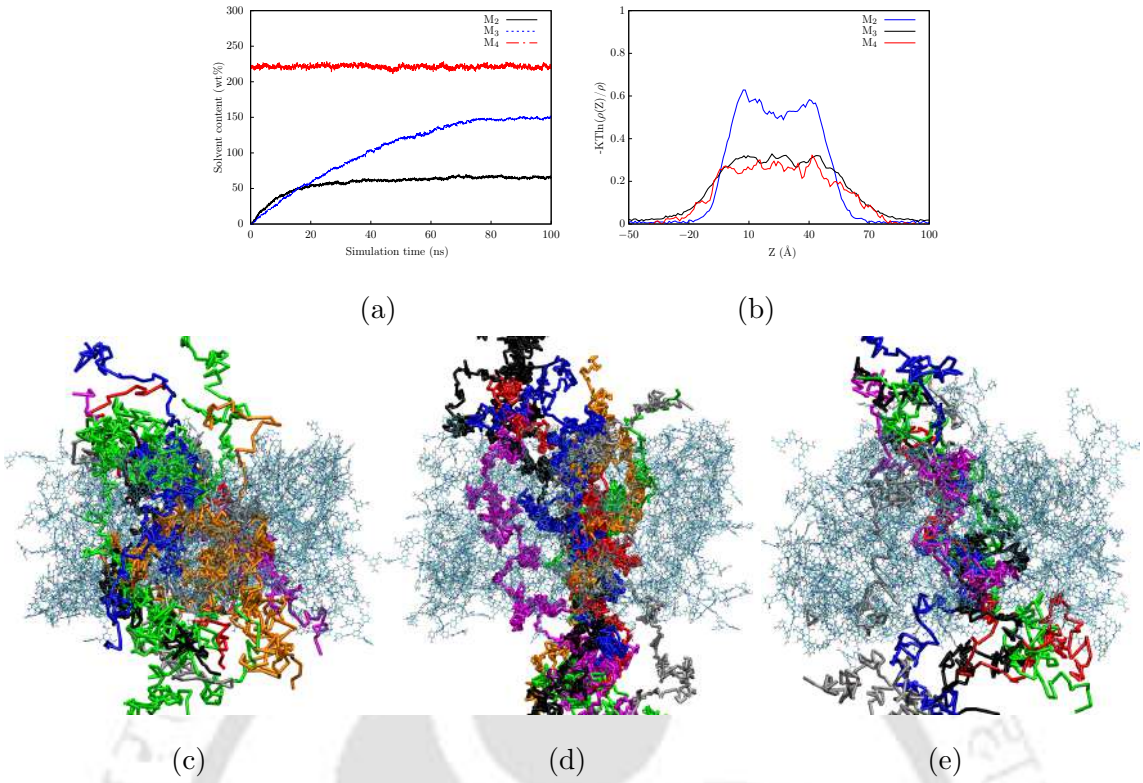

Figure 6.7: Swelling dynamics: (a) solvent content in the inner layer and (b) Free energy profiles for methanol and DMF solvents along the membrane thickness (Z-axis direction); The solvent molecule trajectories through the membranes are shown in (c-e) where (c) represents the pathways of methanol molecules in the M_2 membrane, (d) the pathways of DMF molecules in the M_3 membrane and (e) the pathways of methanol molecules in the M_4 membrane.

Solvent molecules permeate at equal rates in both directions (+Z or -Z). The solvent flux is then calculated using the formula V/ (2. A.t), where V is the volume of solvent permeated through the membrane area (A) over the simulation time (t). Figure B.20 displays the solvent flux of solvent-induced membranes, showing that the DMF-activated membrane (M_4) exhibits a higher solvent flux than the non-DMF-activated membrane (M_2). Specifically, the simulated methanol solvent flux through membrane M_2 is 4.48 $\times$ 10^4 $Lm^{-1}hr^{-1}$, DMF solvent flux through membrane M_3 is 0.35 $\times$ 10^4 $Lm^{-1}hr^{-1}$, and methanol solvent flux through membrane M_4 is 9.59 $\times$ 10^4 $Lm^{-1}hr^{-1}$. Additionally, it is significant that methanol permeance through the DMF-activated membrane increased significantly which was also validate the experimental results. It is important to note that the simulated results we obtained were higher than the experimental values. As a result, the data of macroscale solvent flux from experimental research may not be precisely replicated by these simulated membranes. However, the simulated membranes

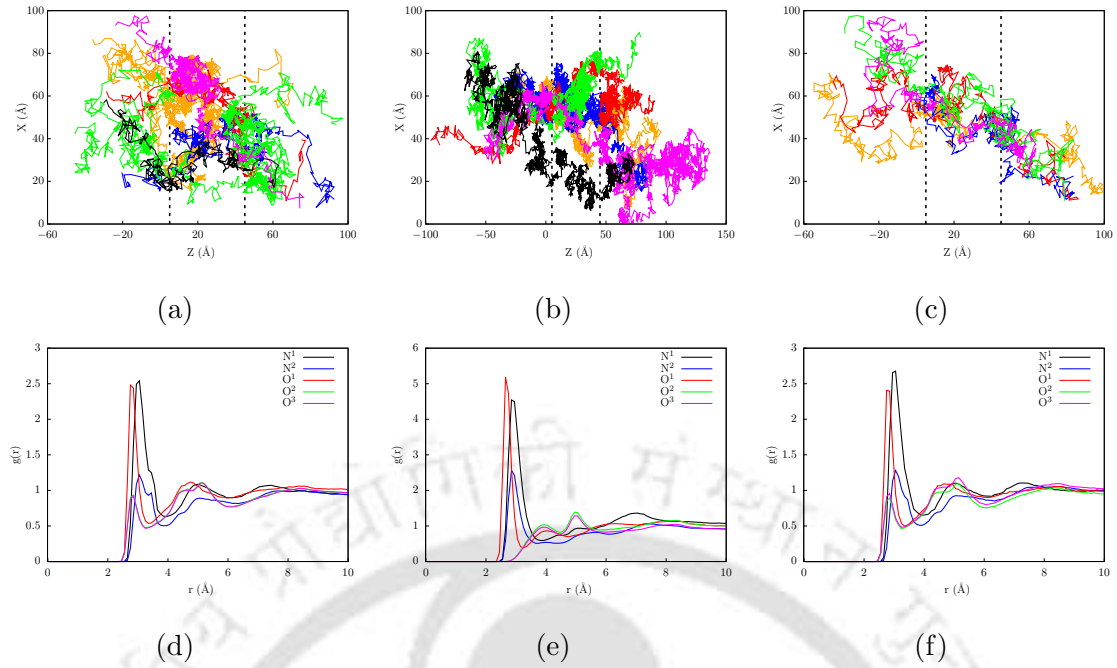

Figure 6.8: Path of the solvent molecule trajectories through the membranes. Where (a) Trajectories of methanol molecules in the M_2 membrane represented in XZ 2D plane, (b) Trajectories of DMF molecules in the M_3 membrane represented in XZ 2D plane, (c) Trajectories of methanol molecules in the M_4 membrane represented in XZ 2D plane. The RDF between the oxygen atoms of methanol and DMF solvents is computed with the membrane functional group atoms. Here N^1 indicates the nitrogen atoms in unreacted $-NH_2$ groups, N^2 represents the nitrogen atoms in amide linkage, O^1 represents the hydroxyl group oxygen atoms of TMC monomers, O^2 represents the oxygen atoms in $-C{=}O$ of $-COOH$ in TMC monomer, and O^3 represents the oxygen atoms in amide linkage. (d) The RDF of M_2 membrane with methanol solvent (e) The RDF of M_3 membrane with DMF solvent (e) The RDF of M_4 membrane with methanol solvent

atomic-level structure is sufficient to provide insight into; how the membranes Angstrom-scale molecular structure affects the solvent transport. Additionally, the trajectories of methanol and DMF molecules were computed as they permeate through the membrane. The selected solvent molecule pathways are shown in Figure 6.7c–e, even though many solvent molecules permeated through the membrane. Figure 6.7c illustrates the trajectories of the methanol molecules through M_2, while Figure 6.7d shows the trajectories of the DMF molecules through M_3. Figure 6.7e represents the pathways of methanol molecules through M_4.

To investigate the solvent transport mechanism through the membranes, individual molec-

ular pathways were observed. Figure 6.8a−c shows the pathways of selected solvent molecules in a 2D plot on the XZ plane (see Figure B.21 for the 2D YZ plane). From the trajectories of methanol molecules in Figure 6.8a, molecules follow a random path as they interact with the neighbouring molecules and membrane atoms. Before entering the membrane, molecules return to bulk methanol solution and reach the membrane boundary as neighbouring molecules buffet them. As indicated in the line segment (magenta colour), the molecule follows a random path as it occupies the pore by interacting with membrane atoms and solvent molecules. This pore appears smaller around 10 Å in diameter but elongated to 30 $\mathring{A}$ (from 30 - 60 $\mathring{A}$ on the X-axis). Later the molecule hops into another wider pore, buffet with the existing molecule, and occupies the pore. Finally, the molecule comes out of the membrane toward the right side. It is observed that most methanol molecules follow similar pathways from one side to the other. The DMF molecules exhibit similar transport mechanisms, however, the specifics vary depending on the exact trajectory and, to some extent, on molecule size. For example, the methanol molecule in Figure 6.8a remains trapped near the left boundary of the membrane. However, the molecule quickly travels to the other side of the membrane. The random movements of the solvent molecules within the pores and interactions with the membrane atoms, enable the solvents to pass through the membrane. The trajectory of DMF molecules in Figure 6.8b differs slightly from the methanol molecules; the pore volumes are larger and broader than the methanol-induced membrane. However, because of its larger size and associated steric effects, it has a narrower trajectory with limited freedom to move randomly within the pore than methanol molecules. Similarly, we have quantified the pathways of methanol molecules in the M_4 membrane as shown in Figure 6.8c. Here, methanol molecules easily permeated through the membrane, unlike the M_2 membrane due to the availability of free volume within the membrane. The radial distribution functions g(r) are also computed to understand the membrane-solvent interactions in solvent transport.

$$g_{ij}(r) = \frac{N_{ij}(r, r + \Delta r)V}{4\pi r^2 \Delta r N_i N_j} \tag{6.3}$$

where r is the distance between atoms i and molecules j, N_{ij}(r, r + Δr) is the number of atom j around i within a shell from r to r + Δr, V is the system volume, and N_i and N_j are the numbers of atoms i and j, respectively. Figure 6.8(d-f) illustrates the g(r) for the solvents around the selected atoms of the membrane. For both solvents, a high peak at about 2.75 $\mathring{A}$ is observed around the oxygen atom (O^1) and 3.05 $\mathring{A}$ for nitrogen (N^1) atoms in the membrane.

This illustrates that methanol and DMF solvents interact preferentially with the unreacted functional groups of the membrane.

6.3.2 Experimental Validation on DMF Activation of the Polyamide Membrane on the Permeance of Methanol

While the present thesis primarily focuses on atomistic simulations, for completeness of the present chapter, we have validated the permeance behavior of polyamide membranes through four cycles of DMF activation. These experiments were conducted by Dr. Santanu Karan, Principal Scientist in the MS&ST Division at CSIR-CSMCRI, Bhavnagar, Gujarat, India. This chapter has been submitted to the Journal of Membrane Science as a collaborative work, integrating experimental and atomistic insights. The detailed experimental procedures are provided in Appendix B.3 of this thesis.

To evaluate the effect of DMF activation on the permeance of methanol through polyamide membrane, the initial methanol permeance was measured. The membrane was then activated by passing DMF through it for 15 min at an operating pressure of 1 bar at 25 °, followed by washing with methanol. The methanol permeance was subsequently re-measured, and the membrane was dried. This sequence of steps is referred to as a cycle of activation. Figure B.23a illustrates the methanol permeance before and after DMF activation, as well as following the drying of the polyamide membrane over four different cycles. Prior to DMF activation, the initial methanol permeance was 7.3 $Lm^{-1}hr^{-1}bar^{-1}$. During the first cycle, the methanol permeance increased significantly to 23.4 $Lm^{-1}hr^{-1}bar^{-1}$ upon DMF activation. However, after drying, the methanol permeance decreased to 7.8 $Lm^{-1}hr^{-1}bar^{-1}$, which is close to the initial value of the dry membrane. The same activation procedure was repeated for three additional cycles. As shown in Figure B.23a, the final methanol permeance after four cycles of DMF activation reached 19.7 $Lm^{-1}hr^{-1}bar^{-1}$. Nevertheless, the methanol permeance after drying remained nearly unchanged at approximately 8.5 $Lm^{-1}hr^{-1}bar^{-1}$, similar to the initial permeance of the dry membrane. This indicates that the network structure of the polyamide membrane reverts to its initial state after each activation and drying process. It can thus be concluded that molecularlevel modifications occur in the polyamide membrane, as the permeance does not exhibit significant variation after four cycles of activation and drying. The changes in methanol permeance following DMF activation and subsequent drying are presented in B.23b.

The figure shows that the increase in methanol permeance upon DMF activation for each cycle ranges from 2.8 to 3.1 times the initial value of the methanol permeance of the dry membrane. After drying, the decrease in methanol permeance is between 2.5 to 3.2 times the value of the methanol permeance after DMF activation. These results demonstrate that polyamide membranes exhibit consistent structural behaviour, with comparable percentage increases and decreases in methanol permeance after each activation and drying cycle. This suggests that the structural orientation of the polyamide membranes remains stable and recurs identically following these processes.

The impact of activation on the presence of water in the activating solvent was investigated using different ratios of DMF and water mixtures (Figure B.23c). In cycle 1, where 80% water was mixed with pure DMF to activate the membrane, the methanol permeance was reduced by 30% from its initial value after activation. After drying the membrane, no significant reduction in methanol permeance was observed. This reduction in permeance is attributed to the presence of water in the activation solution, which promotes the formation of a hydrogen-bonded network structure within the polyamide membrane. This network restricts the structural modification of the polyamide structure. In cycle 2, the membrane was activated using a DMF solution containing 50% water, with methanol permeance measured both without and with drying. The permeance of methanol remained unchanged and no effect of DMF activation was observed. This indicates that the hydrogen-bonded network structure is not disrupted when 50% water is present in the DMF solution. When the DMF concentration was increased to 80%, the methanol permeance after activation rose to 85% of its initial value, but it dropped to 75% after drying. This suggests that higher DMF concentrations during activation disrupt the hydrogen-bonded network structure, leading to structural expansion of the polyamide membrane. In the final cycle, pure DMF was used for activation, resulting in a methanol permeance of 17.7 $Lm^{-1}hr^{-1}bar^{-1}$ after activation (Figure B.23c). This value is similar to the methanol permeance of virgin polyamide membranes activated with pure DMF, as shown in Figure B.23a. After drying, the final methanol permeance was 2.8 times, similar to the result observed for the membrane activated directly with pure DMF (Figure B.23b). This suggests that the overall network structure of the polyamide membrane remains consistent regardless of the activation conditions. Figure B.24 and B.25 show no discernible difference in the surface morphology before and after DMF activation.

6.4 Conclusions

In conclusion, this study demonstrated solvent transport through solvent-activated polyamide membranes by integrating experimental findings with molecular insights from molecular simulations. It examined the distribution of pore sizes, solvent uptake, and the methanol permeation behaviour in DMF-activated polyamide membranes. The molecular dynamics (MD) simulation effectively validates the experimental results for solvent permeance in solvent-activated membranes by modelling the solvent-activated membrane affinity. Furthermore, the structural characteristics of the polyamide membranes were characterized before and after solvent activation. This modelling work reliably elucidates the quantitative structure-property-performance relationship of polyamide membranes. The findings offer a comprehensive understanding of the behaviour and molecular mechanisms of polyamide membranes in different solvents, highlighting their potential applications in organic solvent environments.

Bibliography

[1] Patrizia Marchetti, Maria F Jimenez Solomon, Gyorgy Szekely, and Andrew G Livingston. Molecular separation with organic solvent nanofiltration: a critical review. *Chem. Rev.*, 114(21):10735–10806, 2014.

[2] Santanu Karan, Zhiwei Jiang, and Andrew G Livingston. Sub–10 nm polyamide nanofilms with ultrafast solvent transport for molecular separation. *Science*, 348(6241):1347–1351, 2015.

[3] Manas Ranjan Puhan, Pulak Sarkar, Gunolla Nagendraprasad, K Anki Reddy, Bhaumik Sutariya, and Santanu Karan. Unraveling anomalies in preferential liquid transport through the intrinsic pores of cyclodextrin in polyester nanofilms. *Adv. Mater.*, 36(36): 2404164, 2024.

[4] Zhiwei Jiang, Ruijiao Dong, Austin M Evans, Niklas Biere, Mahmood A Ebrahim, Siyao Li, Dario Anselmetti, William R Dichtel, and Andrew G Livingston. Aligned macrocycle pores in ultrathin films for accurate molecular sieving. *Nature*, 609(7925):58–64, 2022.

[5] Nicholas C Bruno, Ronita Mathias, Young Joo Lee, Guanghui Zhu, Yun-Ho Ahn, Neel D Rangnekar, JR Johnson, Scott Hoy, Irene Bechis, Andrew Tarzia, et al. Solution-processable polytriazoles from spirocyclic monomers for membrane-based hydrocarbon separations. *Nat. Mater.*, 22(12):1540–1547, 2023.

[6] Hongjian Wang, Yeming Zhai, Yang Li, Yu Cao, Benbing Shi, Runlai Li, Zingting Zhu, Haifei Jiang, Zheyuan Guo, Meidi Wang, et al. Covalent organic framework membranes for efficient separation of monovalent cations. *Nat. Commun.*, 13(1):7123, 2022.

[7] Rifan Hardian, Kristen A Miller, Levente Cseri, Soumyabrata Roy, Jessica M Gayle, Robert Vajtai, Pulickel M Ajayan, and Gyorgy Szekely. 2d conjugated microporous polymer membranes for organic solvent nanofiltration. *Chem. Eng. J.*, 452:139457, 2023.

[8] Pulak Sarkar, Solagna Modak, and Santanu Karan. Ultraselective and highly permeable polyamide nanofilms for ionic and molecular nanofiltration. *Adv. Funct. Mater.*, 31(3): 2007054, 2021.

[9] Jennifer Sarah Louie, Ingo Pinnau, and Martin Reinhard. Effects of surface coating process conditions on the water permeation and salt rejection properties of composite polyamide reverse osmosis membranes. *J. Membr. Sci.*, 367(1-2):249–255, 2011.

[10] Manas Ranjan Puhan, Bhaumik Sutariya, and Santanu Karan. Revisiting the alkali hydrolysis of polyamide nanofiltration membranes. *J. Membr. Sci.*, 661:120887, 2022.

[11] Ashish Kulkarni, Debabrata Mukherjee, and William N Gill. Flux enhancement by hydrophilization of thin film composite reverse osmosis membranes. *J. Membr. Sci.*, 114(1): 39–50, 1996.

[12] Ruijun Zhang, Song Su, Shanshan Gao, and Jiayu Tian. Reconstruction of the polyamide film in nanofiltration membranes via the post-treatment with a ternary mixture of ethanol-water-naoh: Mechanism and effect. *Desalination*, 519:115317, 2021.

[13] Min Gyu Shin, Jin Young Seo, Hosik Park, You-In Park, and Jung-Hyun Lee. Overcoming the permeability-selectivity trade-off of desalination membranes via controlled solvent activation. *J. Membr. Sci.*, 620:118870, 2021.

[14] Arpita Sahoo, Manas Ranjan Puhan, Dinesh Bahadursing Vasave, Nitin G Borle, Bhaumik Sutariya, and Santanu Karan. Harnessing the potential of thin film composite membranes for efficient treatment of aqueous streams containing polar aprotic organic solvents. *Chem. Pap.*, 78(2):793–808, 2024.

[15] Min Gyu Shin, Soon Jin Kwon, Hosik Park, You-In Park, and Jung-Hyun Lee. High-performance and acid-resistant nanofiltration membranes prepared by solvent activation on polyamide reverse osmosis membranes. *J. Membr. Sci.*, 595:117590, 2020.

[16] James C Phillips, David J Hardy, Julio DC Maia, John E Stone, Joao V Ribeiro, Rafael C Bernardi, Ronak Buch, Giacomo Fiorin, Jerome Henin, Wei Jiang, et al. Scalable molecular dynamics on cpu and gpu architectures with namd. *J. Chem. Phys.*, 153(4):044130, 2020.

[17] Jumin Lee, Xi Cheng, Jason M Swails, Min Sun Yeom, Peter K Eastman, Justin A Lemkul, Shuai Wei, Joshua Buckner, Jong Cheol Jeong, Yifei Qi, et al. Charmm-gui input generator for namd, gromacs, amber, openmm, and charmm/openmm simulations using the charmm36 additive force field. *J. Chem. Theory Comput.*, 12(1):405–413, 2016.

[18] Jing Huang and Alexander D MacKerell Jr. Charmm36 all-atom additive protein force field: Validation based on comparison to nmr data. *J. Comput. Chem.*, 34(25):2135–2145, 2013.

[19] Edward Harder, D Eric Walters, Yaroslav D Bodnar, Ron S Faibish, and Benoît Roux. Molecular dynamics study of a polymeric reverse osmosis membrane. *J. Phys. Chem. B*, 113(30):10177–10182, 2009.

[20] Leandro Martinez, Ricardo Andrade, Ernesto G Birgin, and Jose Mario Martinez. Packmol:

a package for building initial configurations for molecular dynamics simulations. *J. Comput. Chem.*, 30(13):2157–2164, 2009.

[21] Gunolla Nagendraprasad, Vasista Adupa, K Anki Reddy, Chandan Das, and Santanu Karan. Semiaromatic polyamide-based membrane in forward osmosis: Molecular insights. *J. Phys. Chem. B*, 127(30):6751–6766, 2023.

[22] Tao Wei, Lin Zhang, Haiyang Zhao, Heng Ma, Md Symon Jahan Sajib, Hua Jiang, and Sohail Murad. Aromatic polyamide reverse-osmosis membrane: an atomistic molecular dynamics simulation. *J. Phys. Chem. B*, 120(39):10311–10318, 2016.

[23] Minxia Ding, Anthony Szymczyk, Florent Goujon, Armand Soldera, and Aziz Ghoufi. Structure and dynamics of water confined in a polyamide reverse-osmosis membrane: A molecular-simulation study. *J. Membr. Sci.*, 458:236–244, 2014.

[24] Luying Wang, Randall S Dumont, and James M Dickson. Molecular dynamic simulations of pressure-driven water transport through polyamide nanofiltration membranes at different membrane densities. *RSC Adv.*, 6(68):63586–63596, 2016.

[25] Tom Darden, Darrin York, and Lee Pedersen. Particle mesh ewald: An n· log (n) method for ewald sums in large systems. *J. Chem. Phys.*, 98(12):10089–10092, 1993.

[26] Giovanni Bussi, Tatyana Zykova-Timan, and Michele Parrinello. Isothermal-isobaric molecular dynamics using stochastic velocity rescaling. *J. Chem. Phys.*, 130(7):074101–074109, 2009.

[27] Scott E Feller, Yuhong Zhang, Richard W Pastor, and Bernard R Brooks. Constant pressure molecular dynamics simulation: the langevin piston method. *J. Chem. Phys.*, 103(11):4613–4621, 1995.

[28] William C Swope, Hans C Andersen, Peter H Berens, and Kent R Wilson. A computer simulation method for the calculation of equilibrium constants for the formation of physical clusters of molecules: Application to small water clusters. *J. Chem. Phys.*, 76(1):637–649, 1982.

[29] Supriyo Bhattacharya and Keith E Gubbins. Fast method for computing pore size distributions of model materials. *Langmuir*, 22(18):7726–7731, 2006.

[30] Min Gyu Shin, Wansuk Choi, June Huh, William D Mulhearn, Jung Sun Hwang, Christopher M Stafford, Jeong F Kim, and Jung-Hyun Lee. Solvent transport model for polyamide nanofilm membranes based on accurate hansen solubility parameters. *J. Membr. Sci.*, 674: 121505, 2023.

[31] Yi Li, Junyong Zhu, Sha Li, Zhong Guo, and Bart Van der Bruggen. Flexible aliphatic–aromatic polyamide thin film composite membrane for highly efficient organic solvent nanofiltration. *ACS Appl. Mater. Interfaces*, 12(28):31962–31974, 2020.

[32] Daan Frenkel and Berend Smit. *Understanding molecular simulation: from algorithms to applications*. Elsevier, 2023.

Chapter 7

Conclusions and Future Scope

7.1 Conclusions

From the equilibrium and non-equilibrium MD simulations performed in this Ph.D dissertation study, following conclusions are made:

- Investigating the performance of the semi−aromatic polyamide (SAPA) membrane in forward osmosis highlights several key findings. Water molecules traversing the membrane exhibit a reduced coordination number, resulting in fewer hydrogen bonds per molecule within the membrane. The unreacted functional groups in the membrane at the feed solution/membrane interface facilitate the water molecules to enter the membrane interior. The high density of −COOH functional groups at the water-interfacial region and optimal cross-linking density enhance water transport across the membrane. The ability to trap divalent ions and allow monovalent ions highlights the potential of the SAPA membrane for efficient separation processes and treatment of textile industry wastewater.

- Despite a slight difference in the densities of the membranes, pore connectivity under dynamic conditions and the resulting tortuous pathways for the transport of water and hexane molecules varied amongst polyester membranes. The water and hexane uptake of the membrane directly depends on the free volume within the membrane. Water and hexane pathways imply that solvent transport through the membrane is relatively fast in some places and appears to be trapped in others, waiting to hop into the next pore until they find pathways that open as a result of membrane dynamics. Furthermore, the EMD simulations have revealed that the interconnected hydrophilic cavities formed through

ester linkages are more favorable channels for transporting polar and non−polar solvents through the membranes. It is observed that uncross−linked cyclodextrin molecules facilitate the transport of both solvents, and water molecules permeate the CD−pore via hydrogen bonds among the water molecules. The hexane solvent flux is an order of magnitude lower compared to the water permeance. Our findings conclude that both solvents primarily traverse through the polar aggregate pores in the cross−linked membranes rather than the CD cavity, indicating a lack of functional significance of macrocyclic molecules in solvent transport and the existence of Janus pathways.

- Non-equilibrium molecular dynamics simulations were performed on a polyimine-based membrane, where the feed solution consists of NaCl salt and dye in water. We observed that this polyimine membrane exhibits a high water permeance of 8.3 $\times$ 10^3 $Lm^{-2}hr^{-1}bar^{-1}$, complete rejection of BBR dye (100%), and selective passage of chloride salt (i.e., rejection = 34%). Our study suggests that, while chloride salt ions permeate the membrane, they permeate near the melamine heterocyclic ring compared to the benzene ring of the TFP monomer in the membrane, and dye is rejected due to strong interactions between the benzene rings of dye and the TFP monomer on the membrane surface. This study suggests that monomers with non-aromatic rings are the preferred choices for the permeation of monovalent salt. Analysis of NaCl and dye trajectories and salt ion interactions with membrane atoms suggests that the membrane allows chloride salt permeation while completely rejecting dye, enabling efficient dye separation using a polyimine membrane. Such a membrane, capable of rejecting dye while allowing NaCl passage, could significantly enhance wastewater treatment in the textile industry.

- The performance of solvent-activated polyamide membranes were studied using experimental and molecular dynamics simulation studies. It examined the distribution of pore sizes, solvent uptake, and the methanol permeation behaviour in DMF-activated polyamide membranes. The molecular dynamics (MD) simulation effectively validates the experimental results for solvent permeance in solvent-activated membranes by modelling the solvent-activated membrane affinity. Furthermore, the structural characteristics of the polyamide membranes were characterized before and after solvent activation. This modelling work reliably elucidates the quantitative structure-property-performance relationship of polyamide membranes. The findings offer a comprehensive understanding of

the behaviour and molecular mechanisms of polyamide membranes in different solvents, highlighting their potential applications in organic solvent environments.

7.2 Scope for Future Investigations

The findings from this thesis provide several avenues for future research and development in the field of polymeric membranes using molecular dynamics simulations. Each objective of this thesis highlights critical insights and potential advancements that could significantly enhance the application of polymeric membranes in various separation processes.

- **Exploration of Semi-Aromatic Polyamide (SAPA) membranes with diverse draw solutions:**

  A promising approach in the forward osmosis (FO) process involves exploring diverse draw solutions with SAPA membranes and evaluating performance in challenging feed environments. Ensuring sustainability requires focusing on the regeneration and reuse of draw solutions, making the integration of membrane distillation with FO systems essential. Future efforts will aim to develop and apply this composite simulation setup to various feed and draw solutions, assessing membrane performance and draw solution regeneration. Additionally, research should optimize the density and distribution of $-COOH$ functional groups and cross-linking density to enhance water permeability and selectivity.

- **Preferential solvent transport through intrinsic cyclodextrin pore in a polyester Film:**

  The investigation into cyclodextrin (CD)-based polyester membranes has revealed unique solvent transport mechanisms through interconnected hydrophilic cavities. Future research should explore modifying CD-based membranes to enhance pore connectivity and reduce tortuosity, thereby improving solvent uptake and transport rates. Additionally, functionalizing CD molecules with specific groups to enhance selectivity and affinity for target solvents should be further investigated.

- **Solvent activation of fully aromatic polyamide-based membranes:**

  The research on fully aromatic polyamide membranes has elucidated the solvent uptake and transport pathways for methanol and DMF. Future work should focus on structural

modifications of these membranes to enhance solvent-specific selectivity and permeance. Additionally, investigating the effects of various solvent environments on membrane performance presents a promising direction for further study.

- **Polyimine-based membranes for nanofiltration:**

  The development and simulation of polyimine-based membranes for nanofiltration show promising results in high water flux and selective dye rejection. Future research should explore the scalability of imine-based membrane production, their stability under various conditions, and their application in real-world wastewater treatment, focusing on long-term performance and fouling resistance.

- **General future directions:**

  Integrating multi-scale modeling by combining molecular dynamics with continuum-scale modeling can provide a comprehensive understanding of membrane performance. Advanced material design, guided by simulation insights, could lead to the development of membranes with unprecedented characteristics. Assessing the environmental impact and sustainability of these membranes is crucial, considering production methods, material lifecycle, and recycling potential. Additionally, extending research to other separation processes, such as gas separation, biomedical applications, and energy-related separations, can leverage the unique properties of the investigated membranes.

We hope that the findings presented in this study will serve as valuable insights for future research on polymeric membranes in desalination and wastewater treatment applications.

Appendix A

Research Output

Articles Published

- **G. Nagendraprasad**, V. Adupa, K. Anki Reddy, C. Das, S. Karan, Semiaromatic polyamide based membrane in forward osmosis: Molecular insights, **J. Phys. Chem. B** 127 (30) (2023) 6751–6766.

- **G. Nagendraprasad**, K. Anki Reddy, S. Karan, C. Das, Non−Preferential Solvent Transport Through Intrinsic Cyclodextrin Pore in a Polyester Film, **J. Phys. Chem. B** 127 (30) (2024) 6751–6766.

Manuscripts under preparation

- G. Nagendraprasad, K Anki Reddy,Chandan Das, and Santanu Karan "Atomistic Insights into High-Performance Polyimine-based Membranes for Selective Dye Rejection and Salt Permeation in Nanofiltration" (**revision submitted to Chemical Engineering Science**)

- G. Nagendraprasad, Pulak Sarkar, K Anki Reddy, Chandan Das, Manas Ranjan Puhan, and Santanu Karan, "Investigating Solvent Activation of Polyamide Nanofilm Composite Membranes: Insights from Experimental and Molecular Modelling Approaches" (**submitted to Journal of Membrane Science**)

Conferences

- Presented a research poster at the Outreach Symposium on "**Molecular Simulations: Advances and Applications**", organized by the **Department of Chemical Engineering, IIT Bombay** during 2^{nd} - 3^{rd} June, 2023.
- Presented a research poster in **SCIENTIFIQUE : POSTER PRESENTATION** under department of Chemical Engineering at "**Research & Industrial Conclave - Integration'23**" organized by the **Student's Academic Board, IIT Guwahati and IIT Guwahati Research Park** during 14-16^{th} May, 2023.

Collaborations

- Debarati Mukherjee, Pradip Das, **Gunolla Nagendra Prasad**, Anki Reddy Katha, Sasidhar Gumma and Bishnupada Mandal. "Hierarchical graphite oxide decorated UiO-66 for ultrahigh adsorption of dye with synergistic effect of ultrasonication: Experimental and density functional theory study." **Sep. Purif. Technol.**, 294 (2022), Article 121217.
- Manas Ranjan Puhan, Pulak Sarkar, Amal R, **Gunolla Nagendraprasad**, K. Anki Reddy, Bhaumik Sutariya, and Santanu Karana "Unravelling anomalies in preferential liquid transport through the intrinsic pores of cyclodextrin in polyester nanofilms" (**Adv. Mater.**)

Appendix B

Supplementary Information for Specific Chapters

B.1 Supplementary Information for Chapter 4

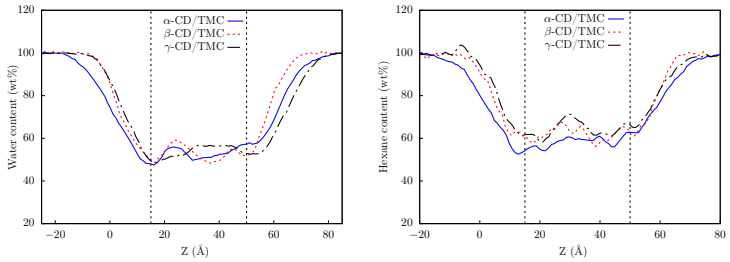

(a) (b)

Figure B.1: (a) Profile of local water content along the z-axis (b) Profile of local hexane content along the z-axis; the verticle lines represents the bulk portion of the membranes

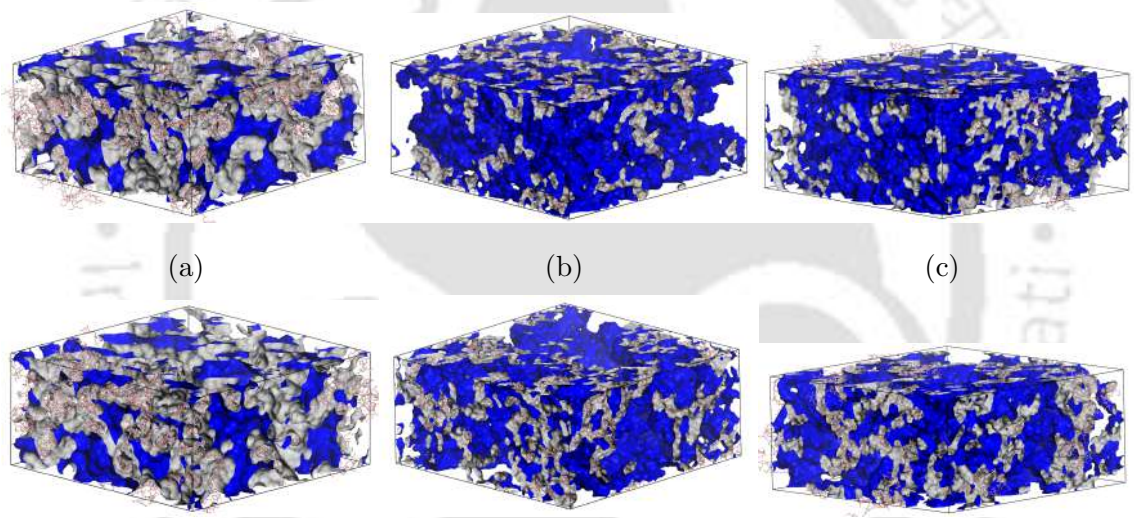

(a) (b) (c)

(d) (e) (f)

Figure B.2: 3D morphology of the membranes visualized using Material Studio Connolly surface module, where blue color represents the accesible free volume for water, while gray indicates the occupied volume of the membrane (a) α-CD/TMC (b) β-CD/TMC (c) γ-CD/TMC; 3D morphology of the membranes visualized using Material Studio Connolly surface module, where blue color represents the accesible free volume for hexane, while gray indicates the occupied volume of the membrane (d) α-CD/TMC (e) β-CD/TMC (f) γ-CD/TMC

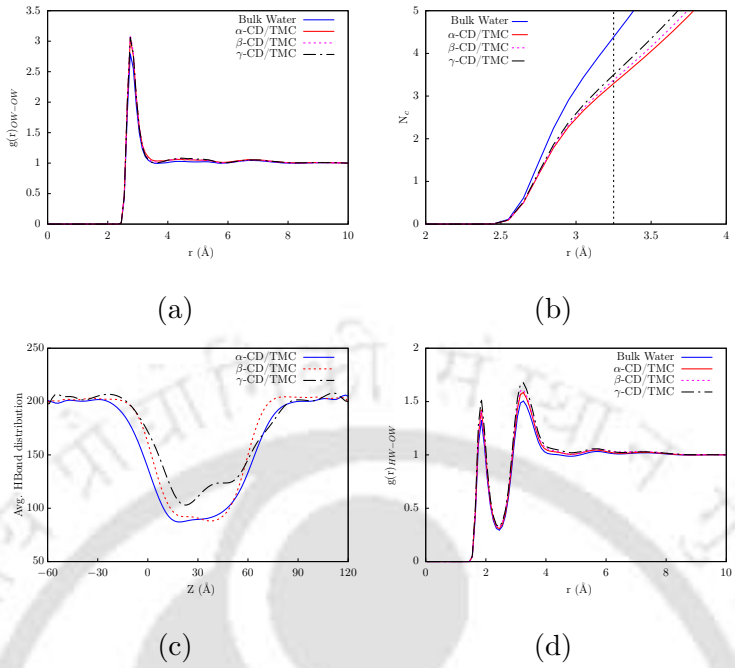

Figure B.3: (a) RDF between oxygen atoms of water molecules in bulk water and within the membrane (b) The coordination number of water molecules (N_c) (c) The average number of hydrogen bonds formed by water molecules along the z−direction (d) RDF between hydrogen and oxygen atoms of water molecules in bulk water and within the membrane

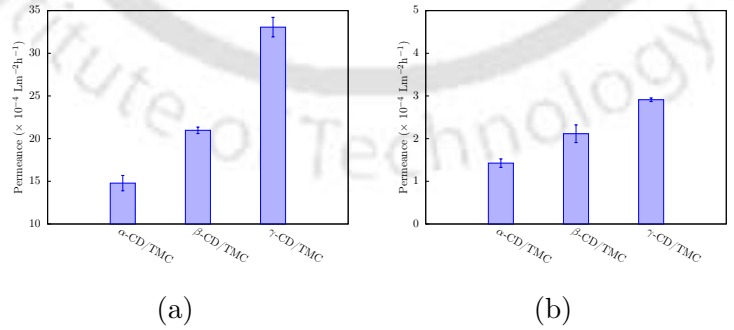

Figure B.4: (a) Water permeance of CD−based membranes (b) Hexane permeance of CD−based membranes

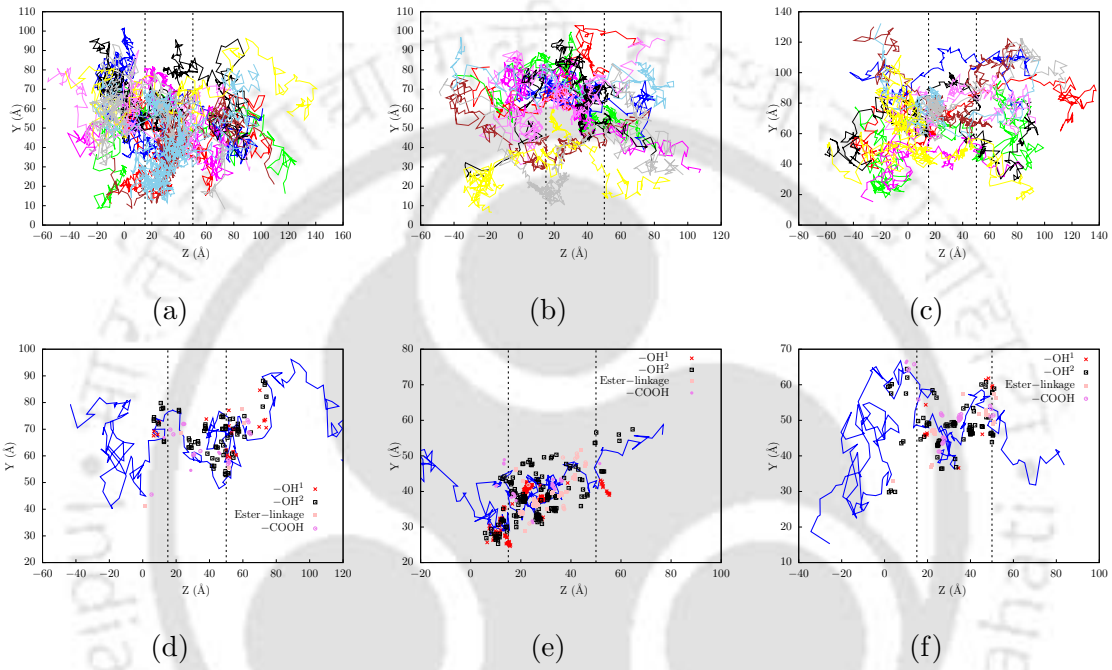

Figure B.5: Trajectories of water molecules perameating through CD−based membrane in 2D YZ plane (a) α-CD/TMC (b) β-CD/TMC (c) γ-CD/TMC; Trajectory of single water molecule permeating through the CD−based membrane in 2D YZ plane and the functional groups present within 5 $\mathring{A}$ along the trajectory, where -OH^1 represents primary hydroxyl group, and -OH^2 represents the secondary hydroxyl groups (d) α-CD/TMC (e) β-CD/TMC (f) γ-CD/TMC

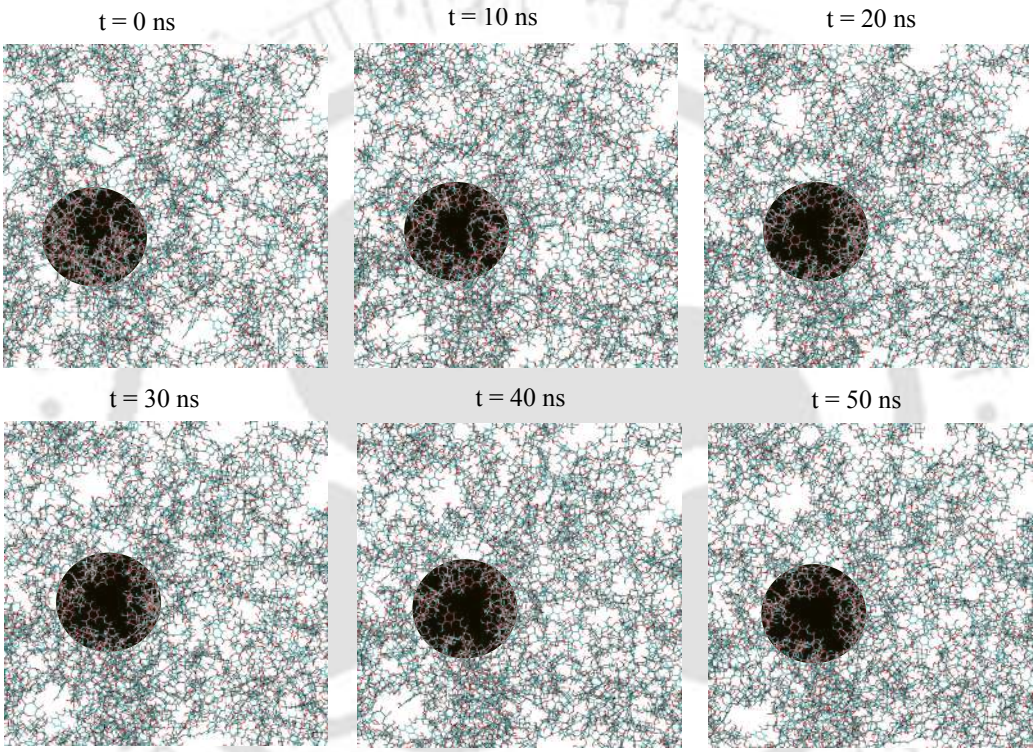

Figure B.6: Time evolution of pore spanning across the membrane

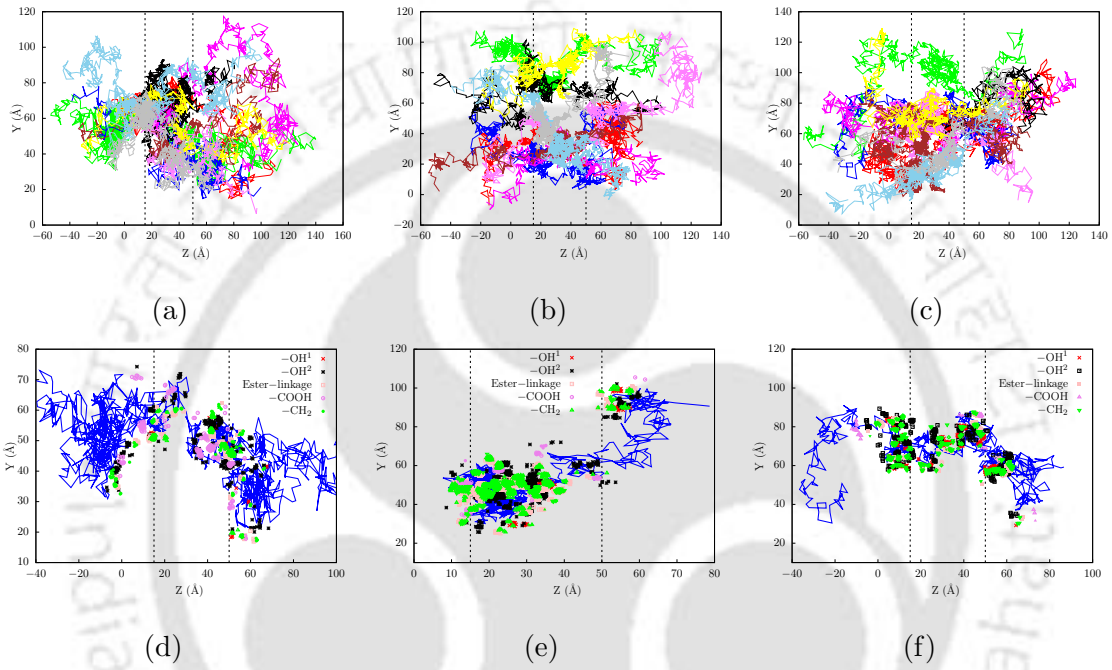

Figure B.7: Trajectories of hexane molecules perameating through CD−based membrane in 2D YZ plane (a) α-CD/TMC (b) β-CD/TMC (c) γ-CD/TMC; Trajectory of single hexane molecule permeating through the CD−based membrane in 2D YZ plane and the functional groups present within 5 $\mathring{A}$ along the trajectory, where -OH^1 represents primary hydroxyl group, and -OH^2 represents the secondary hydroxyl groups (d) α-CD/TMC (e) β-CD/TMC (f) γ-CD/TMC

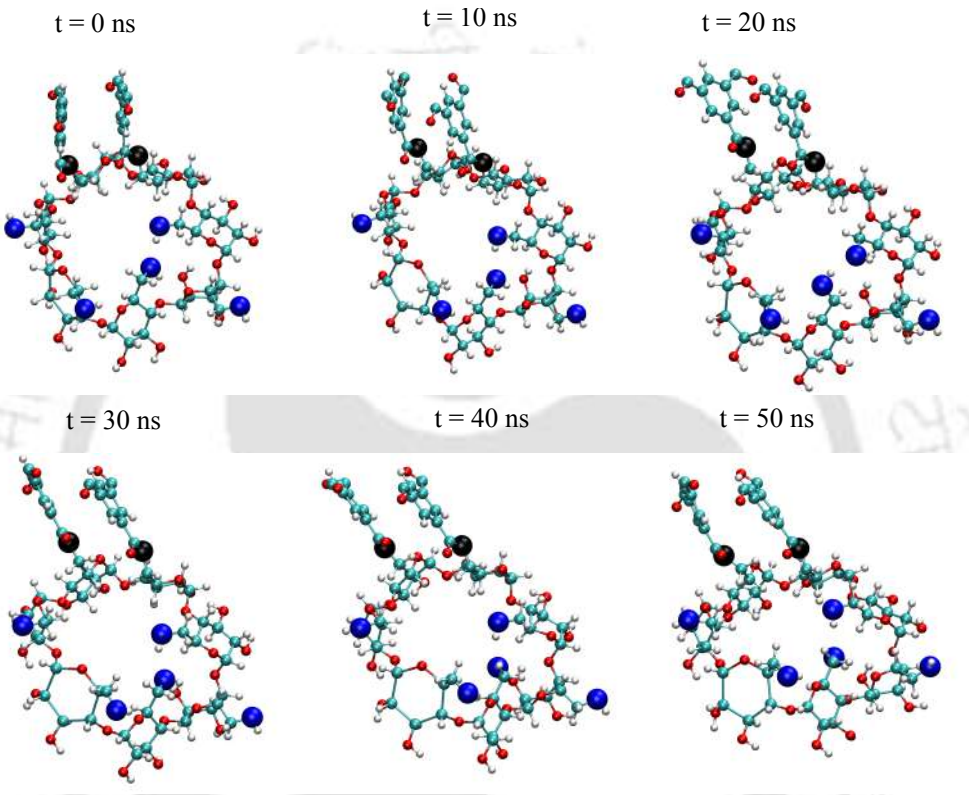

Figure B.8: Time evolution of primary hydroxyl groups facing towards cyclodextrin cavity. Blue color atoms represent the unreacted oxygen atoms of primary hydroxyl groups, and black color indicates reacted functional groups. For clarity's sake, only one CD cavity is shown here.

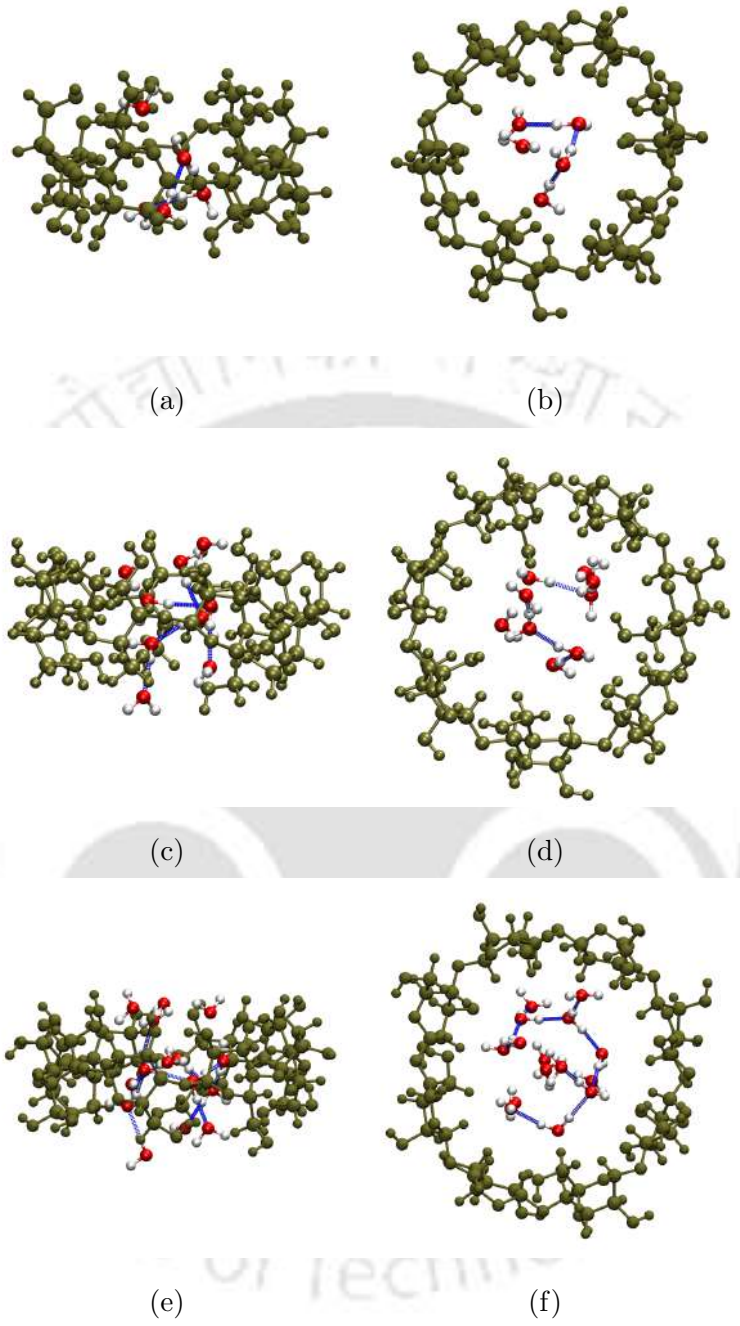

Figure B.9: VMD snapshots showing the structure of native CDs (gray CPK representation) when the maximum number of water molecules (red CPK representation) 5 in α -CD (a,b); 9 in β -CD (c,d); and 14 in γ -CD (e,f) are occupying their cavity. Blue lines correspond to hydrogen bonds.

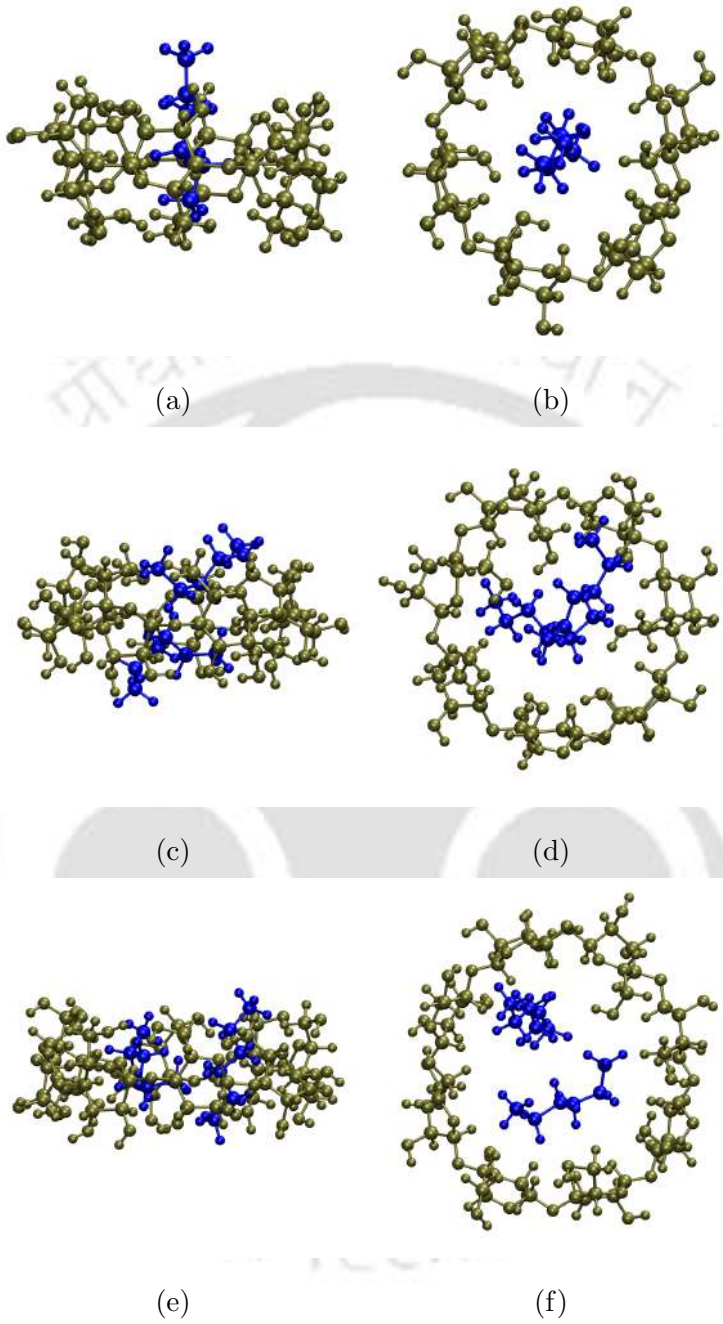

Figure B.10: VMD snapshots showing the structure of native CDs (gray CPK representation) when the maximum number of hexane molecules (blue CPK representation) 1 in α -CD (a,b); 2 in β -CD (c,d); and 2 in γ -CD (e,f) are occupying their cavity.

Forcefield verification

To verify the accuracy of force−field parameters, we computed the average water occupancy of the cyclodextrin cavities and compared them with the experimental literature. The maximum water occupancy inside the cavity is 5 in α-CD, 9 in β-CD, and 14 in γ-CD. The average water occupancy throughout simulation time is 2.7 in α-CD, 6.6 in β-CD, and 8.7 in γ-CD (see Figure B.11a). The results obtained in our simulations agree with the experimental literature, where water occupancy is 2.6 in α-CD [1], 6.5 in β-CD [2], and 8.8 in γ-CD [3]. We computed the dry membrane density after polymerization for polyester membranes, as reported in Figure B.11b. The average dry membrane density for $\alpha/\beta/\gamma$-CD/TMC is 1.05, 1.12, 1.09 gm cm^{-3}, respectively. Our results agree with experimentally reported polyester membranes [4].

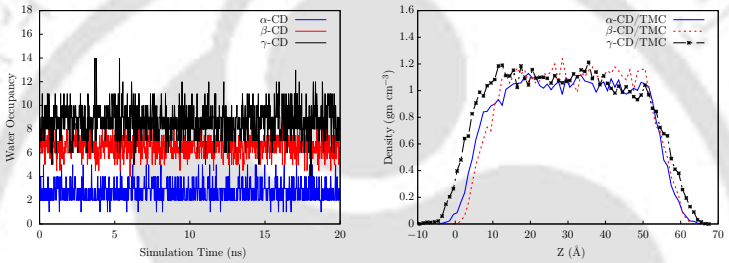

(a) (b)

Figure B.11: (a) Time evolution of water occupancy inside the CD cavity (b) Density profiles of dry membranes after polymerization.

Bibliography

[1] KK Chacko and W Saenger. Topography of cyclodextrin inclusion complexes. 15. crystal and molecular structure of the cyclohexaamylose-7.57 water complex, form iii. four-and six-membered circular hydrogen bonds. *J. Am. Chem. Soc.*, 103(7):1708–1715, 1981.

[2] Klaus Lindner and Wolfram Saenger. β-cyclodextrin dodecahydrate: Crowding of water molecules within a hydrophobic cavity. *Angew. Chem., Int. Ed.*, 17(9):694–695, 1978.

[3] Jianping Ding, Thomas Steiner, Volker Zabel, Brian E Hingerty, Sax A Mason, and Wolfram Saenger. Topography of cyclodextrin inclusion complexes. 28. neutron diffraction study of the hydrogen bonding in partially deuterated. gamma.-cyclodextrin. cntdot. 15. cntdot. 7d2o at t= 110 k. *J. Am. Chem. Soc.*, 113(21):8081–8089, 1991.

[4] Maria F Jimenez-Solomon, Qilei Song, Kim E Jelfs, Marta Munoz-Ibanez, and Andrew G Livingston. Polymer nanofilms with enhanced microporosity by interfacial polymerization. *Nat. Mater*, 15(7):760–767, 2016.

B.2 Supplementary Information for Chapter 5

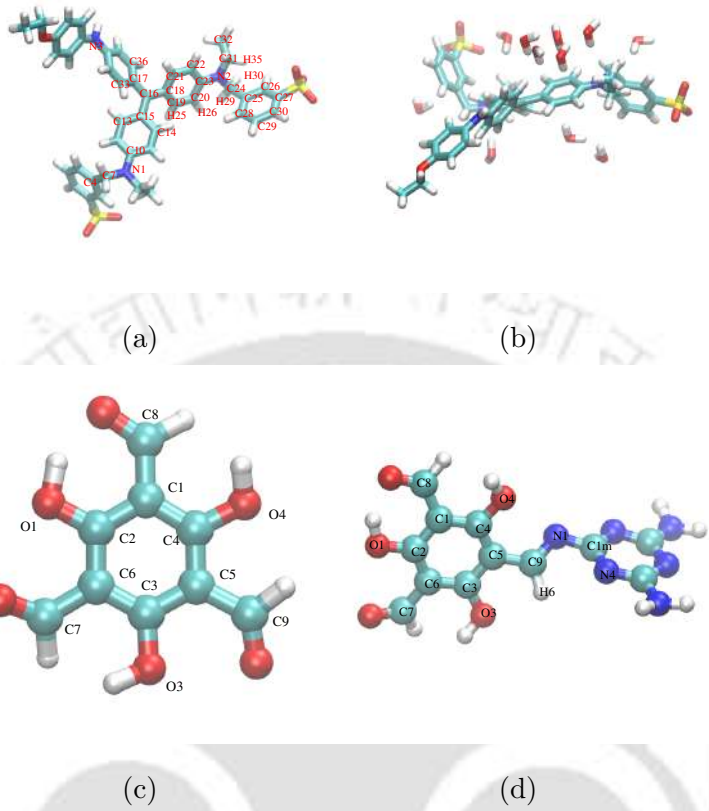

Figure B.12: (a) Optimised structure of BBR (b) BBR and Water interactions (c) Optimised structure of TFP (d) Optimised structure of TFP-MEL. Color code: C-cyan, H-white, O-red, S-yellow, N-blue

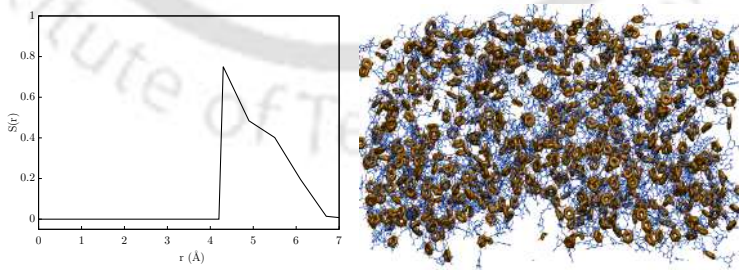

Figure B.13: (a) Benzene rings order parameter S(r) and (b) Arrangement of benzene rings in the membrane.

Table B.1: Optimised Partial Charges for BBR

Sl. No	Atom	Atom type	CGenFF	ffTK
1	C4	CG2R61	0.017	-0.124
2	C7	CG321	-0.045	0.995
3	N1	NG301	-0.312	-0.639
4	C10	CG2R61	0.134	-0.089
5	C18	CG2DC1	0.010	0.125
6	C19	CG2DC2	-0.152	0.057
7	C20	CG2DC2	-0.153	-0.333
8	C21	CG2DC2	-0.152	0.057
9	C22	CG2DC2	-0.153	-0.333
10	C23	CG2DC1	0.576	0.234
11	N2	NG2P1	-0.244	-0.387
12	C24	CG324	0.111	-0.038
13	C25	CG2R61	0.028	0.158
14	C31	CG324	0.219	0.201

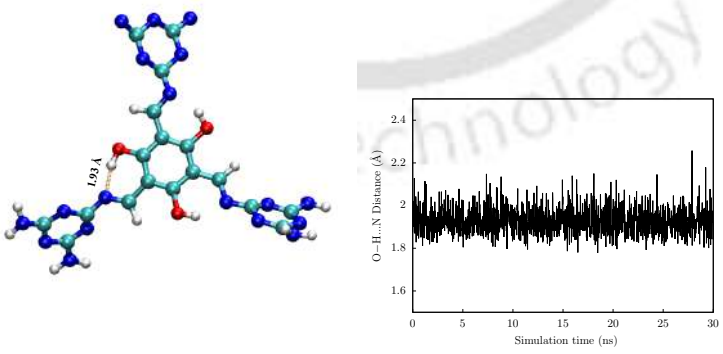

(a) (b)

Figure B.14: (a) Hydrogen bond formation bewteen iminelinkage nitrogen and hdrogen atom of the −OH group of TFP monomer (b) O−H...N distance

Table B.2: Interaction energies (Kcal/mol) for water interactions obtained from QM and MM calculations for BBR

Atom	QM-Energy	MM-energy	Energy Difference (ffTK-QM)
C4	-5.377	-5.120	0.257
C7	-3.519	-3.779	-0.26
N1	-1.492	-1.663	-0.171
C10	-7.136	-6.918	0.218
C18	-2.470	-2.734	-0.264
C19	-3.063	-2.911	0.152
C20	-2.145	-1.813	0.332
C21	-2.624	-2.301	0.323
C22	-3.422	-3.463	-0.041
C23	-4.170	-3.686	0.484
N2	NG2P1	-0.244	-0.387
C24	-5.194	-6.502	-1.308
C25	-4.582	-4.798	-0.216
C31	-1.222	-0.852	0.370
Average of Absolute values			0.350

Table B.3: Angle Parameters of BBR

S.No	Atom	Atom Types	CGenff		ffTK	
			$\mathbf{k}_\theta$	θ	$\mathbf{k}_\theta$	θ
1	C20-C23-C22	CG2DC2-CG2DC1-CG2DC2	48	113	176.933	118.246
2	C15-C16-C17	CG2R61-CG2DC1-CG2R61	48	113	140.694	115.493
3	C25-C24-N2	CG2R61-CG324-NG2P1	53	115.2	142.585	113.149
4	C24-N2-C31	CG324-NG2P1-CG324	53	120	214.734	117.314

Table B.4: Dihedral parameters for BBR

S.No	Atoms/atom types	CGenff			ffTK		
		$\mathbf{k}_\psi$	n	δ	$\mathbf{k}_\psi$	n	δ
1	C21-C18-C16-C17	0.56	1	180	10.027	1	0
	CG2DC2-CG2DC1-CG2DC1-CG2R61	7	2	180	2.223	3	0
2	C21-C18-C19-C20	0.5	1	180	1.447	1	180
	CG2DC2-CG2DC1-CG2DC2-CG2DC2	2	2	0	0.7710	2	180
		1	3	0	2.369	3	180
3	C22-C23-C20-H26	1	2	180	3.199	1	180
	CG2DC2-CG2DC1-CG2DC2-HGA4				0.508	2	180
					1.8070	3	180
4	C17-C16-C15-C14	0.750	2	180	8.183	1	180
	CG2R61-CG2DC1-CG2R61-CG2R61	0.19	4	0	4.202	3	0
5	C26-C25-C24-N2	0.1190	2	0	1.004	1	180
	CG2R61-CG2R61-CG324-NG2P1	0.1320	4	180	0.58	3	180
		0.0130	6	180			
6	C4-C7-N1-C10	2	1	180	5.220	1	180
	CG2R61-CG321-NG3O1-CG2R61	0.3	3	180	0.163	2	0
					2.185	3	180
7	C25-C24-N2-C31	0.1	3	0	1.6510	1	180
	CG2R61-CG324-NG2P1-CG324				1.262	2	180
					0.952	3	0
8	C32-C31-N2-C23	0.61	1	0	0.823	1	180
	CG331-CG324-NG2P1-CG2DC1	0.62	2	180	0.026	2	0
		0.25	3	0	0.032	3	180
		0.60	4	0			
		0.25	6	0			
9	C25-C24-N2-C23	0.61	1	0	0.136	1	0
	CG2R61-CG324-NG2P1-CG2DC1	0.62	2	180	1.047	2	0
		0.25	3	0	0.778	3	0
		0.60	4	0			
		0.25	6	0			
10	C32-C31-N2-C24	0.1	3	0	1.993	1	0
	CG331-CG324-NG2P1-CG324				1.012	2	180
11	H29-C24-N2-C31	0	3	0	0.4320	1	0
	HGA2-CG324-NG2P1-CG2DC1				0.2330	2	180

Table B.5: Dihedral parameters for TFP-MEL polymer

S.No	Atoms/atom types	CGenff			ffTK		
		$\mathbf{k}_\psi$	**n**	δ	$\mathbf{k}_\psi$	**n**	δ
1	C5-C9-N1-C1m	12	2	180	12.866	1	0
	CG2R61-CG2DC1-NG2D1-CG2R64				3.036	2	180
					0.58	3	0
					0.491	4	0
2	H6-C9-N1-C1m	4	2	180	8.01	1	180
	HGA4-CG2DC1-NG2D1-CG2R64				3.992	2	180
					9.024	3	0
					4.202	4	180
3	C9-C5-C4-O4	3.1	2	180	1.732	3	180
	CG2DC1-CG2R61-CG2R61-OG311						
4	C7-C6-C2-O1	2.4	2	180	1.423	3	180
	CG2O4-CG2R61-CG2R61-OG311						
5	N4-C1m-N1-C9	0.8	1	180	15.973	1	0
	NG2R62-CG2R64-NG2D1-CG2DC1	4.82	2	180	0.43	2	0
		0.02	3	180	3.363	3	0
					0.156	4	0

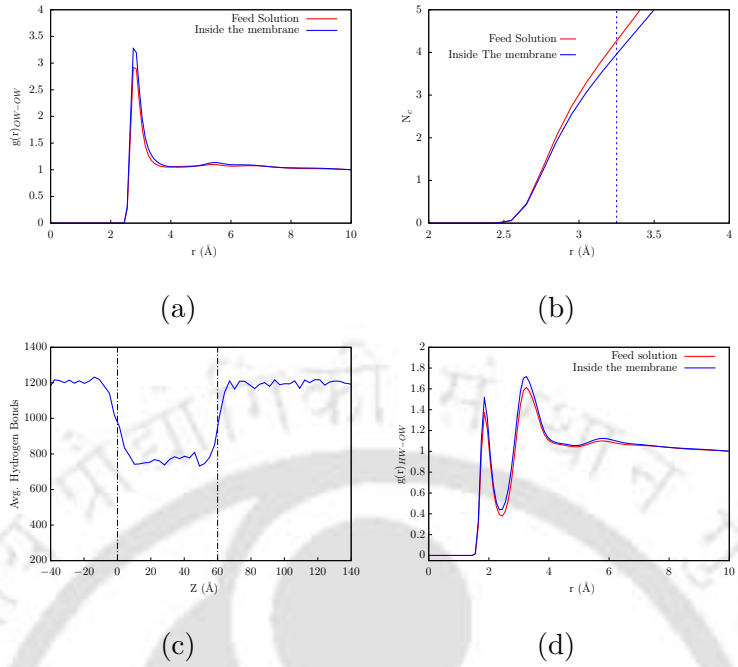

Figure B.15: (a) RDFs of water oxygen atoms in the feed solution and inside the membrane (b) Water coordination number at cutoff distance of 3.25 $\AA$ (c) Average number of hydrogen bonds per water molecules along the Z-axis (d) RDF between hydrogen and oxygen atoms of water molecules in feed solution and inside the polyimine membrane.

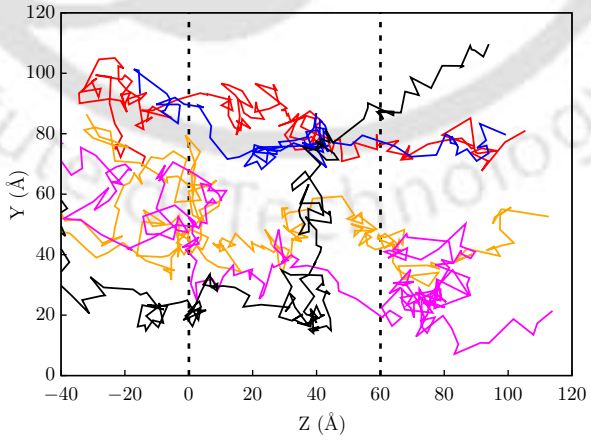

Figure B.16: Trajectories of selected water molecules on 2D YZ plane

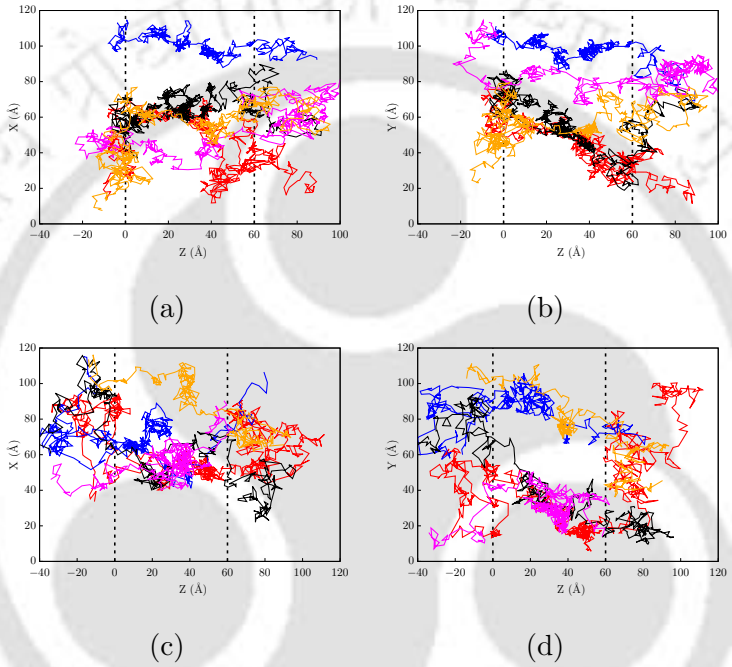

Figure B.17: (a) Pathways of selected Na^+ ions in 2D XZ plane (b) Pathways of selected Na^+ ions in 2D YZ plane (c) Pathways of selected Cl^- ions in 2D XZ plane (d) Pathways of selected Cl^- ions in 2D YZ plane

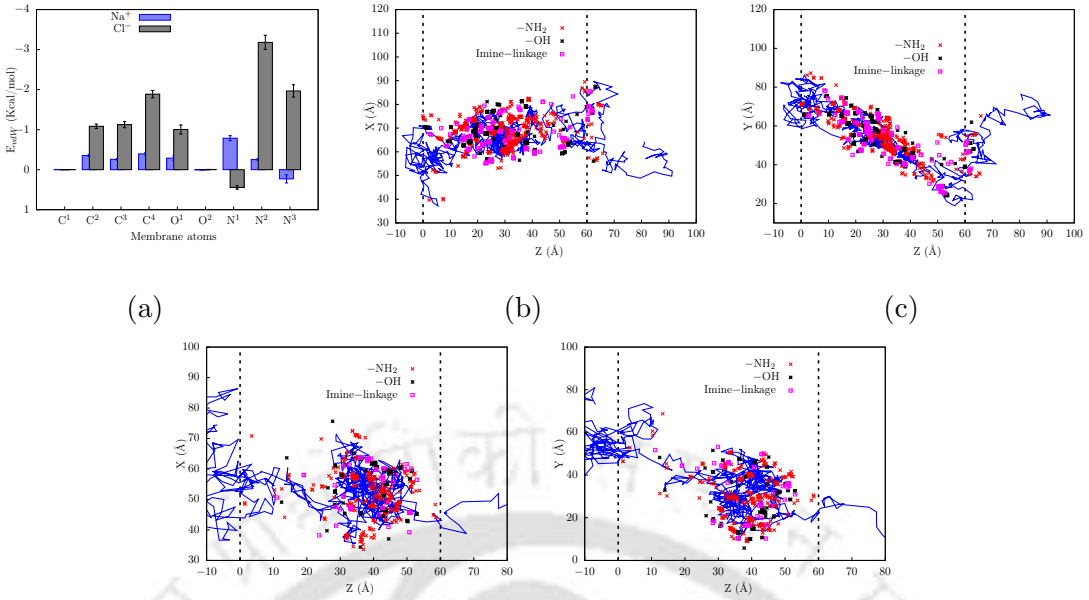

(a) (b) (c)

(d) (e)

Figure B.18: (a) van der Waals interaction energies of chloride salt ions with mebrane atoms (b) Trajectory of single Na^+ ion and fucntional groups of the membrane within 5 $\mathring{A}$ along the trajectory in 2D XZ plane (c) Trajectory of single Na^+ ion and fucntional groups of the membrane within 5 $\mathring{A}$ along the trajectory in 2D YZ plane (d) Trajectory of single Cl^- ion and fucntional groups of the membrane within 5 $\mathring{A}$ along the trajectory in 2D XZ plane (e) Trajectory of single Cl^- ion and fucntional groups of the membrane within 5 $\mathring{A}$ along the trajectory in 2D YZ plane

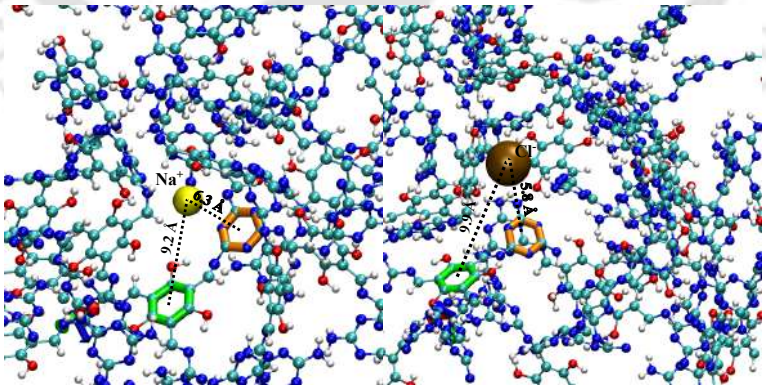

(a) (b)

Figure B.19: (a) Snapshots of the COM distance between Na^+ ion with MEL heterocyclic ring and TFP benzene ring (b) Snapshots of the COM distance between Cl^- ion with MEL heterocyclic and TFP benzene ring; color code of ring; green - TFP, orange - MEL heteroring

B.3 Supplementary Information for Chapter 6

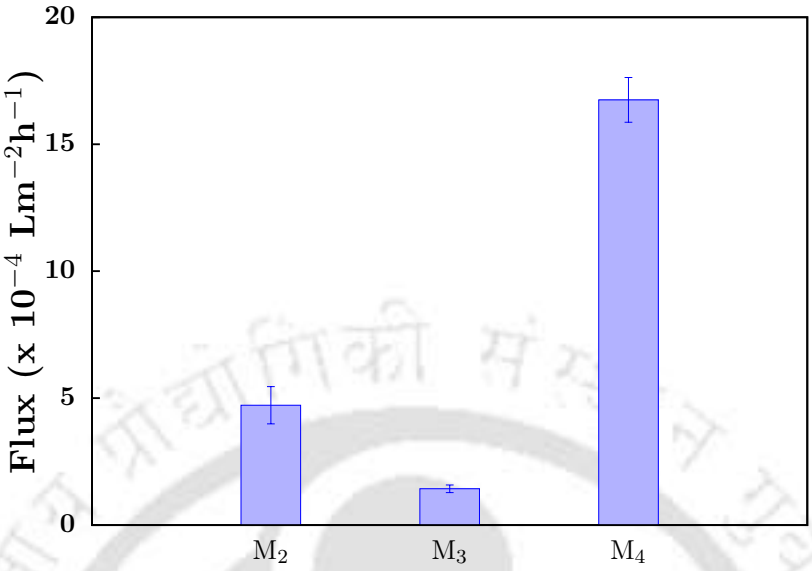

Figure B.20: Solvent permeance through the membranes using the simulation study

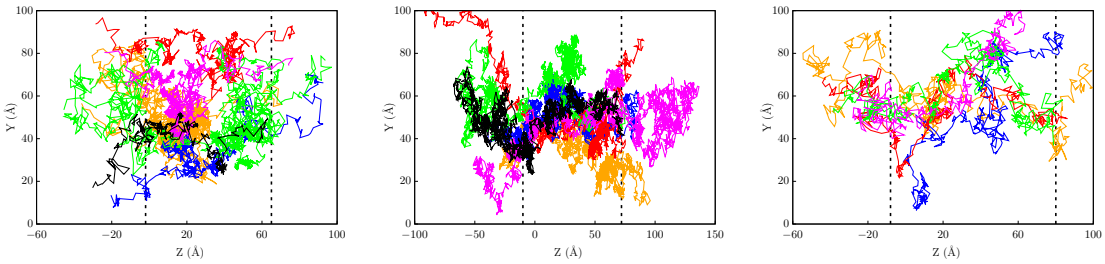

(a) (b) (c)

Figure B.21: Path of the solvent molecule trajectories through the membranes. Where (a) Trajectories of methanol molecules in the M_2 membrane represented in YZ 2D plane, (b) Trajectories of DMF molecules in the M_3 membrane represented in YZ 2D plane, (c) Trajectories of methanol molecules in the M_4 membrane represented in YZ 2D plane.

B.3.1 Fabrication of Freestanding Polyamide Nanofilm and Transfer Onto Porous Alumina Substrates

Porous alumina supports (Whatman^{TM} Anodisc^{TM}; 0.2 μm) were obtained from Whatman International Ltd., England. $m-$phenylenediamine (MPD, 99%) and trimesoyl chloride (TMC, 98%) was obtained from Sigma Aldrich, India. Hexane (99% HPLC) and methanol (99%) were purchased from Sisco Research Laboratories Pvt. Ltd. (SRL), India. Dimethylformamide (DMF) was purchased from Qualikems Fine Chem Pvt. Ltd., India. Acetone was obtained from Thermo Fisher Scientific India Pvt Ltd. Pure water (conductivity < 1.5 μS) was used to prepare the aqueous solution of MPD which was prepared from a double pass RO facility.

Freestanding polyamide nanofilm was prepared via the interfacial polymerization (IP) process at the water-hexane interface as shown in Figure B.22. The aqueous solution containing $m-$phenylenediamine (MPD) with a concentration of 2.0 wt% was poured into a glass Petri dish. After that, hexane solution containing TMC with a concentration of 0.15 wt% was gently poured on top of the aqueous amine solution to allow the interfacial polymerization for 1 min. After 1 min of IP reaction, freestanding polyamide nanofilm was picked up on top of a presubmerged porous alumina substrate by using a metal frame. Finally, the nanofilm composite membrane was post-treated at 70 ($\pm$1) °C for 2 min in a hot air oven to complete the polymerization process and achieving a high degree of network crosslinked structure.

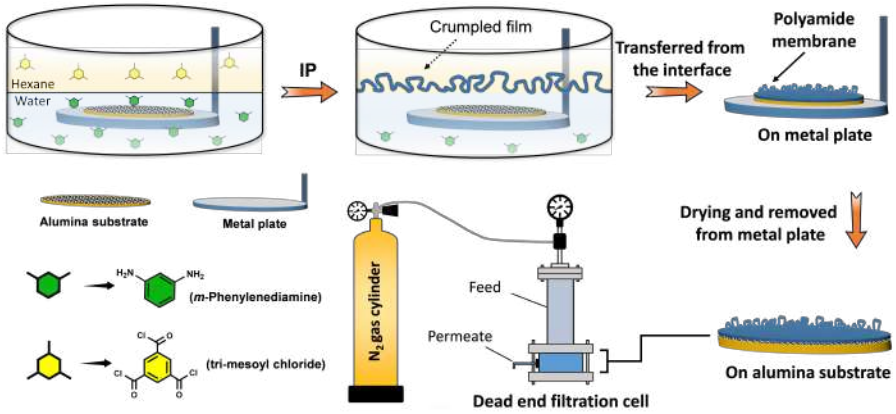

Figure B.22: Schematic presentation of the fabrication and transferring of the freestanding polyamide membrane on top of porous alumina substrates.

B.3.2 Characterization of the Polyamide Nanofilm Composite Membranes

A scanning electron microscope (SEM), JEOL JSM 7100F, Japan, was used to characterize the surface morphology and the thickness of the polyamide nanofilm layer before and after DMF activation. A 15 kV accelerating voltage was used for the operation of the SEM instrument. Leica Microsystems (EM ACE200) was used to sputter-coat a gold layer that was $2-5$ nm thick before imaging. To measure the thickness of the nanofilm after DMF activation, the composite membrane was activated by passing pure DMF through it for 15 min at an operating pressure of 1 bar at 25 °C. Following that, the porous alumina substrate with the DMF-activated nanofilm on top was taken out of the DMF and left to air dry before being dried for 30 minutes at 45 ($\pm$1) °C in a hot air oven. Finally, samples were cleaned in pure methanol by submerging them for 10 minutes, followed by 30 minutes of drying at 45 ($\pm$1) °C in a hot air oven. A small piece was fractured-cut from the alumina support and positioned vertically in the SEM sample stub. The fractured-cut samples were adhered to the SEM stub by using silver paint to prevent sample charging during SEM imaging. The elemental composition and chemical structure of the polyamide nanofilm were analysed by X-ray photoelectron spectroscopy (XPS). For the XPS analysis, freestanding polyamide nanofilm was transferred onto gold-coated silicon wafers and left to air dry at room temperature. Before the XPS study, the samples were activated by pure DMF and then washed in pure water by immersing them in water for $15-20$ minutes, followed by drying for 30 minutes at 45 ($\pm$1) °C in a hot air oven. The analysis was conducted

using Thermo Scientific^{TM} Nexsa X-ray photoelectron spectrometers, employing a microfocused monochromatic AlKα X-ray source for excitation, pass energy of 20 eV and a lowenergy flood gun for charge compensation. An X-ray spot size of 400 $\times$ 400 μm^2 was chosen and the analysis was conducted at three different spots to ensure accuracy and determine the average values of the results.

B.3.3 Filtration Setup and Performance Measurements of the Polyamide Membranes

A dead-end filtration system was employed to evaluate the solvent permeation capability of the polyamide membrane fabricated on the porous alumina substrate as presented in Figure **??**. The effective surface area of each membrane was 2.7 cm^2. In this study, methanol was used as a feed solution at 25 ($\pm$1) °C, and the applied pressure was maintained at 1 bar by using N_2 gas. Prior to measurement, each membrane was pre-compacted for at least $3-4$ hours to get constant methanol permeance. The methanol permeance was evaluated according to the following equation (1);

$$P\ (Lm^{-2}hr^{-1}bar^{-1}) = \frac{V}{A.t.\Delta p} \tag{B.1}$$

where V is the volume of the permeated methanol (liter), A is the effective membrane area (m^2) and t is the collection time (hour) under an operating pressure of Δp.

B.3.4 Characterization of the Polyamide Nanofilm Before and After DMF Activation

The morphological characteristics of the composite membranes and their nanofilms, before and after DMF activation, were examined using SEM. For this, polyamide nanofilm on top of porous alumina substrate were activated with DMF and analyzed using SEM to investigate how the activation affected the surface morphology and thickness of the polyamide nanofilm. The surface morphology and thickness of the nanofilms made on top of porous alumina support before and after activation with DMF are shown in Figure B.24a and c. The DMF-activated polyamide nanofilm composite membrane exhibits a morphology roughly comparable to that of the non-activated composite membrane. Thus, no discernible difference is observed in the surface morphology before and after DMF activation. The cross-sectional SEM images of

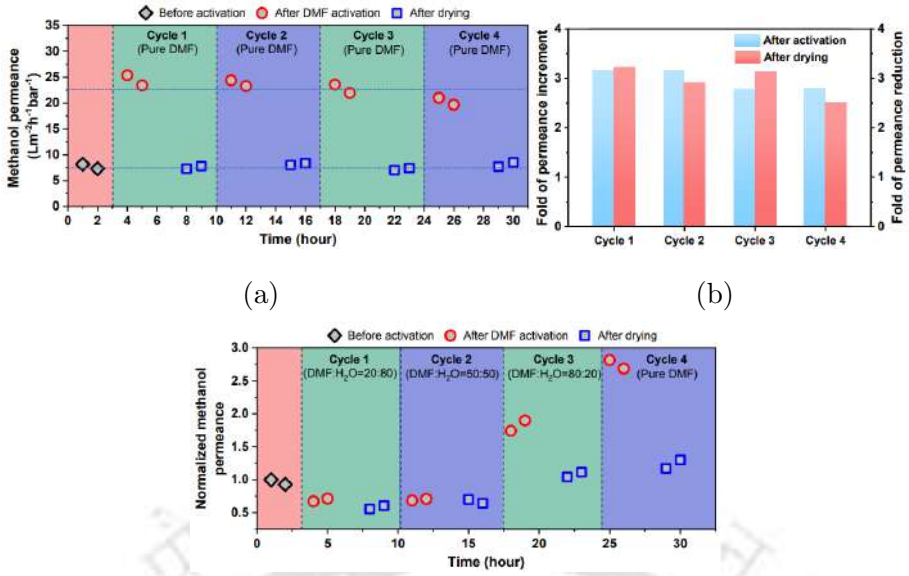

Figure B.23: (a) Methanol permeance of the polyamide membrane after DMF activation followed by drying after every cycle where pure DMF was used for activation. The membrane was prepared by reacting 2.0 wt% MPD in the aqueous phase and 0.15 wt% TMC in the organic phase at the water-hexane interface for 1 min (b) The plot of the fold of increment in methanol permeance upon DMF activation and subsequent fold of reduction of methanol permeance after drying of the polyamide membranes in each cycle (c) Methanol permeance of the polyamide membrane after DMF activation followed by drying after every cycle where a different ratio of DMF and H2O mixture was used. The membrane was prepared by reacting 2.0 wt% MPD in the aqueous phase and 0.15 wt% TMC in the organic phase at the water-hexane interface for 1 min.

the polyamide nanofilms on top of the alumina substrate are shown in Figure B.24b and d. According to the cross-sectional SEM images, the top layer thickness of the polyamide nanofilm after DMF activation slightly reduced to 26.2 nm compared to the nanofilm without activation (thickness ≈27.0 nm). However, this change is not statistically significant.

X-ray photoelectron spectroscopy (XPS) was used to examine the chemical structures and elemental compositions of the polyamide nanofilms before and after DMF activation. Figure B.25 presents the XPS results, including survey spectra, relative percentages of C, N, and O, and core-level C1s spectra of the polyamide nanofilms obtained before and after DMF activation. The survey spectrum and the C, N, and O percentages did not show any significant differences

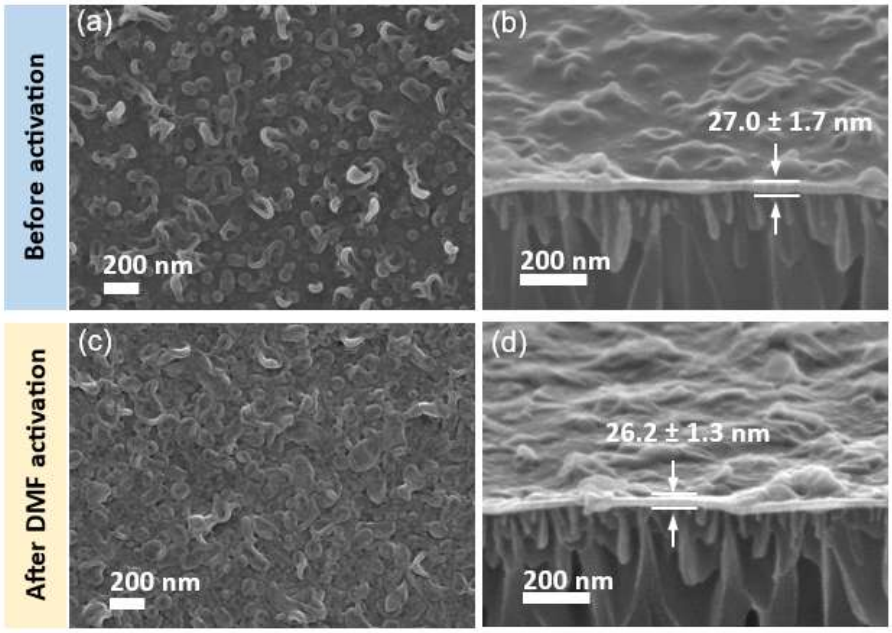

Figure B.24: Surface morphology and thicknesses of the polyamide membranes before and after DMF activation. (a,b) Before DMF activation, and (c,d) After DMF activation. The membrane was prepared by reacting 2.0 wt% MPD in the aqueous phase and 0.15 wt% TMC in the organic phase at the water-hexane interface for 1 min.

before and after DMF activation, as depicted in Figure B.25a and b. To analyse the chemical species present in the nanofilm before and after DMF activation, the C1s peak of the nanofilms (Figure B.25c and d) was deconvoluted into five peaks at 284.3 eV (C-C, C=C, and C-H), 285.0 eV (β-shift for C-CONH, C-COO), 285.8 eV (C-N), 287.8 eV (N-C=O), and 288.4 eV (O-C=O). It is observed from Figure B.25c and d (before and after activation) that the amount of C-N (-C-NH_2, -CONH-C in C1s) and carboxylic acid group (O-C=O in C1s) remained similar at around 7.8% and 4.8%, respectively.

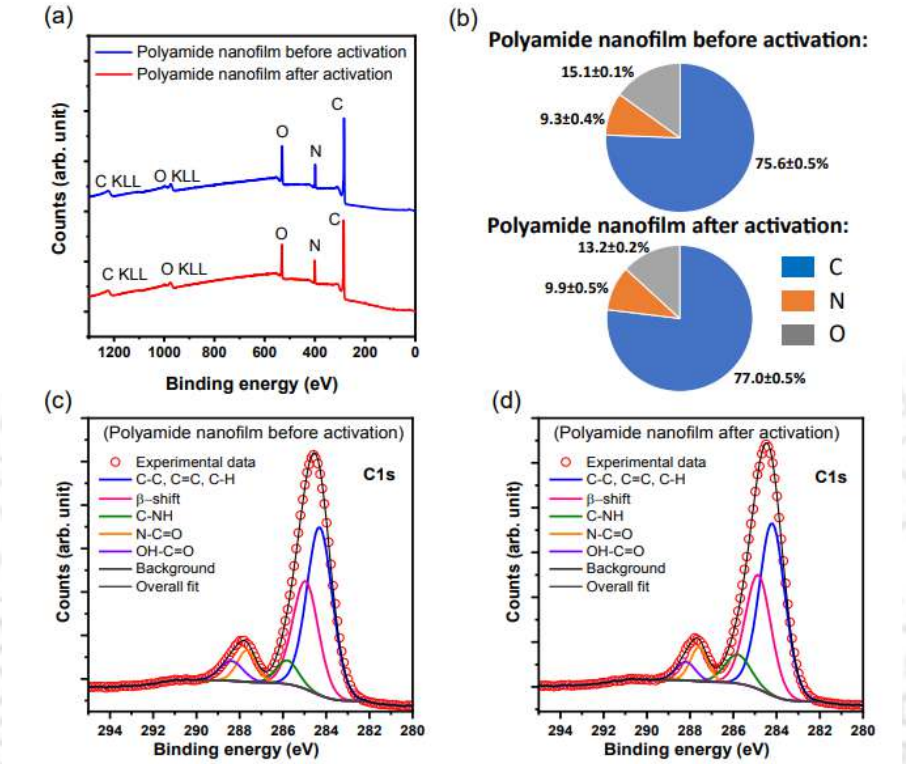

Figure B.25: XPS survey and C1s spectra of the polyamide nanofilms onto a gold-coated silicon wafer. (a, b) Survey spectra and percentage of C, N, and O of the polyamide nanofilms before and after DMF activation. (c) C1s spectra of the polyamide nanofilms before DMF activation. (d) C1s spectra of the polyamide nanofilm after DMF activation. The membrane was prepared by reacting 2.0 wt% MPD in the aqueous phase and 0.15 wt% TMC in the organic phase at the water-hexane interface for 1 min.